USAATCOM TR 94-D-22

U.S. ARMY AVIATION
AND TROOP COMMAND

APPLICATION OF MULTIGRID COMPUTATIONAL FLUID DYNAMICS (CFD) METHODS TO ROTOR ANALYSIS

Hong Hu

Hampton University
Hampton, VA 23668

March 1995

Final Report

Prepared for

AVIATION APPLIED TECHNOLOGY DIRECTORATE
U.S. ARMY AVIATION AND TROOP COMMAND
FORT EUSTIS, VA 23604-5577

TECHNICAL POSITION STATEMENT

Currently, there are only two computer codes which solve the Euler/Navier-Stokes (ENS) equations for rotorcraft applications. Both of these methods are variations on established fixed-wing codes based on the implicit algorithm approach. All of these methods have problems with convergence, dissipation, and time stepping. There remains a large body of ENS technology which has yet to be applied to rotor applications. The report details the development of the application of an advanced computational fluid dynamics (CFD) model to the problem of helicopter rotor aerodynamic prediction. The new method makes use of the classic Jameson 4th order Runge-Kutta method coupled with multigrid acceleration. The approach used in this work was to modify an existing code, TLNS3D (developed at Langley Research Center), to include the appropriate rotational terms. The code was then used to compute both rotating and nonrotating solutions on selected rotor platforms. Emphasis was placed on studying the tip vortex formation and surface pressures of these blades. A limited comparison with experimental data is presented. More detailed comparisons with other codes and data sets will await further work.

REPORT DOCUMENTATION PAGE

Form Approved
OMB No. 0704-0188

1. AGENCY USE ONLY *(Leave blank)*

2. REPORT DATE
March 1995

3. REPORT TYPE AND DATES COVERED
Final Report 1 Sep 93 - 31 Aug 94

4. TITLE AND SUBTITLE
Application of Multigrid Computational Fluid Dynamics (CFD)
Methods to Rotor Analysis

5. FUNDING NUMBERS
(C) DAAJ02-93-C-0021

6. AUTHOR(S)
Hong Hu

7. PERFORMING ORGANIZATION NAME(S) AND ADDRESS(ES)
Hampton University
Hampton, VA 23668

8. PERFORMING ORGANIZATION REPORT NUMBER

9. SPONSORING/MONITORING AGENCY NAME(S) AND ADDRESS(ES)
Aviation Applied Technology Directorate
U.S. Army Aviation and Troop Command
Fort Eustis, VA 23604-5577

10. SPONSORING/MONITORING AGENCY REPORT NUMBER
USAATCOM TR 94-D-22

11. SUPPLEMENTARY NOTES

12a. DISTRIBUTION/AVAILABILITY STATEMENT
Approved for public release; distribution is unlimited.

12b. DISTRIBUTION CODE

13. ABSTRACT *(Maximum 200 words)*

The TLNS3DR code is applied to various advanced rotor blades to study tip vortex and to investigate the gêneral capabilities of the code. For nonrotating flows, the solutions in terms of the tip vortex and surface pressure coefficients are obtained for realistic helicopter rotor-tip configurations to study effects of blade planforms on the tip vortex under incompressible flow condition. Calculated results are compared with experimentally obtained data at NASA-Langley's Basic Aerodynamic Research Wind Tunnel (BART). A Berp-type tip, a swept-type tip and its equivalent taper-type tip configurations are investigated. For both nonrotating and rotating flows, the Berp-type blade, the swept-type blade, and its equivalent taper-type and rectangle-type blades with zero twist are considered under compressible flow condition. Solutions are presented.

14. SUBJECT TERMS
Rotor-tip, rotor-blade, hovering motion, Navier-Stokes equations, multigrid method, CFD, TLNS3DR

15. NUMBER OF PAGES
146

16. PRICE CODE

17. SECURITY CLASSIFICATION OF REPORT	**18. SECURITY CLASSIFICATION OF THIS PAGE**	**19. SECURITY CLASSIFICATION OF ABSTRACT**	**20. LIMITATION OF ABSTRACT**
UNCLASSIFIED	UNCLASSIFIED	UNCLASSIFIED	

PREFACE

The research reported in this document was performed under contract DAAJ02-93-C-0021 from the U.S. Army Aviation Applied Technology Directorate. Dr. Henry Jones is the Contracting Officer's Technical Representative, and he has provided helpful suggestions and guidance during this investigation. The TLNS3D code and WTCO code were provided by Dr. Veer Vatsa of NASA Langley Research Center. Mr. Bill Jones at GEO Lab of NASA Langley Research Center helped to generate the C-O meshes for the Berp-tip and the Berp-blade. Their assistance is truly appreciated.

SUMMARY

This report documents the application of a multigrid Computational Fluid Dynamics (CFD) method to rotor aerodynamic prediction. The CFD code TLNS3DR is used. The code is the modified version of the nonrotating wing TLNS3D code with the addition of the rotation term. The code solves the three-dimensional thin-layer Navier-Stokes equations using an explicit multistage Runge-Kutta type of time stepping with multigrid method. For nonrotating wings, the TLNS3DR code is identical to the TLNS3D code.

The TLNS3DR code is applied to various advanced rotor blades to study tip vortex and to investigate the capability of the code in rotor analysis. For nonrotating flows, the solutions in terms of the tip vortex and surface pressure coefficients are obtained for realistic helicopter rotor-tip configurations to study effects of blade planforms on the tip vortex under incompressible flow condition. Calculated results are compared with experimentally obtained data at NASA-Langley's Basic Aerodynamic Research Wind Tunnel (BART). The Berp-tip, the swept-tip and an equivalent taper-tip configurations are investigated. For both nonrotating and rotating flows, the Berp-type blade, the swept-type blade, and equivalent taper-type and rectangle-type blades with zero twist are considered under compressible flow condition. Solutions for rotating flows are presented along with those of nonrotating flows to study the effect of the rotation term added to the TLNS3DR code in addition to the study of the tip vortex.

CONTENTS

FIGURES

1. INTRODUCTION

The accurate and efficient prediction of rotor flow fields poses a particularly challenging problem in helicopter rotor design. The accurate prediction of the aerodynamic forces on the rotor requires a correct prediction of the vortex wake, including the blade trailing wake as well as the blade-vortex interaction (BVI). The BVI noise is also one of the most important noise sources for rotary wings. The detailed experimental test for predicting rotor flow field is very expensive and complex, which limits the amount of available data, particularly on advanced rotors. Therefore, other methods such as Computational Fluid Dynamics (CFD) are needed in rotor analysis.

The CFD methods for calculating helicopter rotor flow fields can be divided into two types: integral equation methods (panel methods) and finite-difference/finite-volume methods. Integral equation methods are restricted to linear, low-speed, subsonic, or at most, to nonlinear flows with weak shocks. This is a very serious limitation, because modern rotor blades operate in the transonic regime, where the nonlinear compressibility is important and shocks can exist in the flow field. Finite-difference/finite-volume methods based on Navier-Stokes (NS) equations with a single grid for rotor flow fields were developed[1,2]. The methods can treat compressible flows with shocks, including strong shocks, in the region of the rotor blade accurately. However, the calculation of NS equations on a fine, single grid is expensive.

A multigrid NS CFD computer code, TLNS3D, was developed[3] for the fixed-wing motion. The TLNS3D code solves the three-dimensional thin-layer NS equations using an explicit multistage Runge-Kutta type of time-stepping with multigrid method. The philosophy of the multigrid method is the use of successively coarser grids to compute corrections to a fine grid solution. The use of multigrid strategy results in a much faster convergence than the single-grid method. The efficiency of the multigrid method using five-stage Runge-Kutta time-stepping was demonstrated[3] through computations for transonic flows over fixed wings. The code was shown to result in a significant reduction in CPU time as compared to the single-grid multistage time-stepping method. The code is recently modified for rotary-wing calculations[4] with the addition of the rotation term, although the accuracy of the code for rotary-wing calculations has not been tested. The new code called TLNS3DR is identical to the TLNS3D code for nonrotating wings.

The purpose of the present work is to use the efficient multigrid TLNS3DR CFD code to analyze advanced rotor tip designs and to further investigate the capability of the code for rotor aerodynamic analysis. For nonrotating flows, the solutions in terms of the tip vortex and surface pressure coefficients are obtained for realistic helicopter rotor-tip configurations to study the effects of blade planforms on the tip vortex under incompressible flow condition. Calculated results are compared with experimentally obtained data at NASA-Langley's Basic Aerodynamic Research Wind Tunnel (BART). The Berp-tip, the swept-tip and an equivalent taper-tip configurations are investigated. For both nonrotating and rotating flows, the Berp-type blade, the swept-type blade, and equivalent taper-type and rectangle-type blades with zero twist are considered under compressible flow condition. Solutions for rotating flows are presented along with those of nonrotating flows to study the effect of the rotation term added to the TLNS3DR code in addition to the tip vortex study.

2. METHODOLOGY OF THE TLNS3DR CODE

2.1 NS Equations in Blade-fixed Frame

For a general motion of a rotor blade, the governing equations are simple to solve if a rotor blade-fixed moving frame of reference formulation is used. The moving frame of reference (x, y, z) is translating at a velocity of $\vec{V}_o(t)$ and rotating around a pivot point (rotor blade axis: $\vec{r}_p = (x_p, y_p, z_p)$) at an angular velocity of $\vec{\Omega}(t)$. The relation for the absolute velocity ($\vec{V} = (u, v, w)$), relative velocity ($\vec{V}_r = (u_r, v_r, w_r)$) and transformation velocity ($\vec{V}_t = (u_t, v_t, w_t) = \vec{V}_o + \vec{V}_e = \vec{V}_o + \vec{\Omega} \times \vec{r}$) is given by

$$\vec{V} = \vec{V}_r + \vec{V}_o + \vec{\Omega} \times \vec{r} \tag{1}$$

where $\vec{r}$ is the position vector measured in the blade-fixed moving frame of reference relative to $\vec{r}_p$. It should be noted that the transformation velocity ($\vec{V}_t$) includes both translation ($\vec{V}_o$) and rotation ($\vec{\Omega} \times \vec{r}$) velocities and therefore this formulation is general for both hovering and forwarding motion of the helicopter. For the fixed-wing motion, the transformation velocity is set to zero, and hence the relative velocity is the same as the absolute velocity.

The NS equations in terms of the relative velocity in the blade-fixed moving frame of reference is specialized to a body fitted coordinate system (ξ, η, ζ) in computational space, where ξ, η and ζ represent the streamwise, normal and spanwise directions, respectively. The thin-layer assumption is employed by keeping a viscous diffusion term in the normal (η) direction only, since the dominant viscous effects arise from viscous diffusion normal to the body surface for high-Reynolds-number turbulent flows. For the time-independent (ξ, η, ζ) coordinate system in the blade-fixed moving frame of reference, the thin-layer NS equations take the following form[3,4]:

$$\frac{\partial'}{\partial t'}(J^{-1}U_r) + \frac{\partial F_r}{\partial \xi} + \frac{\partial G_r}{\partial \eta} + \frac{\partial H_r}{\partial \zeta} = \frac{\partial G_{vr}}{\partial \eta} + J^{-1}S \tag{2}$$

with

$$U_r = [\rho, \rho u_r, \rho v_r, \rho w_r, \rho e_r]^t \tag{3}$$

$$F_r = J^{-1}[\rho\tilde{u}_r, \rho\tilde{u}_r u_r + \xi_x p, \rho\tilde{u}_r v_r + \xi_y p, \rho\tilde{u}_r w_r + \xi_z p, \rho\tilde{u}_r h_r]^t \tag{4}$$

$$G_r = J^{-1}[\rho\tilde{v}_r, \rho\tilde{v}_r u_r + \eta_x p, \rho\tilde{v}_r v_r + \eta_y p, \rho\tilde{v}_r w_r + \eta_z p, \rho\tilde{v}_r h_r]^t \tag{5}$$

$$H_r = J^{-1}[\rho\tilde{w}_r, \rho\tilde{w}_r u_r + \zeta_x p, \rho\tilde{w}_r v_r + \zeta_y p, \rho\tilde{w}_r w_r + \zeta_z p, \rho\tilde{w}_r h_r]^t \tag{6}$$

$$G_{vr} = J^{-1}\frac{\sqrt{\gamma}M_\infty \mu \bar{\epsilon}}{R_e}[0, \phi_1 u_{r_\eta} + \eta_x\phi_2, \phi_1 v_{r_\eta} + \eta_y\phi_2, \phi_1 w_{r_\eta} + \eta_z\phi_2, \phi_1 a + \tilde{v}_r\phi_2]^t \tag{7}$$

$$\begin{aligned} S = [0, -\rho a_{t_x}, -\rho a_{t_y}, -\rho a_{t_z},\\ -\rho[\vec{V}_r \cdot \vec{a}_o + (\vec{\Omega} \times \vec{r}) \cdot \vec{a}_o + \vec{V}_o \cdot (\vec{a}_t - \vec{\Omega} \times \vec{V}_r)\\ + \vec{V}_r \cdot (\frac{\partial'\vec{\Omega}}{\partial t'} \times \vec{r}) + (\vec{\Omega} \times \vec{r}) \cdot (\frac{\partial'\vec{\Omega}}{\partial t'} \times \vec{r})]]^t \end{aligned} \tag{8}$$

where

$$\phi_1 = \eta_x^2 + \eta_y^2 + \eta_z^2 \tag{9}$$

$$\phi_2 = \frac{1}{3}(\eta_x u_{r\eta} + \eta_y v_{r\eta} + \eta_z w_{r\eta}) \tag{10}$$

$$a = (\frac{q^2}{2})_\eta + (\frac{\gamma}{\gamma - 1})\frac{\tilde{\epsilon}}{P_r \bar{\epsilon}} T_\eta \tag{11}$$

$$q^2 = u_r^2 + v_r^2 + w_r^2 \tag{12}$$

where the prime ($\prime$) denotes the operation with respect to the blade-fixed moving frame of reference. In Eqs. (7) and (11), the turbulent eddy-viscosity correction $\bar{\epsilon}$ and turbulent eddy-conductivity correction $\tilde{\epsilon}$ are used. The algebraic turbulent model of Baldwin and Lomax[5] is employed.

The pressure p and the total enthalpy h_r are calculated by

$$p = (\gamma - 1)\rho(e_r - \frac{V_r^2}{2} + \frac{V_t^2}{2}) \tag{13}$$

and

$$h_r = \frac{\gamma p}{\rho(\gamma - 1)} + \frac{V_r^2}{2} - \frac{V_t^2}{2} \tag{14}$$

respectively. The $\vec{a}_t$ is the acceleration of the transformation velocity due to the moving frame of reference given by

$$\begin{aligned} \vec{a}_t = (a_{tx}, a_{ty}, a_{tz}) &= \frac{D\vec{V}}{Dt} - \frac{D'\vec{V}_r}{Dt'} \\ &= \vec{a}_o + (\frac{\partial'\vec{\Omega}}{\partial t'} \times \vec{r}) + 2(\vec{\Omega} \times \vec{V}_r) + \vec{\Omega} \times (\vec{\Omega} \times \vec{r}) \end{aligned} \tag{15}$$

The contravariant velocity components used in Eqs. (4) -(7) are given by

$$\tilde{u}_r = \xi_x u_r + \xi_y v_r + \xi_z w_r \tag{16}$$

$$\tilde{v}_r = \eta_x u_r + \eta_y v_r + \eta_z w_r \tag{17}$$

$$\tilde{w}_r = \zeta_x u_r + \zeta_y v_r + \zeta_z w_r \tag{18}$$

Equation (2) is the most general form of thin-layer NS equations in the blade-fixed moving frame of reference in terms of relative velocity. The S-term in Eq. (2) is the source term contributed from the time-dependent rotation ($\vec{\Omega}(t)$) and translation ($\vec{V}_o(t)$) of the rotor blade. For the hovering motion case considered here, $\vec{V}_o = 0$ and $\vec{\Omega} = 0\vec{i} - \Omega\vec{j} + 0\vec{k}$ with $\Omega = constant$, the S-term in Eq. (2), or Eq. (8), reduces to

$$S = \rho[0, (x - x_p)\Omega^2 + 2\Omega w_r, 0, (z - z_p)\Omega^2 - 2\Omega u_r, 0]^t \tag{19}$$

For fixed-wing motion, the source term S is zero and the relative velocity $\vec{V}_r$ is the same as the absolute velocity $\vec{V}$; in this case, the TLNS3DR code is identical to the fixed-wing TLNS3D code.

2.2 Finite-Volume Discretization

The TLNS3DR code is based on the fixed-wing TLNS3D code[3] as mentioned earlier. The difference of the formulation of TLNS3DR from that of TLNS3D is due to the source term S. Hence the numerical scheme follows exactly the one of the TLNS3D code with the addition of the source term S, along with the necessary modification of the boundary conditions for hovering motion.

The semi-discrete form of Eq. (2) is obtained after replacing the spatial derivatives by central differences,

$$\begin{aligned}\frac{\partial'}{\partial t'}(J^{-1}U_r)_{i,j,k} &+ (F_{ri+1/2,j,k} - F_{ri-1/2,j,k}) \\ &+ (G_{ri,j+1/2,k} - G_{ri,j-1/2,k}) \\ &+ (H_{ri,j,k+1/2} - H_{ri,j,k-1/2}) \\ &= (G_{vri,j+1/2,k} - G_{vri,j-1/2,k}) + J^{-1}_{i,j,k}S_{i,j,k}\end{aligned} \tag{20}$$

Using the notation Q_r to represent all inviscid flux terms, Q_{vr} to represent the viscous flux terms and D_r to represent the artificial dissipative fluxes for convenience, Eq. (20) is rewritten as

$$\frac{\partial'}{\partial t'}(J^{-1}U_r)_{i,j,k} + Q_r = Q_{vr} + D_r + J^{-1}_{i,j,k}S_{i,j,k} \tag{21}$$

2.3 Multi-stage Time-Stepping Scheme

The source term S is added into the five-stage Runge-Kutta time-stepping scheme of the TLNS3D code. The time-stepping scheme thus becomes

$$\begin{aligned}
U_r^{(0)} &= U_r^{(n)} \\
U_r^{(1)} &= U_r^{(0)} - \alpha_1\frac{\Delta t}{J^{-1}}[Q_r^{(0)} + \beta_1 Q_{vr}^{(0)} - \gamma_1 D_r^{(0)} - J^{-1}S] \\
U_r^{(2)} &= U_r^{(0)} - \alpha_2\frac{\Delta t}{J^{-1}}[Q_r^{(1)} + \beta_2 Q_{vr}^{(1)} - \gamma_1 D_r^{(0)} - \gamma_2 D_r^{(1)} - J^{-1}S] \\
U_r^{(3)} &= U_r^{(0)} - \alpha_3\frac{\Delta t}{J^{-1}}[Q_r^{(2)} + \beta_3 Q_{vr}^{(2)} - \gamma_1 D_r^{(0)} - \gamma_2 D_r^{(1)} - \gamma_3 D_r^{(2)} - J^{-1}S] \\
U_r^{(4)} &= U_r^{(0)} - \alpha_4\frac{\Delta t}{J^{-1}}[Q_r^{(3)} + \beta_4 Q_{vr}^{(3)} - \gamma_1 D_r^{(0)} - \gamma_2 D_r^{(1)} - \gamma_3 D_r^{(2)} - \gamma_4 D_r^{(3)} - J^{-1}S] \\
U_r^{(5)} &= U_r^{(0)} - \alpha_5\frac{\Delta t}{J^{-1}}[Q_r^{(4)} + \beta_5 Q_{vr}^{(4)} - \gamma_1 D_r^{(0)} - \gamma_2 D_r^{(1)} - \gamma_3 D_r^{(2)} - \gamma_4 D_r^{(3)} - \gamma_5 D_r^{(4)} \\
&\quad - J^{-1}S] \\
U_r^{(n+1)} &= U_r^{(5)}
\end{aligned} \tag{22}$$

where the superscripts (n) and $(n+1)$ refer to time levels and the superscripts (0) through (5) refer to multistage levels within each time step.

In addition to the five-stage time-stepping scheme, the local time-stepping and residual smoothing techniques are applied to accelerate the convergence of the scheme to steady state for both fixed-wing and hovering motions. The details of the residual smoothing are discussed in Ref. [3].

2.4 Multigrid Acceleration Technique

The multigrid scheme of TLNS3D is employed. The idea of the multigrid is the use of successively coarser grids to compute corrections to a fine grid solution. The use of multigrid technique can significantly accelerate the convergence rate. The coefficients of β's and γ's in Eq. (22) as well as those for the residual smoothing are carefully selected to provide optimum damping of errors. The results presented in this report are obtained using a V-cycle multigrid scheme.

2.5 Boundary Conditions and Grid

A C-O type grid is employed. The grid is generated using either GRIDGEN3D or WTCO^3 code. On the blade surface, no-slip and no-penetration conditions are used by setting relative velocity ($\vec{V}_r$) to zero. The adiabatic wall condition and zero-normal pressure gradient condition at the wall are also applied at the blade surface. The farfield boundaries are treated by using Riemann invariants condition. At the inboard plane, near the rotation axis of the blade, the condition of $u_r/w_r = u_t/w_t = -(z-z_p)/(x-x_p)$ is used to guarantee that the radial velocity is zero at this boundary for hovering motion; for the fixed-wing motion, the plane-of-symmetry condition is used.

3. COMPUTATIONAL RESULTS

Application of the TLNS3DR code is made for realistic helicopter rotor blade configurations to study the rotor design. For nonrotating flows, calculated results of the Berp-tip, the swept-tip and the equivalent taper-tip are presented in the Subsection 3.1, along with comparison of some experimental data. For both rotating and nonrotating flows, the similar results are presented in the Subsection 3.2 for the Berp-type blade, the swept-type blade, and the equivalent taper-type and rectangle-type blades without twist.

3.1 Nonrotating Blade Tips

The planforms of the Berp-tip, the swept-tip, and the taper-tip are given in Figures 1, 2 and 3, respectively. Figures 4, 5 and 6 are the views of the twist and airfoil section geometry. The C-O grids are generated for the Berp-tip by GRIDGEN3D and for the swept- and the taper-tips by WTCO grid generators, where a single isolated blade-tip is considered in each case. Figures 7, 8 and 9 are the partial views of the mesh around the Berp-tip, the swept-tip and the taper-tip, respectively, where $129 \times 65 \times 49$ mesh points are used in the streamwise, normal and spanwise directions, respectively. The grid of this size is used in most cases. Flows at three angle-of-attack conditions are considered. Tip flow fields in terms of the downwash, axial velocity and crossflow velocity vector field are presented. The surface pressure coefficients and the convergence history in terms of the residual are also given.

3.1.1 Tip-flow field at $\alpha = 15^o$

Figures 10, 11 and 12 are the calculated downwash velocity contours for the Berp-tip, the swept-tip and the taper-tip, respectively, at angle of attack of 15^o under an incompressible free-stream Mach number. Figure 13 gives the same result for the taper-tip with a finer grid where $161 \times 97 \times 97$ mesh points are used to study the effect of the mesh refinement to the solution. Figures 14, 15 and 16 are the experimentally measured downwash velocity contours for the Berp-tip, the swept-tip and the taper-tip, respectively. The comparison of the calculated results with the experimental data shows that both the TLNS3DR code and experiment produce similar results in the region near the blade tips, and that the tip vortex is diffused when it convects to downstream in the calculated solution. The comparison of the solution of Figure 12 with that of Figure 13 shows that the finer grid does give a slightly better solution.

Figures 17, 18 and 19 are the calculated axial velocity contours for the Berp-tip, the swept-tip and the taper-tip, respectively. Figure 20 gives the same result for the taper-tip with a finer grid where $161 \times 97 \times 97$ mesh points are used. Figures 21, 22 and 23 are the experimentally measured axial velocity contours for the Berp-tip, the swept-tip and the taper-tip, respectively. Both calculated solutions and experimental data give quantitatively similar results. It is seen that the Berp-tip produces the largest tip-vortex in terms of the diameter of the vortex cylinder from both calculated results and experiment. From the calculated results, the taper-tip has a tightest tip vortex structure; from the experiment, the swept-tip has the tightest tip vortex structure.

Figures 24, 25 and 26 are the calculated crossflow velocity vector fields for the Berp-tip, the swept-tip and the taper-tip, respectively. Figure 27 gives the same result for the taper-tip with a finer grid where $161 \times 97 \times 97$ mesh points are used. Figures 28, 29 and 30 are the experimentally measured crossflow velocity vector fields for the Berp-tip, the swept-tip and the taper-tip, respectively. Both calculated solution and experimental data show quantitatively similar tip vortex pattern, and tell us that the strength of the tip vortex in terms of the crossflow velocity of the Berp-tip is slightly weaker than that of the swept-tip. The calculated solution of the crossflow field of the taper-tip is likely diffused.

3.1.2 Tip-flow field at $\alpha = 5^o - 7.5^o$

Figures 31, 32 and 33 are the calculated downwash velocity contours for the Berp-tip, the swept-tip and the taper-tip, respectively, at angle of attack of 5^o to 7.5^o under an incompressible free-stream Mach number. At this angle-of-attack condition, the effective angle of attack is near zero due to the negative twist angle near the tip. Figures 34, 35 and 36 are the calculated axial velocity contours for the Berp-tip, the swept-tip and the taper-tip, respectively. Figures 37, 38 and 39 are the calculated crossflow velocity vector fields. Figure 40 shows the experimentally measured crossflow velocity vector fields for these three tips at $x = 1.65$ chord length station measured from the leading edge of the root. The calculated solution shows reasonable results in terms of the downwash, axial velocity and crossflow velocity, but at the location away from the blade, such as at $x = 1.65$ chord length station, the tip vortex is diffused due to the coarse grid used in that region.

3.1.3 Tip-flow field at $\alpha = 0^o$

Figures 41, 42 and 43 are the calculated downwash velocity contours for the Berp-tip, the swept-tip and the taper-tip, respectively, at angle of attack of 0^o under an incompressible free-stream Mach number. At this angle-of-attack condition, the effective angle of attack is a negative value due to the negative twist angle near the tip. Figure 44 gives the same result for the taper-tip with a finer grid where $161 \times 97 \times 97$ mesh points are used. Figures 45, 46 and 47 are the calculated axial velocity contours. Figure 48 gives the same result for the taper-tip with a finer grid where $161 \times 97 \times 97$ mesh points are used. Figures 49, 50 and 51 are the calculated crossflow velocity vector fields. Figure 52 gives the same result for the taper-tip with a finer grid where $161 \times 97 \times 97$ mesh points are used. Figures 53 is the experimentally measured crossflow velocity vector fields for the Berp-tip, the swept-tip and the taper-tip at x-station of 1.65 chord length from the leading edge of the root. Calculated solution and experimental data agree quantitatively. It can be seen from both the experimental data and the calculated solution that the Berp-tip does not produce a significant tip vortex, and that the tip vortex from the taper-tip is flatter than that from the swept-tip. Since the effective angle of attack is a negative value, the tip vortex rotates in the clockwise direction and formed under the blade tip.

3.1.4 Surface pressure and convergence history

Figures 54, 55 and 56 are the calculated surface pressure coefficient contours for the Berp-tip, the swept-tip and the taper-tip, respectively, at angle of attack of 15^o. Figures 57, 58 and 59 are the calculated surface pressure coefficient contours at angle of attack of 5^o to 7.5^o. Figures 60, 61 and 62 are the calculated surface pressure coefficient contours at angle of attack of 0^o. These results are self-explanatory.

Figures 63, 64 and 65 are the convergence history in terms of residual for the Berp-tip, the swept-tip and the taper-tip, respectively. Figure 66 is the convergence history for the taper-tip with a finer grid. As mentioned earlier, a V-cycle multigrid scheme is employed. A total of 375 equivalent fine grid time steps (based on the equivalent CPU time required) are used. The CPU time on the NASA-Langley's Cray-YMP with a single processor for cases with $129 \times 65 \times 49$ fine grid points is 4600 seconds, which is 0.011 second per fine grid point, or 29.8×10^{-6} second per fine grid per time step. Comparing with the single-grid method, the current code is very efficient. Figures 65 and 66 show that, on the other hand, the convergence rate is dependent on the grid size, and that the rate decreases when the grid size decreases.

3.2 Comparison of Rotating and Nonrotating Rotor Flows

The planforms and partial views of the C-O grid of the Berp-blade, the swept-blade, and the equivalent taper-blade and rectangle-blade without twist are given in Figures 67 through 74. A mesh of $129 \times 65 \times 65$ grid points is used in the streamwise, normal and spanwise directions, respectively. Flows at angle of attack of 2 degrees under a compressible free-stream / tip Mach number of 0.628 are considered for both nonrotating and rotating flows. Tip flow fields in terms of the axial velocity and crossflow velocity vector field are presented. The blade-surface pressure coefficients, local Mach number, local spanwise velocity and the convergence history in terms of the residual are also presented.

For nonrotating motion of the Berp-blade, calculated tip flow field in terms of axial velocity and crossflow velocity vector are presented in Figures 75 and 76, respectively. Figures 77, 78 and 79 are the calculated surface pressure coefficients, surface local Mach number and local spanwise velocity, respectively, where the surface local Mach number and local spanwise velocity are calculated at $j = 33$ which is about just outside of the boundary layer. Figure 80 is the convergence history.

For rotating, hovering motion of the Berp-blade, calculated tip flow field in terms of relative and absolute axial velocities and relative and absolute crossflow velocity vectors are presented in Figures 81, 82, 83 and 84, respectively. Figures 85, 86, 87 and 88 are calculated surface pressure coefficients, surface local relative Mach number and local relative and absolute spanwise velocities, respectively. Figure 89 is the convergence history.

The same sets of results as those for the Berp-blade are presented for the swept-blade, the taper-blade and the rectangle-blade. Figures 90 through 104 are results of the swept-blade; Figures 105 through 119 are results of the taper-blade; and Figures 120 through 134 are results of the rectangle-blade.

All results presented are self-explanatory. The CPU time used is 6100 seconds on the Cray-YMP with a single processor. The results on the rotating, hovering motion of the blade are quantitatively correct where tip vortex in terms of both relative and absolute velocities are captured, and where the blade surface flow field shows that the rotating effects are correctly calculated.

4. CONCLUDING REMARKS

The TLNS3DR code is applied to various realistic helicopter rotor blade configurations to study the advanced rotor tip flow and to further investigate the capability of the code. For nonrotating tip geometry, three tips are computationally investigated and briefly compared with the experimental data. For both rotating hovering motion and nonrotating motion of blade geometry, four blades are computationally investigated. The results of rotating flows are presented along with those of equivalent nonrotating results for studying the effects of rotation term in the TLNS3DR code to validate the code. The detailed results with limited discussion presented in this report are expected to be useful in undestanding the rotor design, particularly in studying the tip vortex. Througth this investigation, several concluding remarks can be drawn:

1. The TLNS3DR code is an efficient and accurate CFD tool for nonrotating flow calculations.

2. The TLNS3DR code efficiently produces quantitatively correct solution for rotating hovering motion; however, the accuracy of the code for rotating flows needs to be tested.

3. The TLNS3DR code has capability to capture the tip vortex and the solution of the tip vortex generally agrees with that of experiment; it is very promising for using the code as an analysis tool in rotor tip design.

4. The structure of the tip vortex does depend on the planform of the rotor blade, and it is predictable by the TLNS3DR code.

5. A computational grid finer than the current ones is needed to accurately capture the tip vortex.

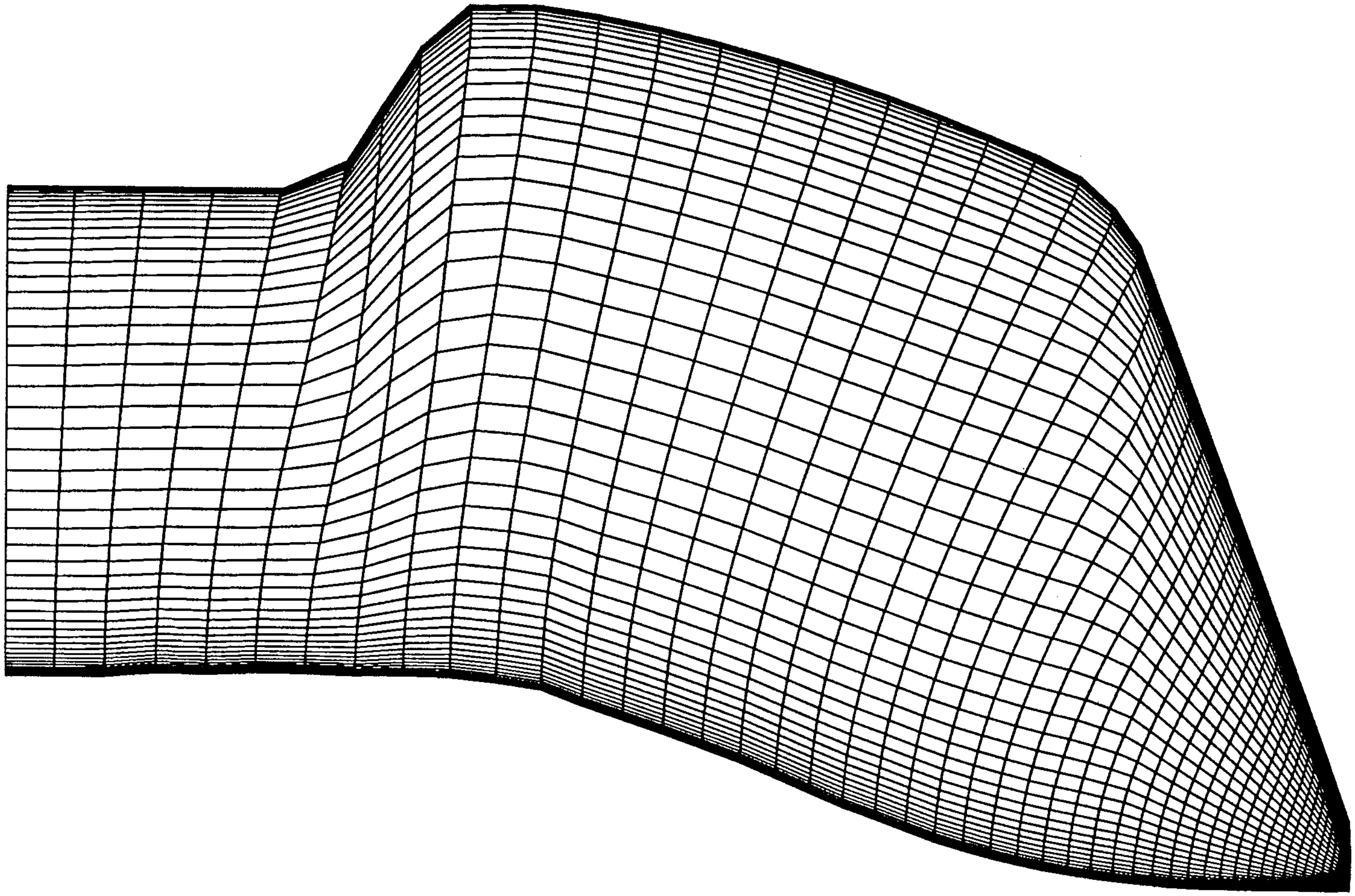

Figure 1. Plane form of Berp-tip.

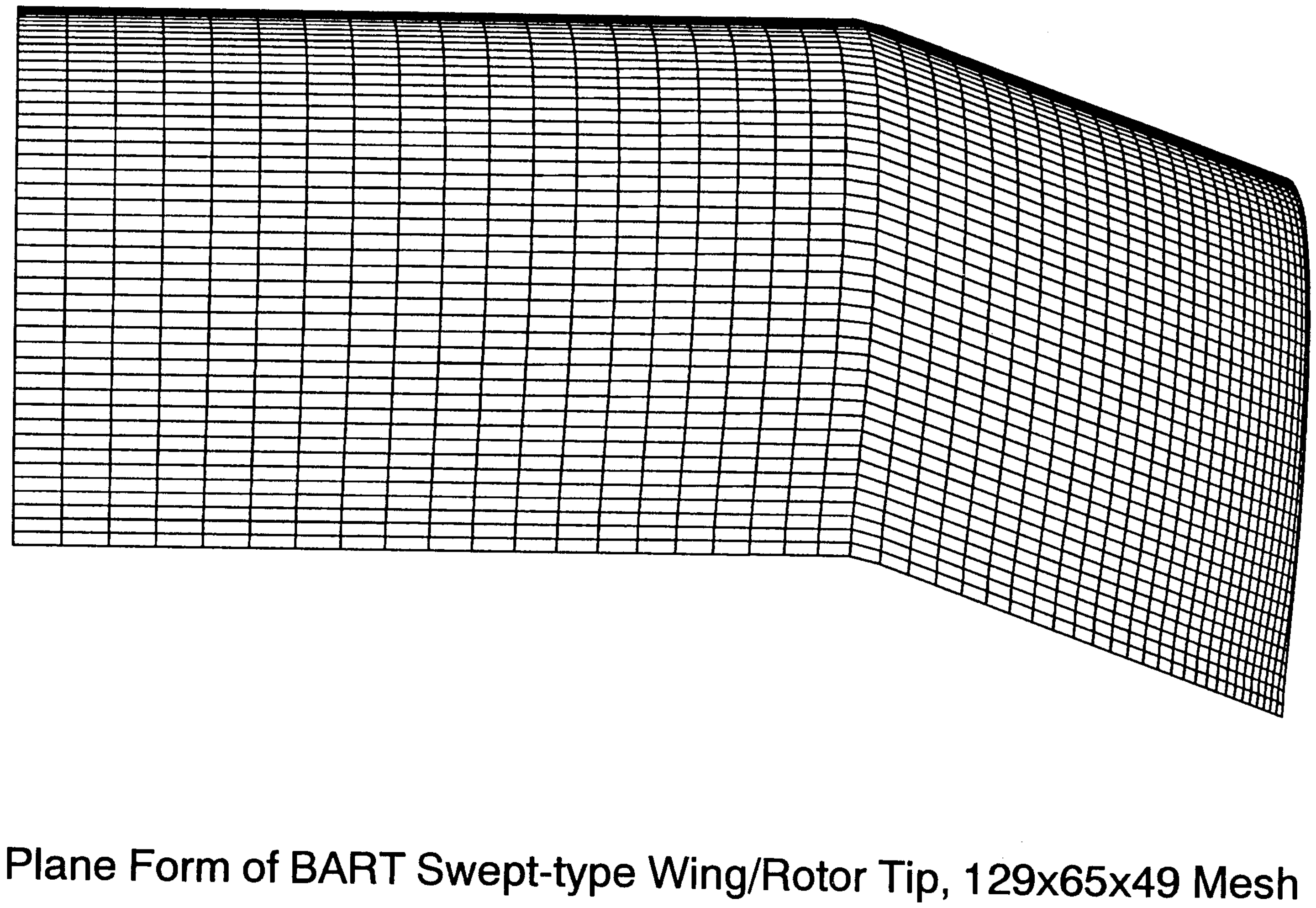

Figure 2. Plane form of swept-tip.

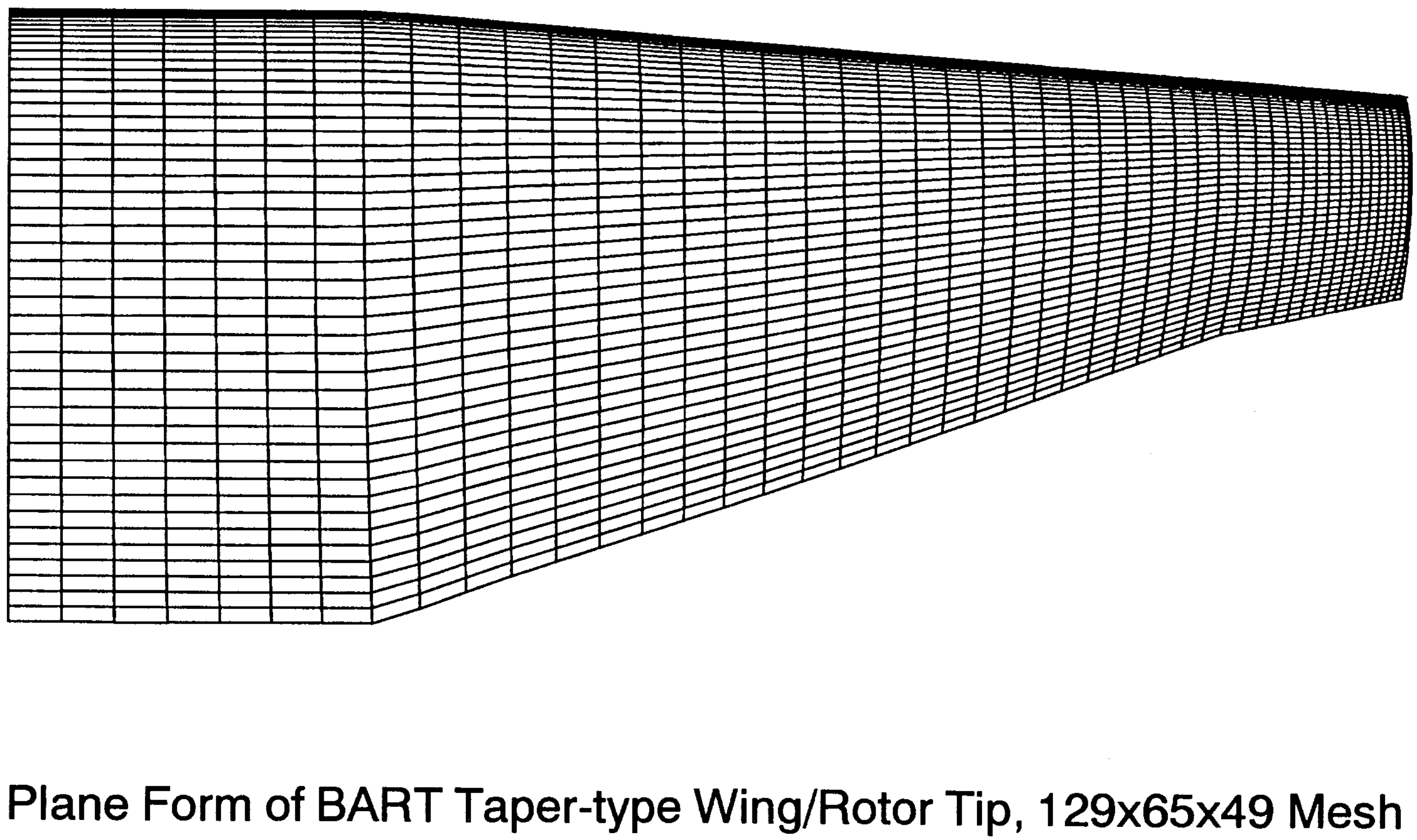

Plane Form of BART Taper-type Wing/Rotor Tip, 129x65x49 Mesh

Figure 3. Plane form of taper-tip.

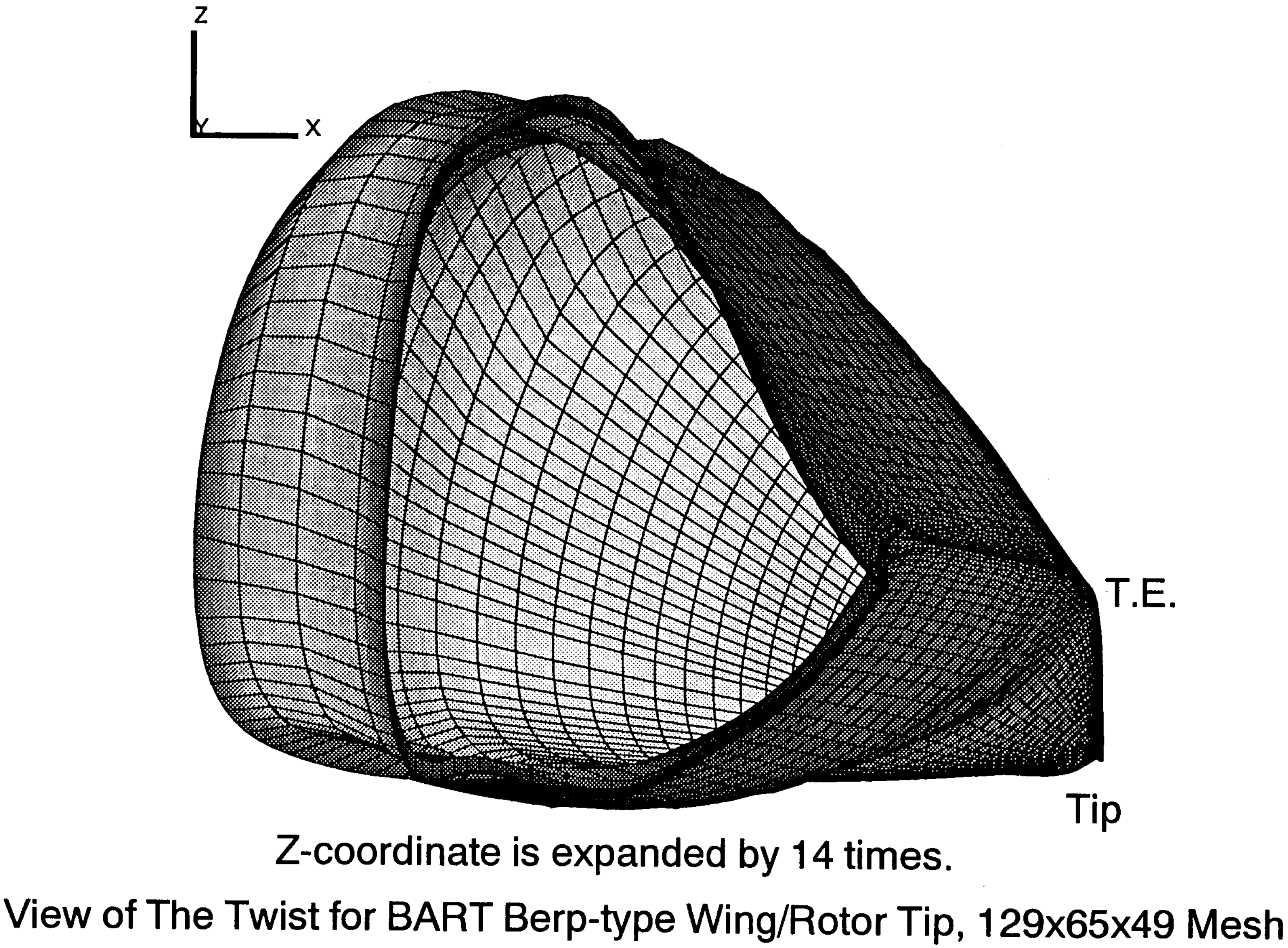

Figure 4. View of the twist for Berp-tip.

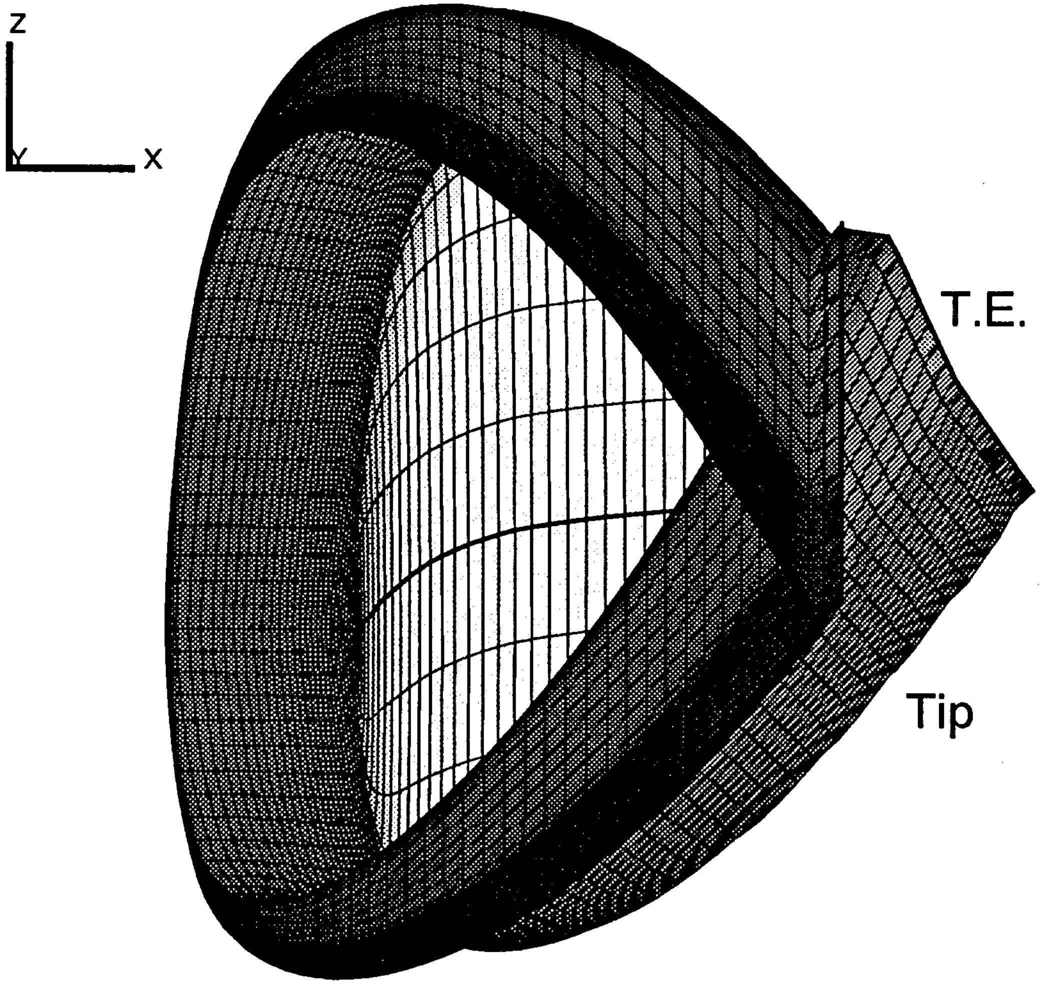

Figure 5. View of the twist for swept-tip.

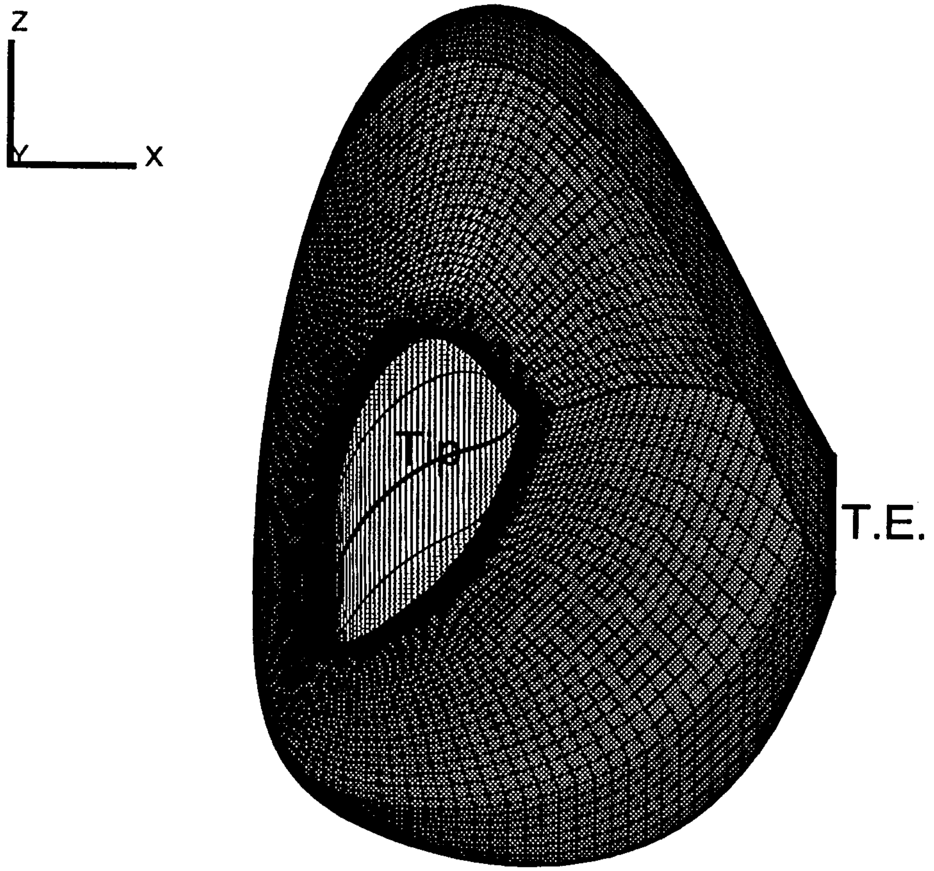

Z-coordinate is expanded by 14 times.

View of The Twist for BART Taper-type Wing/Rotor Tip, 129x65x49 Mesh

Figure 6. View of the twist for taper-tip.

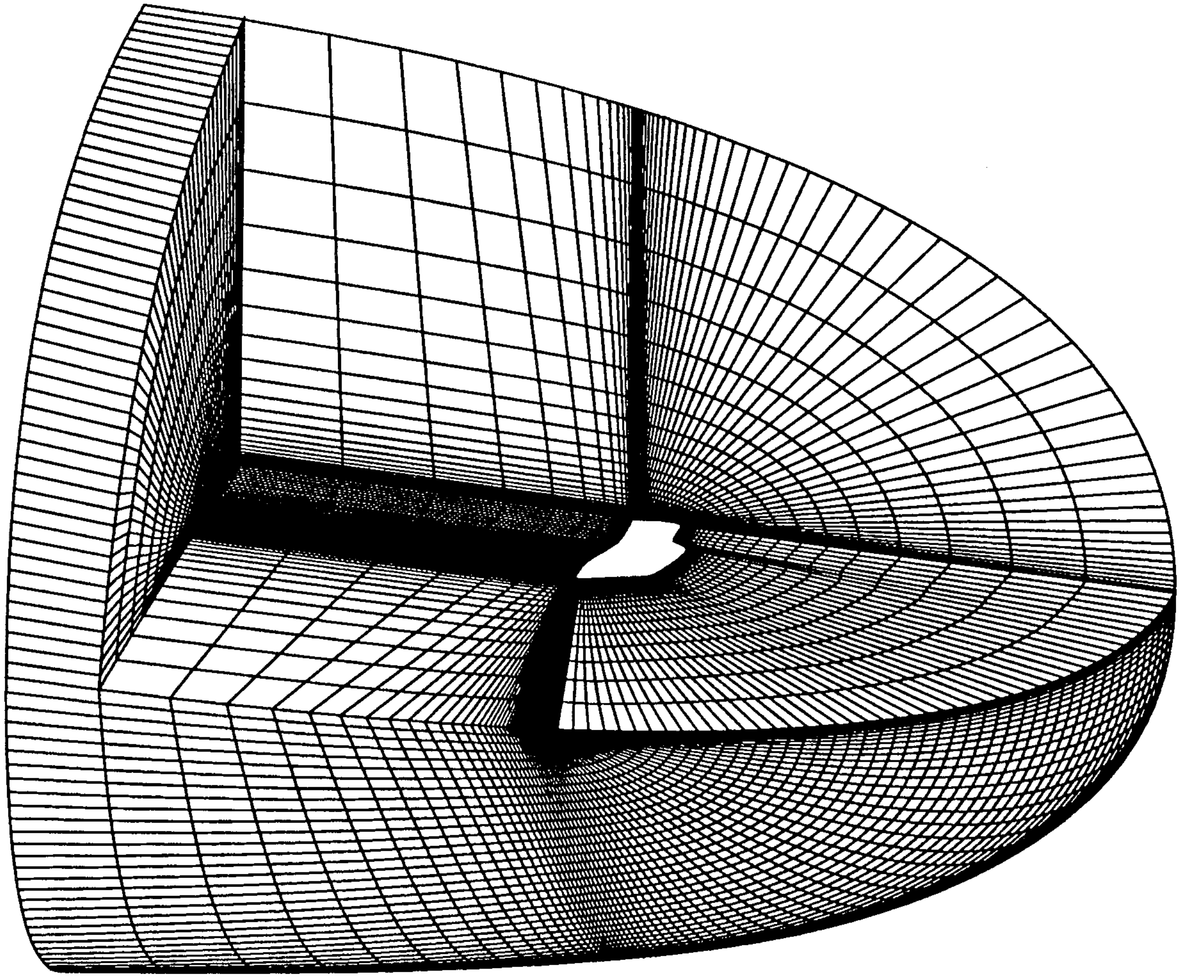

Partial View of C-O Mesh for BART Berp-type Wing/Rotor Tip, 129x65x49 Mesh

Figure 7. Partial view of C-O mesh for Berp-tip.

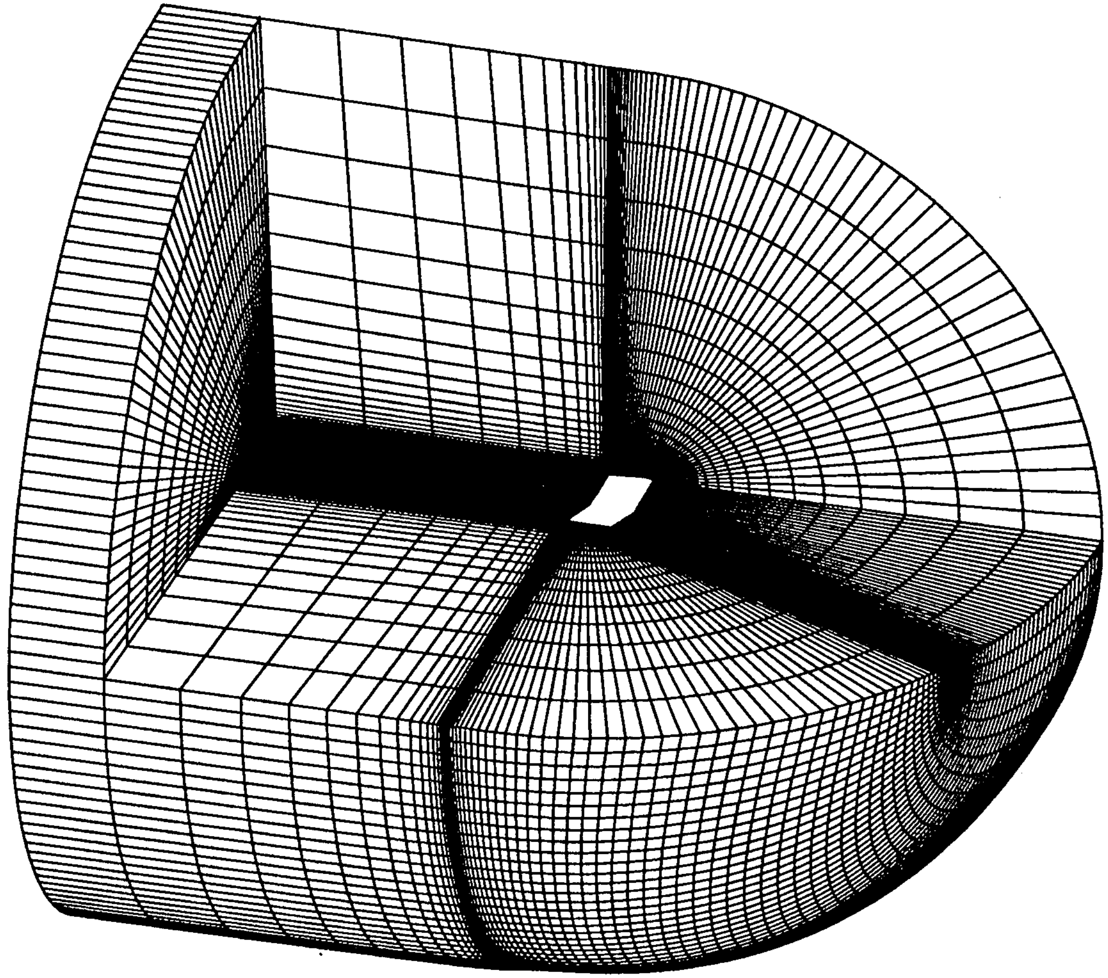

Figure 8. Partial view of C-O mesh for swept-tip.

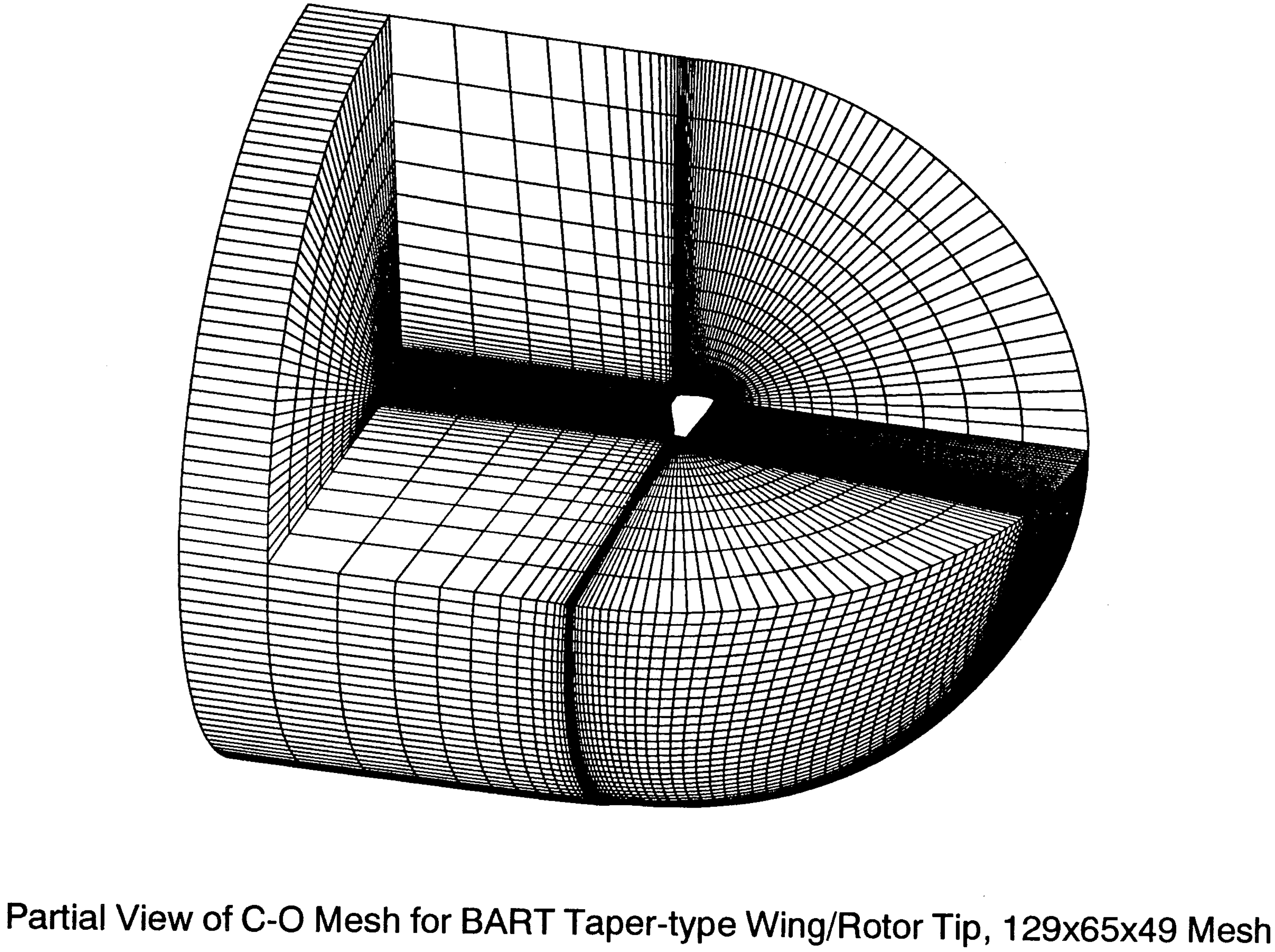

Figure 9. Partial view of C-O mesh for taper-tip.

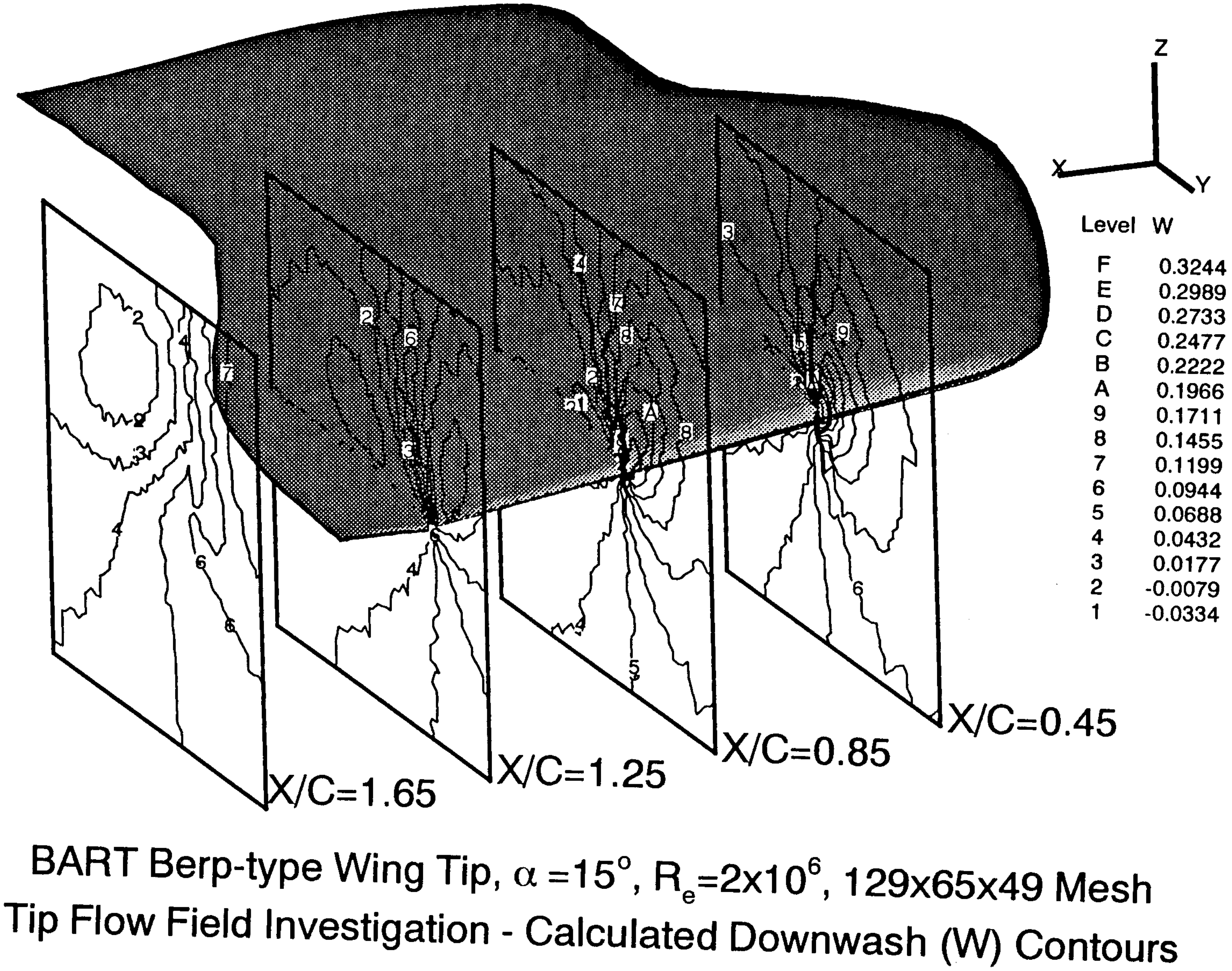

Figure 10. Calculated tip flow field in terms of downwash for Berp-tip at $\alpha=15°$.

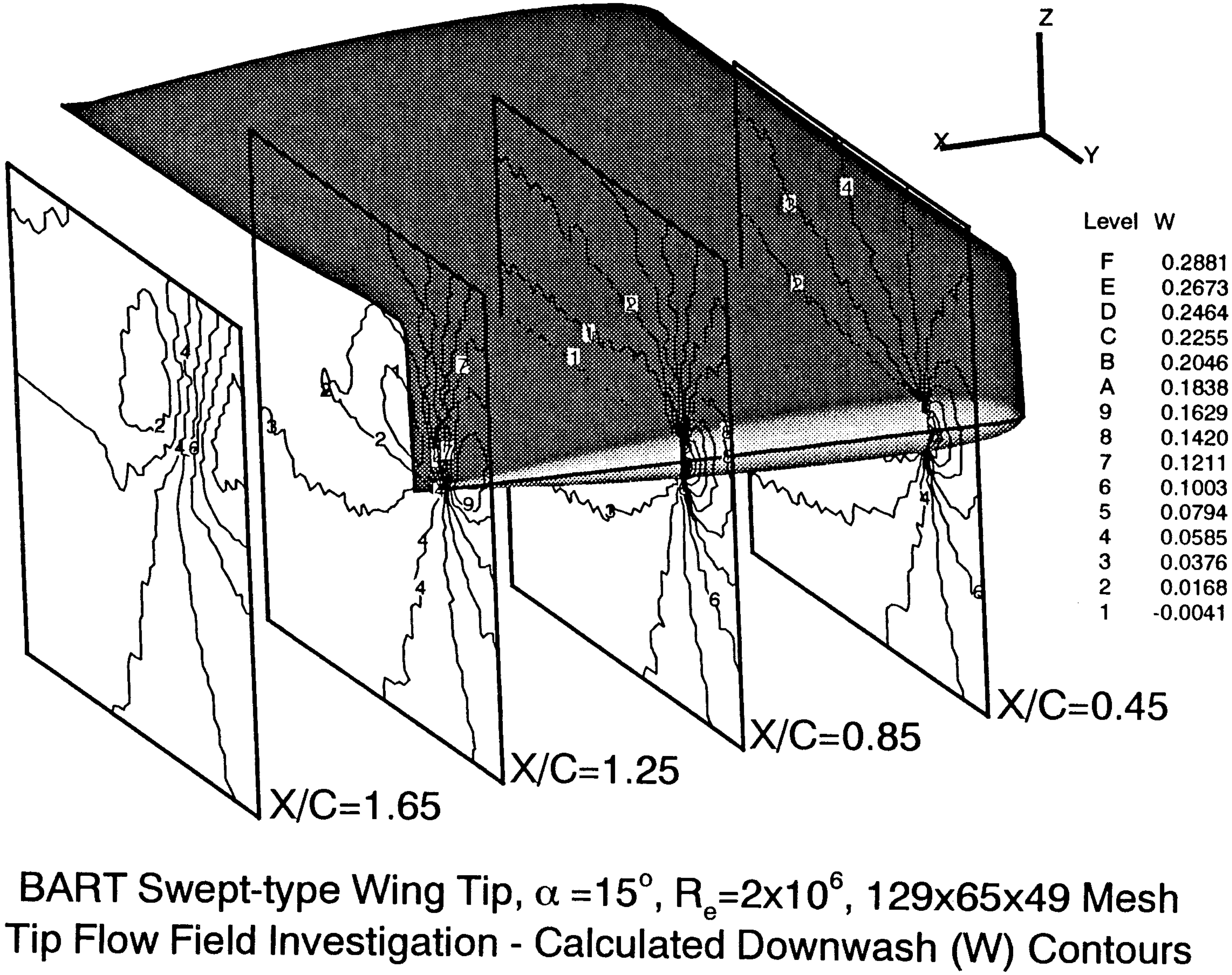

Figure 11. Calculated tip flow field in terms of downwash for swept-tip at α=15°.

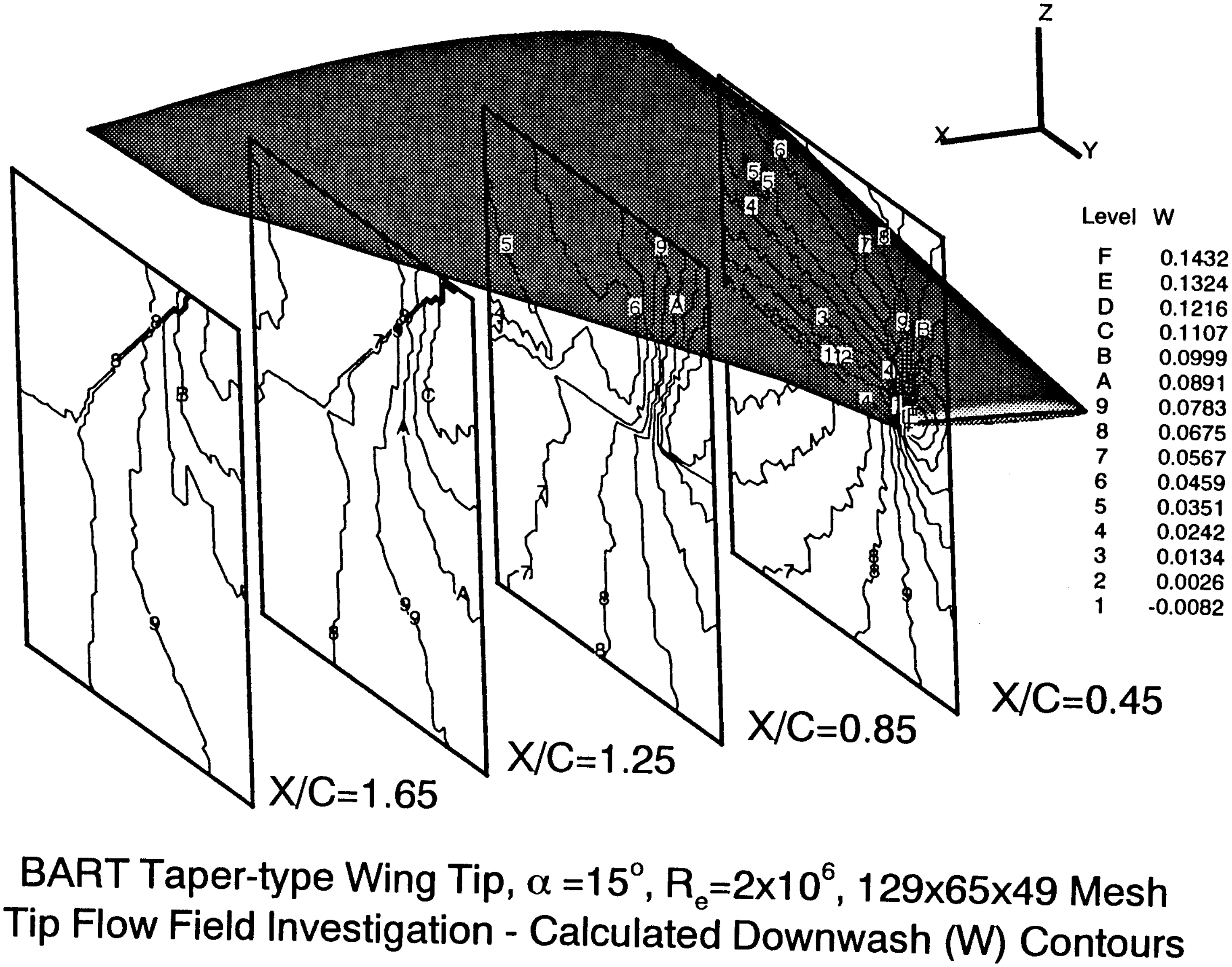

Figure 12. Calculated tip flow field in terms of downwash for taper-tip at α=15°.

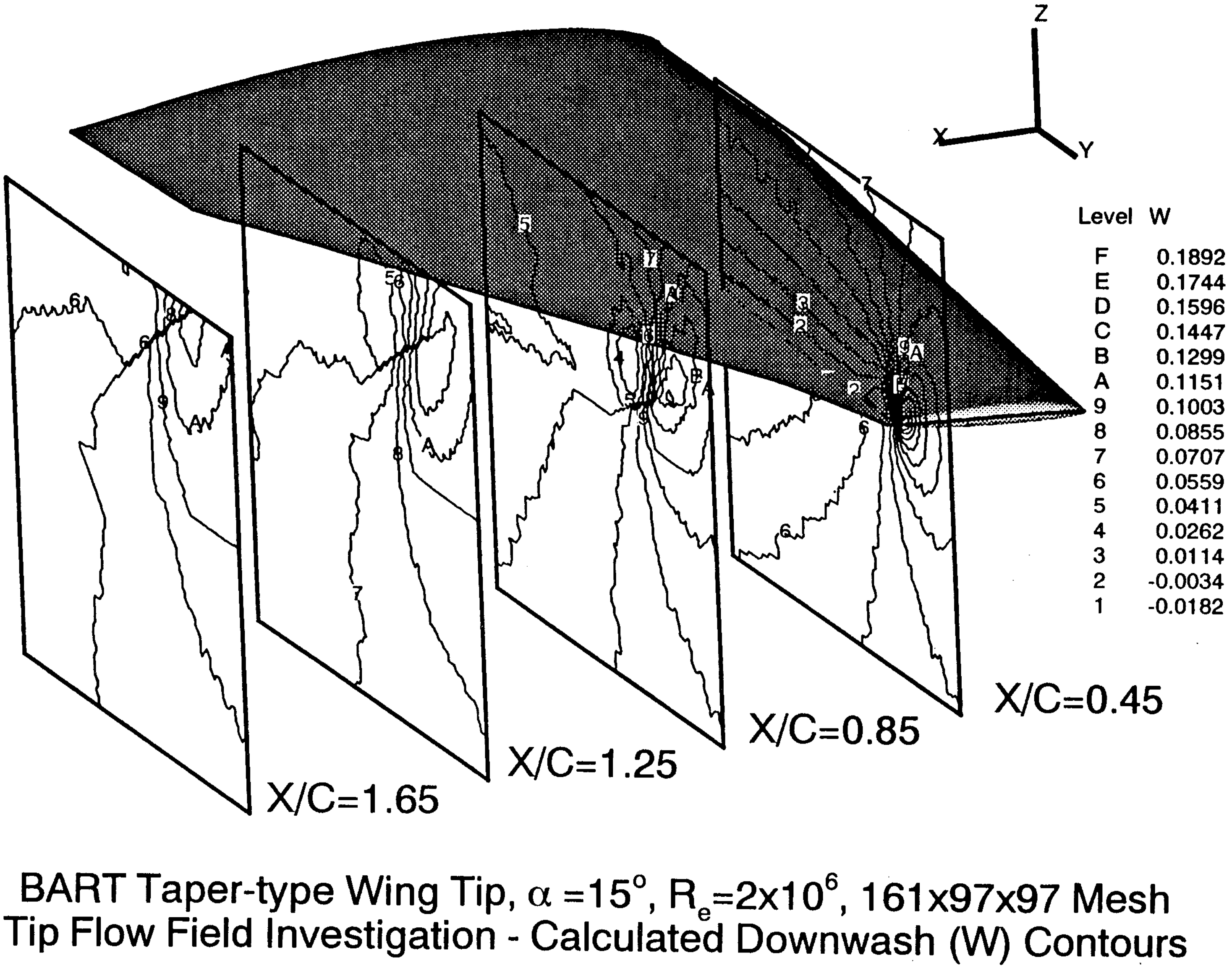

Figure 13. Calculated tip flow field in terms of downwash for taper-tip at α=15° with a fine grid.

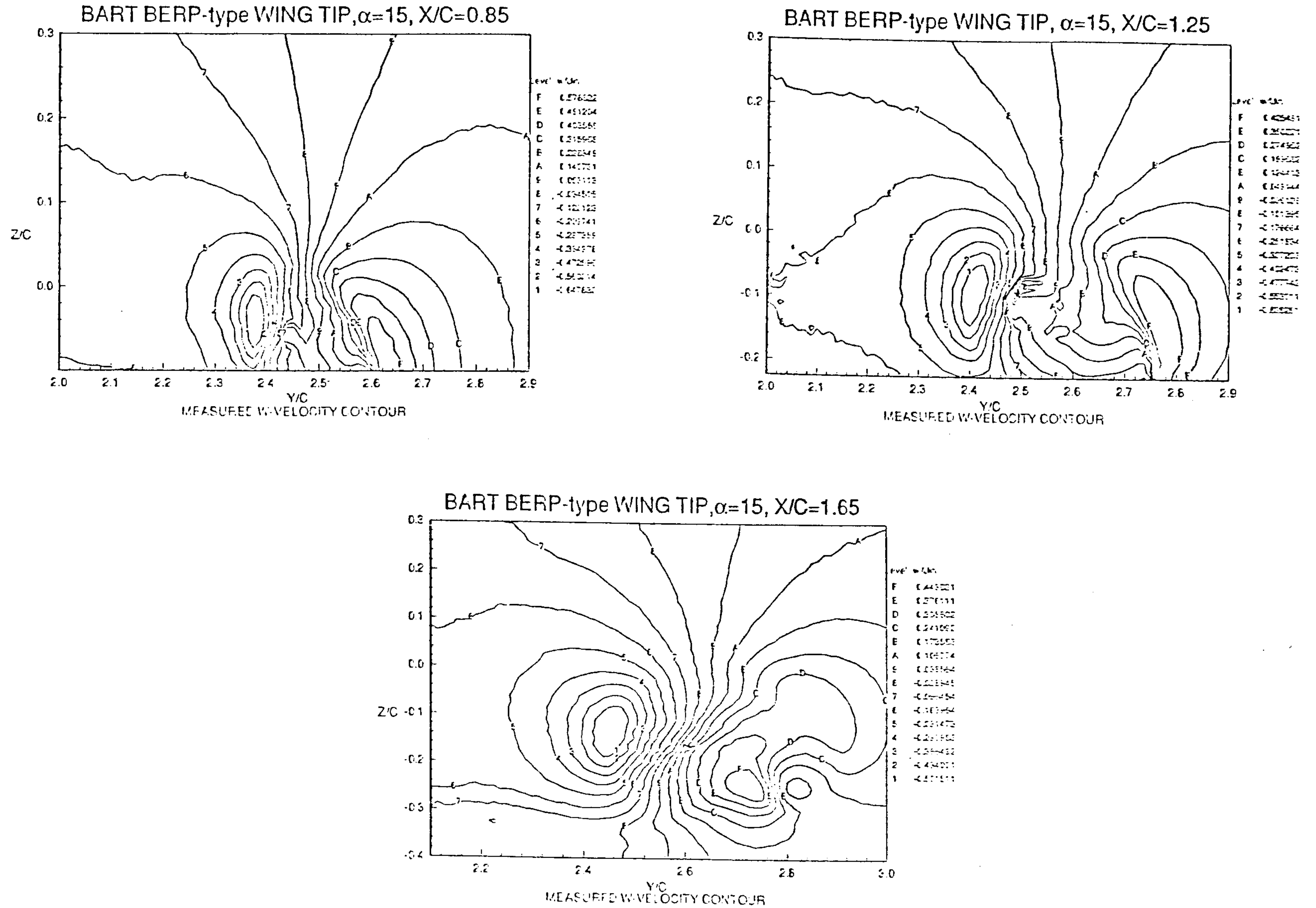

Figure 14. Measured tip flow field in terms of downwash for Berp-tip at α=15°.

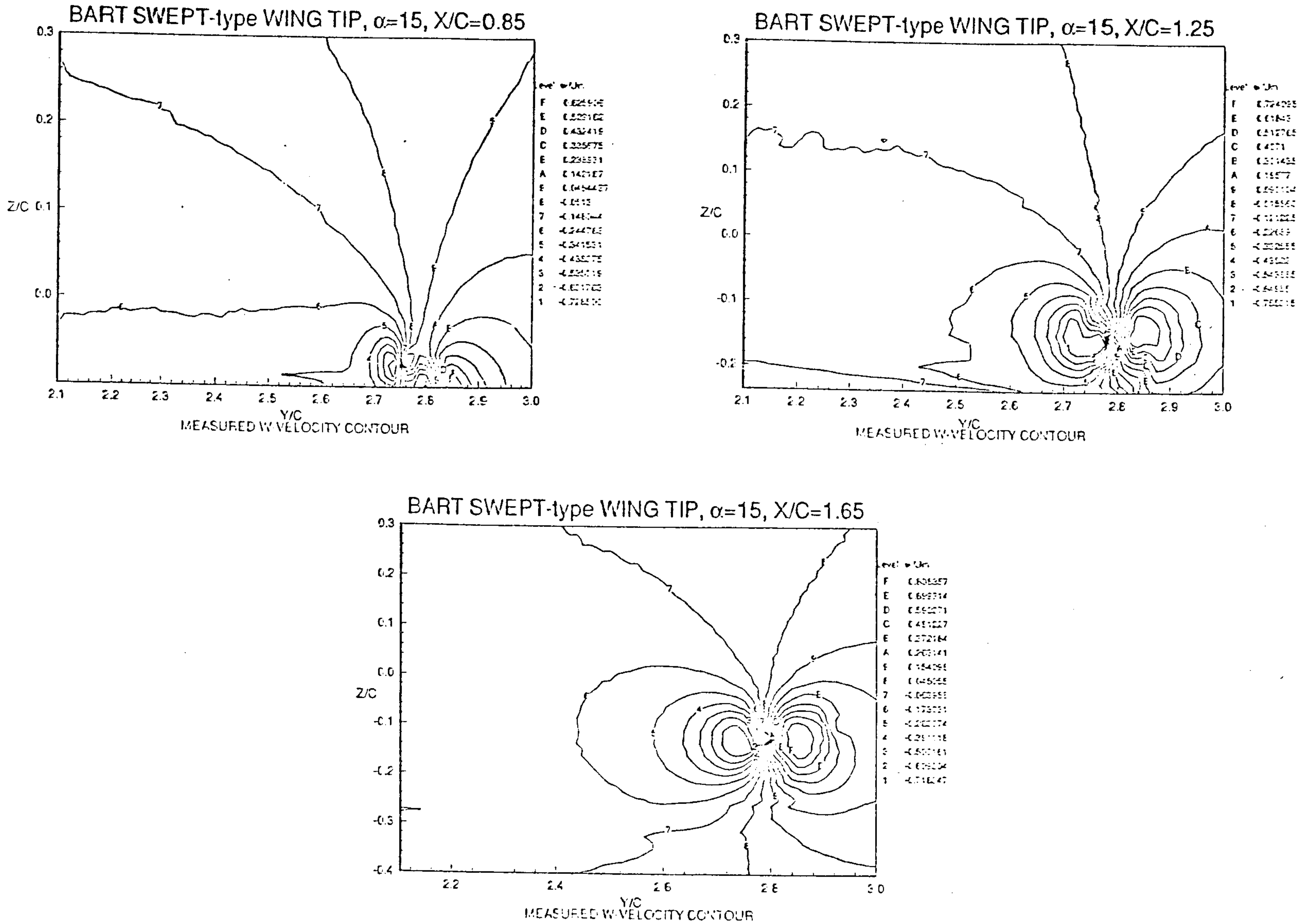

Figure 15. Measured tip flow field in terms of downwash for swept-tip at α=15°.

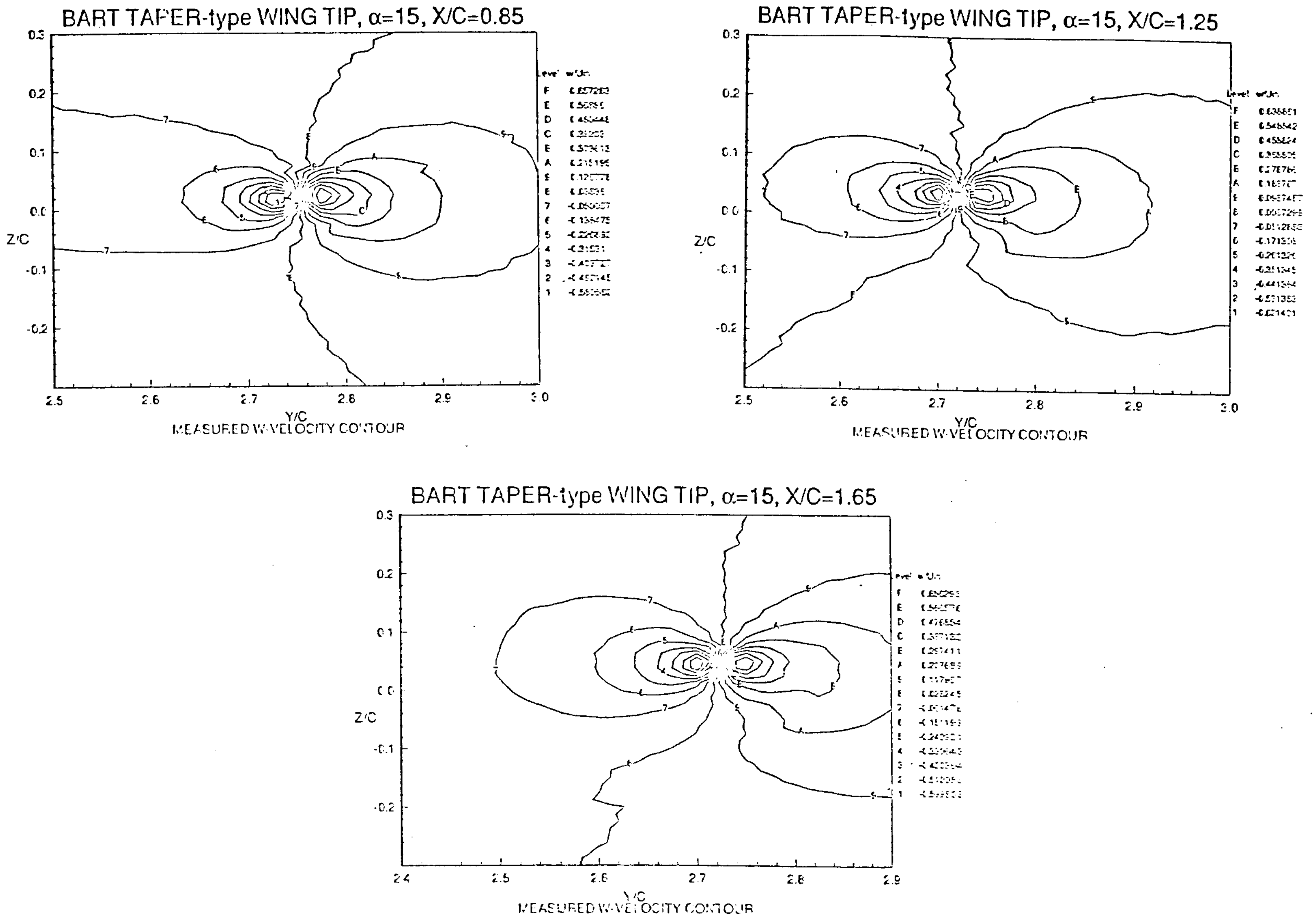

Figure 16. Measured tip flow field in terms of downwash for taper-tip at α=15°.

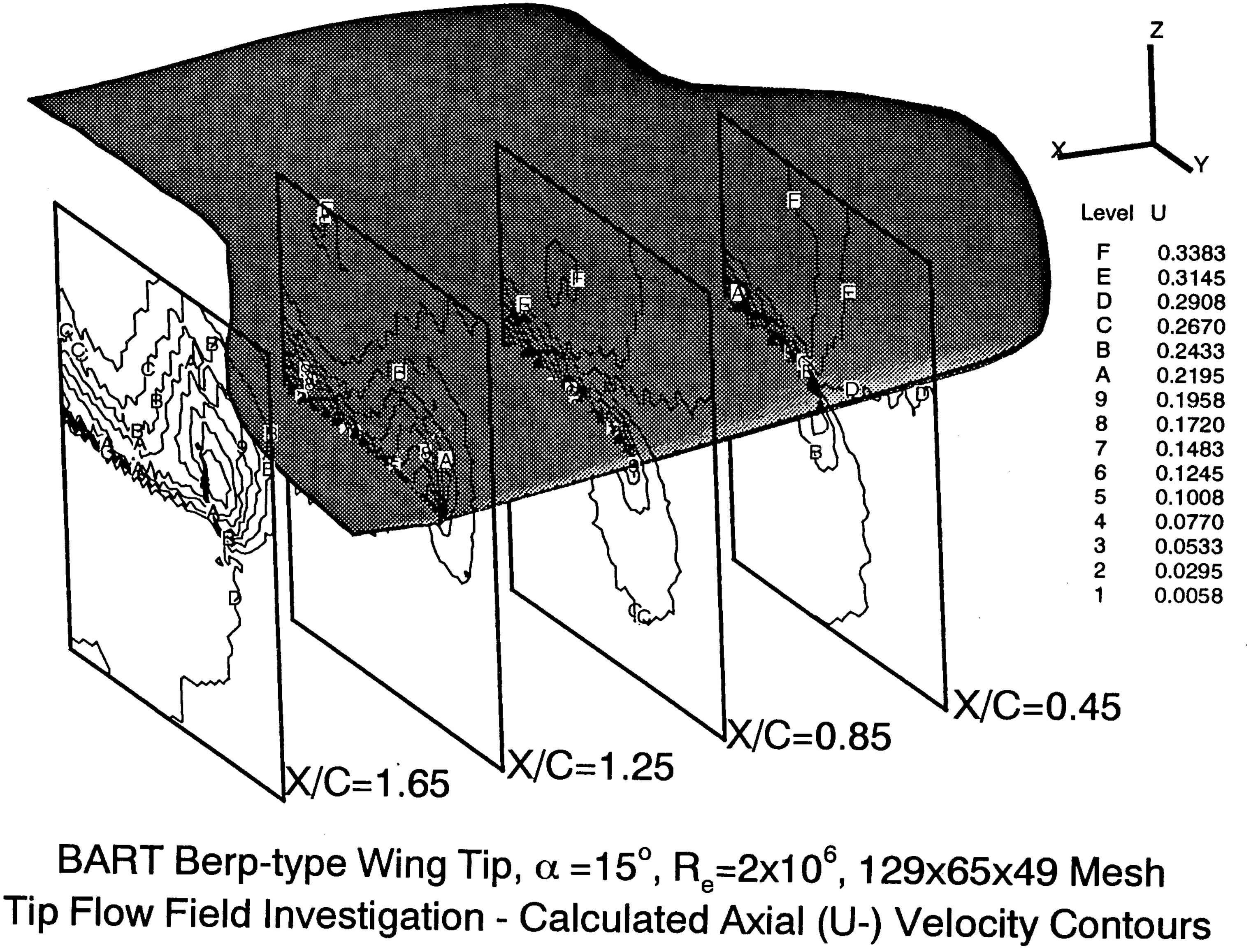

Figure 17. Calculated tip flow field in terms of axial velocity for Berp-tip at $\alpha=15^0$.

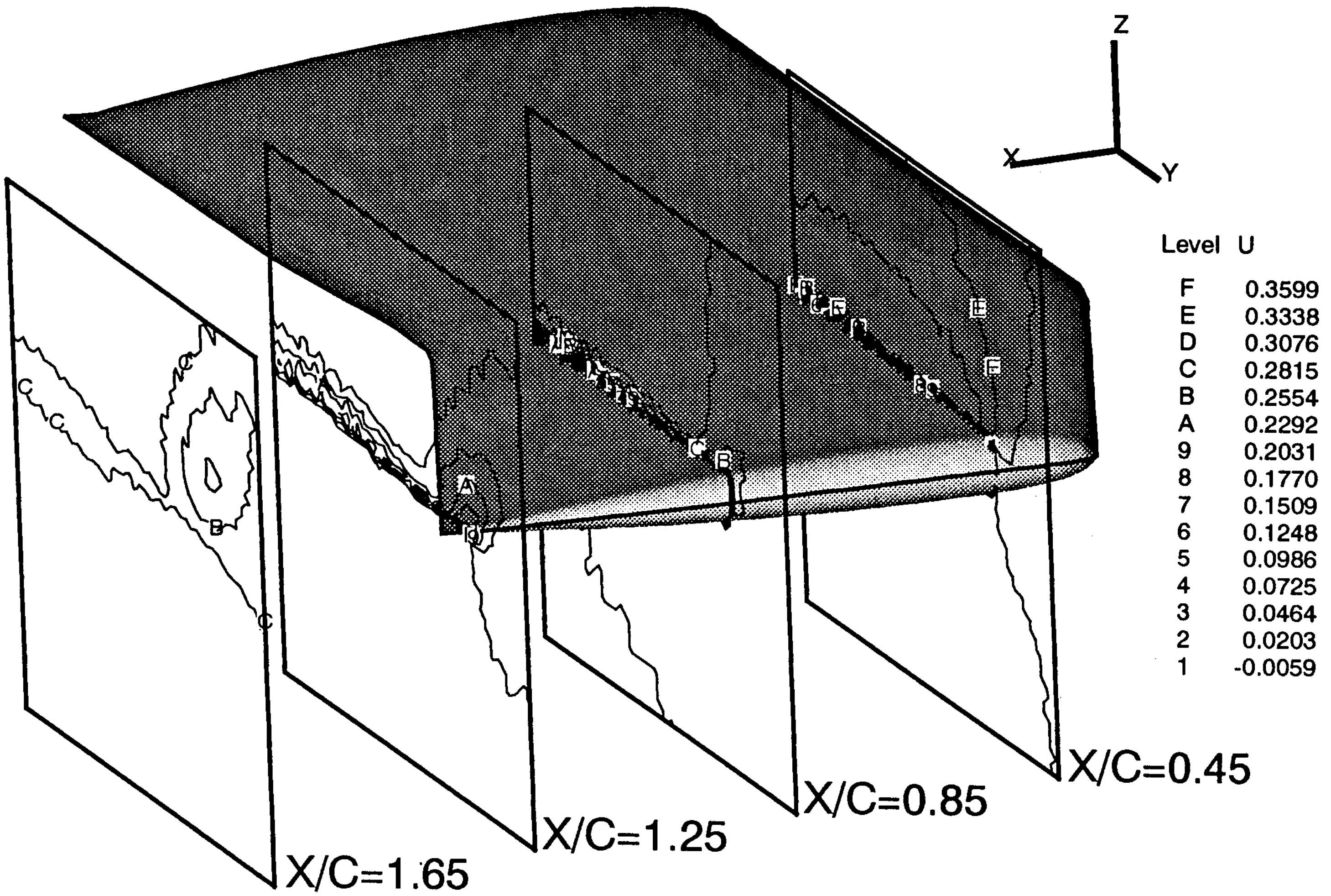

BART Swept-type Wing Tip, $\alpha = 15^\circ$, $R_e = 2\times10^6$, 129x65x49 Mesh
Tip Flow Field Investigation - Calculated Axial (U-) Velocity Contours

Figure 18. Calculated tip flow field in terms of axial velocity for swept-tip at $\alpha = 15^0$.

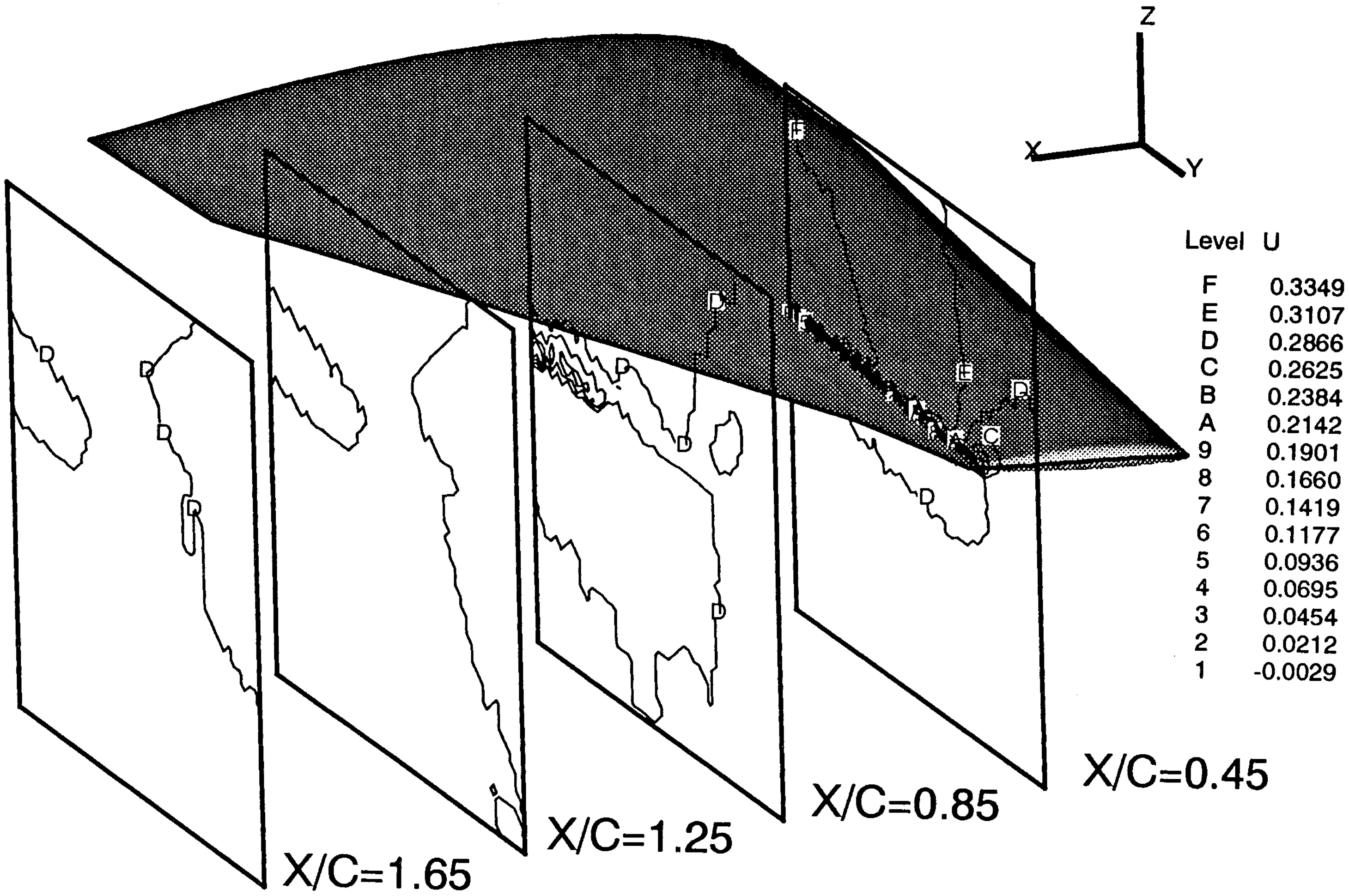

BART Taper-type Wing Tip, α =15°, R_e=2x10^6, 129x65x49 Mesh
Tip Flow Field Investigation - Calculated Axial (U-) Velocity Contours

Figure 19. Calculated tip flow field in terms of axial velocity for taper-tip at α=15^0.

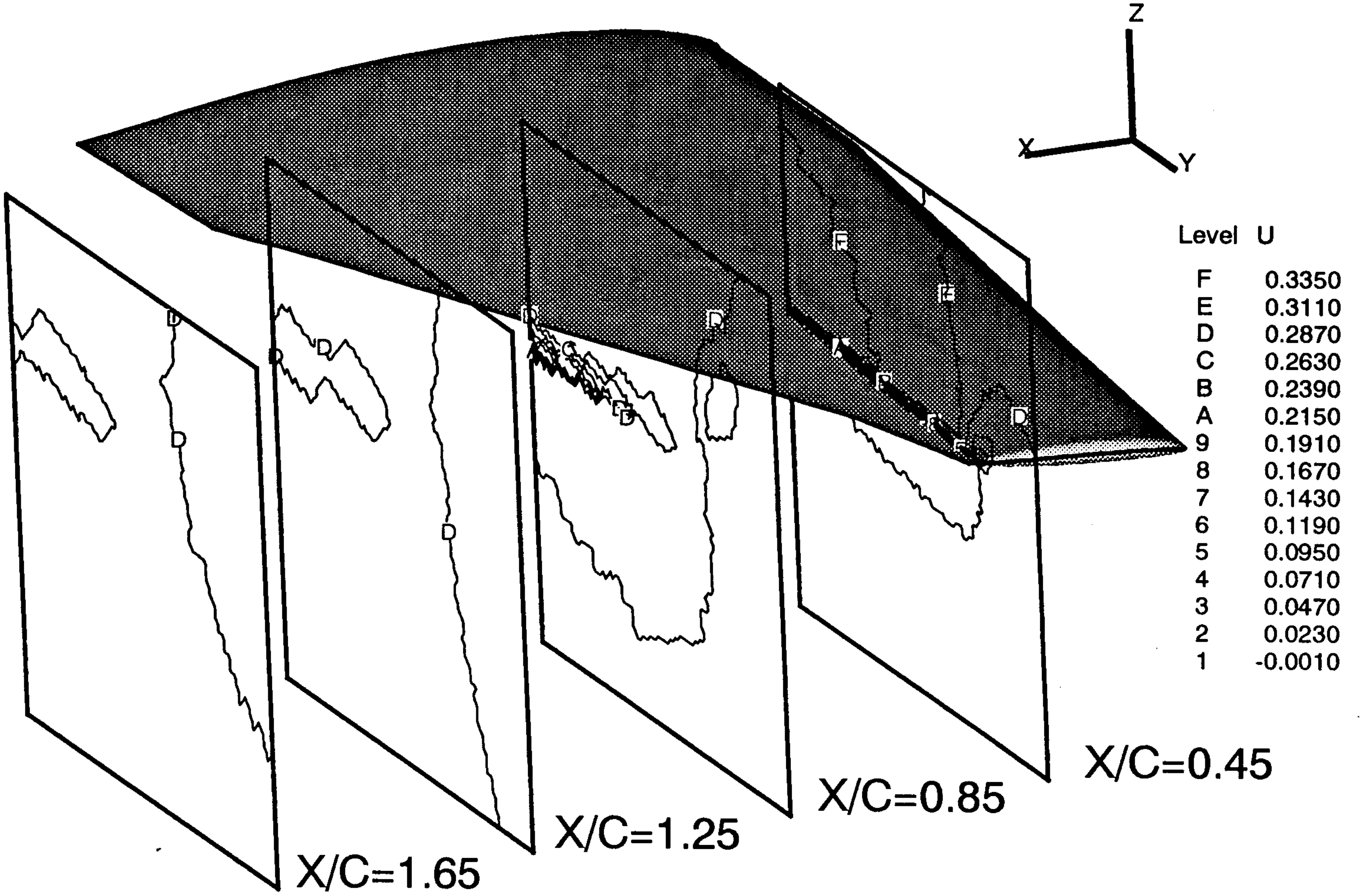

BART Taper-type Wing Tip, $\alpha = 15^{\circ}$, $R_e = 2\times10^{6}$, 161x97x97 Mesh
Tip Flow Field Investigation - Calculated Axial (U-) Velocity Contours

Figure 20. Calculated tip flow field in terms of axial velocity for taper-tip at $\alpha=15^{0}$ with a fine grid.

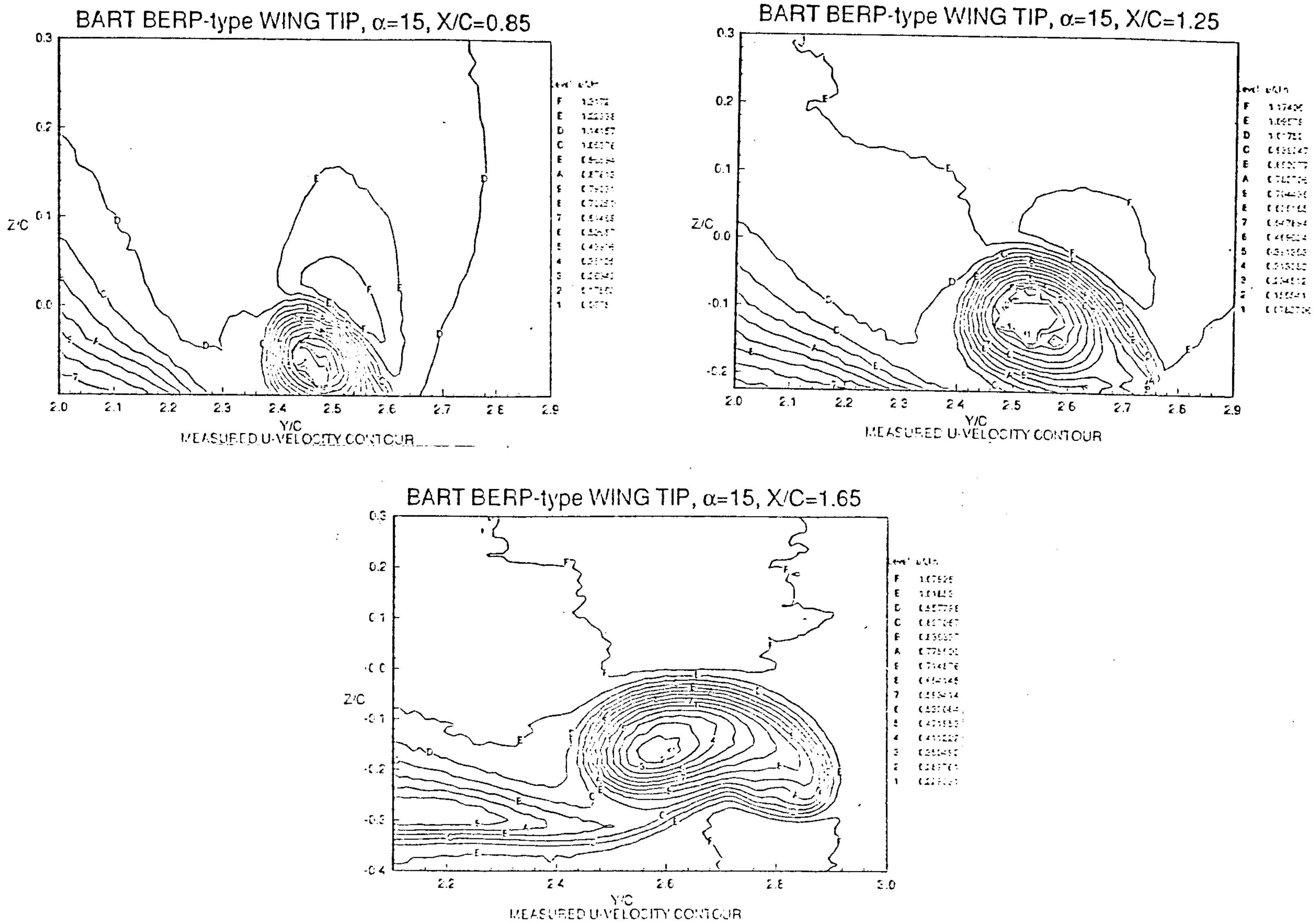

Figure 21. Measured tip flow field in terms of axial velocity for Berp-tip at $\alpha=15^0$.

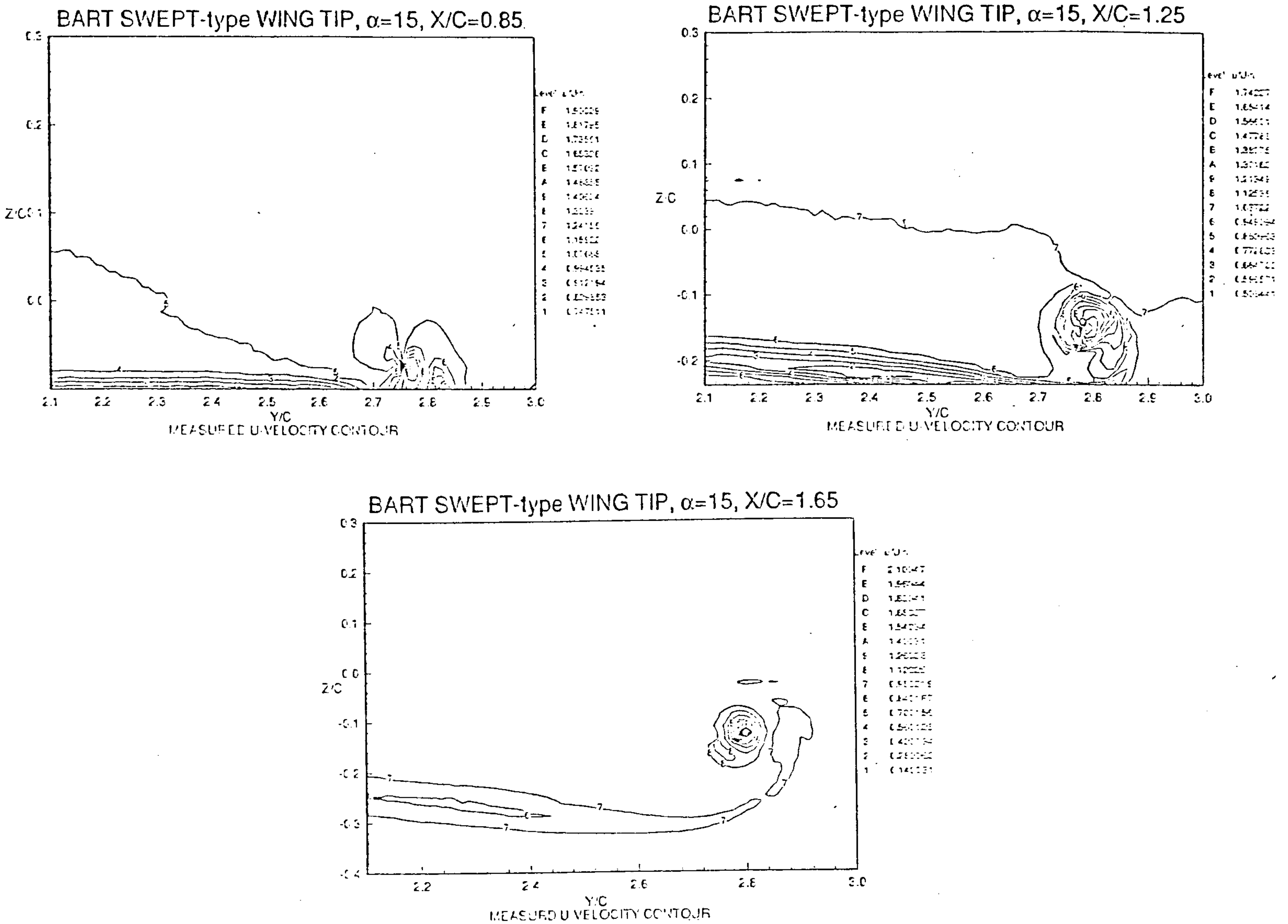

Figure 22. Measured tip flow field in terms of axial velocity for swept-tip at $\alpha=15^0$.

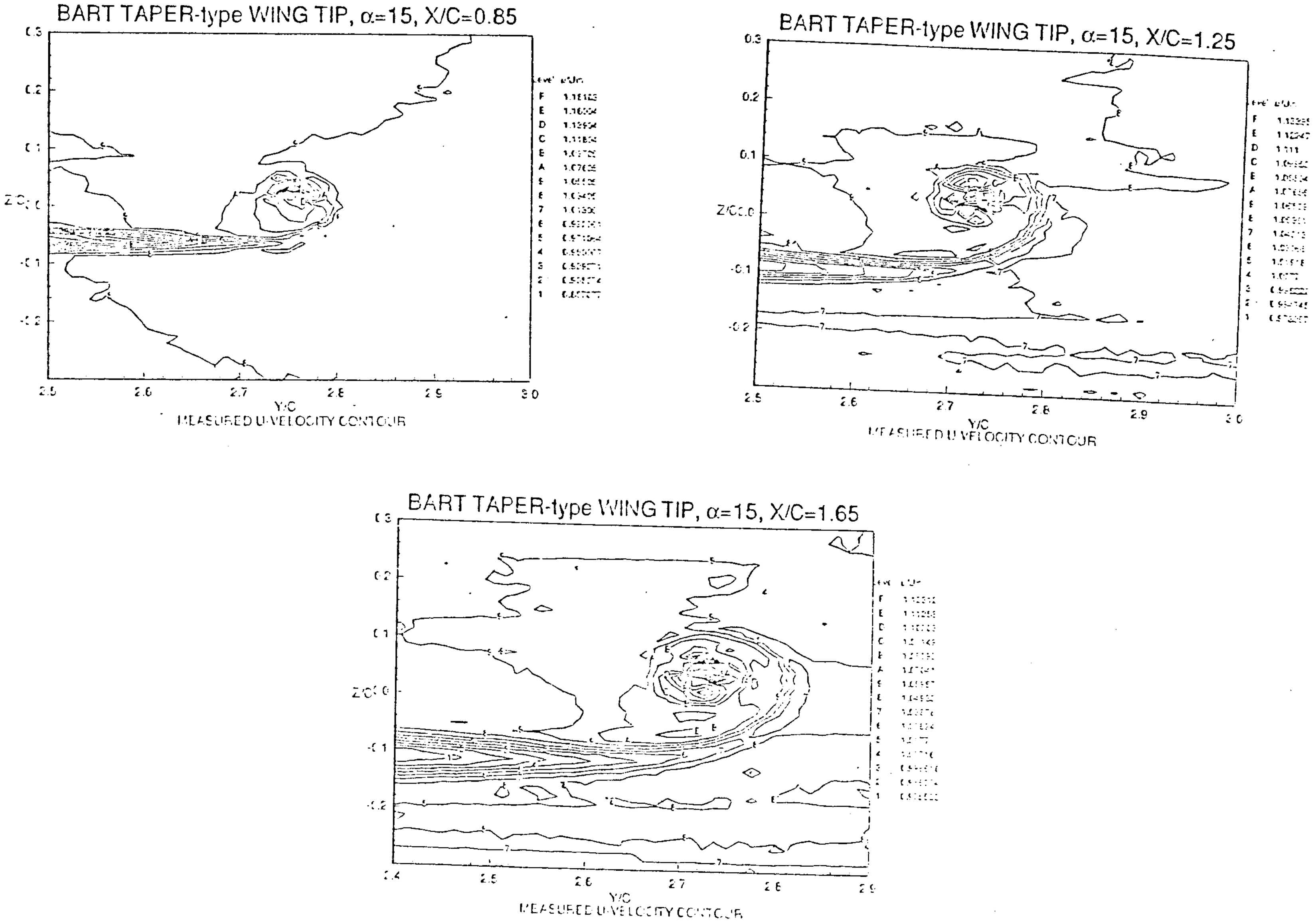
BART TAPER-type WING TIP, α=15, X/C=0.85

BART TAPER-type WING TIP, α=15, X/C=1.25

BART TAPER-type WING TIP, α=15, X/C=1.65

Figure 23. Measured tip flow field in terms of axial velocity for taper-tip at $\alpha=15^0$.

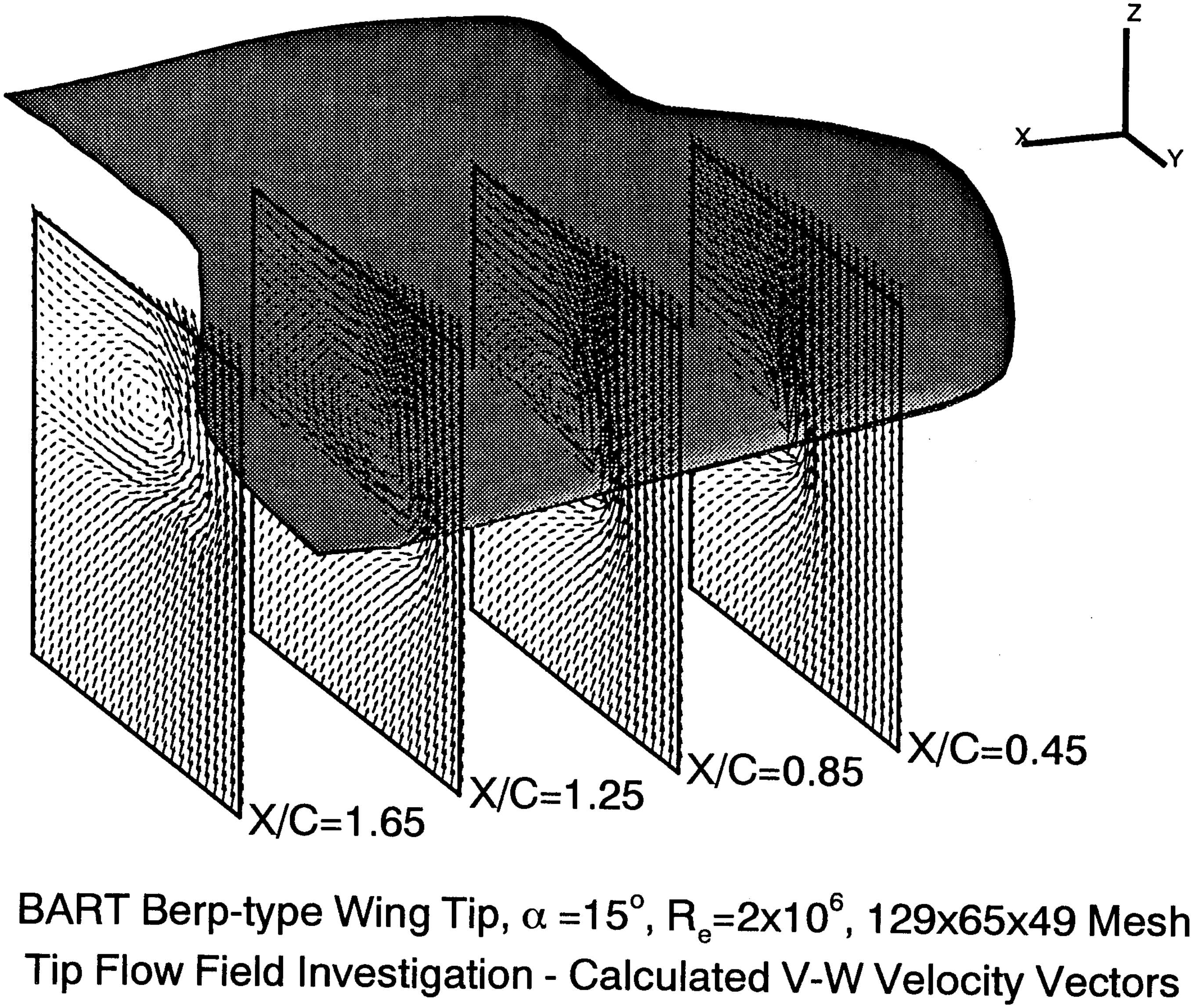

Figure 24. Calculated tip flow field in terms of crossflow velocity vector for Berp-tip at $\alpha=15^0$.

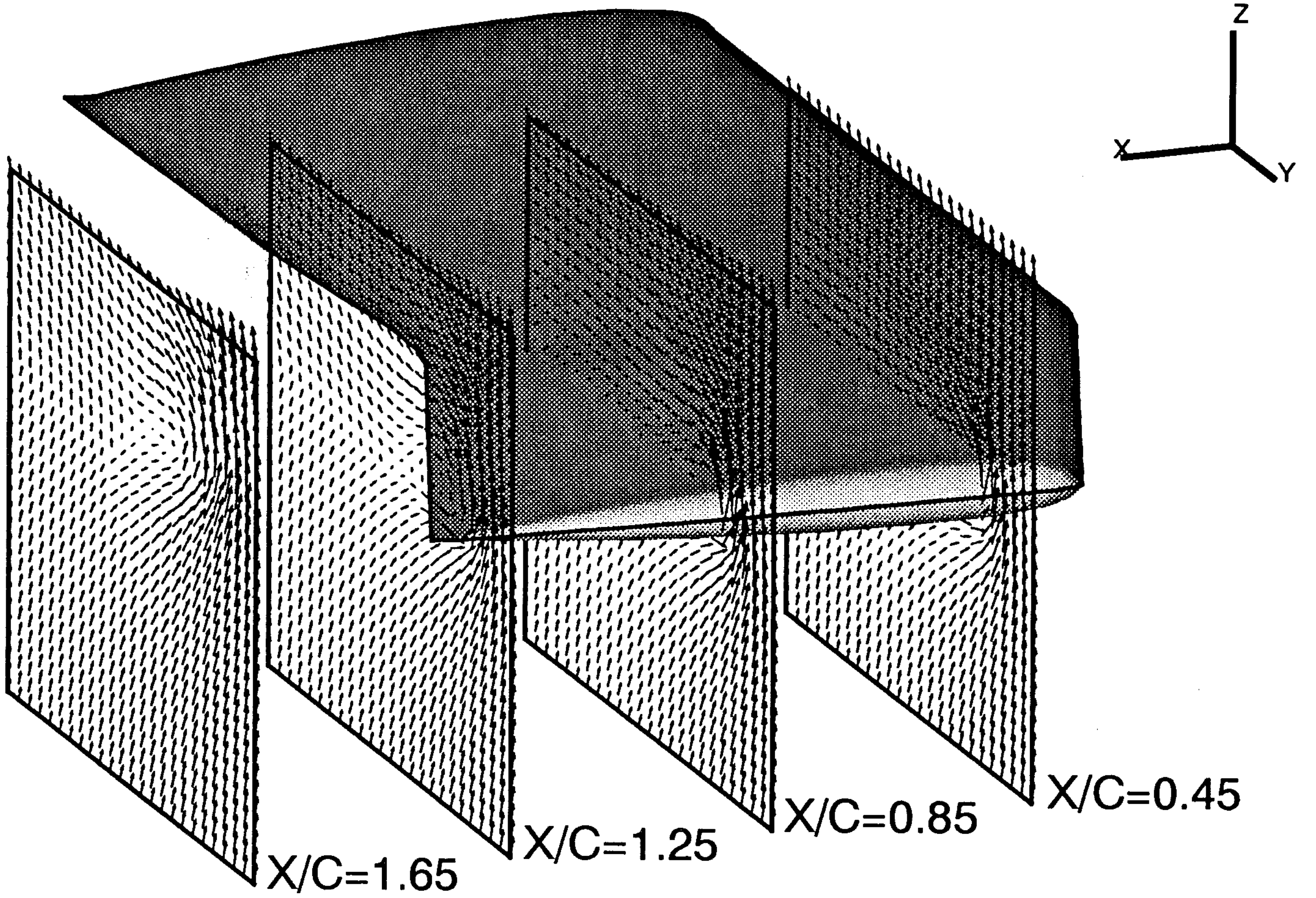

BART Swept-type Wing Tip, $\alpha = 15^{\circ}$, $R_e = 2 \times 10^6$, 129x65x49 Mesh
Tip Flow Field Investigation - Calculated V-W Velocity Vectors

Figure 25. Calculated tip flow field in terms of crossflow velocity vector for swept-tip at $\alpha = 15^0$.

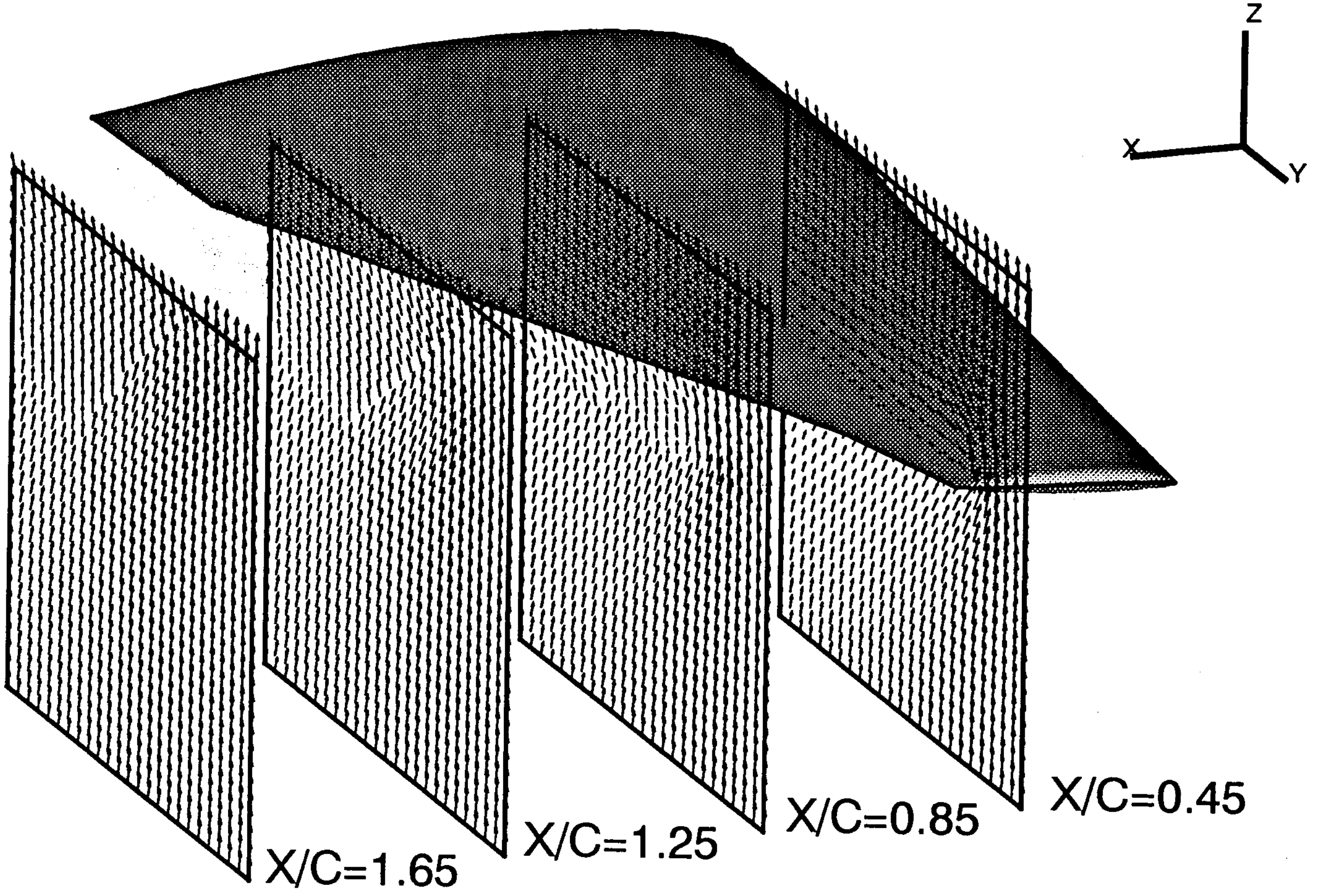

BART Taper-type Wing Tip, $\alpha = 15^{\circ}$, $R_e = 2x10^6$, 129x65x49 Mesh
Tip Flow Field Investigation - Calculated V-W Velocity Vectors

Figure 26. Calculated tip flow field in terms of crossflow velocity vector for taper-tip at $\alpha = 15^0$.

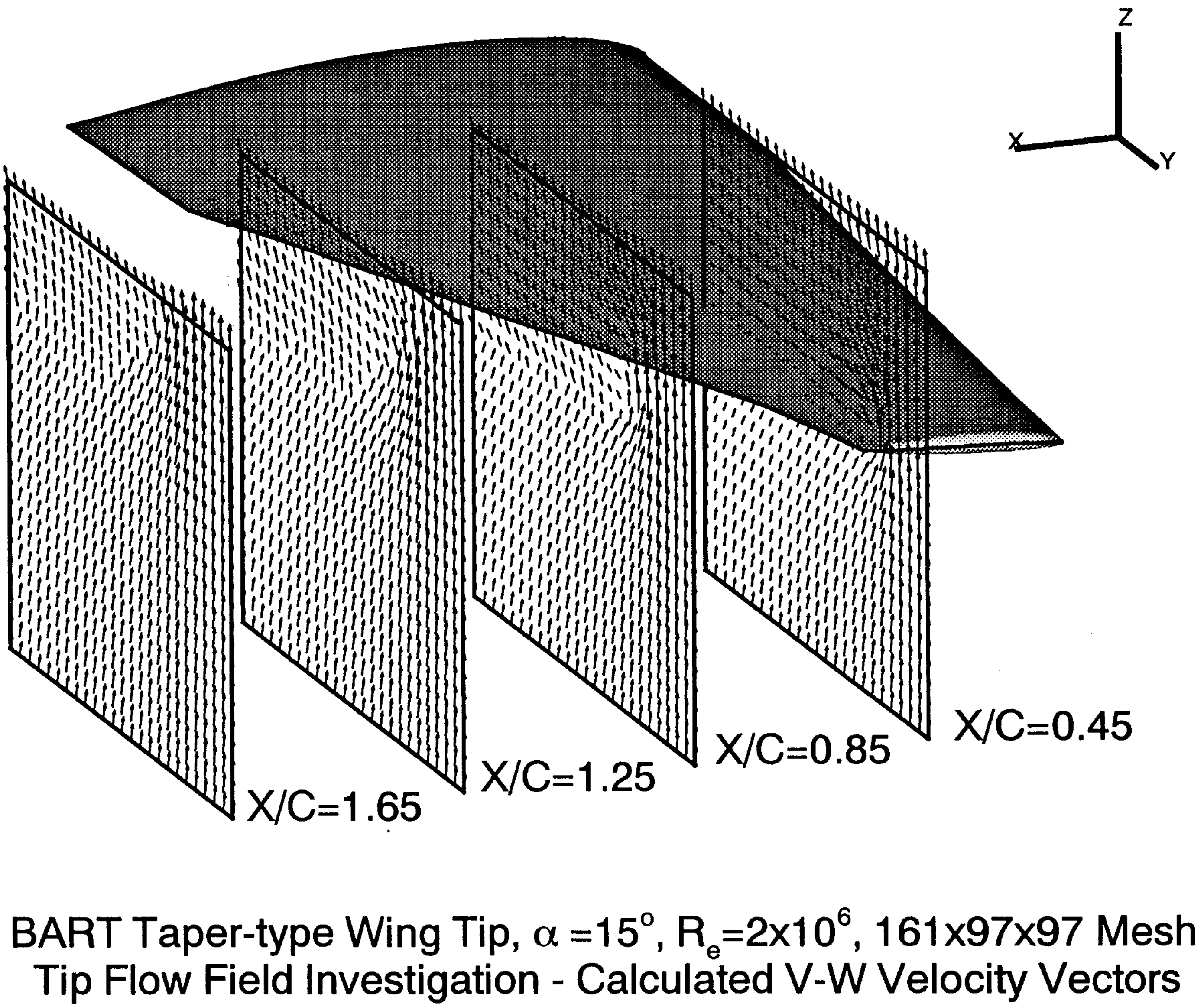

Figure 27. Calculated tip flow field in terms of crossflow velocity vector for taper-tip at $\alpha = 15^0$ with a fine grid.

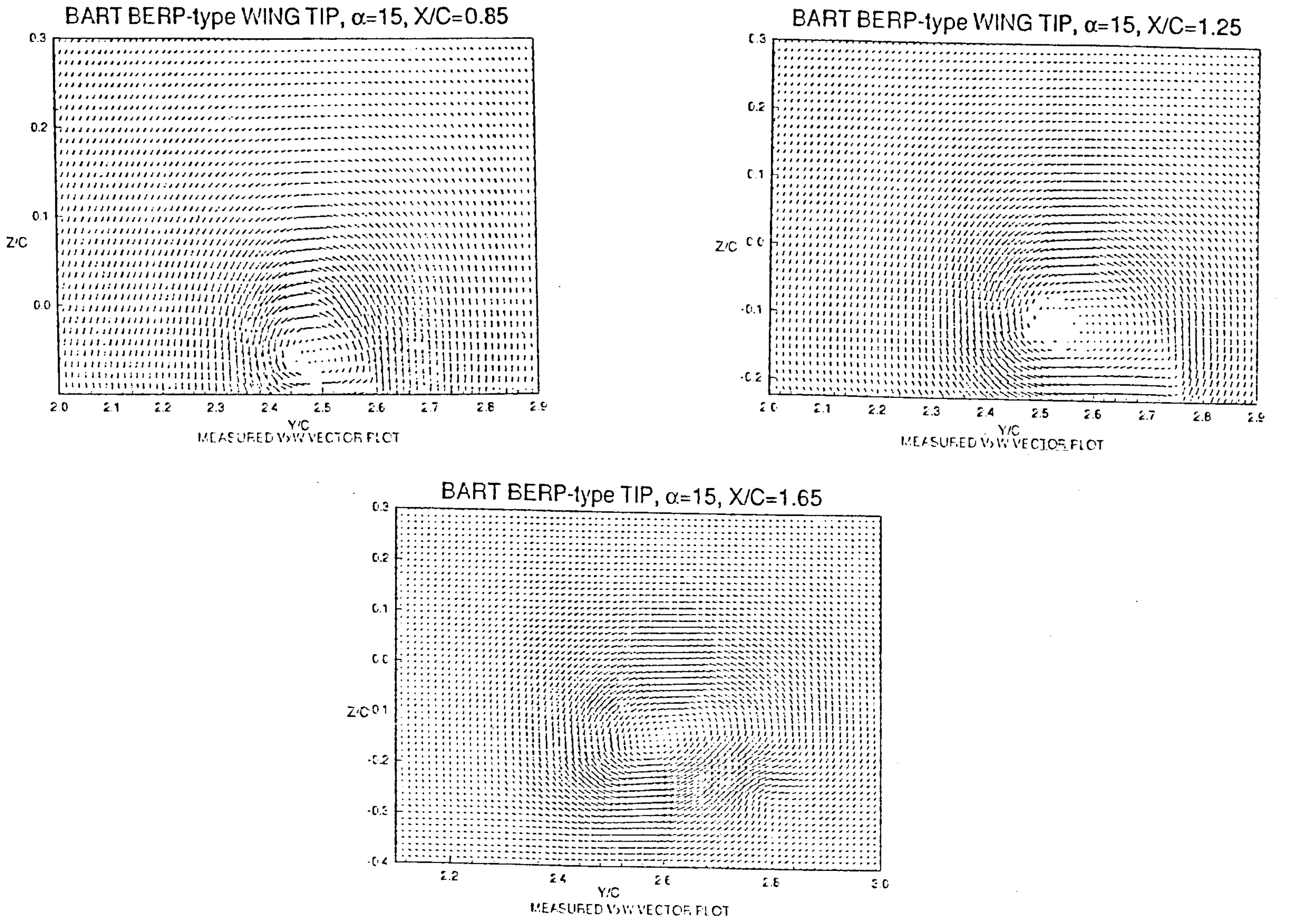

Figure 28. Measured tip flow field in terms of crossflow velocity vector for Berp-tip at $\alpha=15^0$.

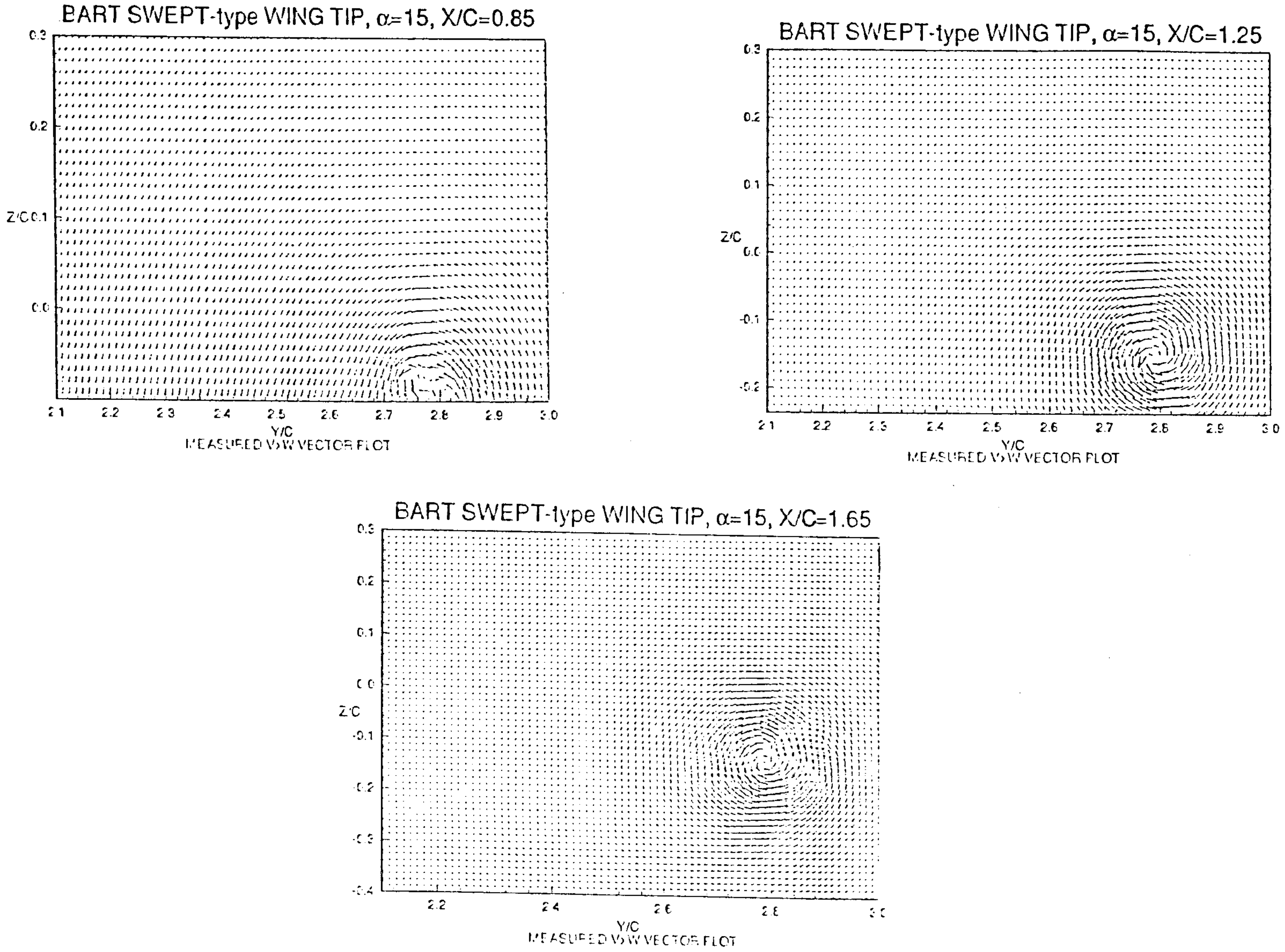
BART SWEPT-type WING TIP, α=15, X/C=0.85

BART SWEPT-type WING TIP, α=15, X/C=1.25

BART SWEPT-type WING TIP, α=15, X/C=1.65

Figure 29. Measured tip flow field in terms of crossflow velocity vector for swept-tip at $\alpha=15^0$.

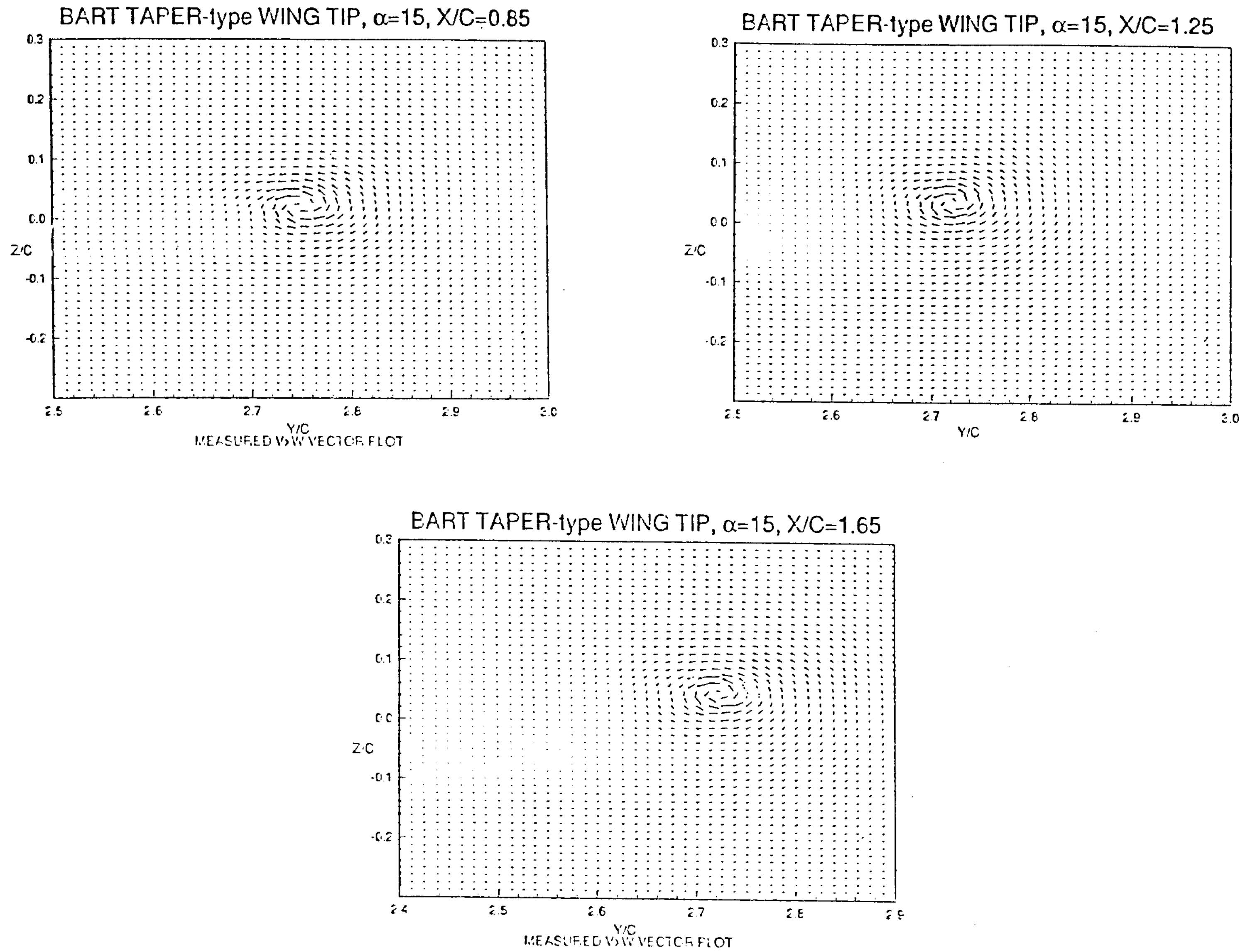

Figure 30. Measured tip flow field in terms of crossflow velocity vector for taper-tip at $\alpha=15^0$.

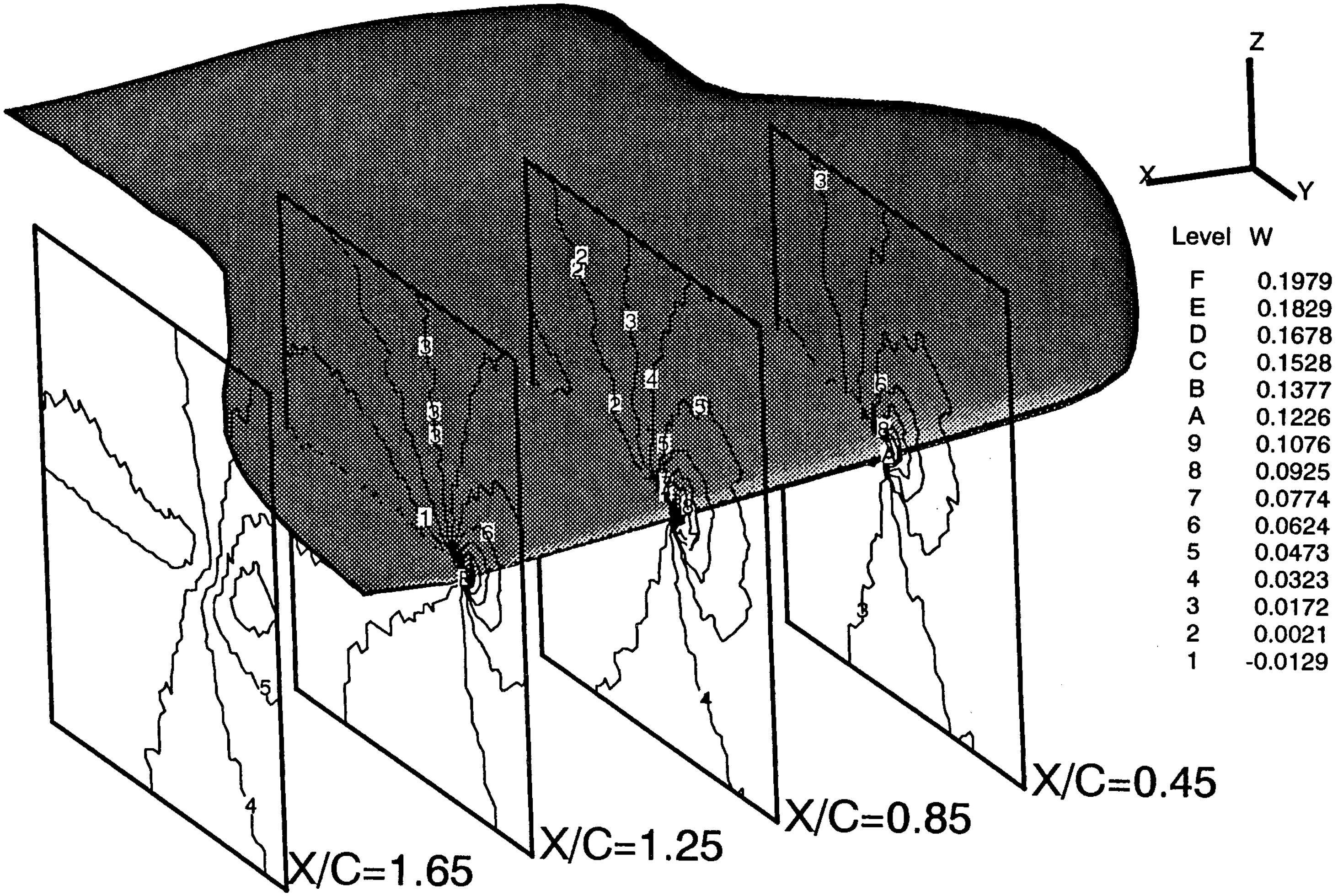

BART Berp-type Wing Tip, $\alpha = 5^{\circ}$, $R_e = 2 \times 10^6$, 129x65x49 Mesh
Tip Flow Field Investigation - Calculated Downwash (W) Contours

Figure 31. Calculated tip flow field in terms of downwash for Berp-tip at $\alpha = 5^0$.

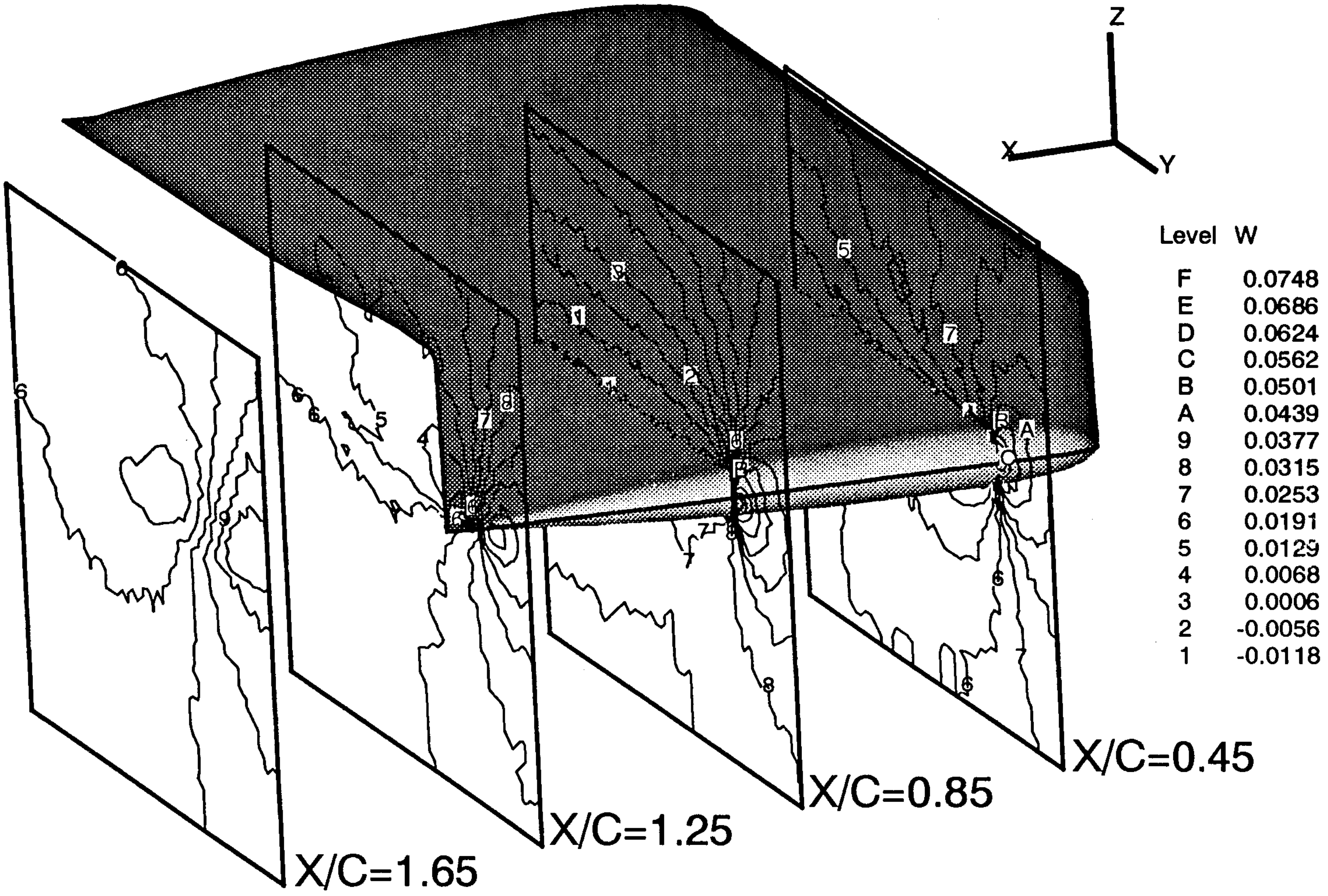

BART Swept-type Wing Tip, $\alpha = 5^\circ$, $R_e = 2\times10^6$, 129x65x49 Mesh
Tip Flow Field Investigation - Calculated Downwash (W) Contours

Figure 32. Calculated tip flow field in terms of downwash for swept-tip at $\alpha = 5^0$.

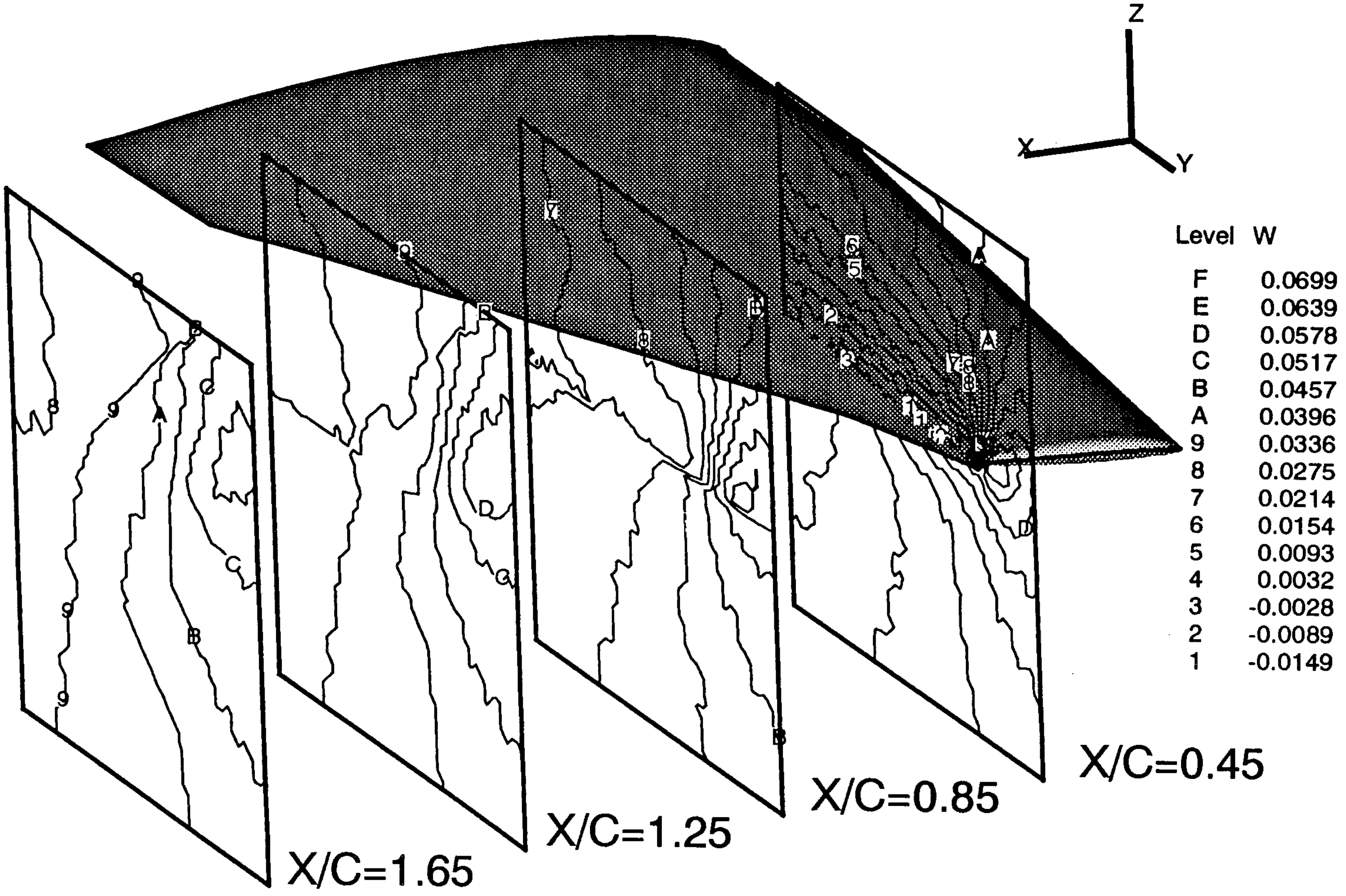

BART Taper-type Wing Tip, α =7.5°, R_e=2x10^6, 129x65x49 Mesh
Tip Flow Field Investigation - Calculated Downwash (W) Contours

Figure 33. Calculated tip flow field in terms of downwash for taper-tip at α=7.5^0.

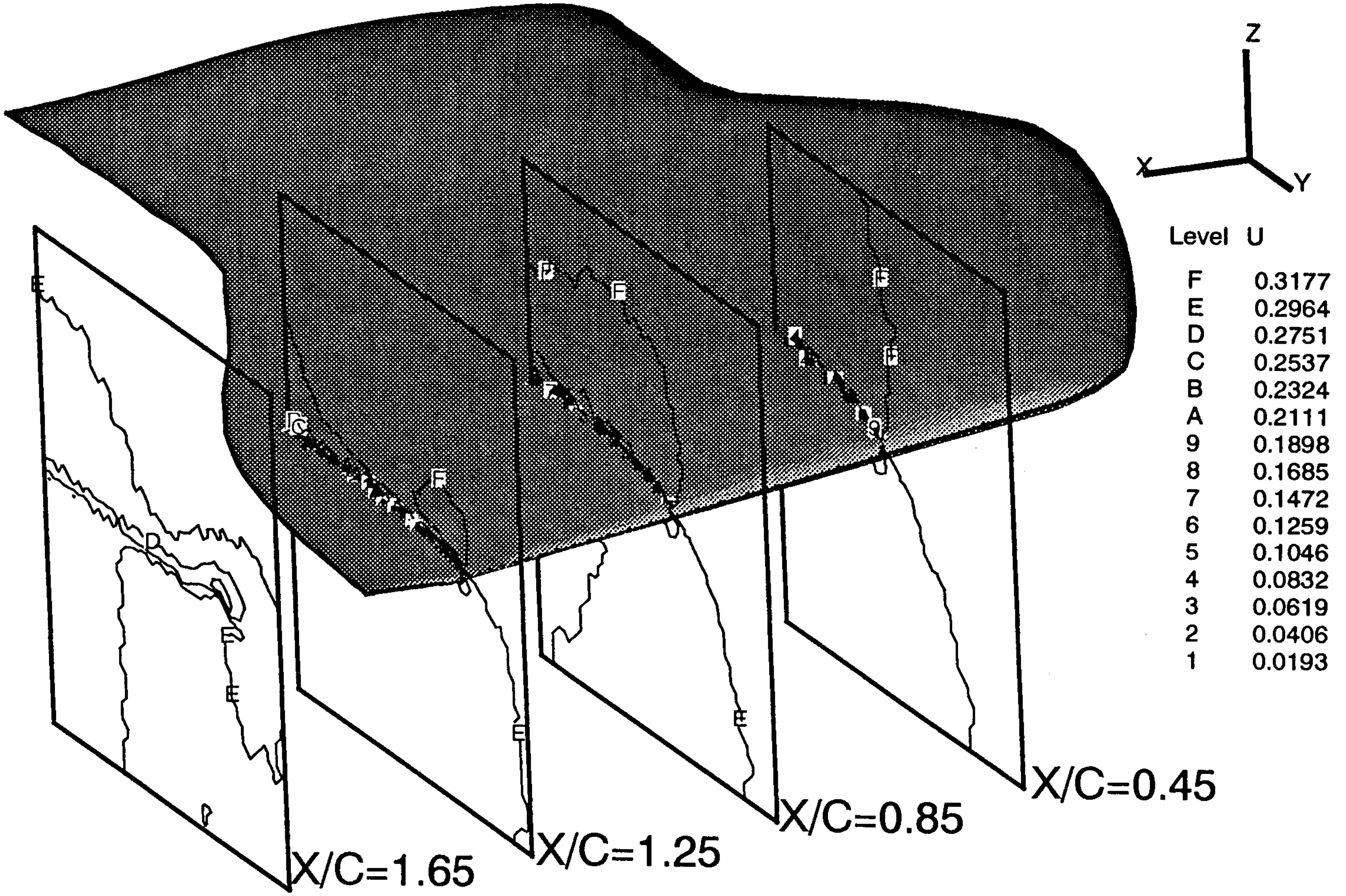

BART Berp-type Wing Tip, $\alpha = 5^{\circ}$, $R_e = 2\times10^6$, 129x65x49 Mesh
Tip Flow Field Investigation - Calculated Axial (U-) Velocity Contours

Figure 34. Calculated tip flow field in terms of axial velocity for Berp-tip at $\alpha=5^{0}$.

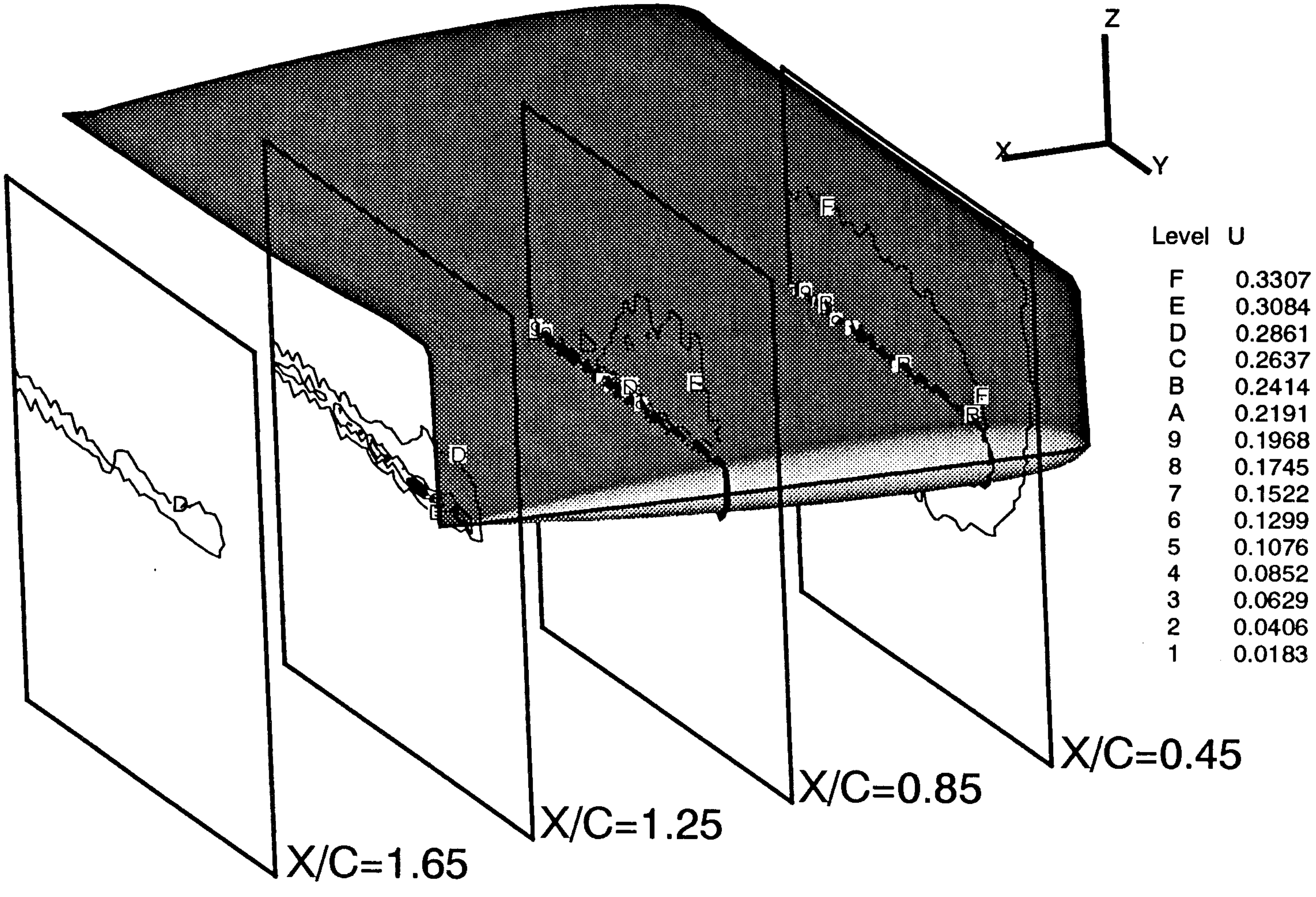

BART Swept-type Wing Tip, $\alpha = 5^{\circ}$, $R_e = 2\times10^6$, 129x65x49 Mesh
Tip Flow Field Investigation - Calculated Axial (U-) Velocity Contours

Figure 35. Calculated tip flow field in terms of axial velocity for swept-tip at $\alpha = 5^0$.

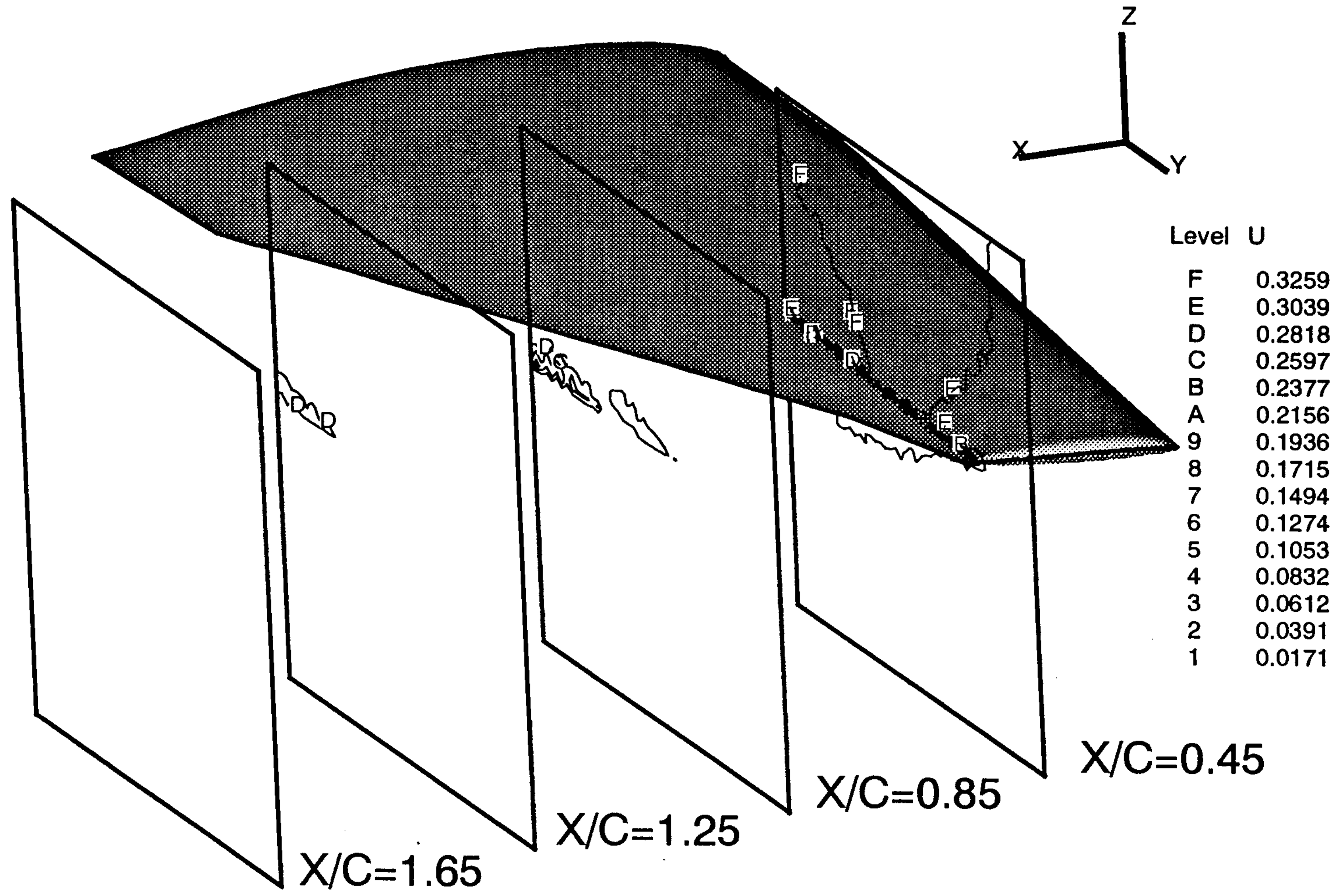

BART Taper-type Wing Tip, $\alpha = 7.5^\circ$, $R_e = 2\text{x}10^6$, 129x65x49 Mesh
Tip Flow Field Investigation - Calculated Axial (U-) Velocity Contours

Figure 36. Calculated tip flow field in terms of axial velocity for taper-tip at $\alpha = 7.5^0$.

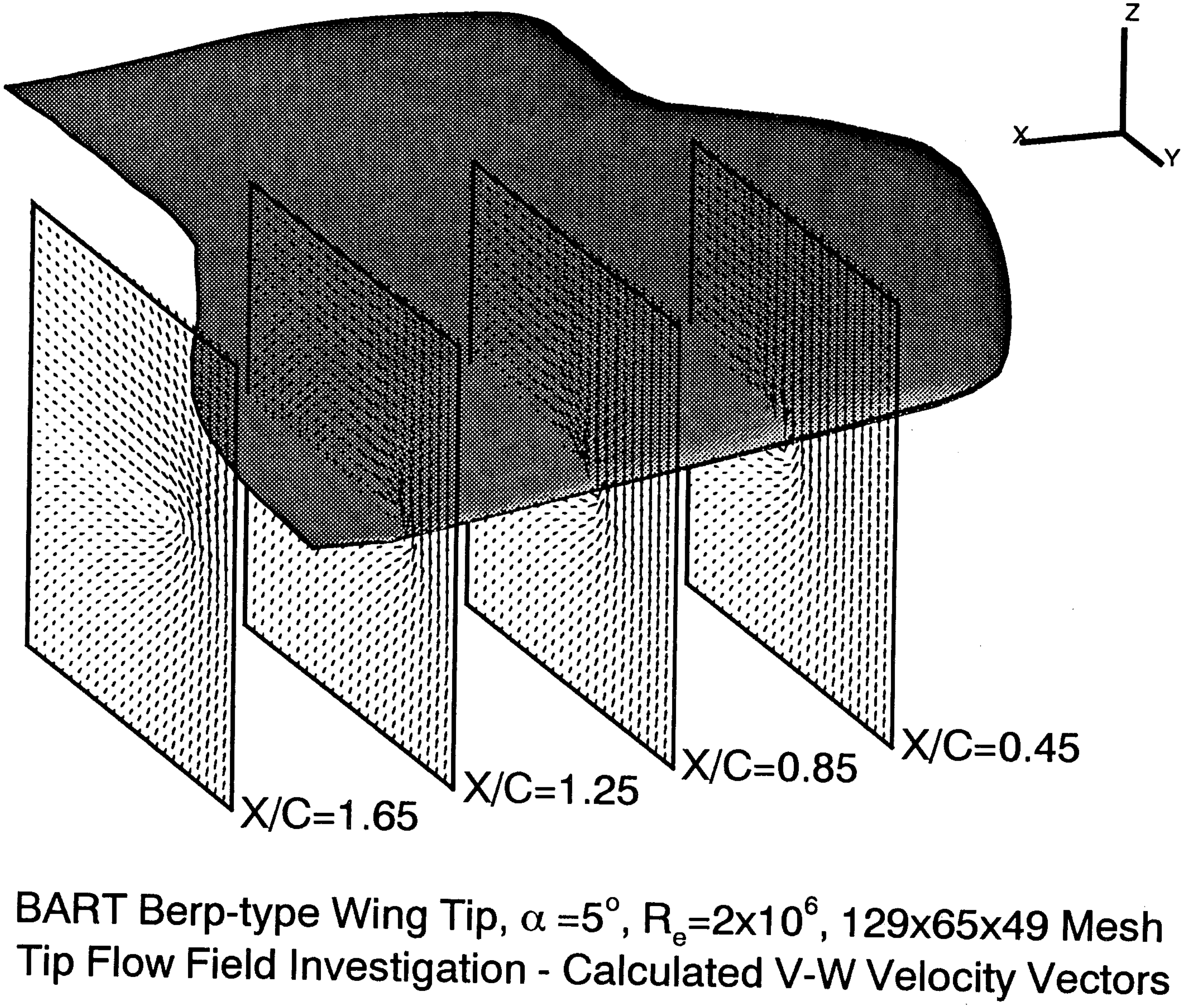

Figure 37. Calculated tip flow field in terms of crossflow velocity vector for Berp-tip at $\alpha=5^0$.

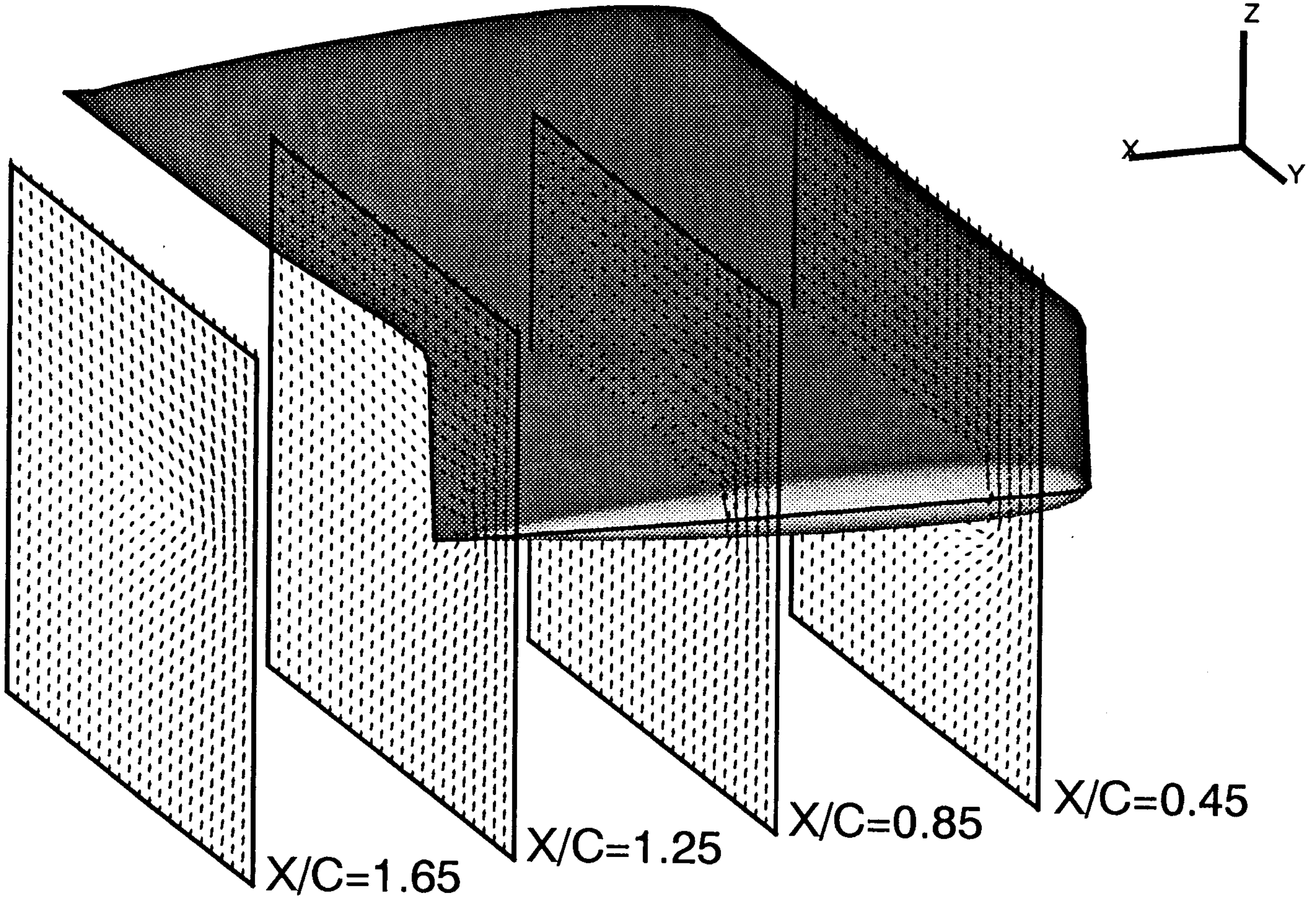

BART Swept-type Wing Tip, α =5°, R_e=2x10^6, 129x65x49 Mesh
Tip Flow Field Investigation - Calculated V-W Velocity Vectors

Figure 38. Calculated tip flow field in terms of crossflow velocity vector for swept-tip at α=5^0.

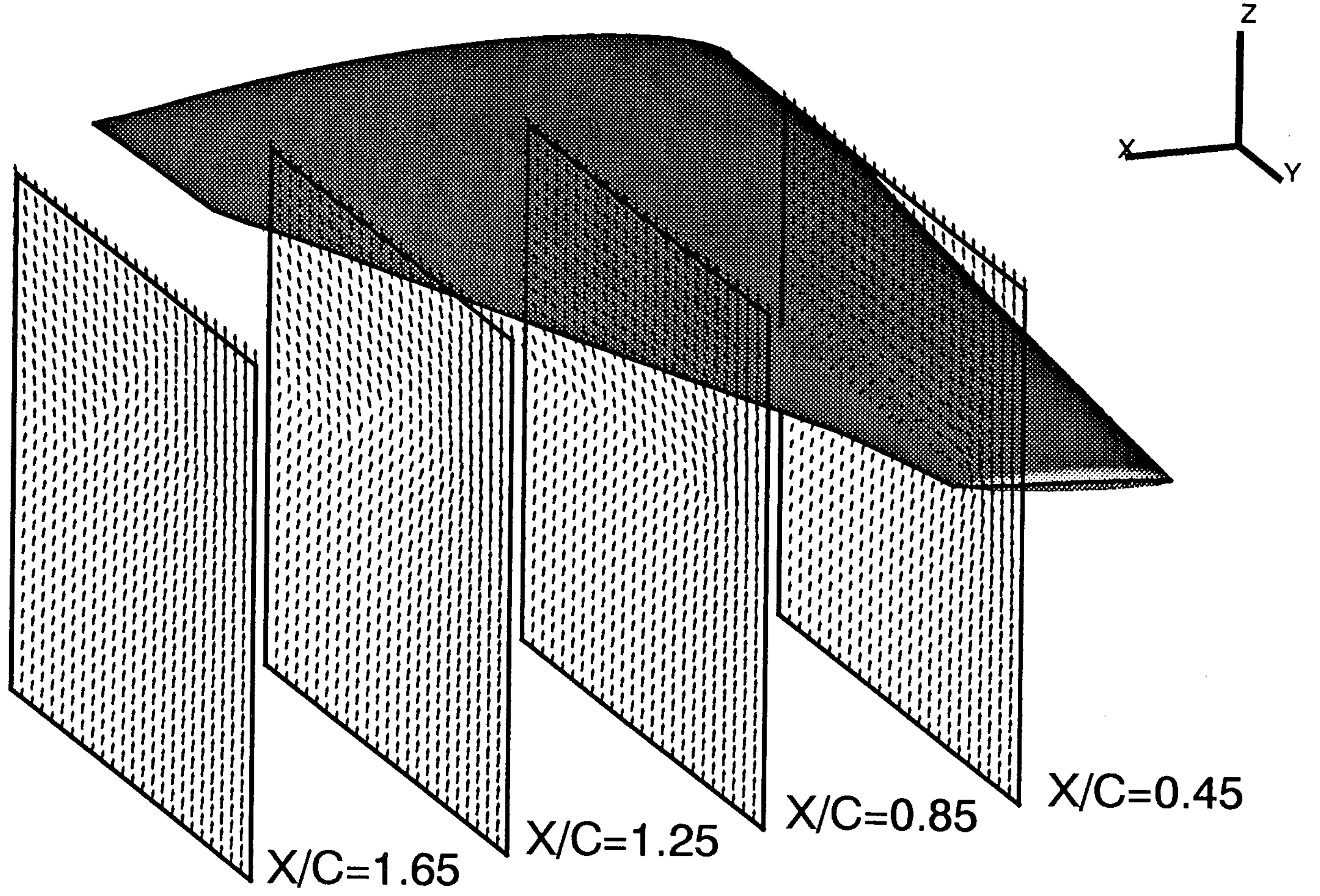

BART Taper-type Wing Tip, α =7.5°, R_e=2x10^6, 129x65x49 Mesh
Tip Flow Field Investigation - Calculated V-W Velocity Vectors

Figure 39. Calculated tip flow field in terms of crossflow velocity vector for taper-tip at α=7.5^0.

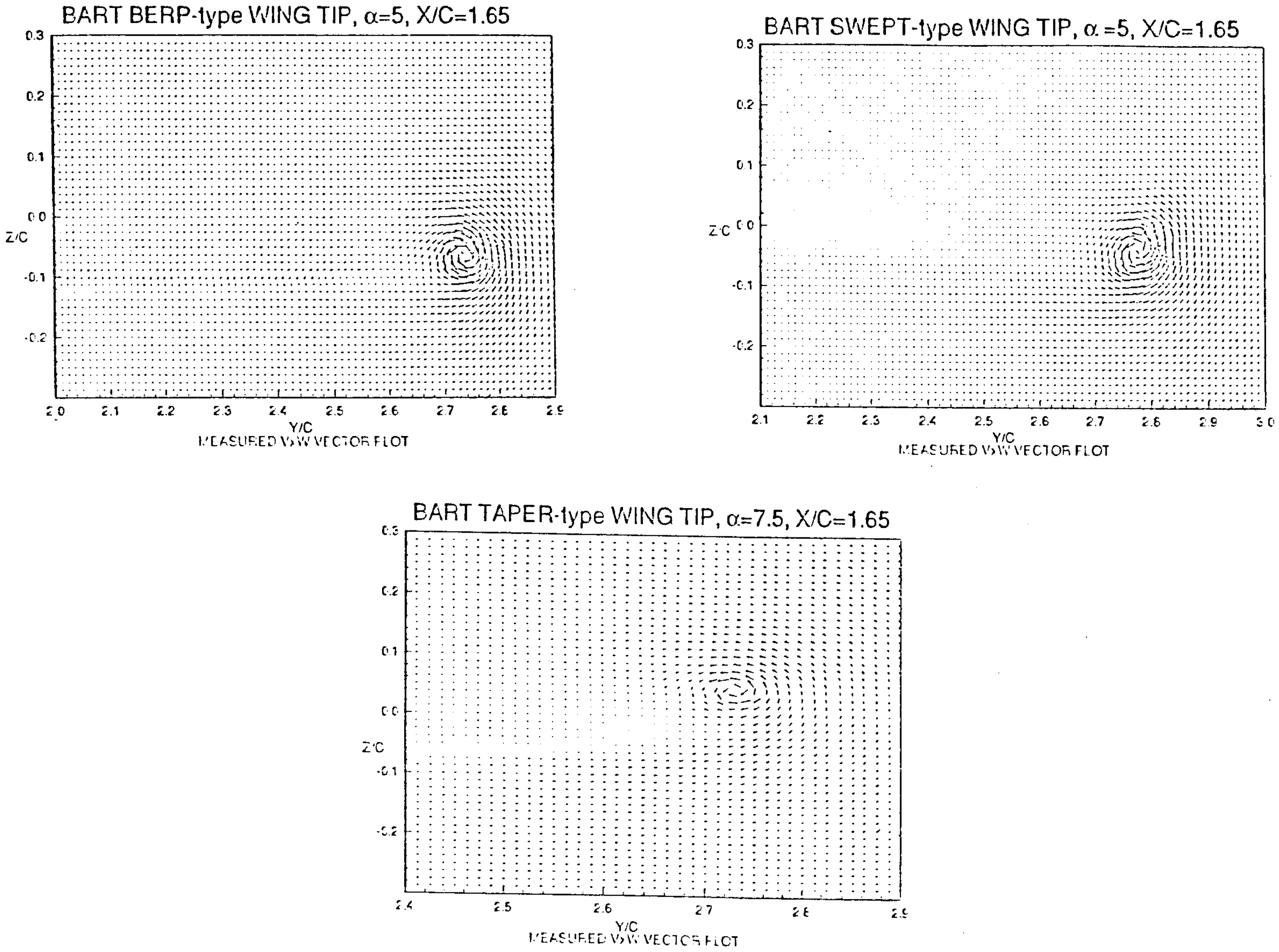

Figure 40. Measured tip flow field in terms of crossflow velocity vector for three tips at α=5° to 7.5° and x/c=1.65.

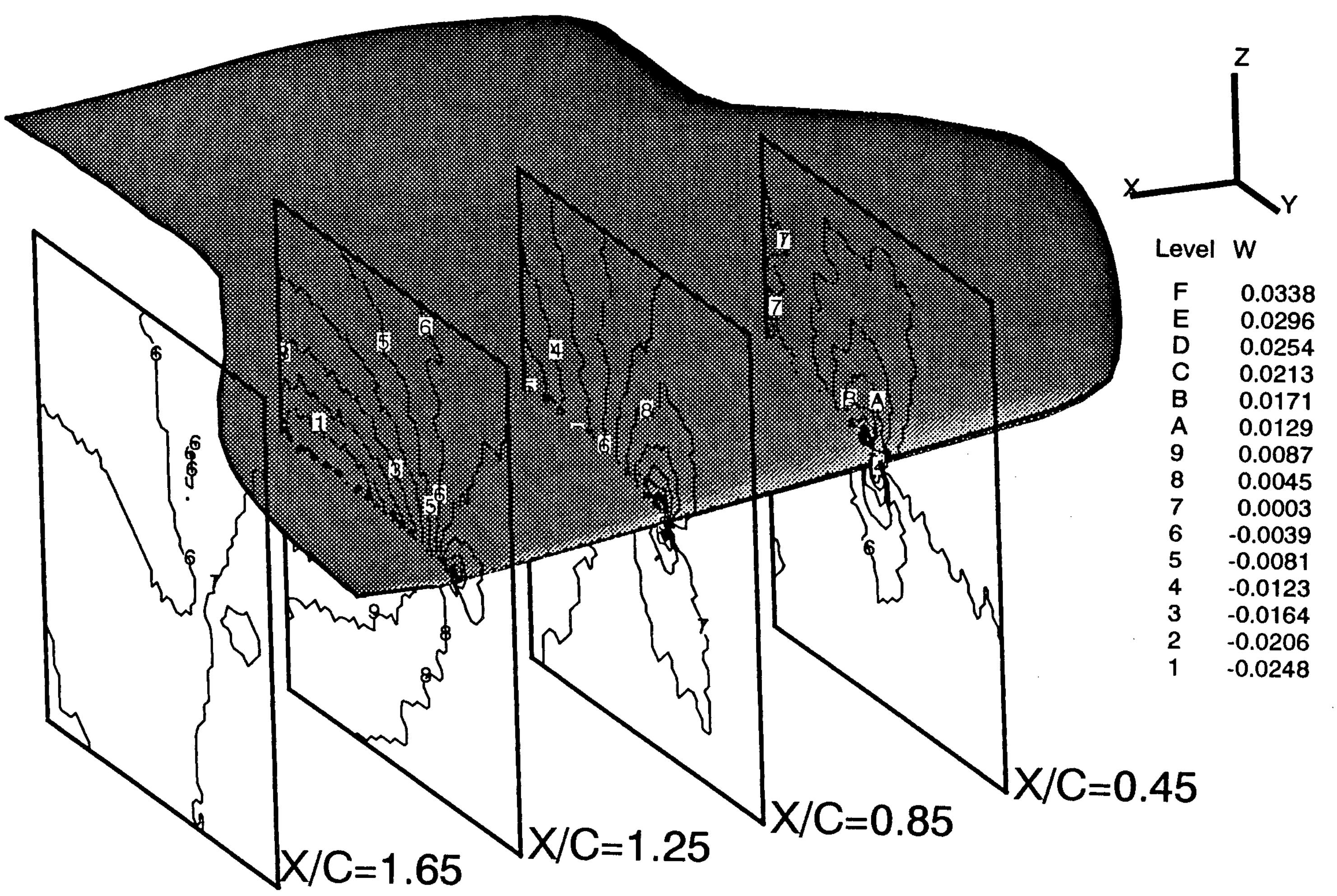

BART Berp-type Wing Tip, $\alpha = 0^\circ$, $R_e = 2x10^6$, 129x65x49 Mesh
Tip Flow Field Investigation - Calculated Downwash (W) Contours

Figure 41. Calculated tip flow field in terms of downwash for Berp-tip at $\alpha = 0^\circ$.

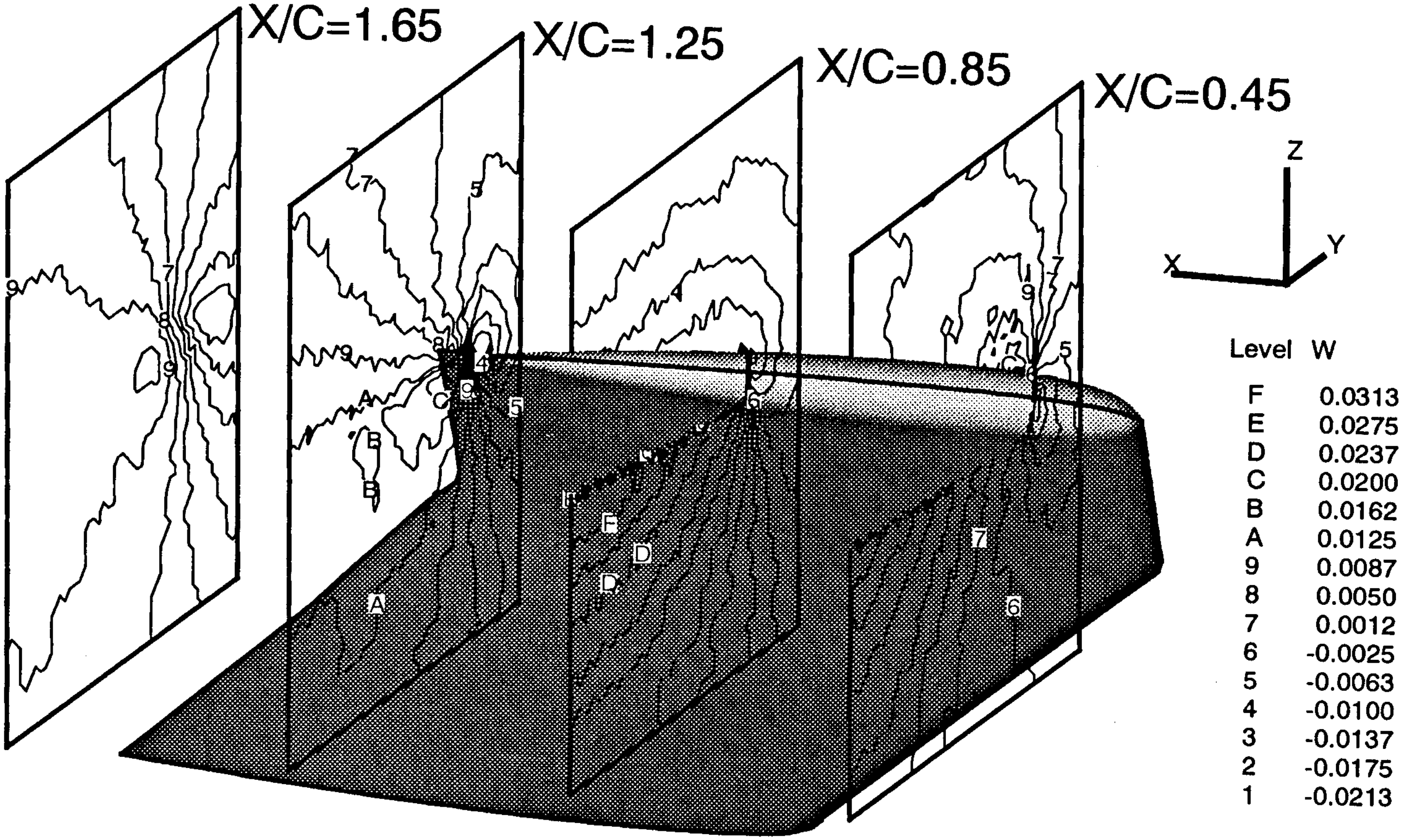

BART Swept-type Wing Tip, $\alpha = 0^\circ$, $R_e = 2x10^6$, 129x65x49 Mesh
Tip Flow Field Investigation - Calculated Downwash (W) Contours

Figure 42. Calculated tip flow field in terms of downwash for swept-tip at $\alpha = 0^\circ$.

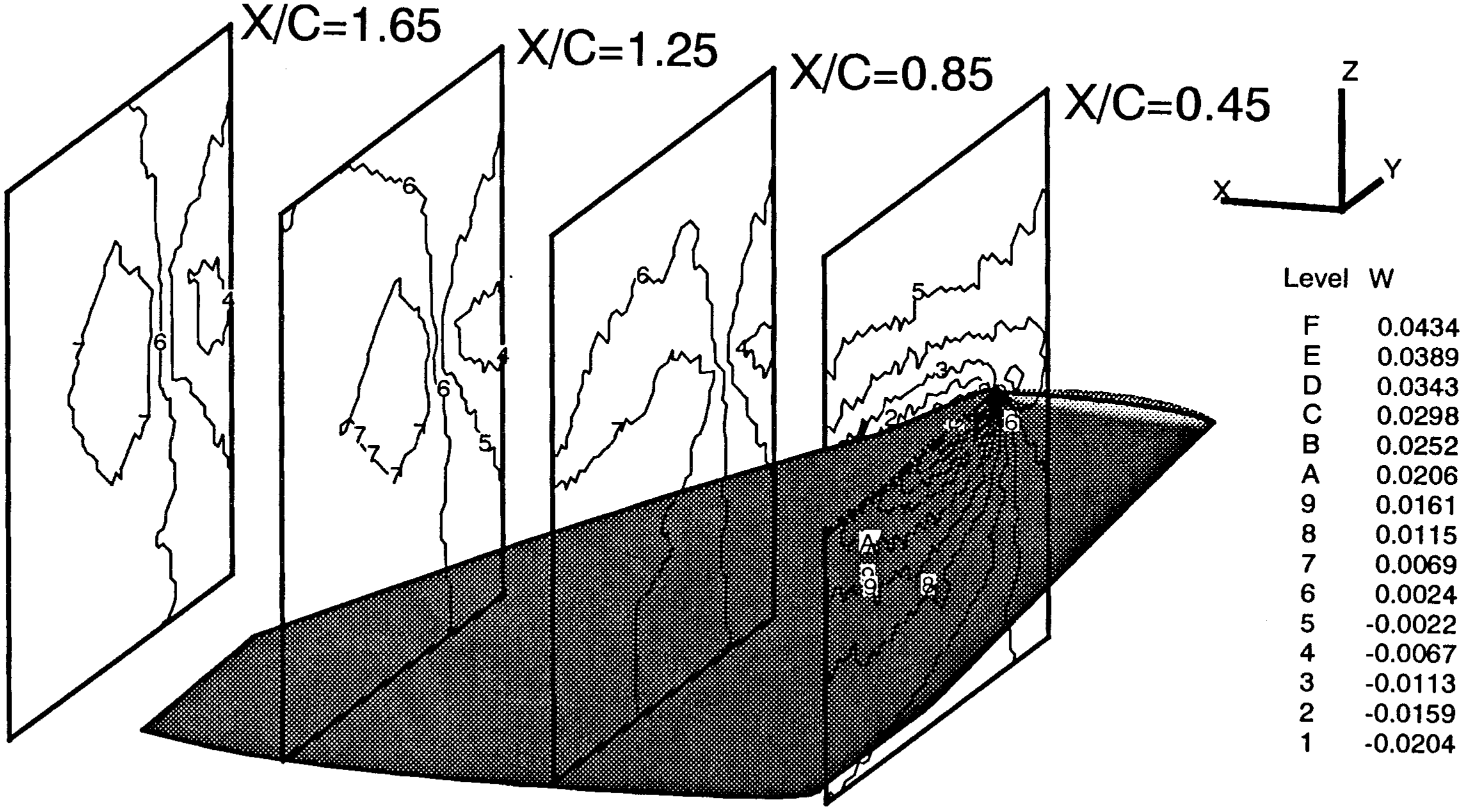

BART Taper-type Wing Tip, $\alpha = 0°$, $R_e = 2\text{x}10^6$, 129x65x49 Mesh
Tip Flow Field Investigation - Calculated Downwash (W) Contours

Figure 43. Calculated tip flow field in terms of downwash for taper-tip at α=0°.

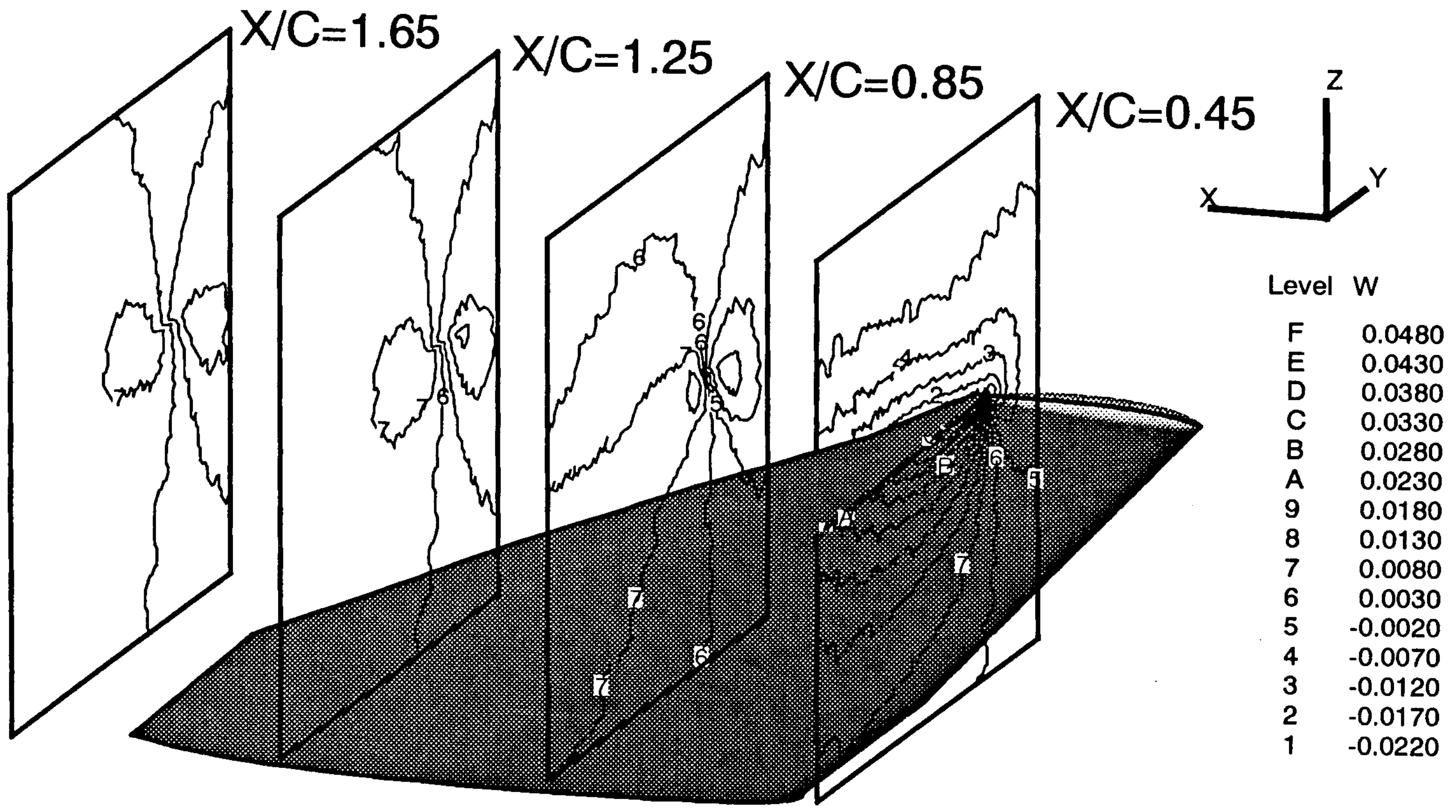

BART Taper-type Wing Tip, $\alpha = 0^\circ$, $R_e = 2x10^6$, 161x97x97 Mesh
Tip Flow Field Investigation - Calculated Downwash (W) Contours

Figure 44. Calculated tip flow field in terms of downwash for taper-tip at $\alpha = 0^\circ$ with a fine grid.

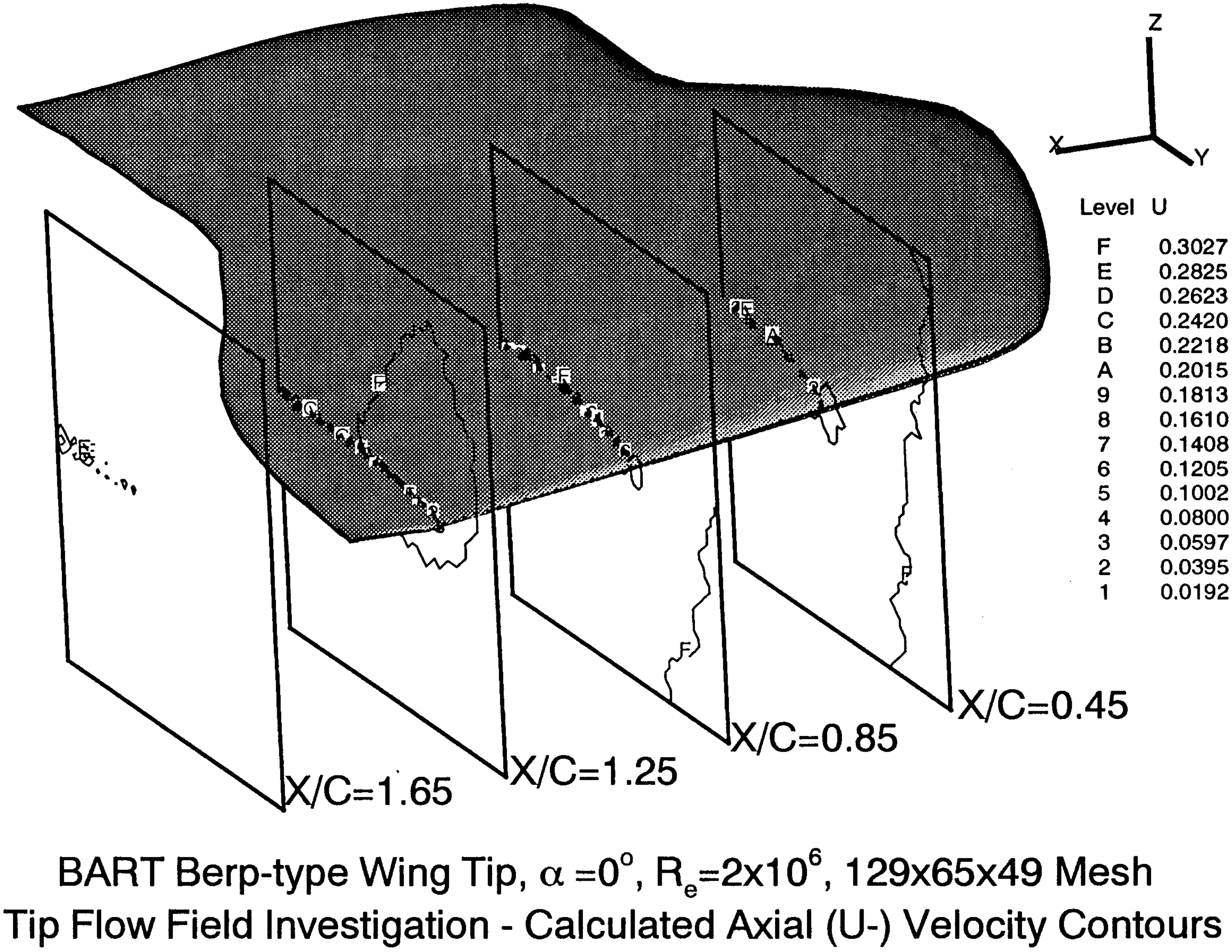

Figure 45. Calculated tip flow field in terms of axial velocity for Berp-tip at α=0°.

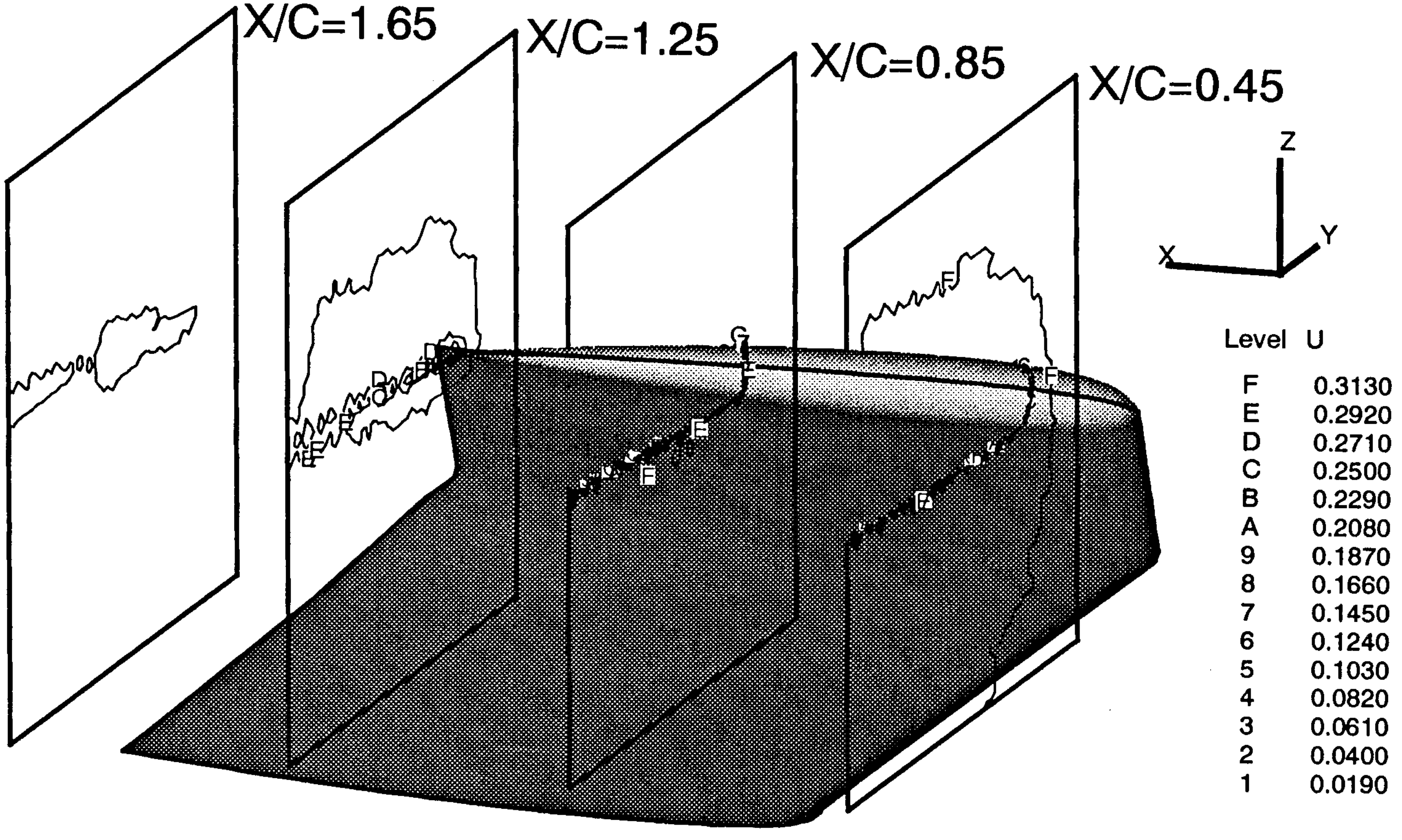

BART Swept-type Wing Tip, $\alpha = 0^\circ$, $R_e = 2 \times 10^6$, 129x65x49 Mesh
Tip Flow Field Investigation - Calculated Axial (U-) Velocity Contours

Figure 46. Calculated tip flow field in terms of axial velocity for swept-tip at $\alpha = 0^\circ$.

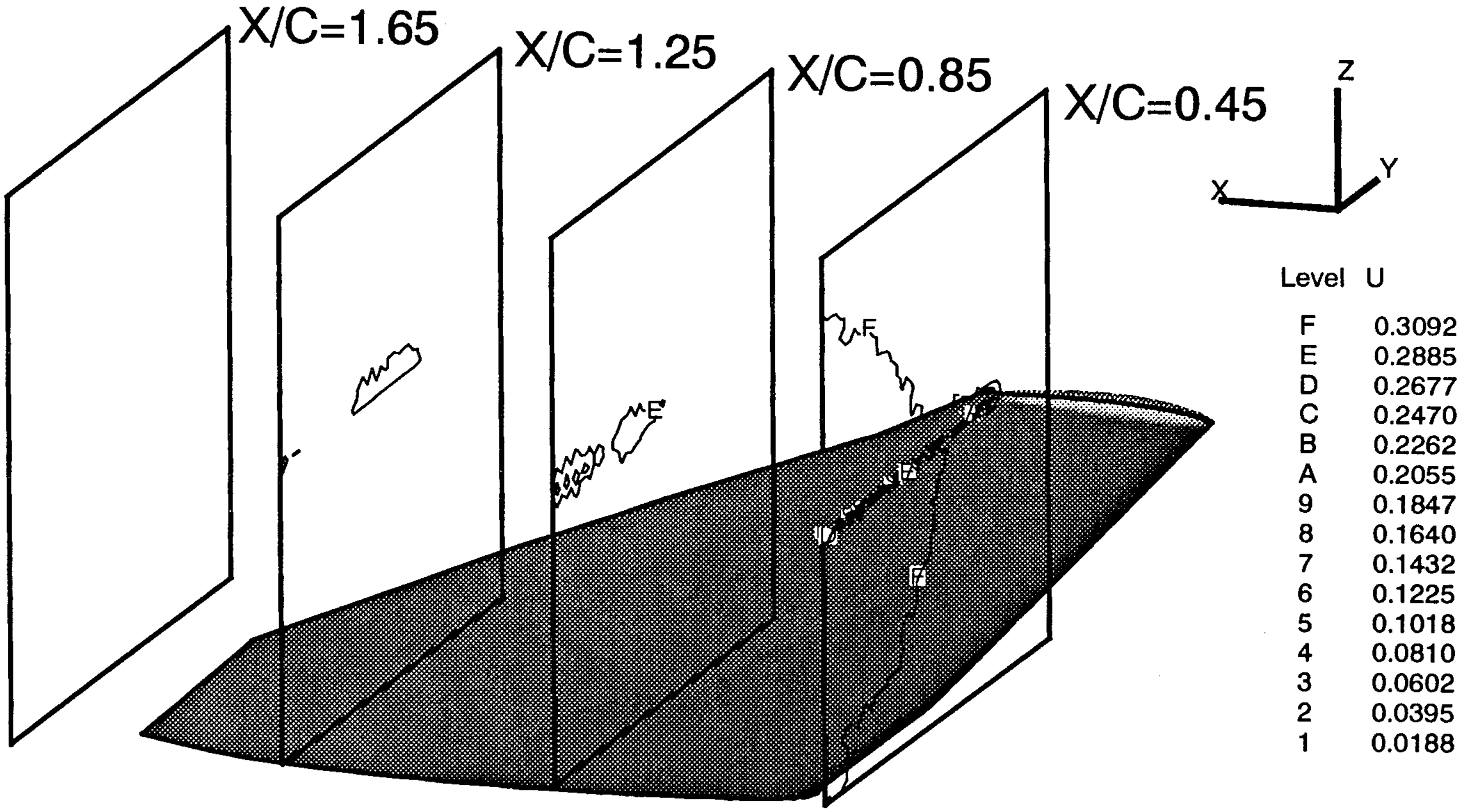

BART Taper-type Wing Tip, α =0°, R_e=2x10^6, 129x65x49 Mesh
Tip Flow Field Investigation - Calculated Axial (U-) Velocity Contours

Figure 47. Calculated tip flow field in terms of axial velocity for taper-tip at α=0°.

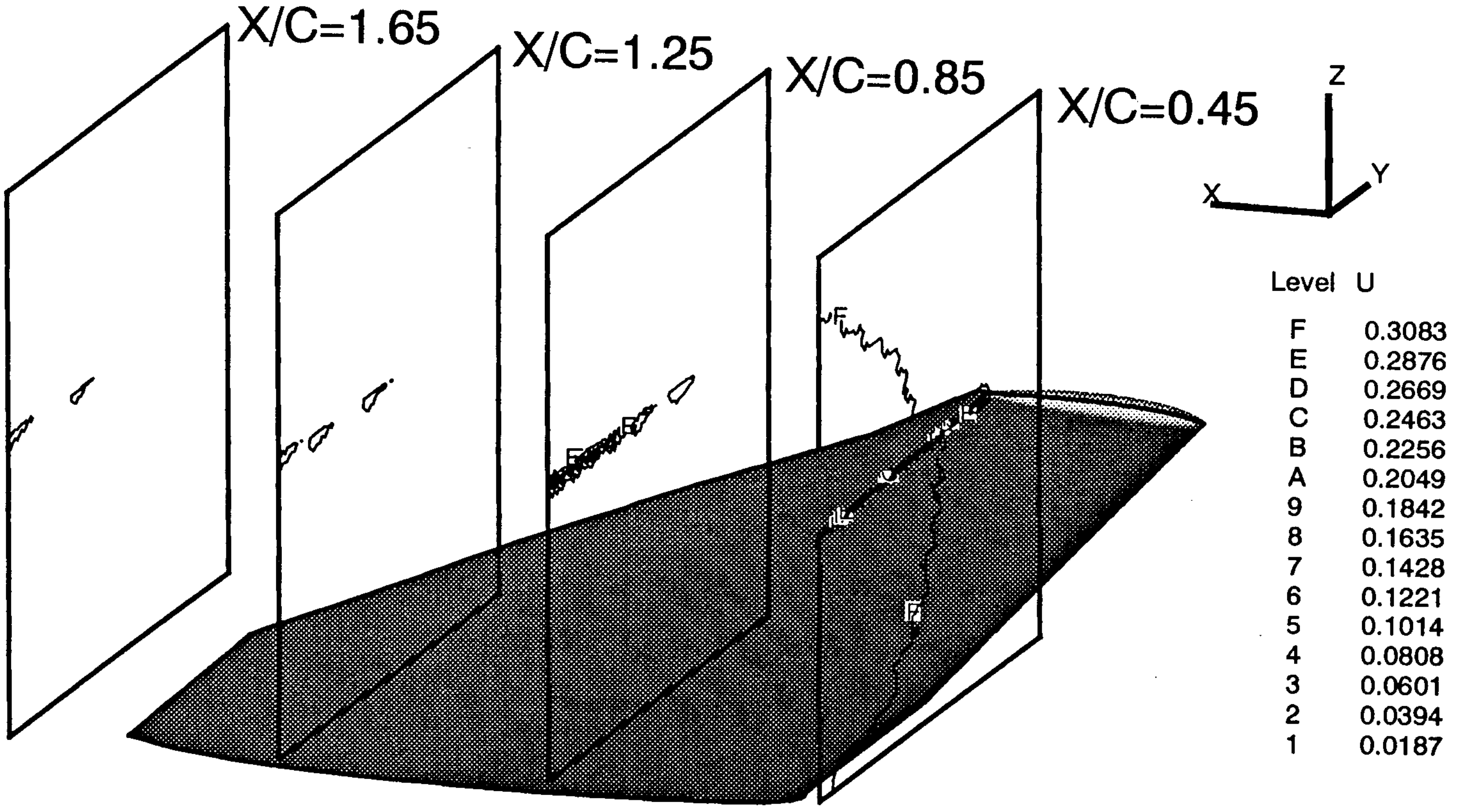

BART Taper-type Wing Tip, $\alpha=0^\circ$, $R_e=2\times10^6$, 161x97x97 Mesh
Tip Flow Field Investigation - Calculated Axial (U-) Velocity Contours

Figure 48. Calculated tip flow field in terms of axial velocity for taper-tip at $\alpha=0^\circ$ with a fine grid.

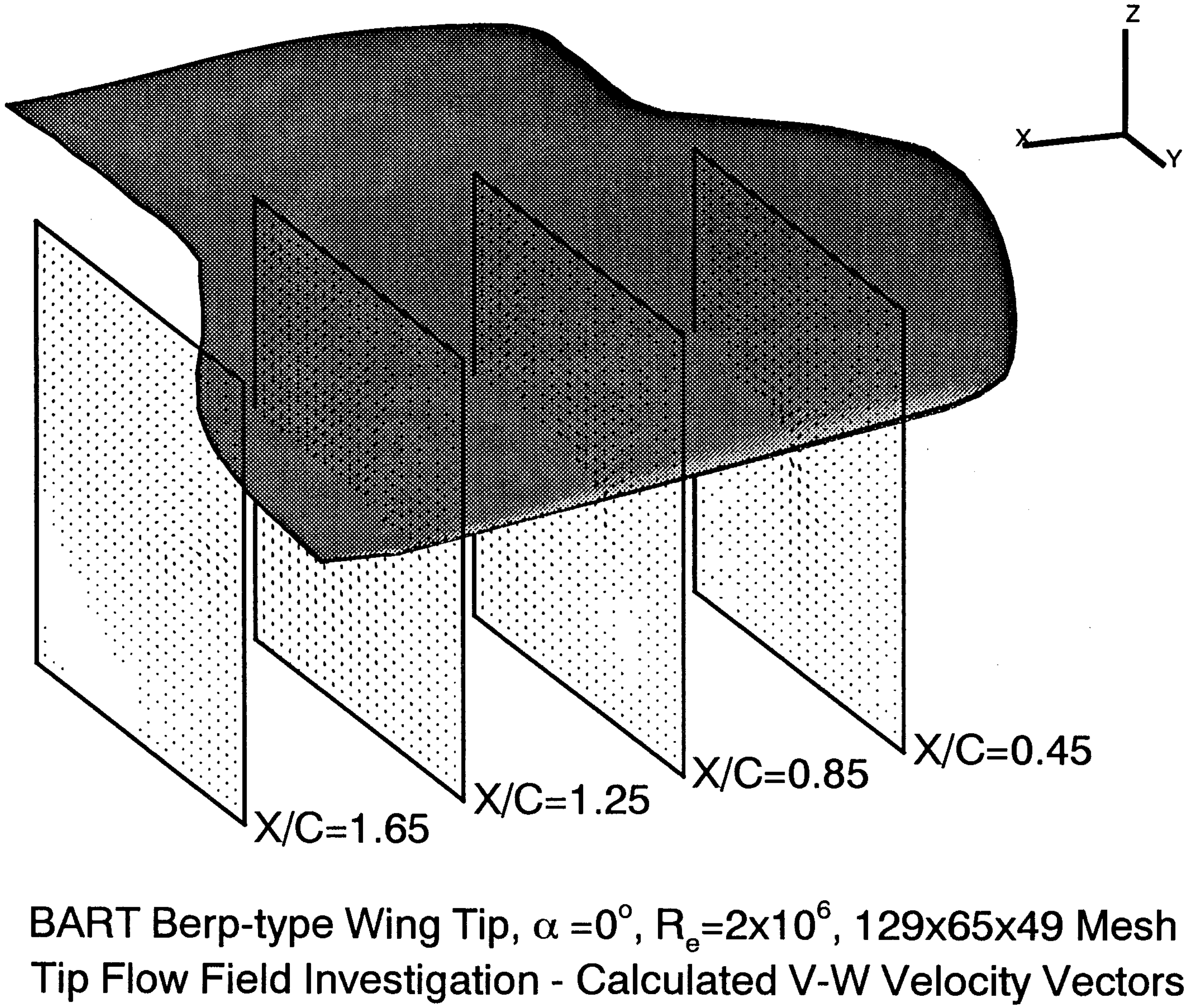

Figure 49. Calculated tip flow field in terms of crossflow velocity vector for Berp-tip at α=0°.

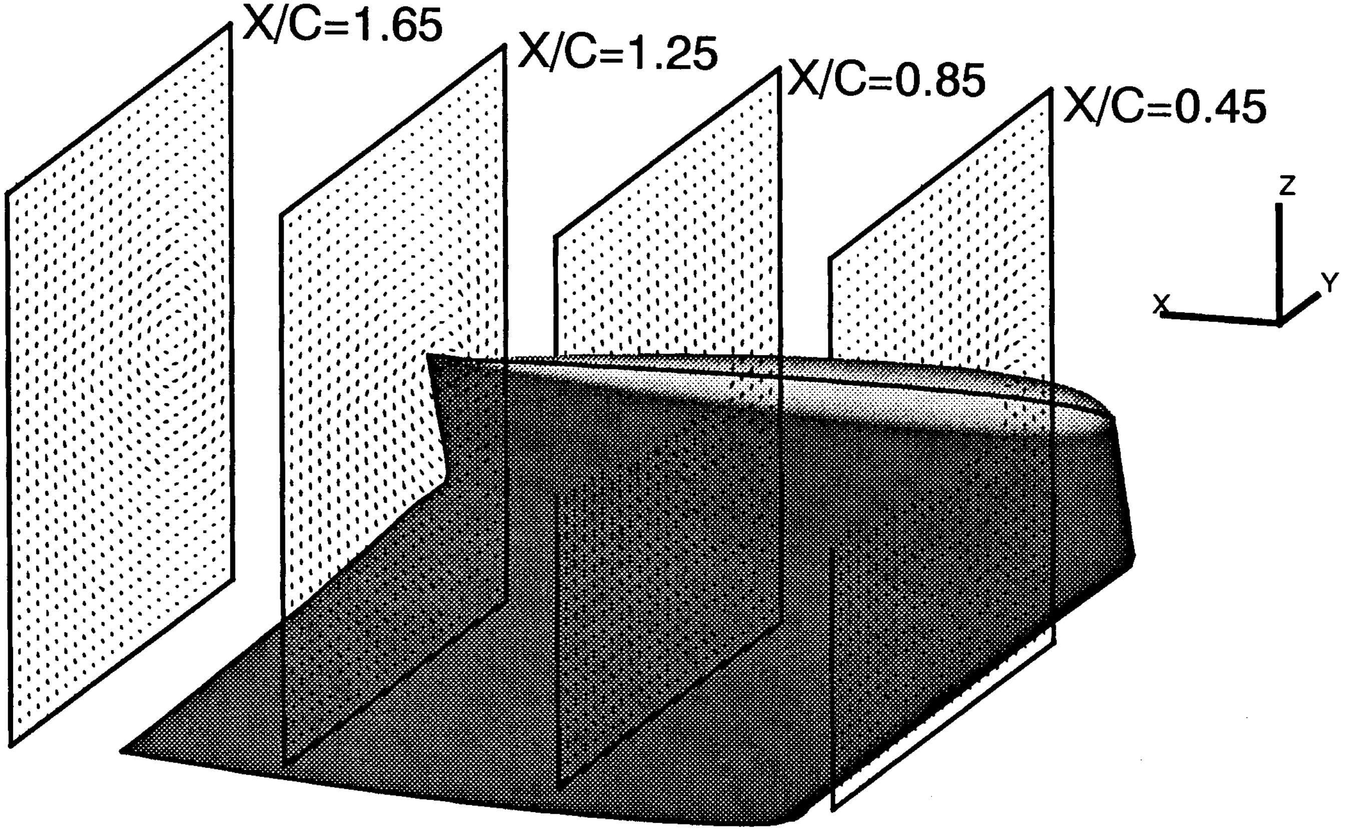

BART Swept-type Wing Tip, $\alpha = 0^\circ$, $R_e = 2\text{x}10^6$, 129x65x49 Mesh
Tip Flow Field Investigation - Calculated V-W Velocity Vectors

Figure 50. Calculated tip flow field in terms of crossflow velocity vector for swept-tip at α=0°.

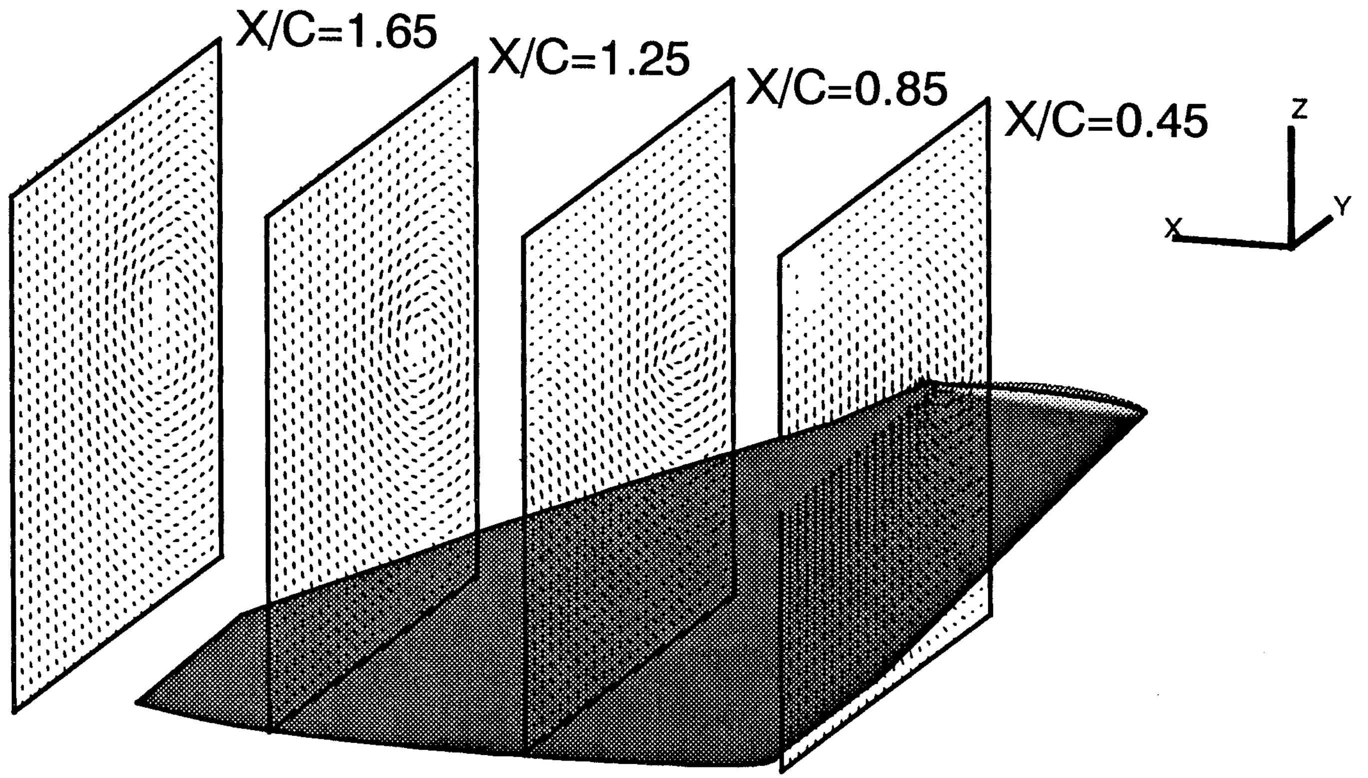

BART Taper-type Wing Tip, $\alpha = 0^\circ$, $R_e = 2\text{x}10^6$, 129x65x49 Mesh
Tip Flow Field Investigation - Calculated V-W Velocity Vectors

Figure 51. Calculated tip flow field in terms of crossflow velocity vector for taper-tip at α=0°.

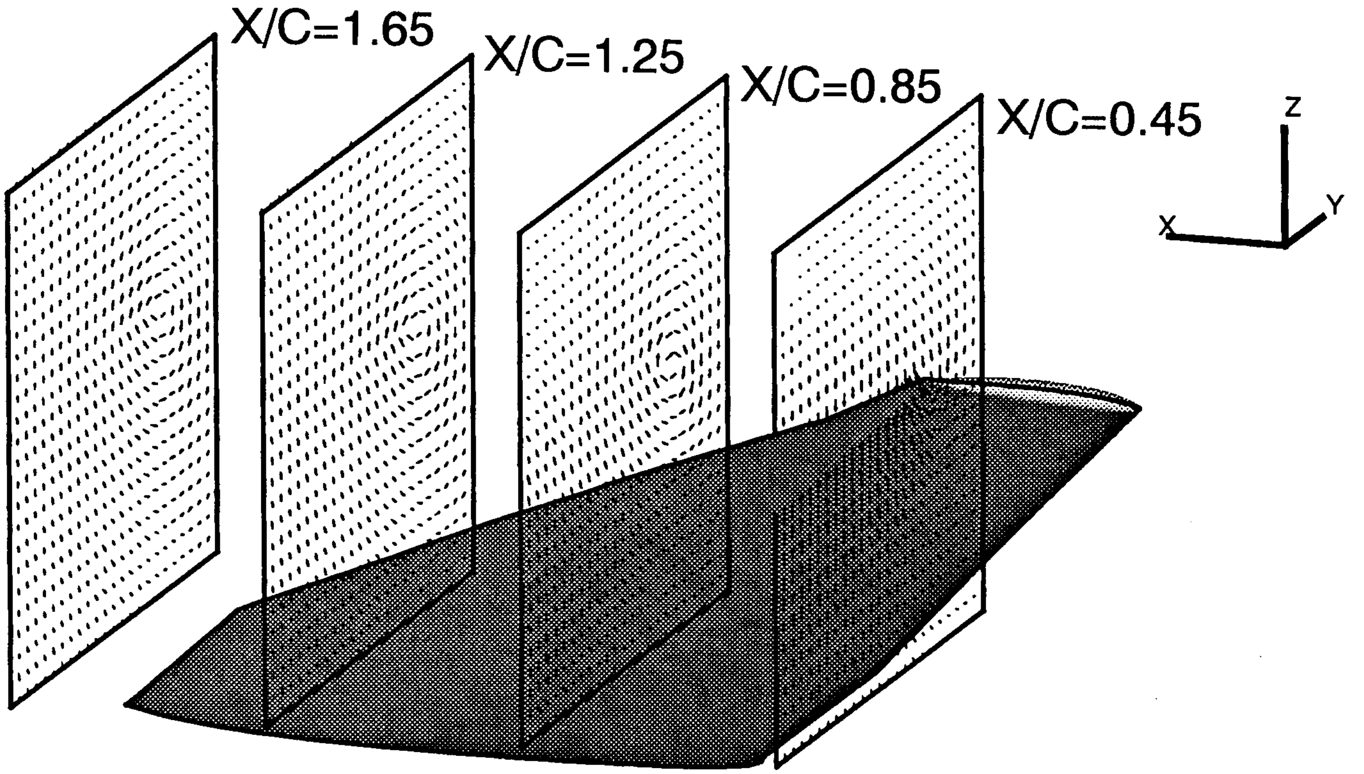

BART Taper-type Wing Tip, $\alpha = 0^\circ$, $R_e = 2\times10^6$, 161x97x97 Mesh
Tip Flow Field Investigation - Calculated V-W Velocity Vectors

Figure 52. Calculated tip flow field in terms of crossflow velocity vector for taper-tip at $\alpha = 0^\circ$ with a fine grid.

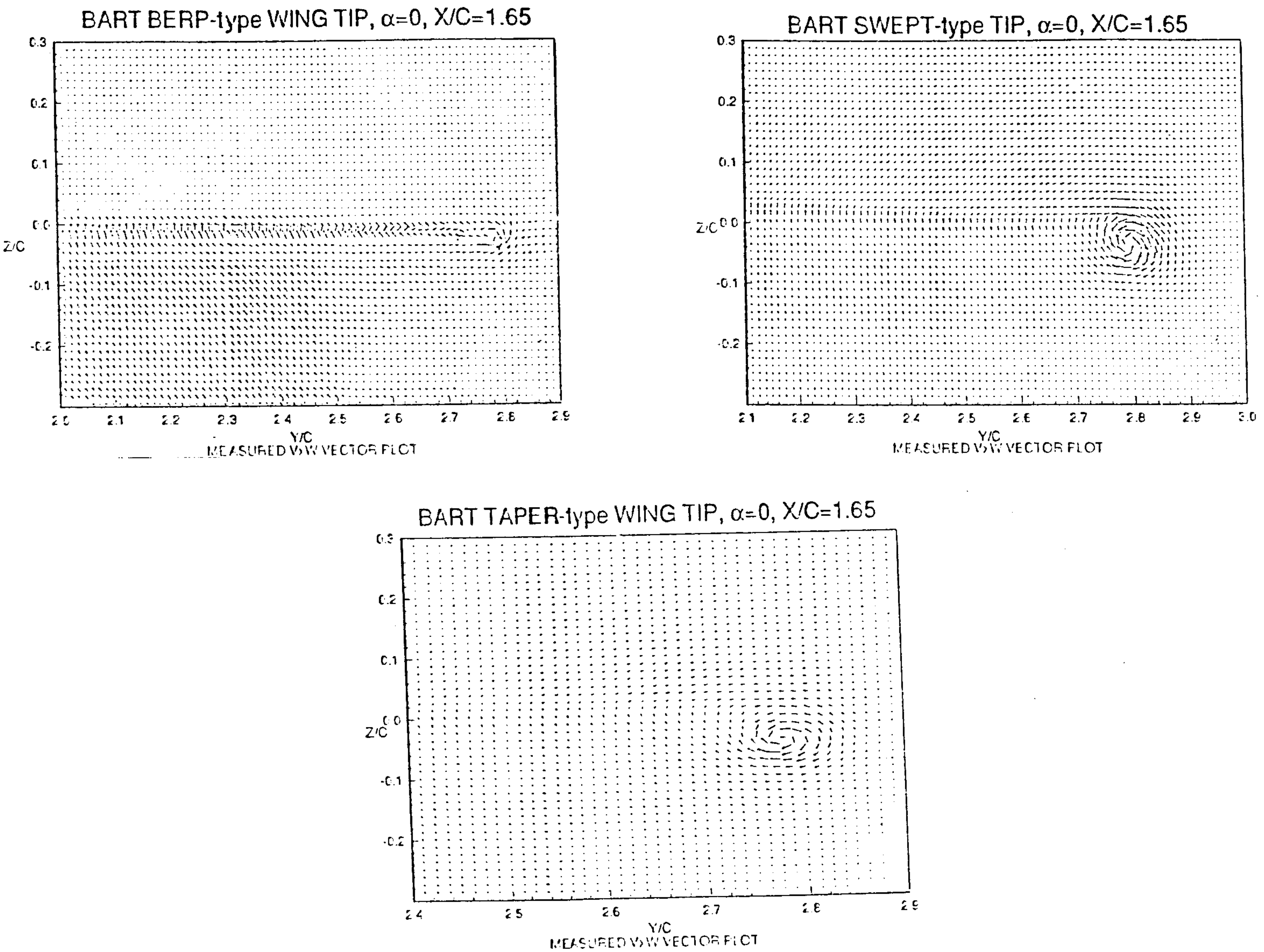

BART BERP-type WING TIP, α=0, X/C=1.65

BART SWEPT-type TIP, α=0, X/C=1.65

BART TAPER-type WING TIP, α=0, X/C=1.65

Figure 53. Measured tip flow field in terms of crossflow velocity vector for three tips at α=0° and x/c=1.65.

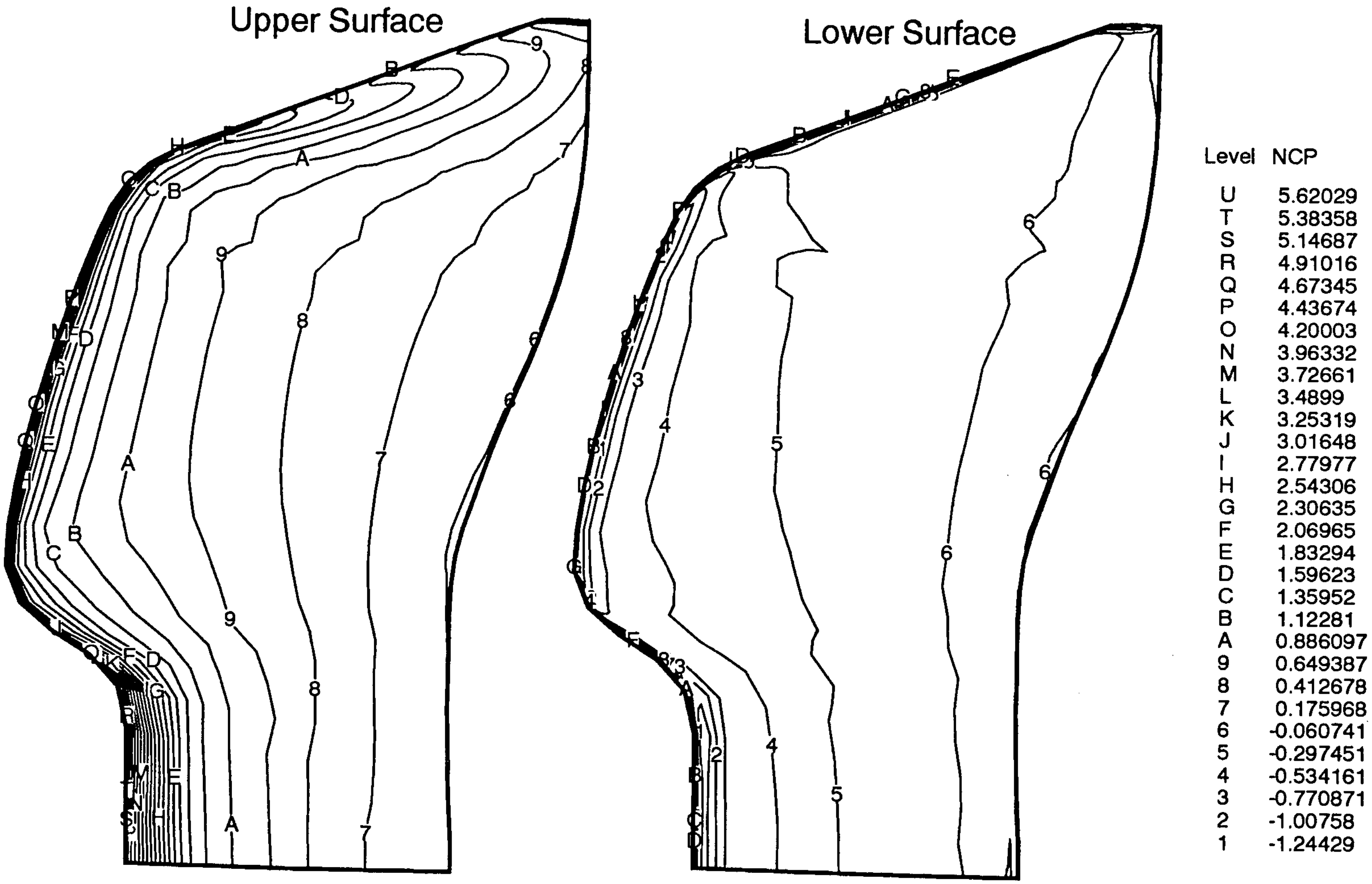

BART Berp-type Wing Tip, $\alpha=15^{\circ}$, $R_e=2x10^6$, 129x65x49 Mesh

Calculated Surface Pressure Coefficient Contours

Figure 54. Calculated surface pressure coefficients for Berp-tip at $\alpha=15^{\circ}$.

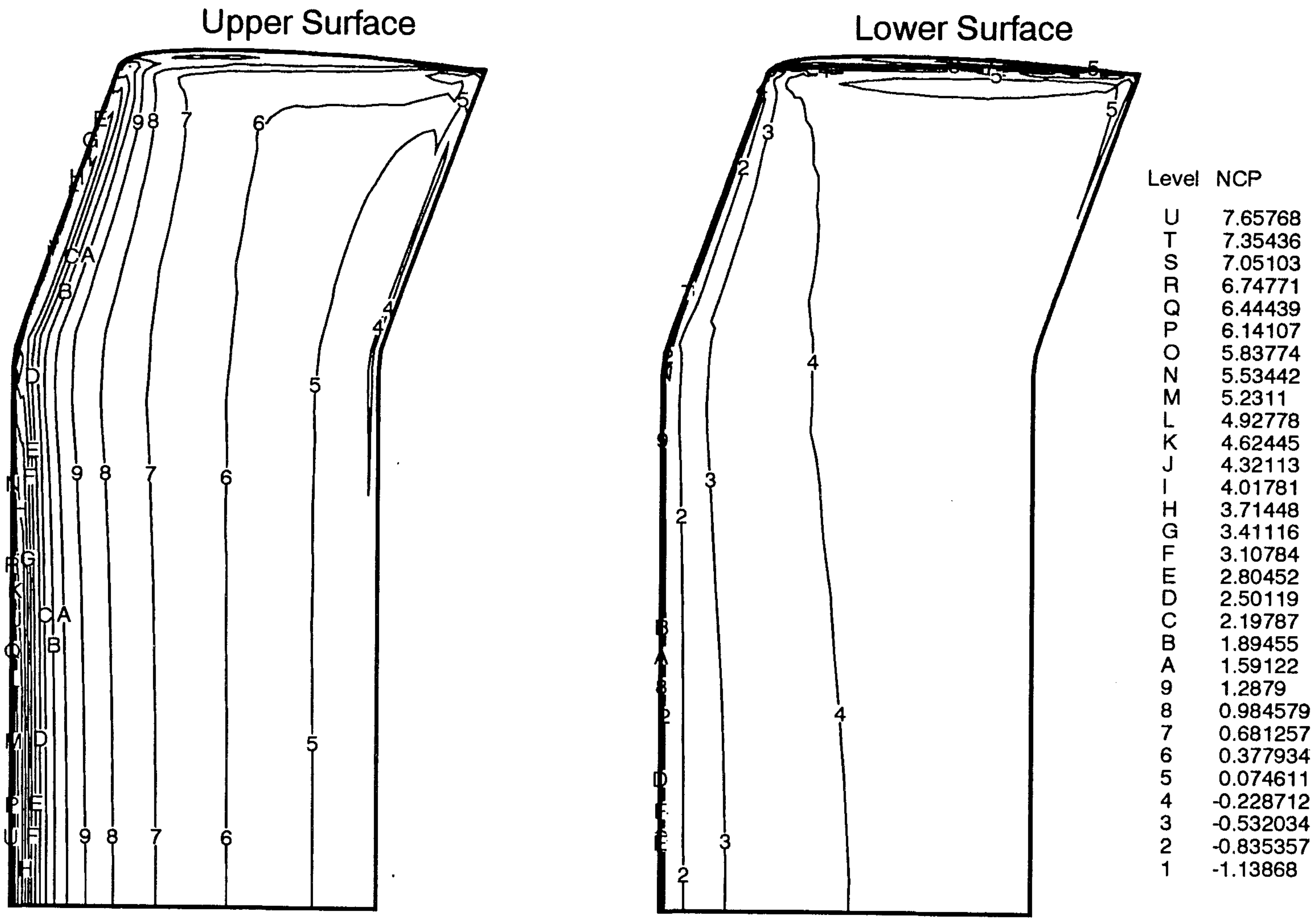

Level	NCP
U	7.65768
T	7.35436
S	7.05103
R	6.74771
Q	6.44439
P	6.14107
O	5.83774
N	5.53442
M	5.2311
L	4.92778
K	4.62445
J	4.32113
I	4.01781
H	3.71448
G	3.41116
F	3.10784
E	2.80452
D	2.50119
C	2.19787
B	1.89455
A	1.59122
9	1.2879
8	0.984579
7	0.681257
6	0.377934
5	0.074611
4	-0.228712
3	-0.532034
2	-0.835357
1	-1.13868

BART Swept-type Wing Tip, $\alpha=15^{\circ}$, $R_e=2\text{x}10^6$, 129x65x49 Mesh

Calculated Surface Pressure Coefficient Contours

Figure 55. Calculated surface pressure coefficients for swept-tip at α=15°.

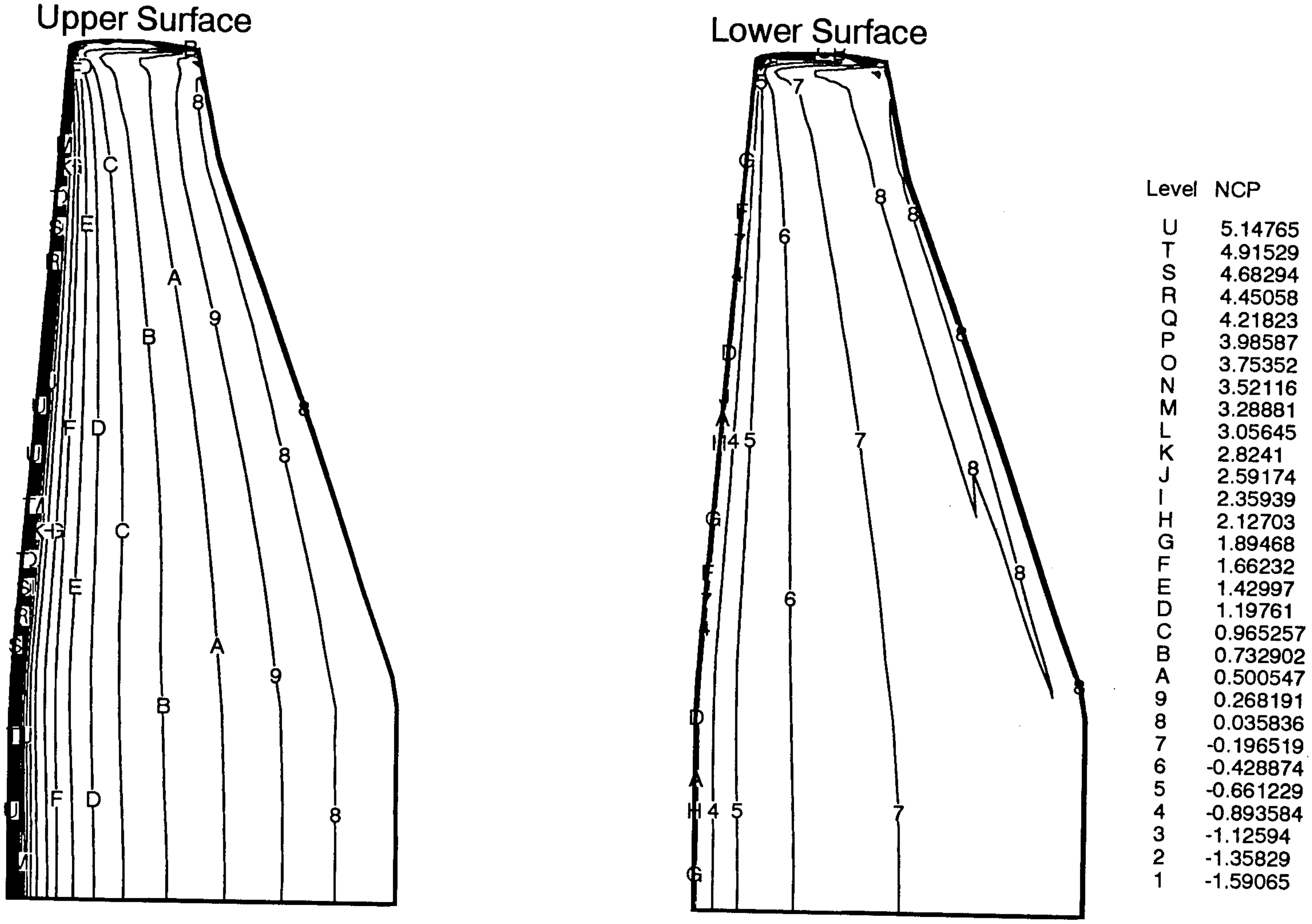

BART Taper-type Wing Tip, $\alpha=15^{\circ}$, $R_e=2x10^6$, 129x65x49 Mesh

Calculated Surface Pressure Coefficient Contours

Figure 56. Calculated surface pressure coefficients for taper-tip at $\alpha=15^{\circ}$.

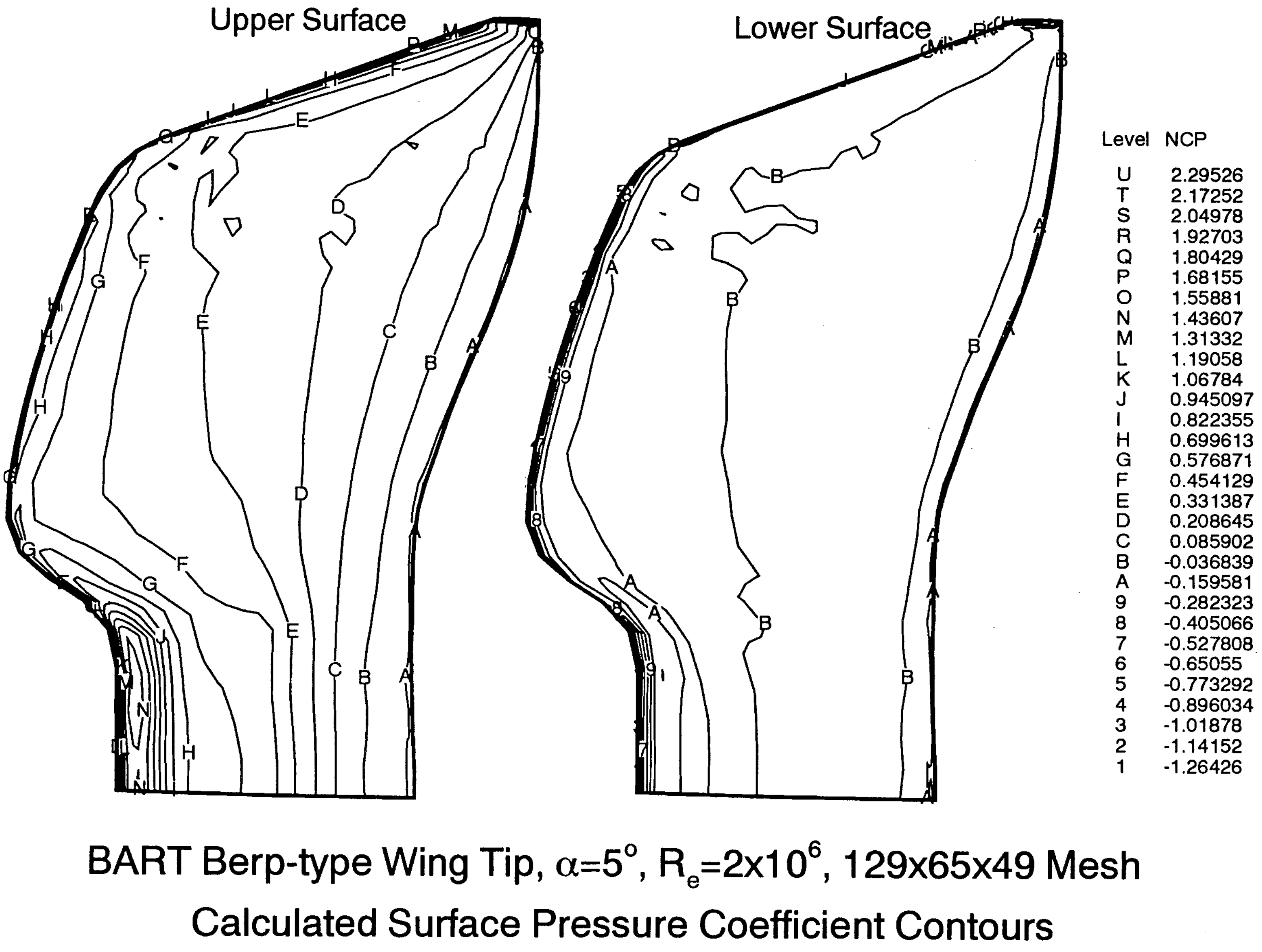

Figure 57. Calculated surface pressure coefficients for Berp-tip at α=5°.

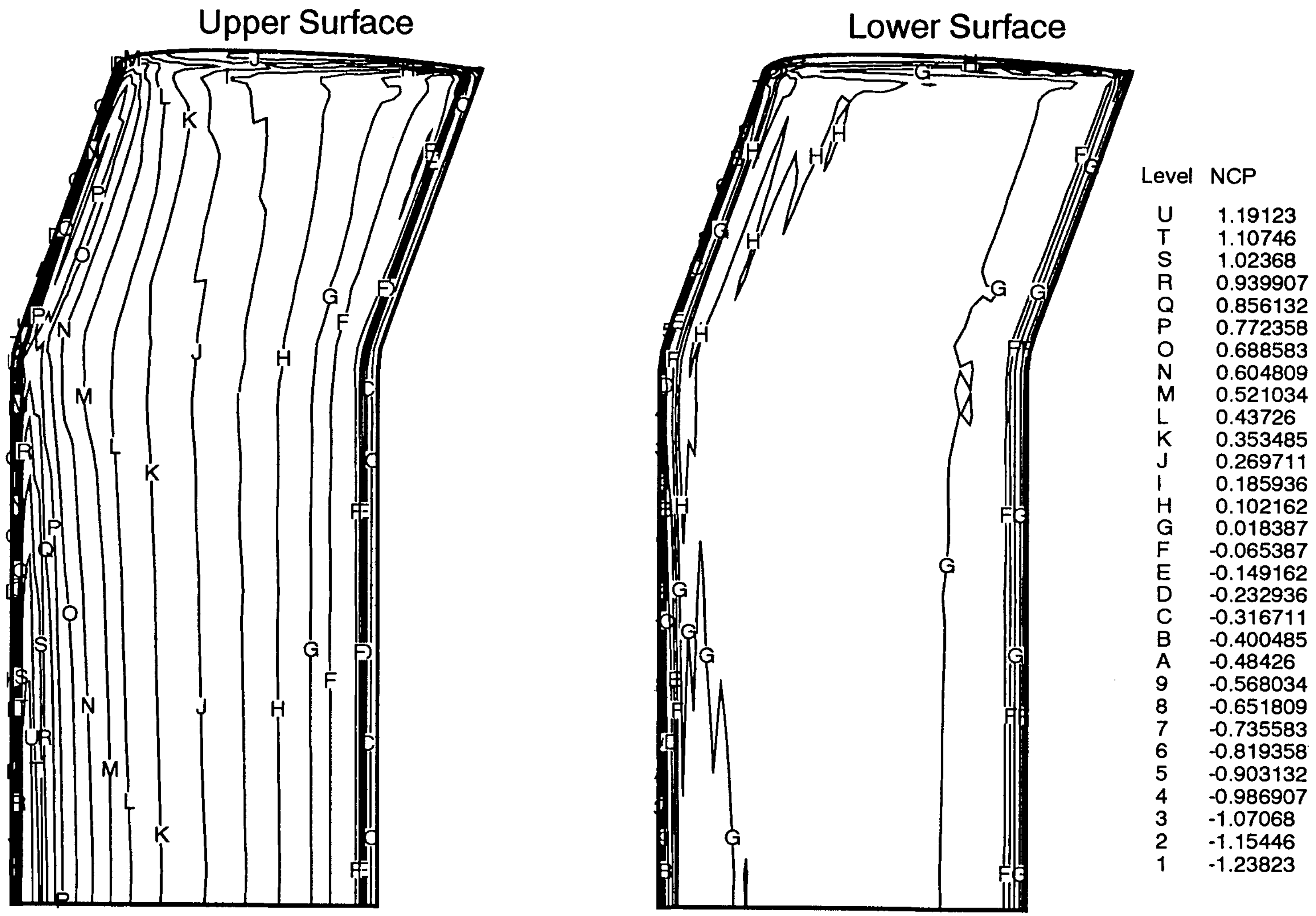

BART Swept-type Wing Tip, $\alpha=5^\circ$, $R_e=2\times10^6$, 129x65x49 Mesh

Calculated Surface Pressure Coefficient Contours

Figure 58. Calculated surface pressure coefficients for swept-tip at $\alpha=5^\circ$.

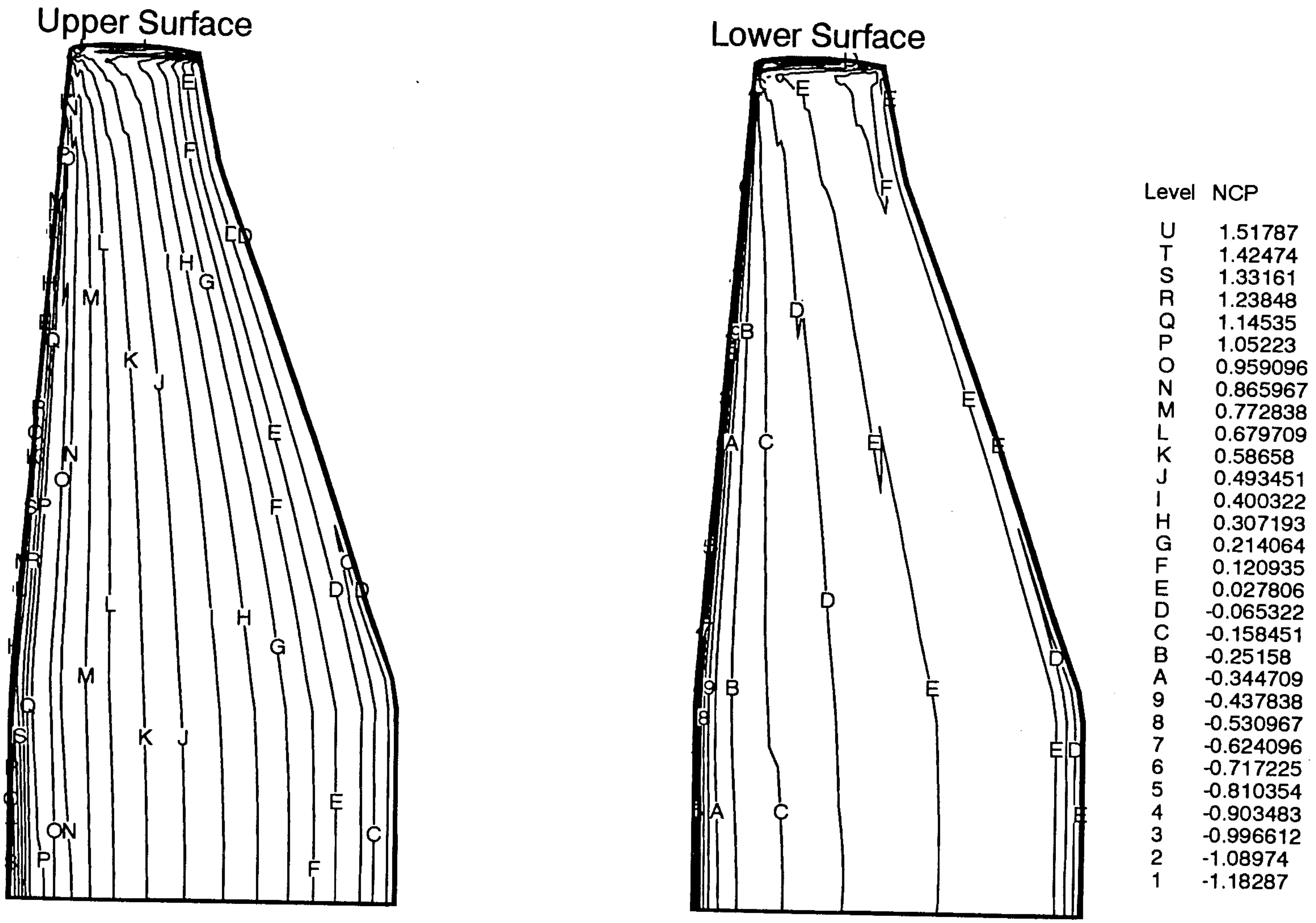

BART Taper-type Wing Tip, $\alpha=7.5^\circ$, $R_e=2\times10^6$, 129x65x49 Mesh
Calculated Surface Pressure Coefficient Contours

Figure 59. Calculated surface pressure coefficients for taper-tip at $\alpha=7.5^\circ$.

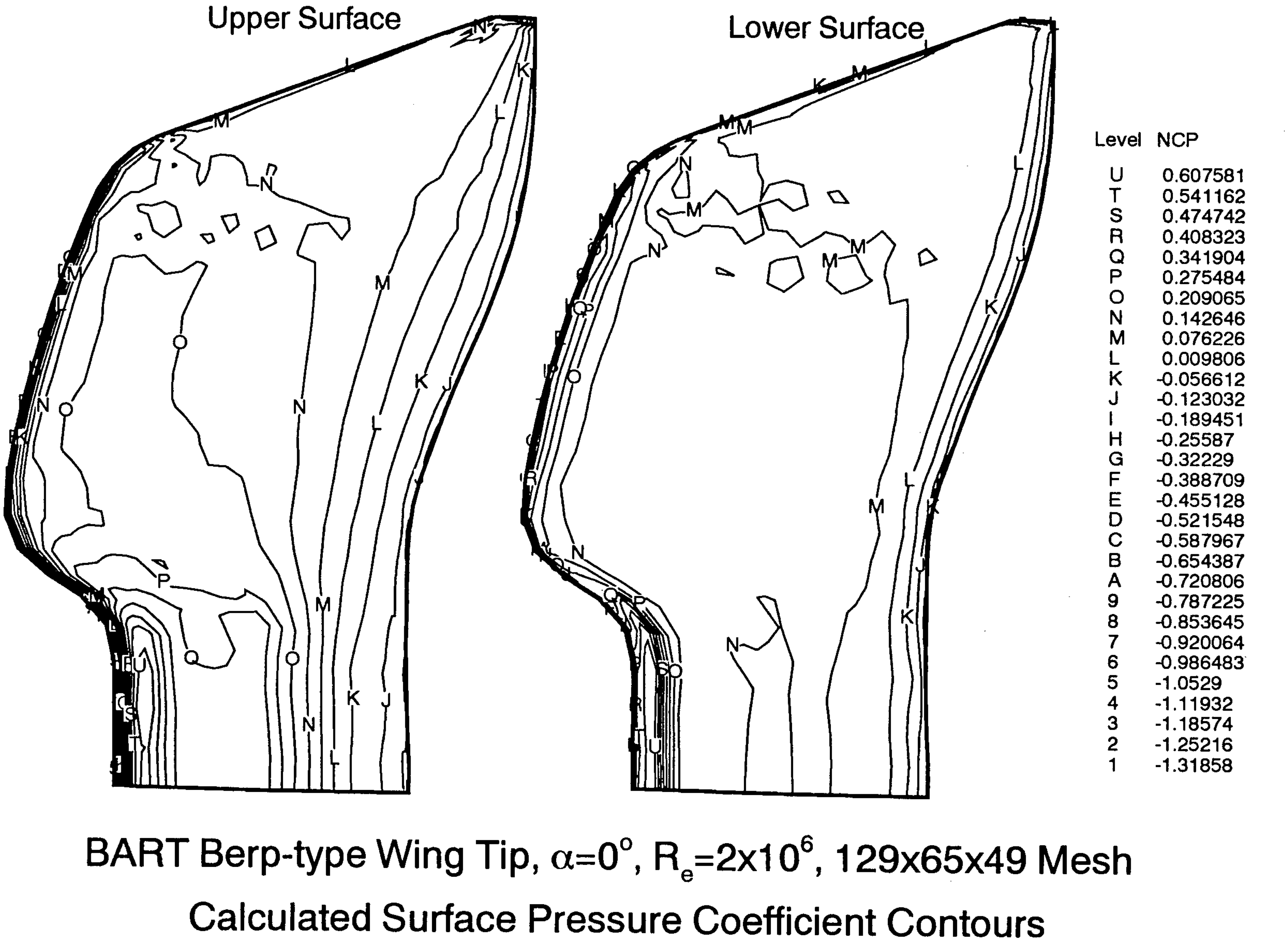

Figure 60. Calculated surface pressure coefficients for Berp-tip at $\alpha=0^\circ$.

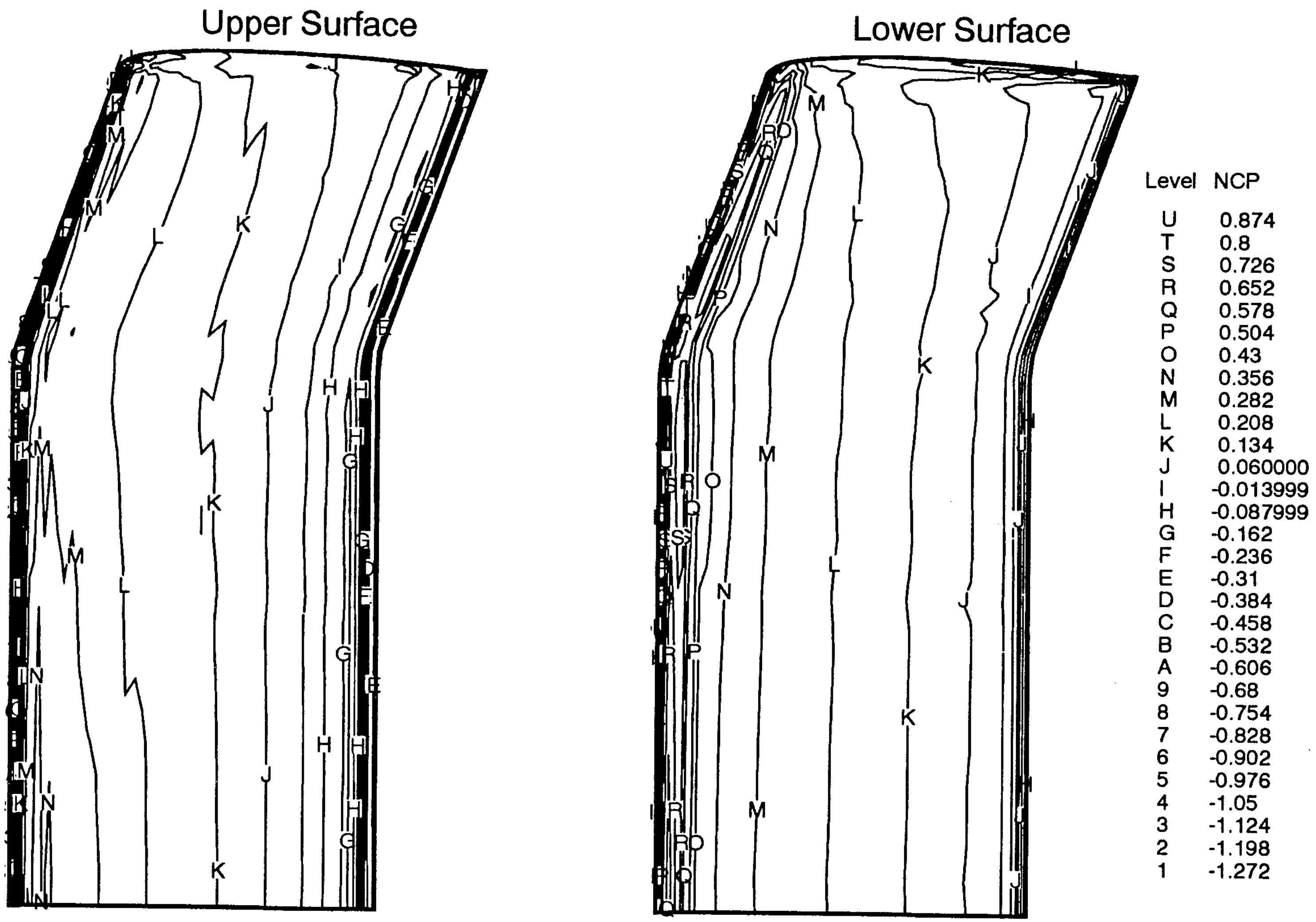

BART Swept-type Wing Tip, $\alpha=0^\circ$, $R_e=2\times10^6$, 129x65x49 Mesh
Calculated Surface Pressure Coefficient Contours

Figure 61. Calculated surface pressure coefficients for swept-tip at $\alpha=0^\circ$.

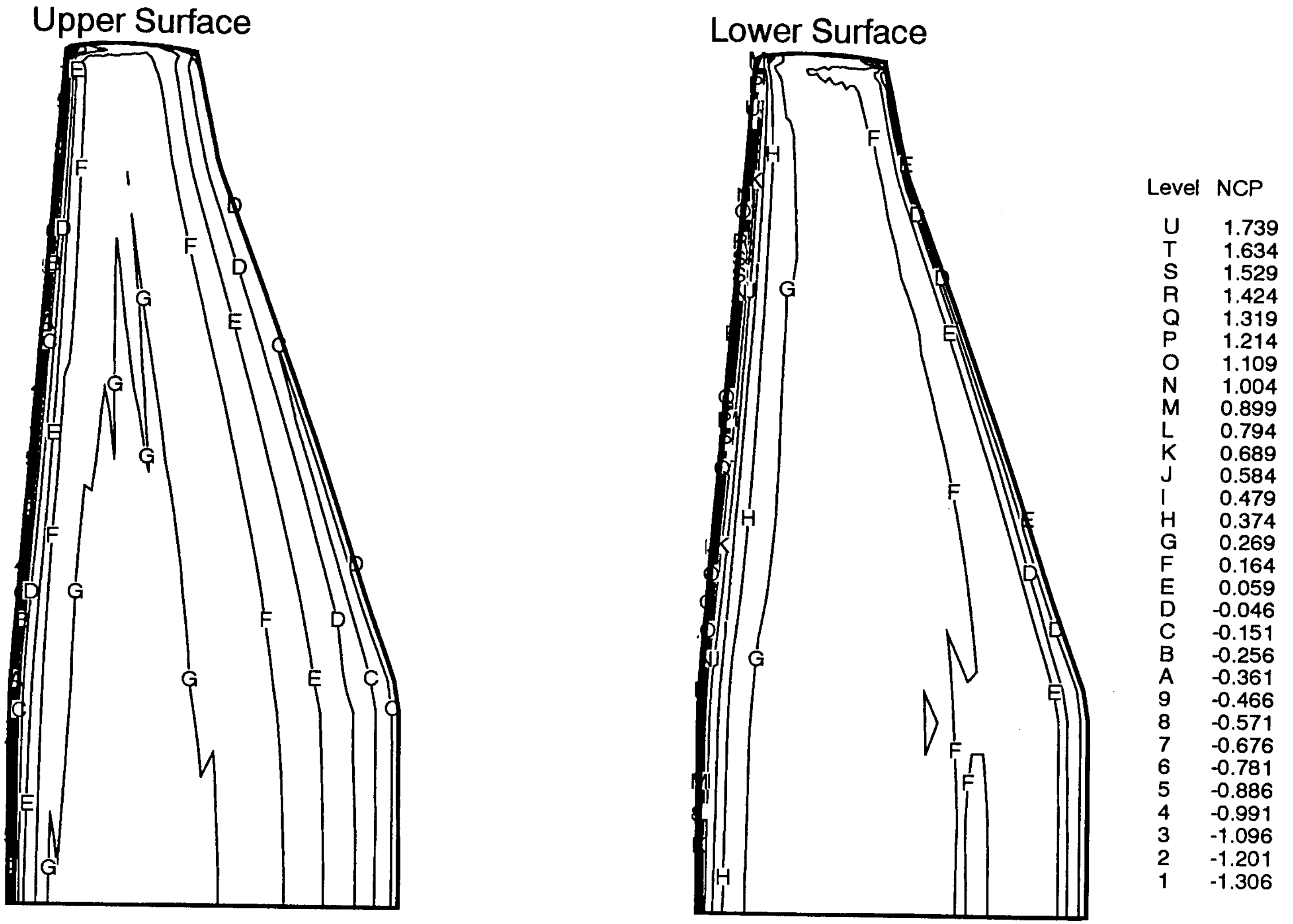

BART Taper-type Wing Tip, $\alpha=0^{\circ}$, $R_e=2x10^6$, 129x65x49 Mesh
Calculated Surface Pressure Coefficient Contours

Figure 62. Calculated surface pressure coefficients for taper-tip at $\alpha=0^{\circ}$.

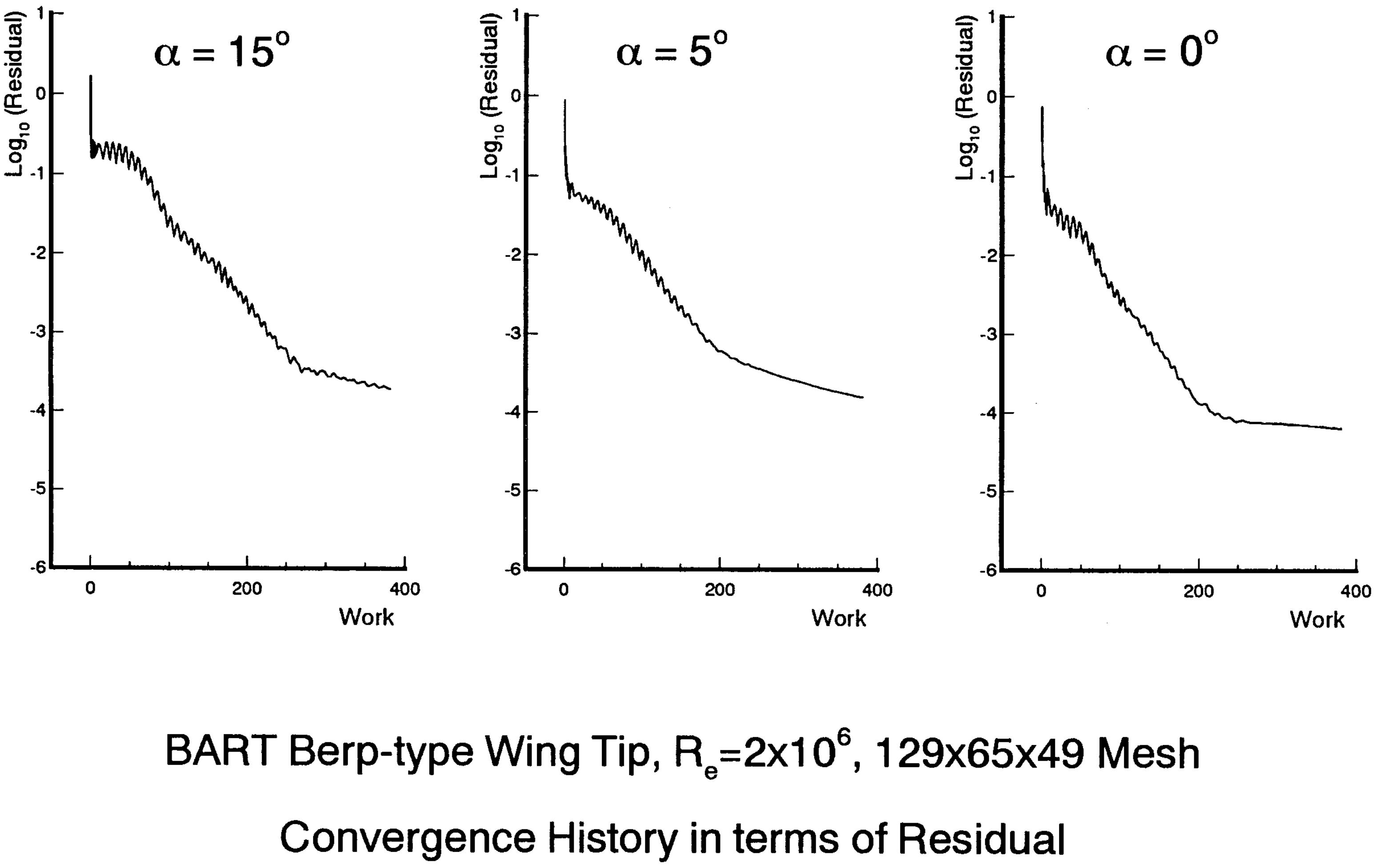

Figure 63. Convergence history in terms of residuals for Berp-tip at $\alpha=15^\circ$, $\alpha=5^\circ$ and $\alpha=0^\circ$.

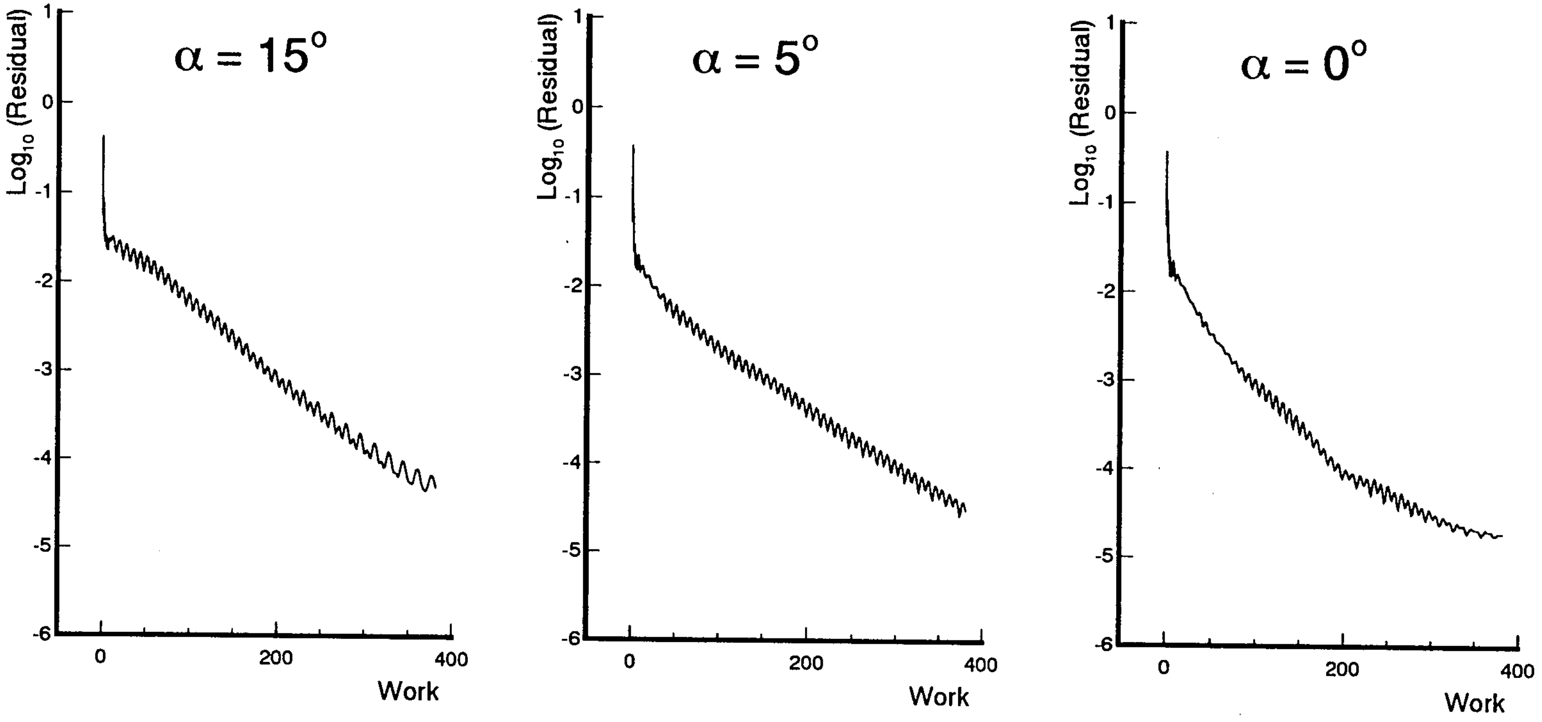

BART Swept-type Wing Tip, $R_e=2x10^6$, 129x65x49 Mesh

Convergence History in terms of Residual

Figure 64. Convergence history in terms of residuals for swept-tip at $\alpha=15°$, $\alpha=5°$ and $\alpha=0°$.

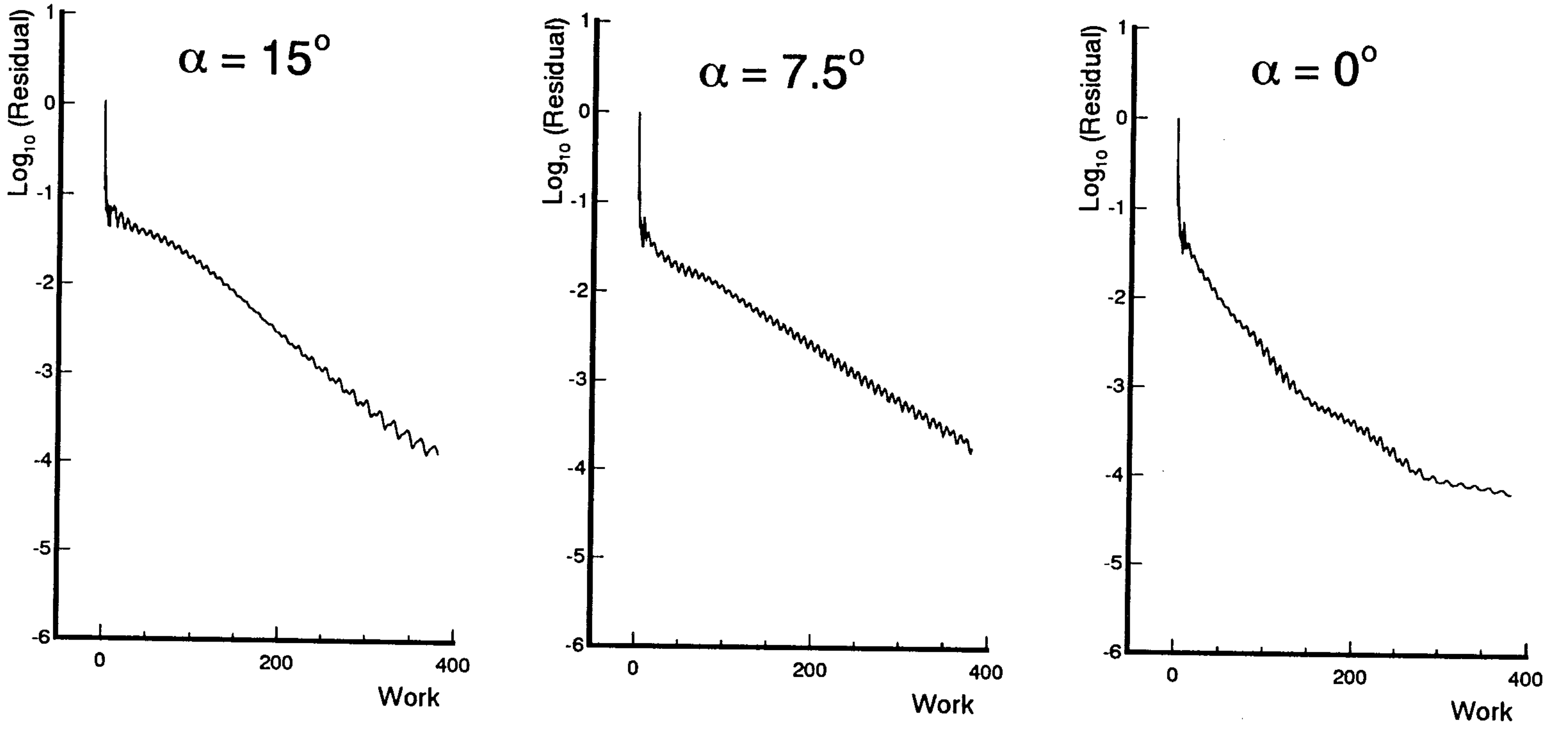

BART Taper-type Wing Tip, $R_e=2x10^6$, 129x65x49 Mesh

Convergence History in terms of Residual

Figure 65. Convergence history in terms of residuals for taper-tip at $\alpha=15^\circ$, $\alpha=7.5^\circ$ and $\alpha=0^\circ$.

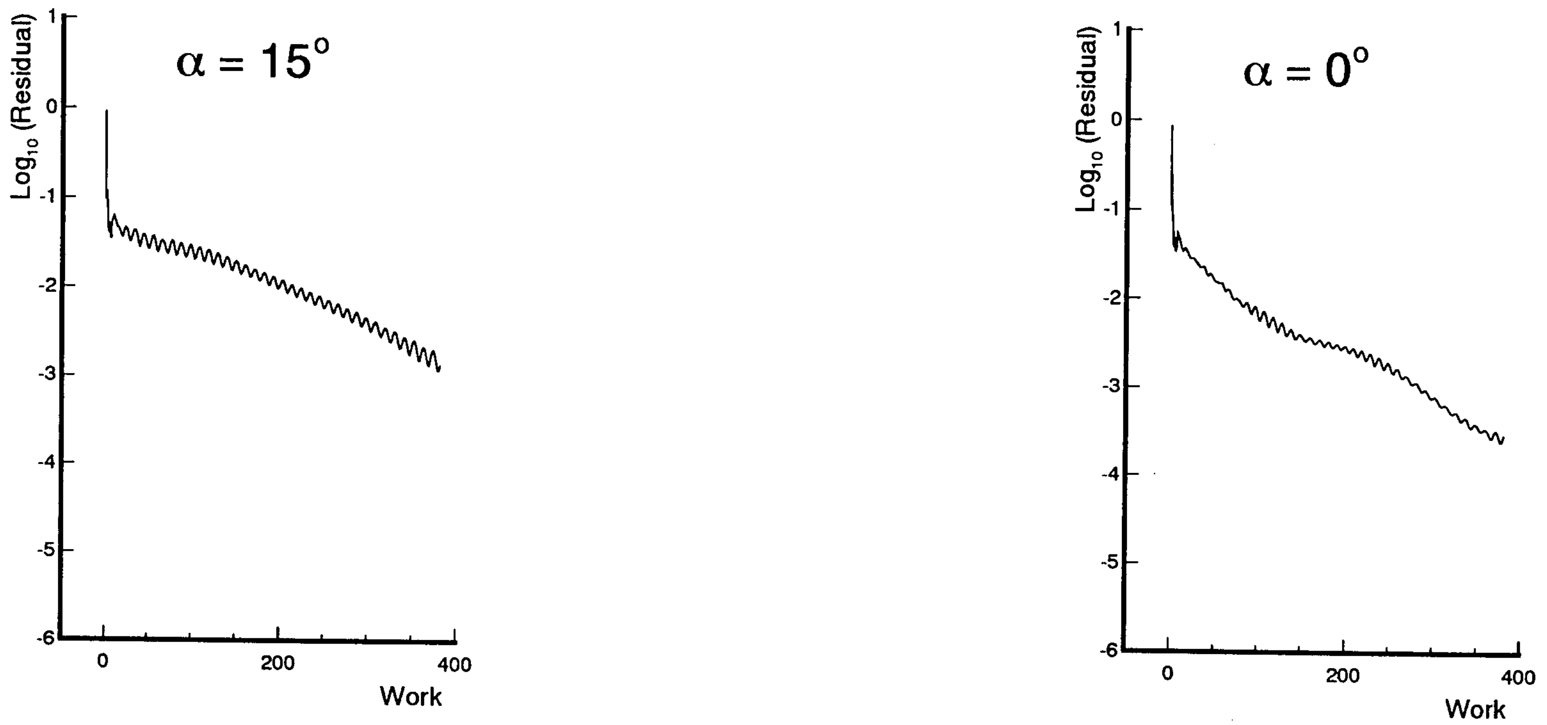

BART Taper-type Wing Tip, R_e=2x10^6, 161x97x97 Mesh

Convergence History in terms of Residual

Figure 66. Convergence history in terms of residuals for taper-tip at α=15° and α=0° with a fine grid.

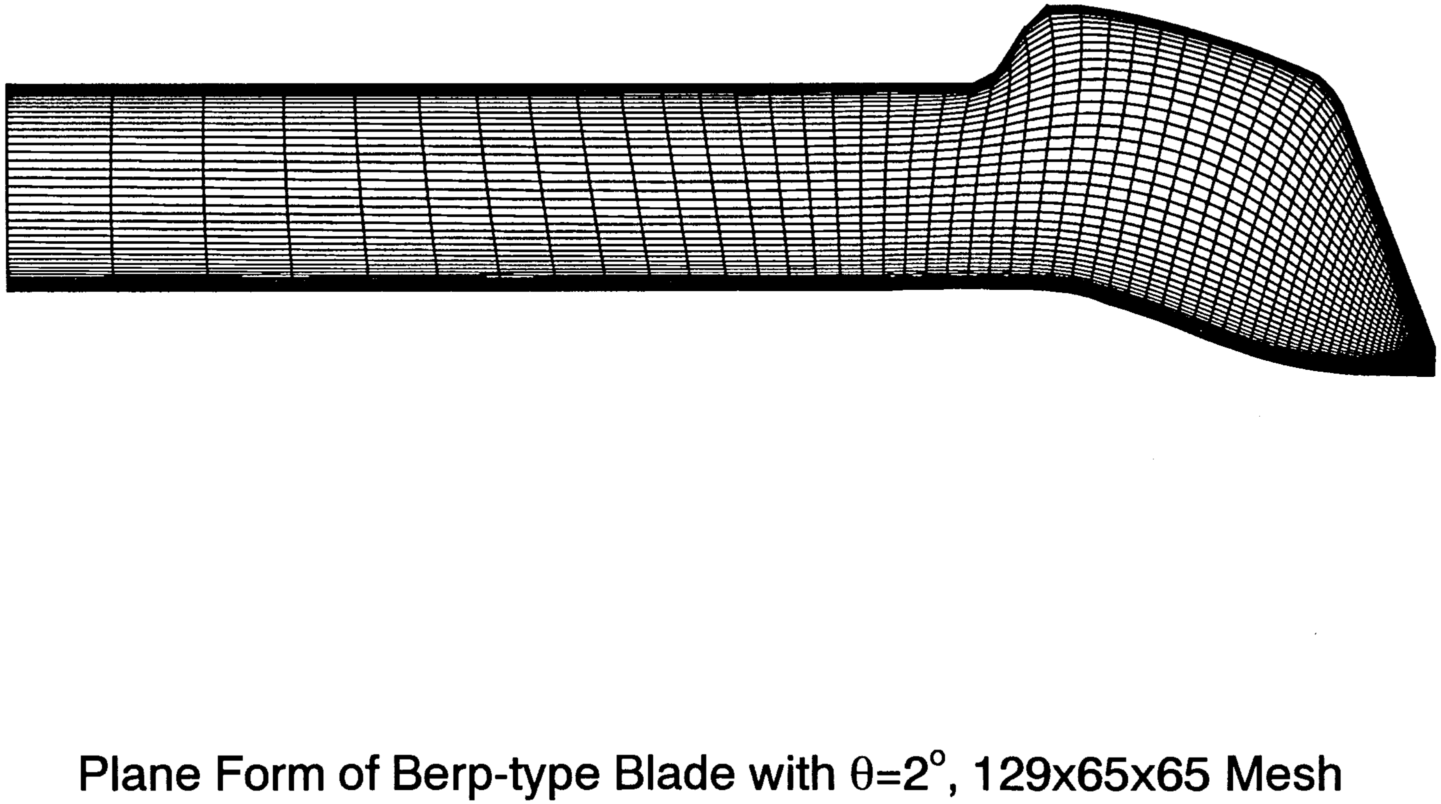

Figure 67. Plane form of Berp-blade.

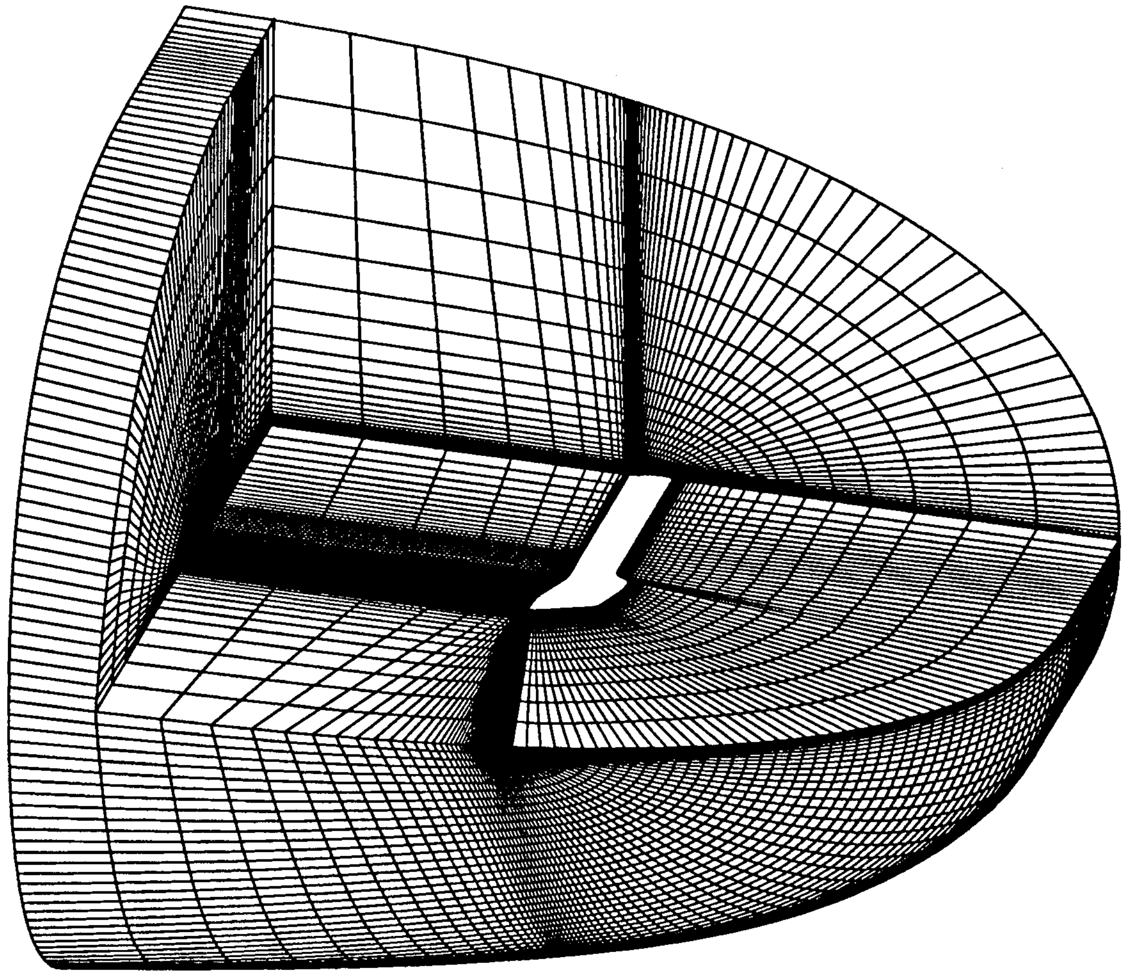

Partial View of C-O Mesh for Berp-type Blade with θ=2°, 129x65x65 Mesh

Figure 68. Partial view of C-O mesh for Berp-blade.

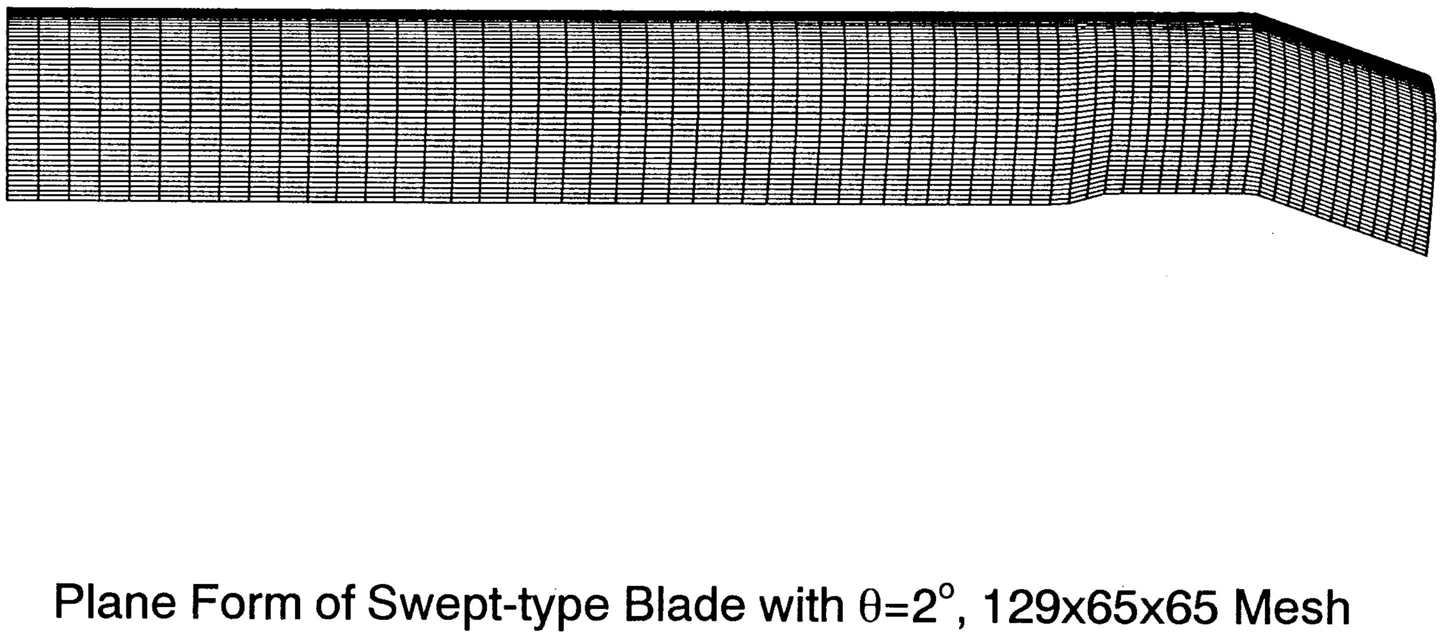

Figure 69. Plane form of swept-blade.

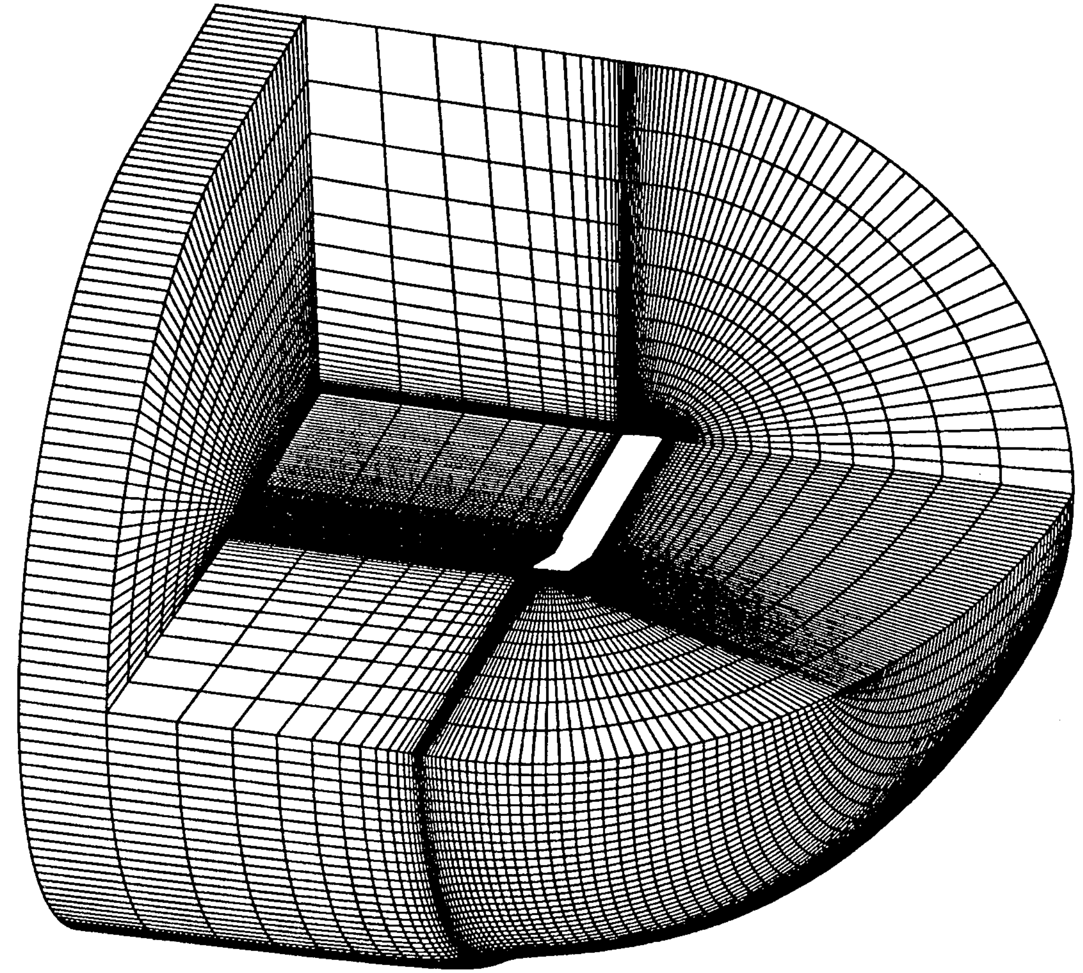

Partial View of C-O Mesh for Swept-type Blade with $\theta=2^\circ$, 129x65x65 Mesh

Figure 70. Partial view of C-O mesh for swept-blade.

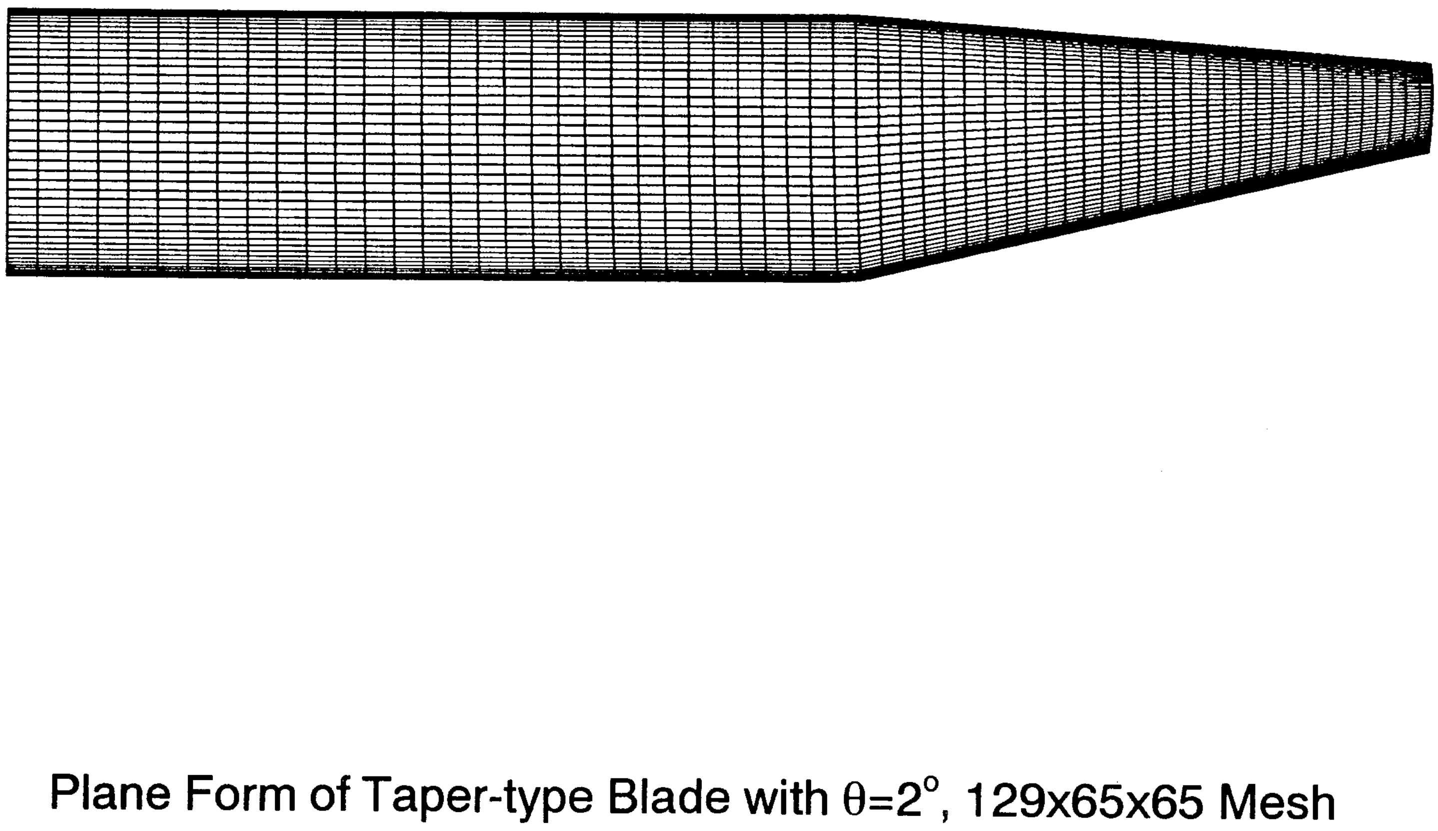

Figure 71. Plane form of taper-blade.

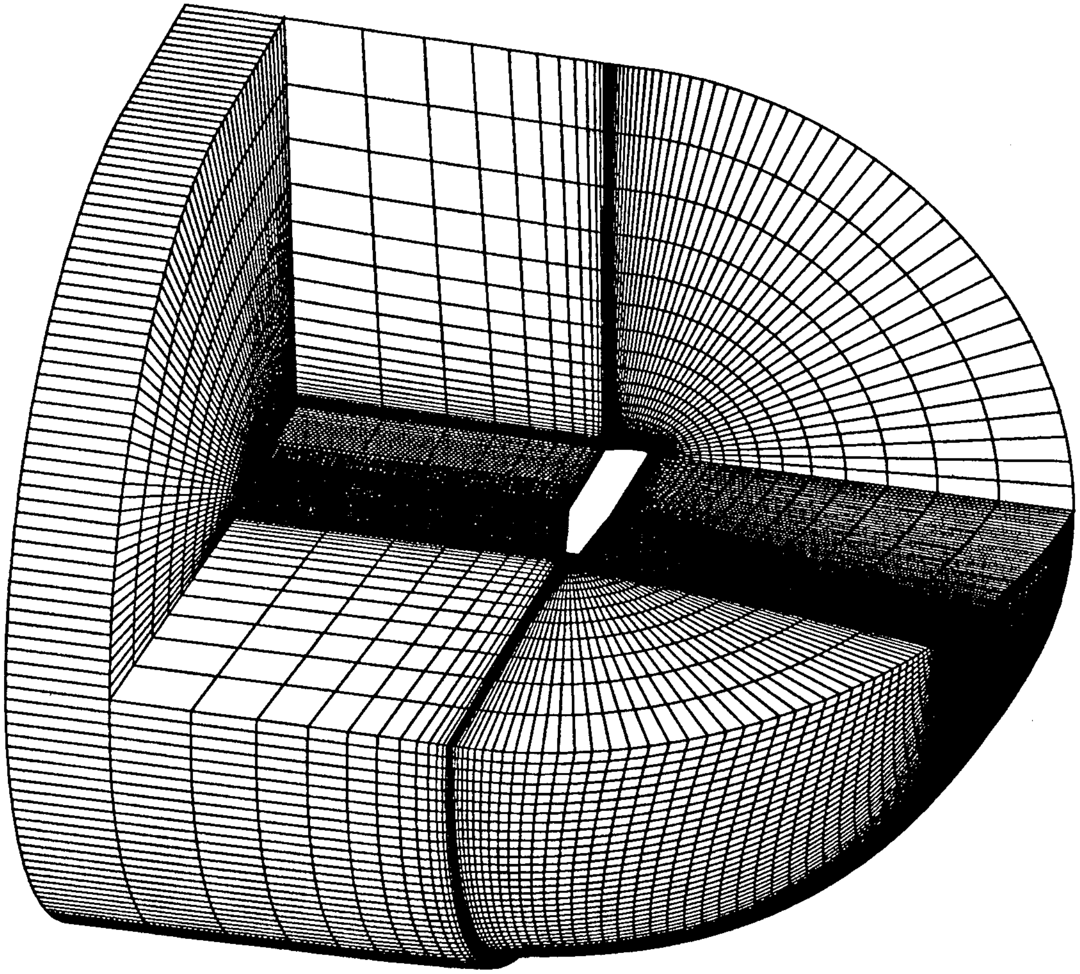

Figure 72. Partial view of C-O mesh for taper-blade.

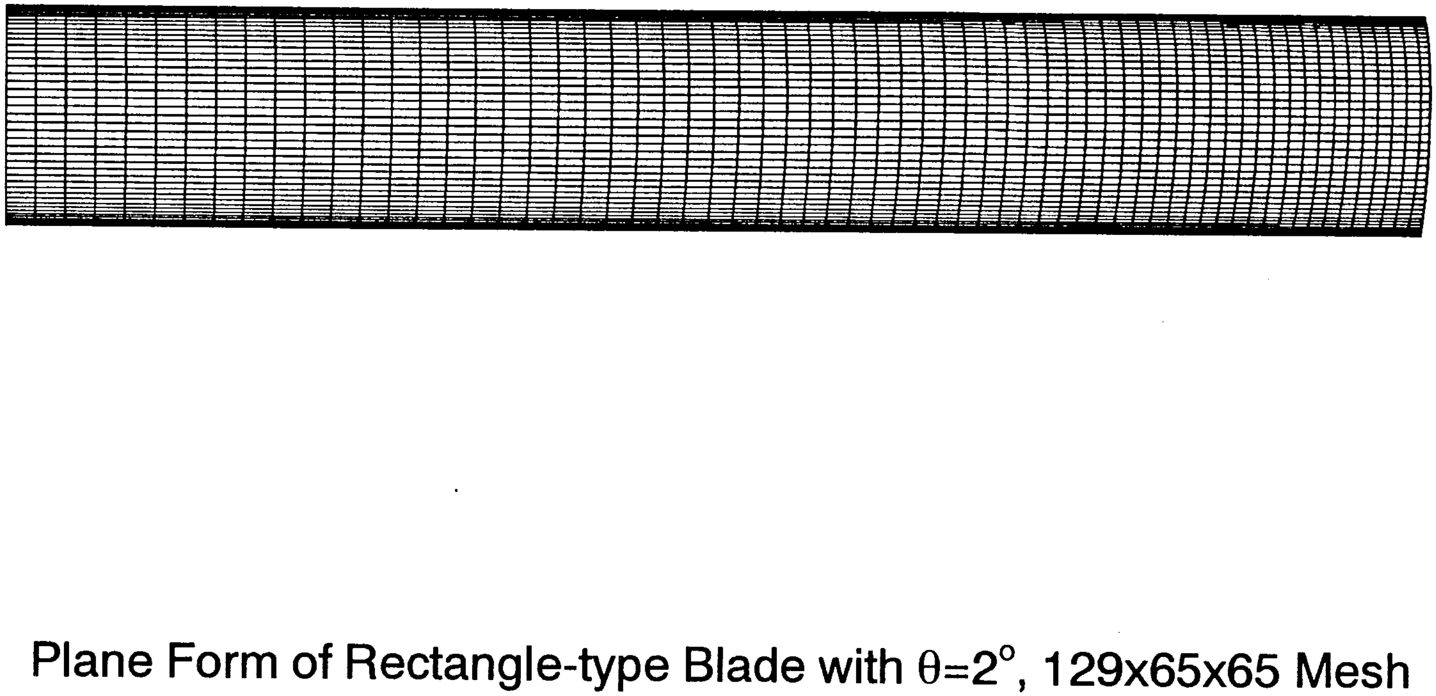

Figure 73. Plane form of rectangle-blade.

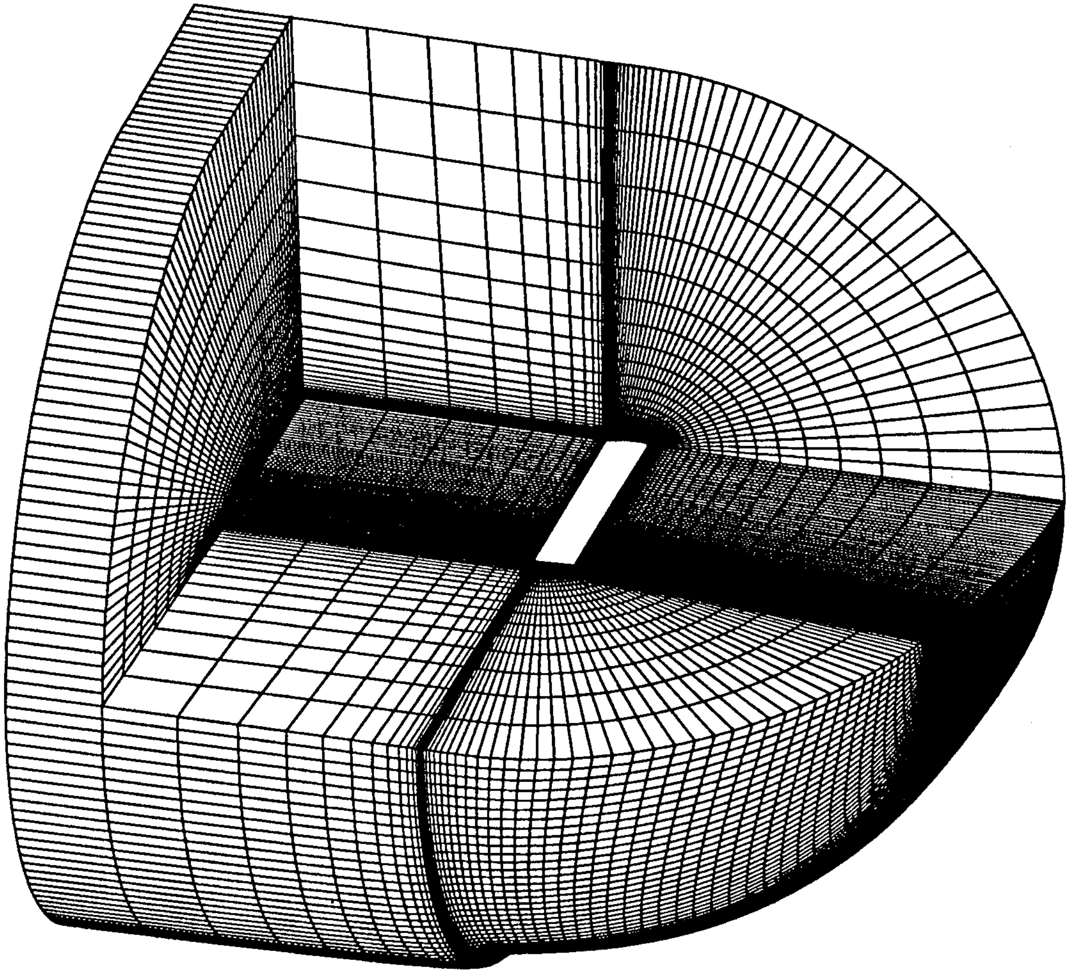

Figure 74. Partial view of C-O mesh for rectangle-blade.

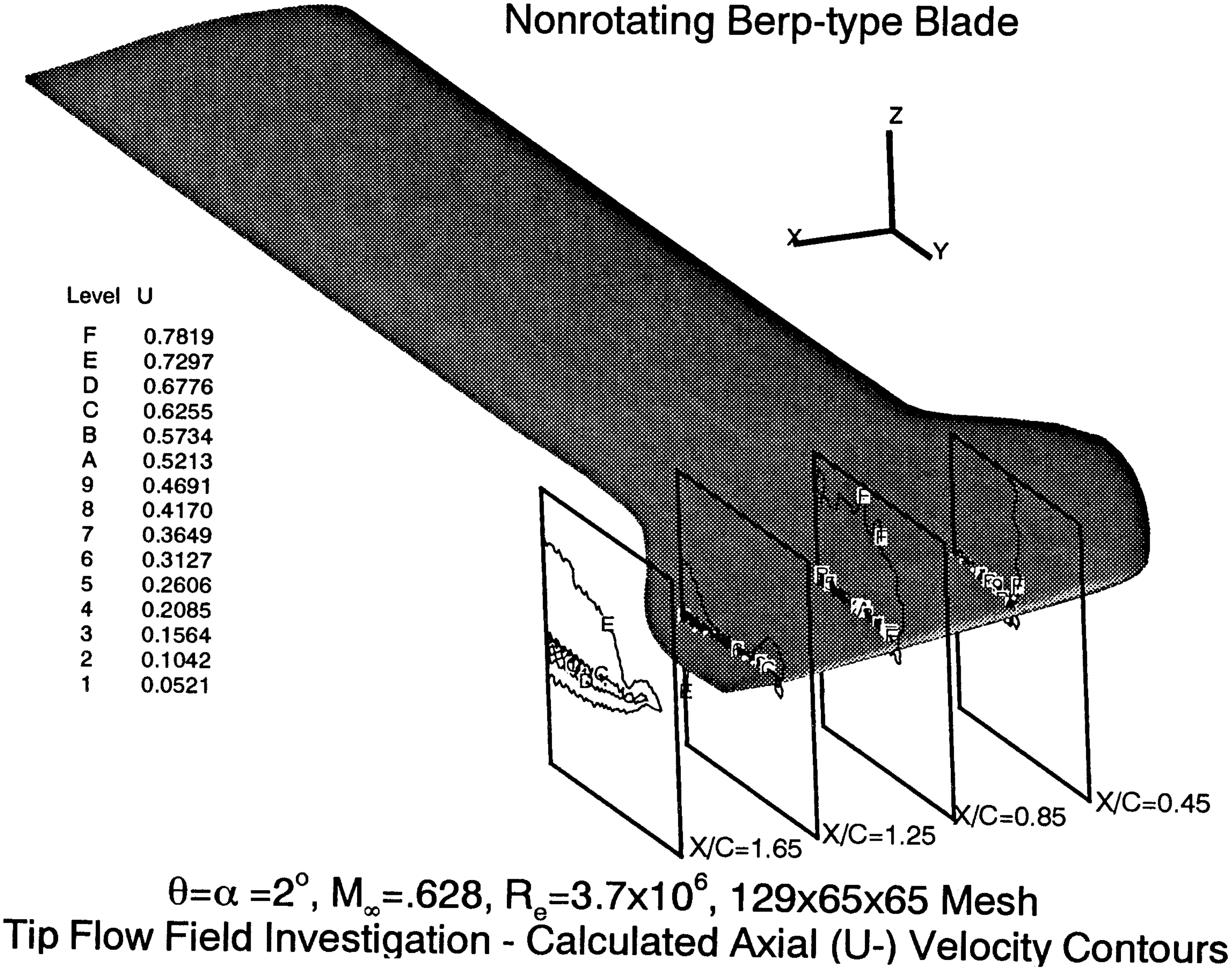

Figure 75. Calculated tip flow field in terms of axial velocity for nonrotating Berp-blade.

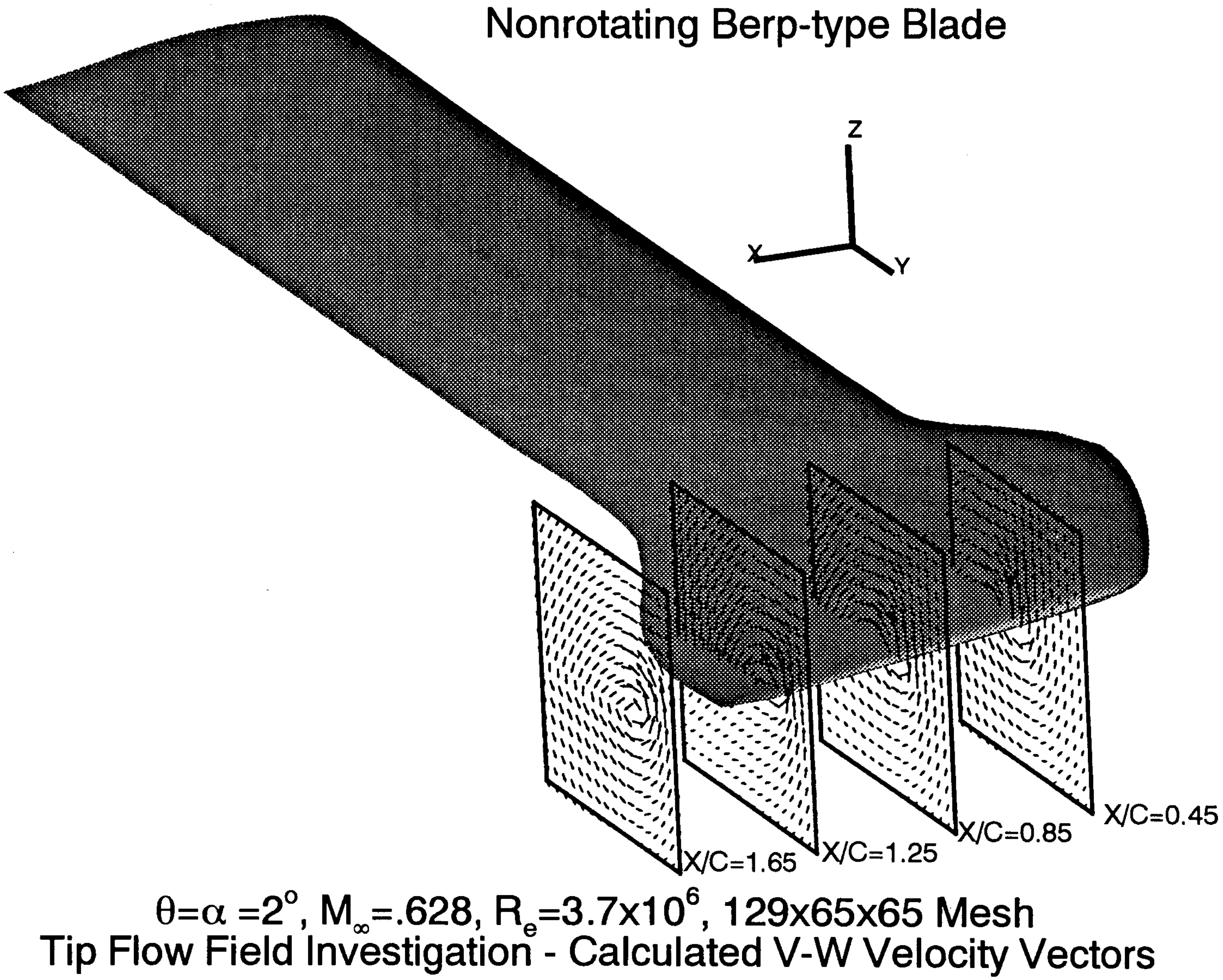

Figure 76. Calculated tip flow field in terms of crossflow velocity vector for nonrotating Berp-blade.

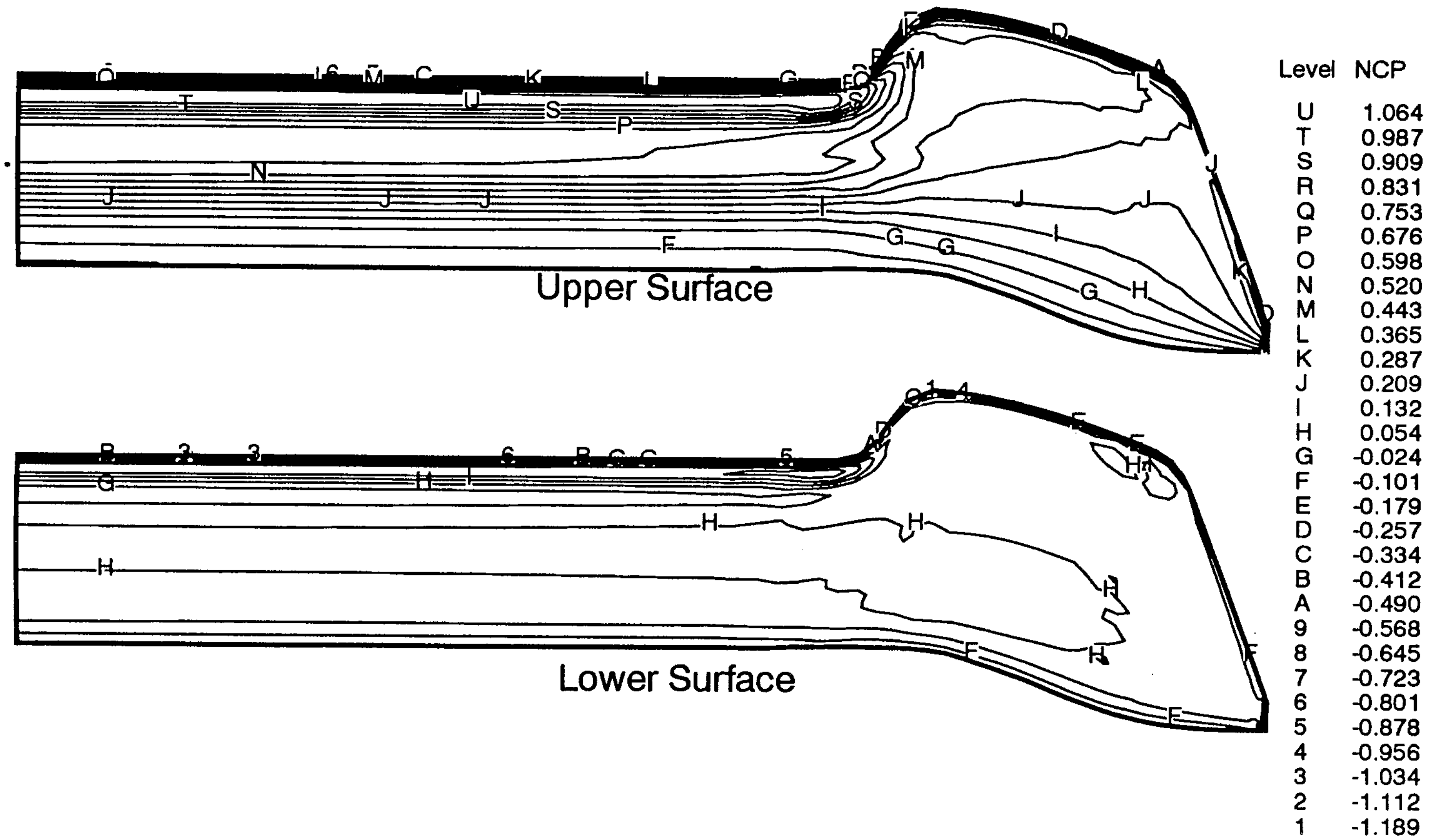

Nonrotating Berp-type Blade

$\theta=\alpha=2^{\circ}$, $M_{\infty}=.628$, $R_e=3.7\times10^6$, 129x65x65 Mesh
Calculated Surface Pressure Coefficient Contours

Figure 77. Calculated surface pressure coefficients for nonrotating Berp-blade.

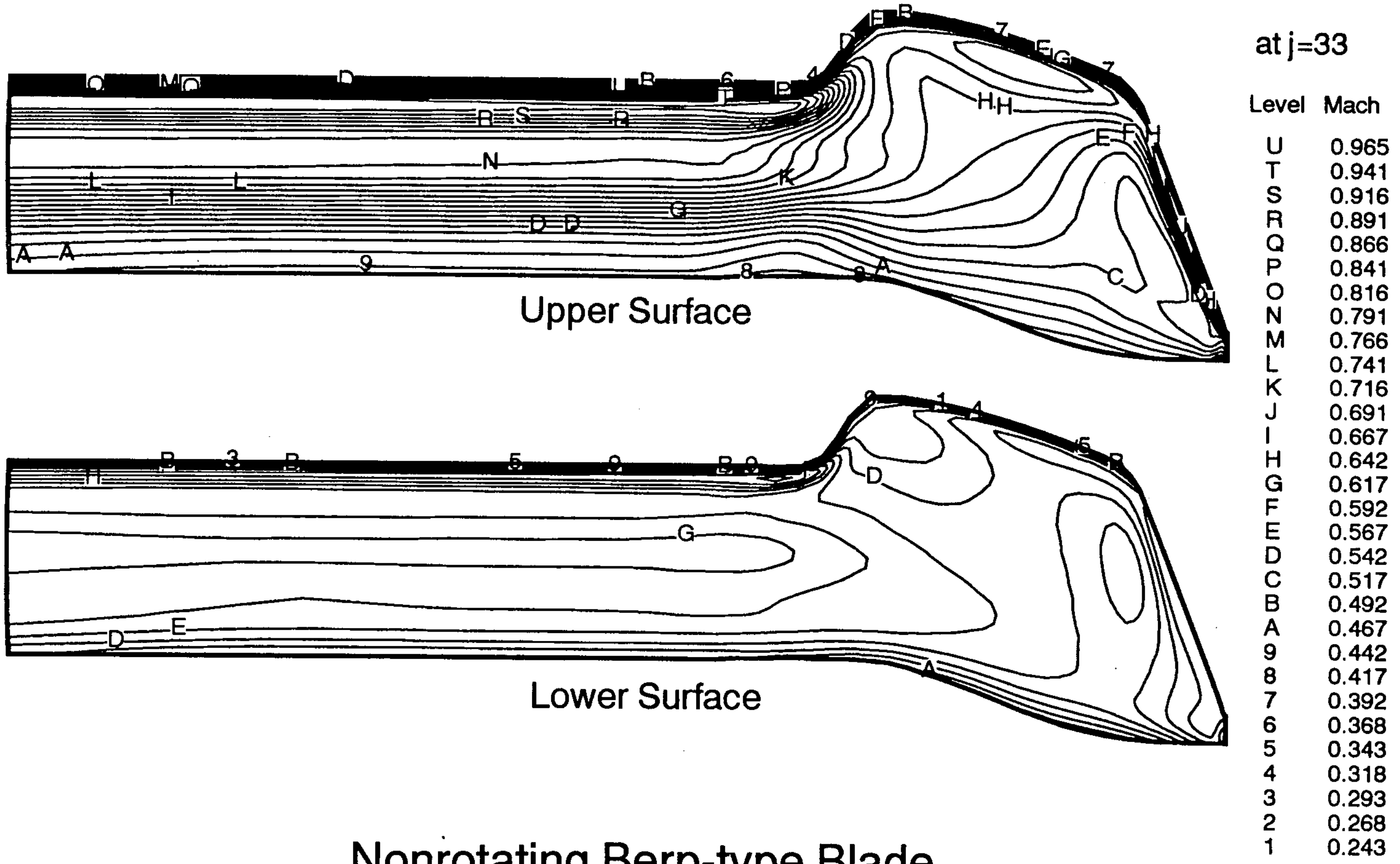

Nonrotating Berp-type Blade

$\theta=\alpha=2^{\circ}$, $M_{\infty}=.628$, $R_e=3.7\times10^6$, 129x65x65 Mesh

Calculated Local Mach Contours

Figure 78. Calculated local Mach contours for nonrotating Berp-blade.

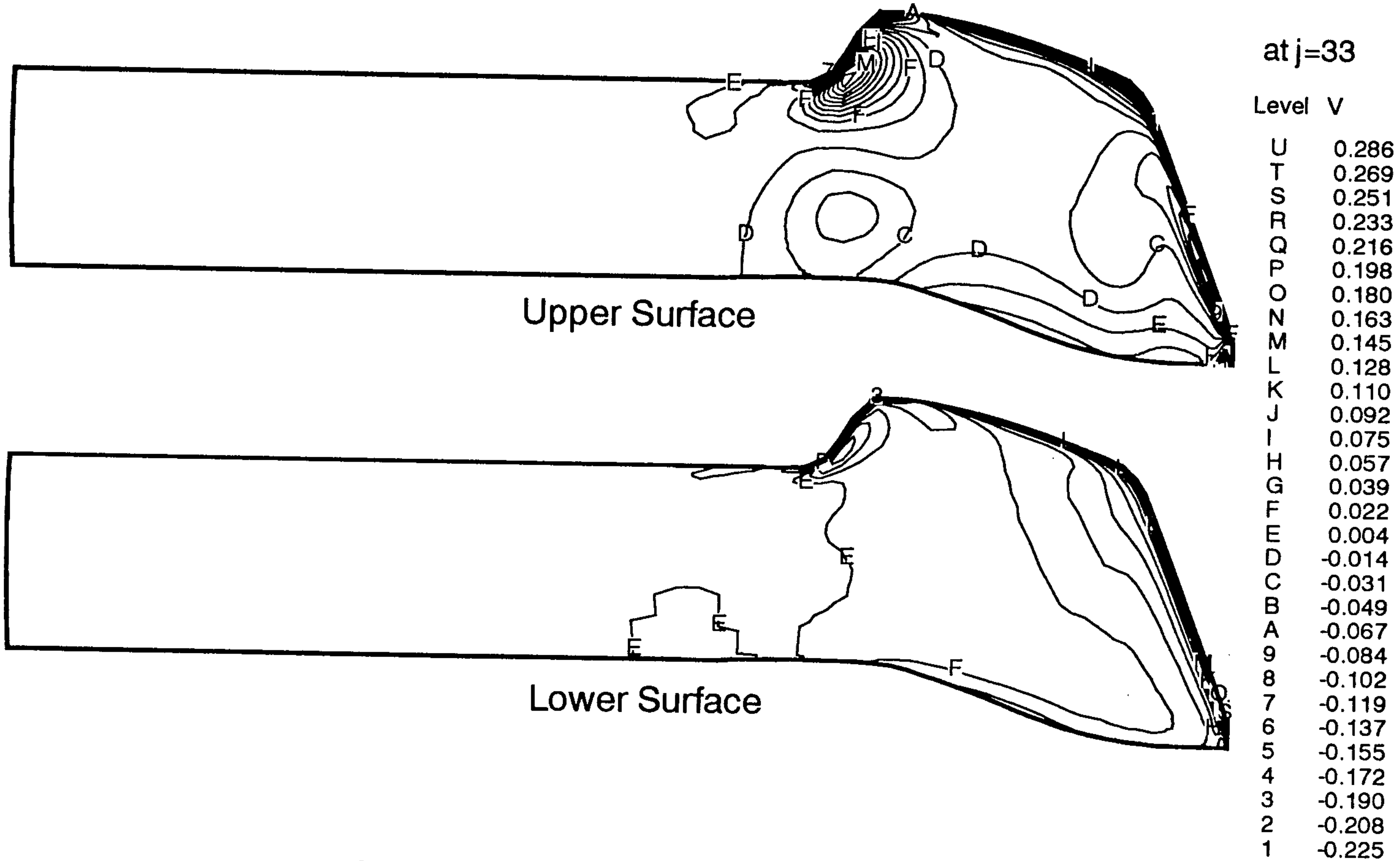

Nonrotating Berp-type Blade

$\theta=\alpha=2^{o}$, $M_{\infty}=.628$, $R_e=3.7\text{x}10^6$, 129x65x65 Mesh

Calculated V-Velocity Contours

Figure 79. Calculated local V-velocity contours for nonrotating Berp-blade.

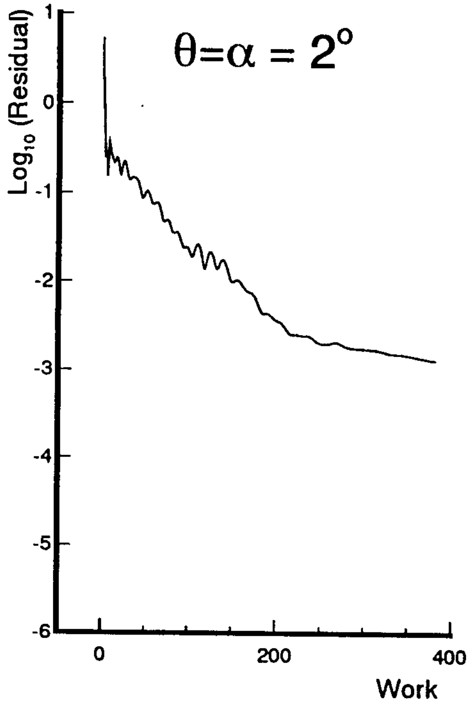

Nonrotating Berp-type Blade

M_∞=.628, R_e=3.7x10^6, 129x65x65 Mesh
Convergence History in terms of Residual

Figure 80. Convergence history in terms of residuals for nonrotating Berp-blade.

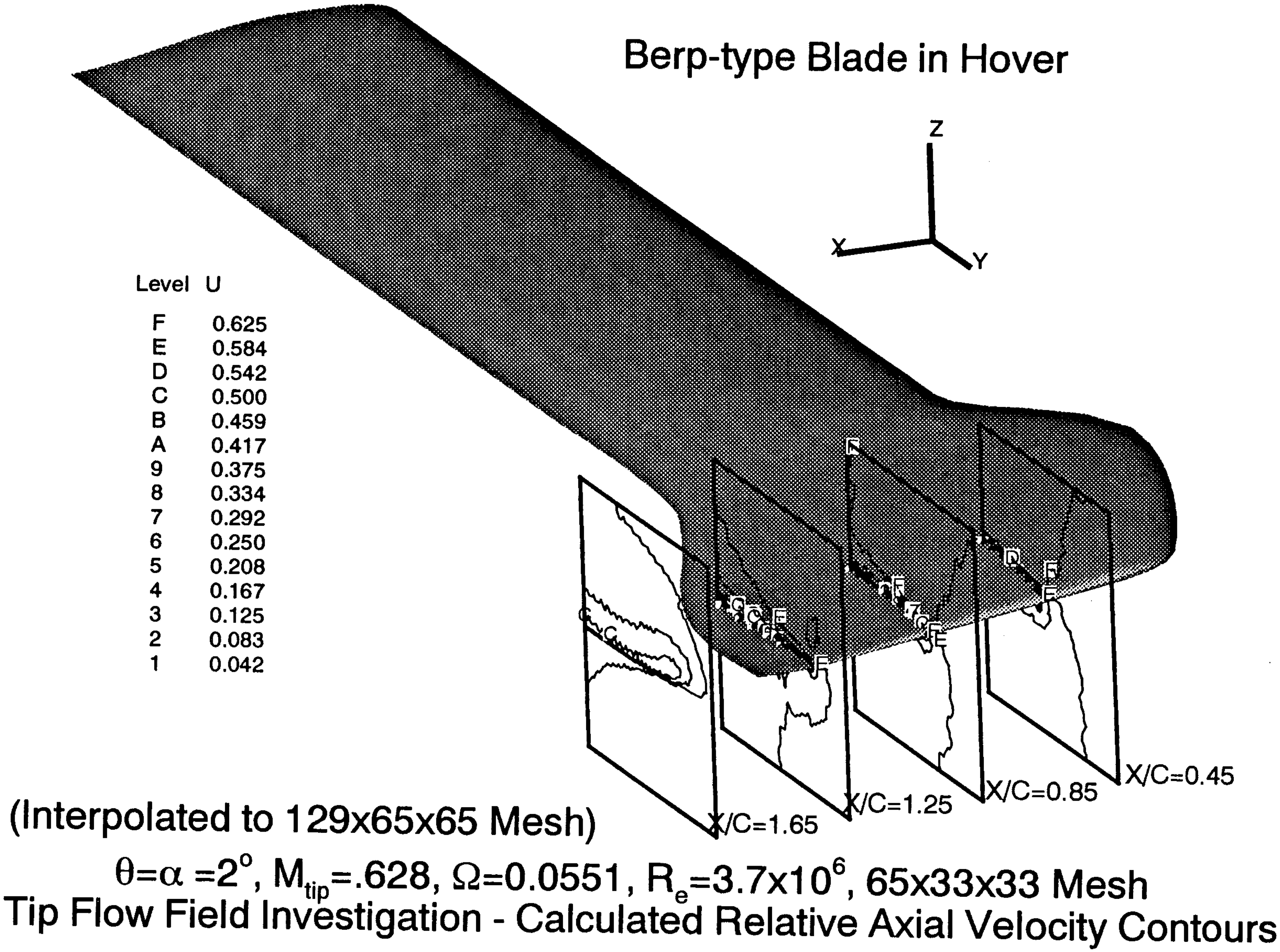

Figure 81. Calculated tip flow field in terms of relative axial velocity for Berp-blade in hover.

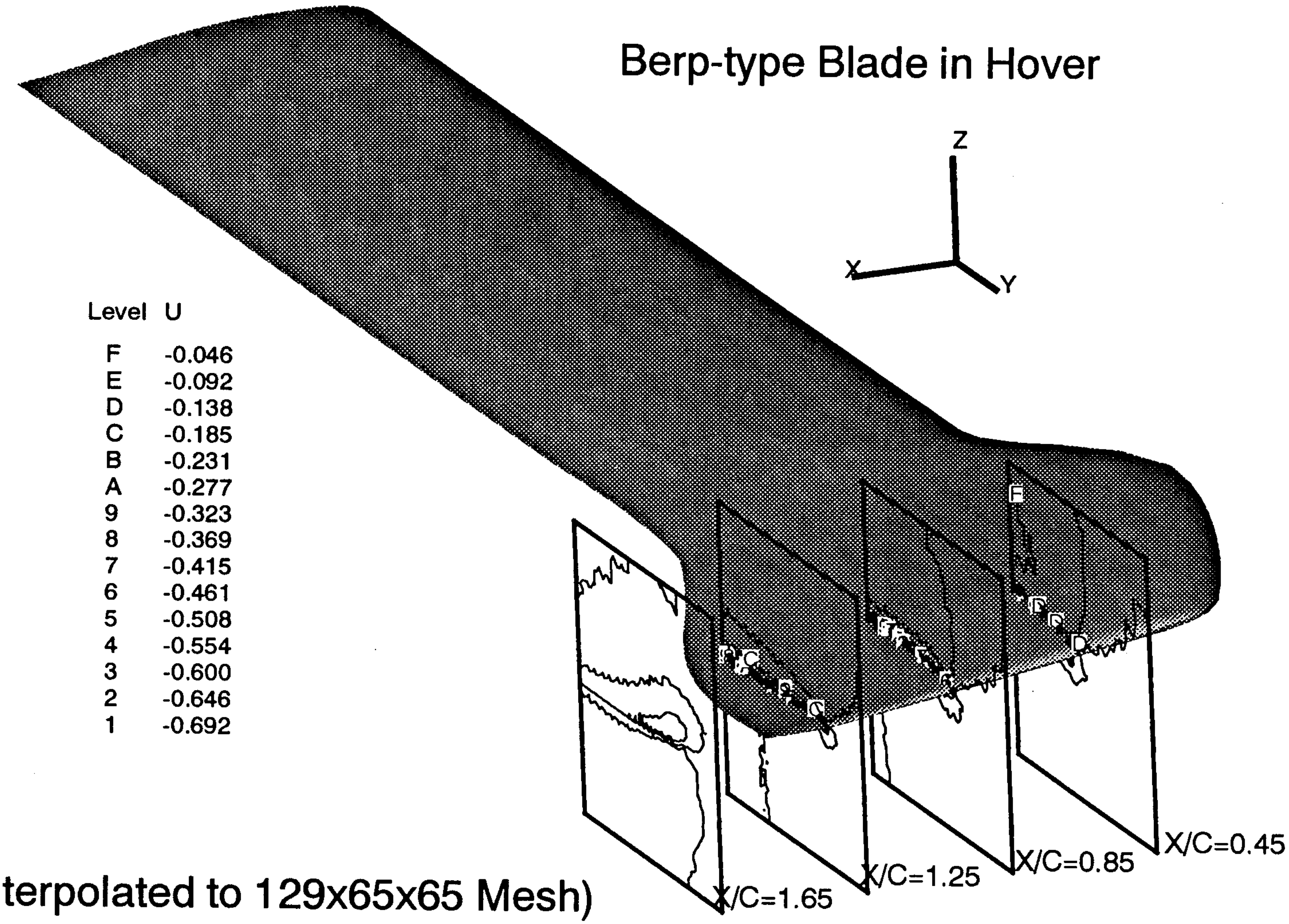

(Interpolated to 129x65x65 Mesh)

$\theta=\alpha=2^{o}$, $M_{tip}=.628$, $\Omega=0.0551$, $R_e=3.7\text{x}10^6$, 65x33x33 Mesh

Tip Flow Field Investigation - Calculated Absolute Axial Velocity Contours

Figure 82. Calculated tip flow field in terms of absolute axial velocity for Berp-blade in hover.

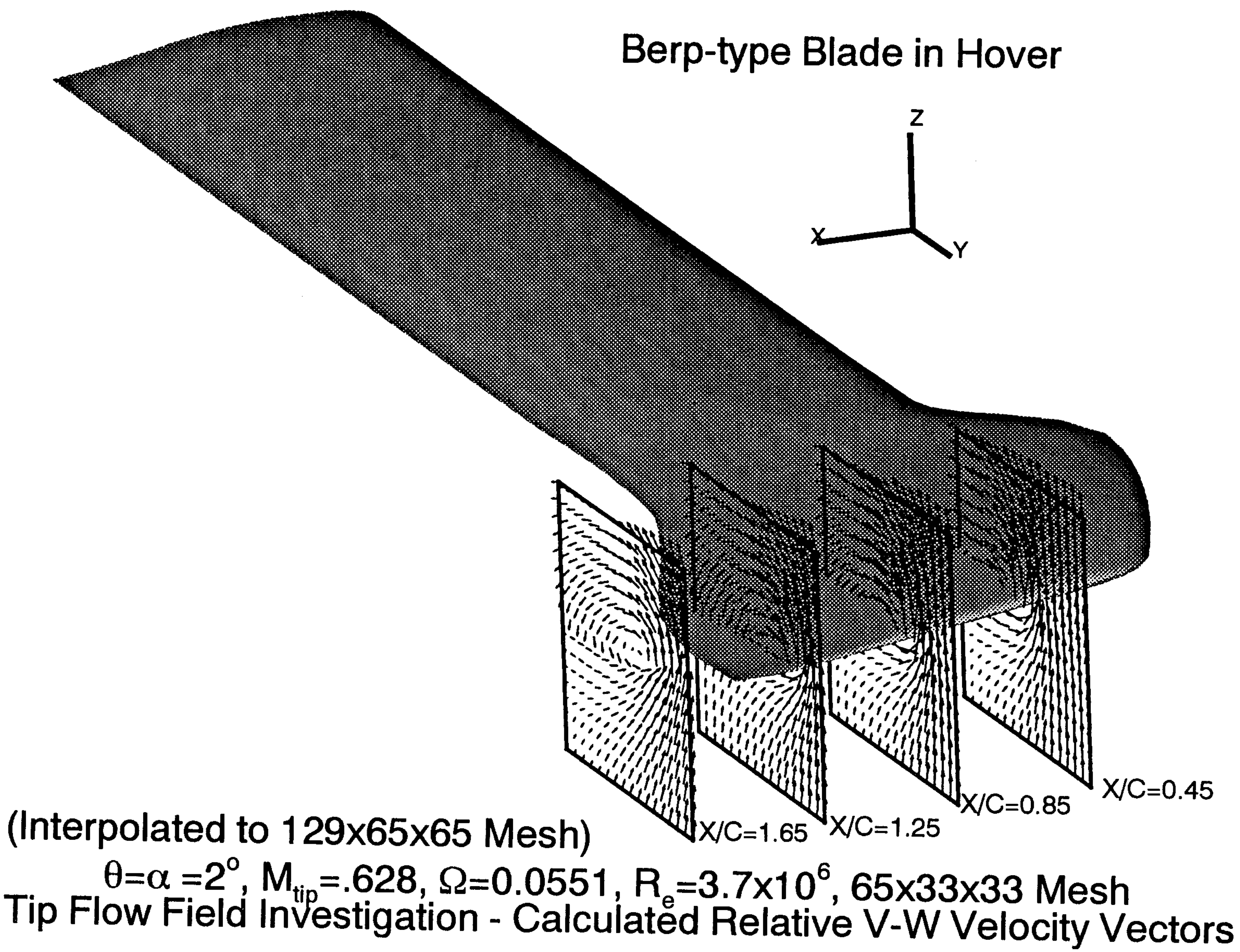

Figure 83. Calculated tip flow field in terms of relative crossflow velocity vector for Berp-blade in hover.

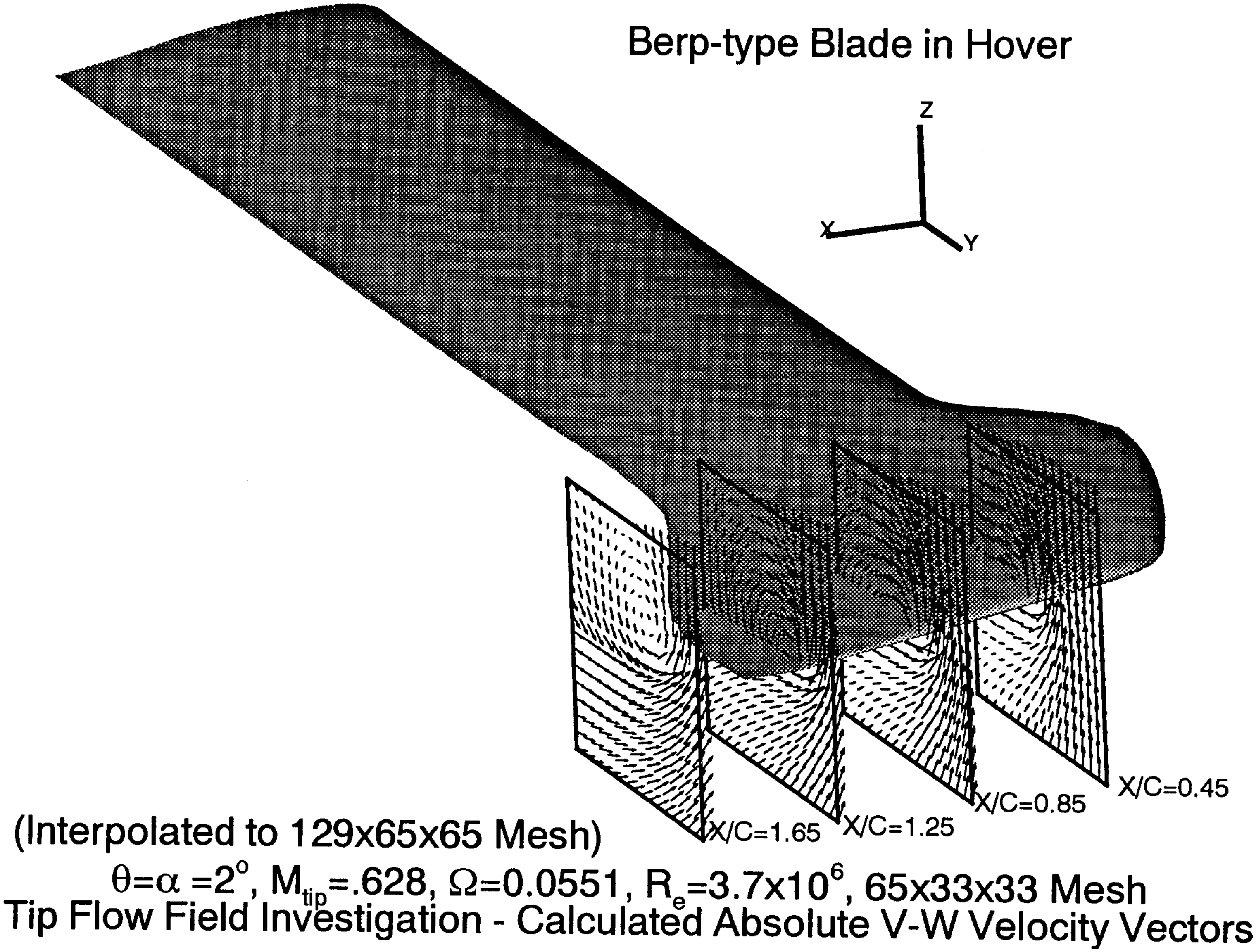

Figure 84. Calculated tip flow field in terms of absolute crossflow velocity vector for Berp-blade in hover.

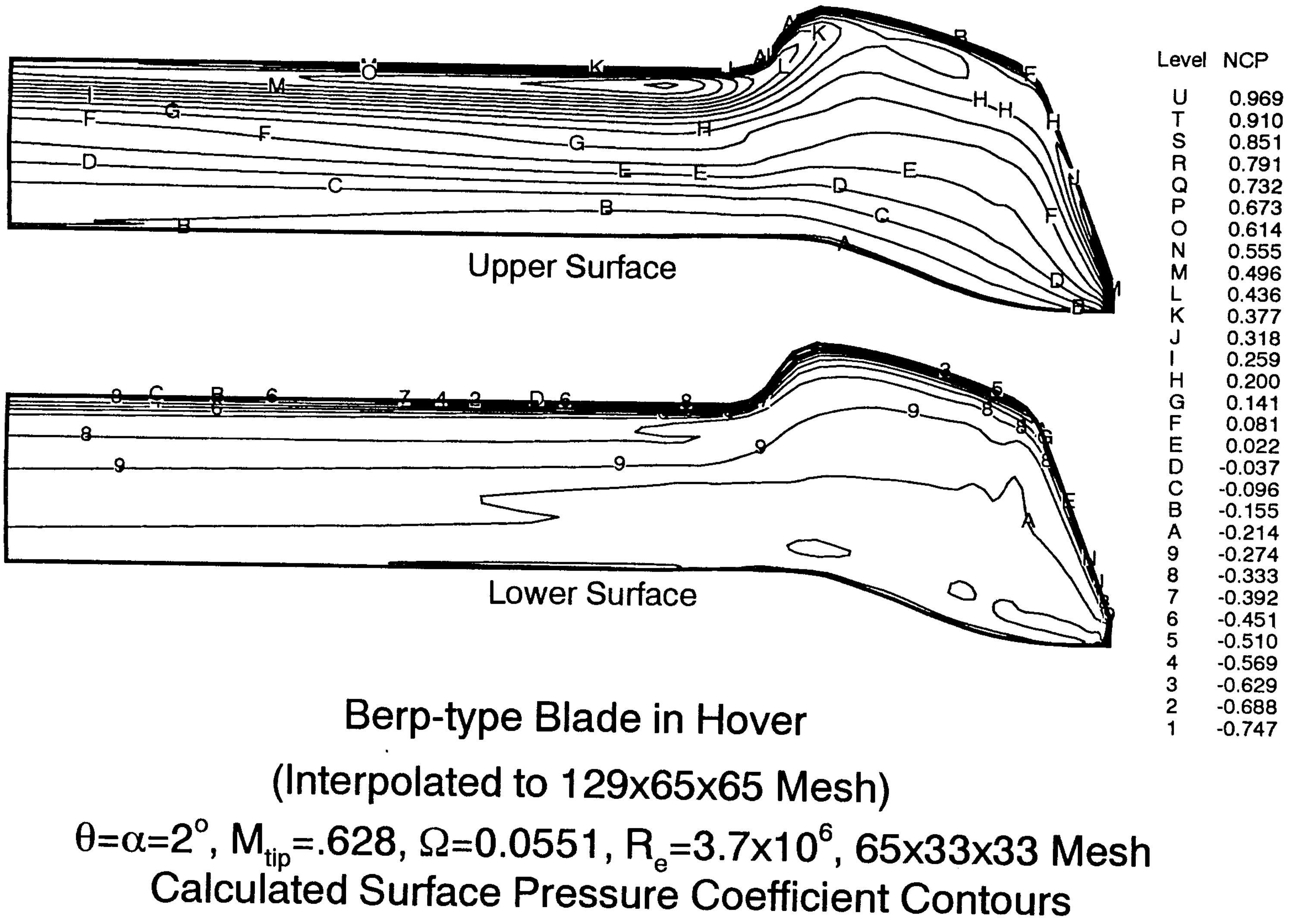

Figure 85. Calculated surface pressure coefficients for Berp-blade in hover.

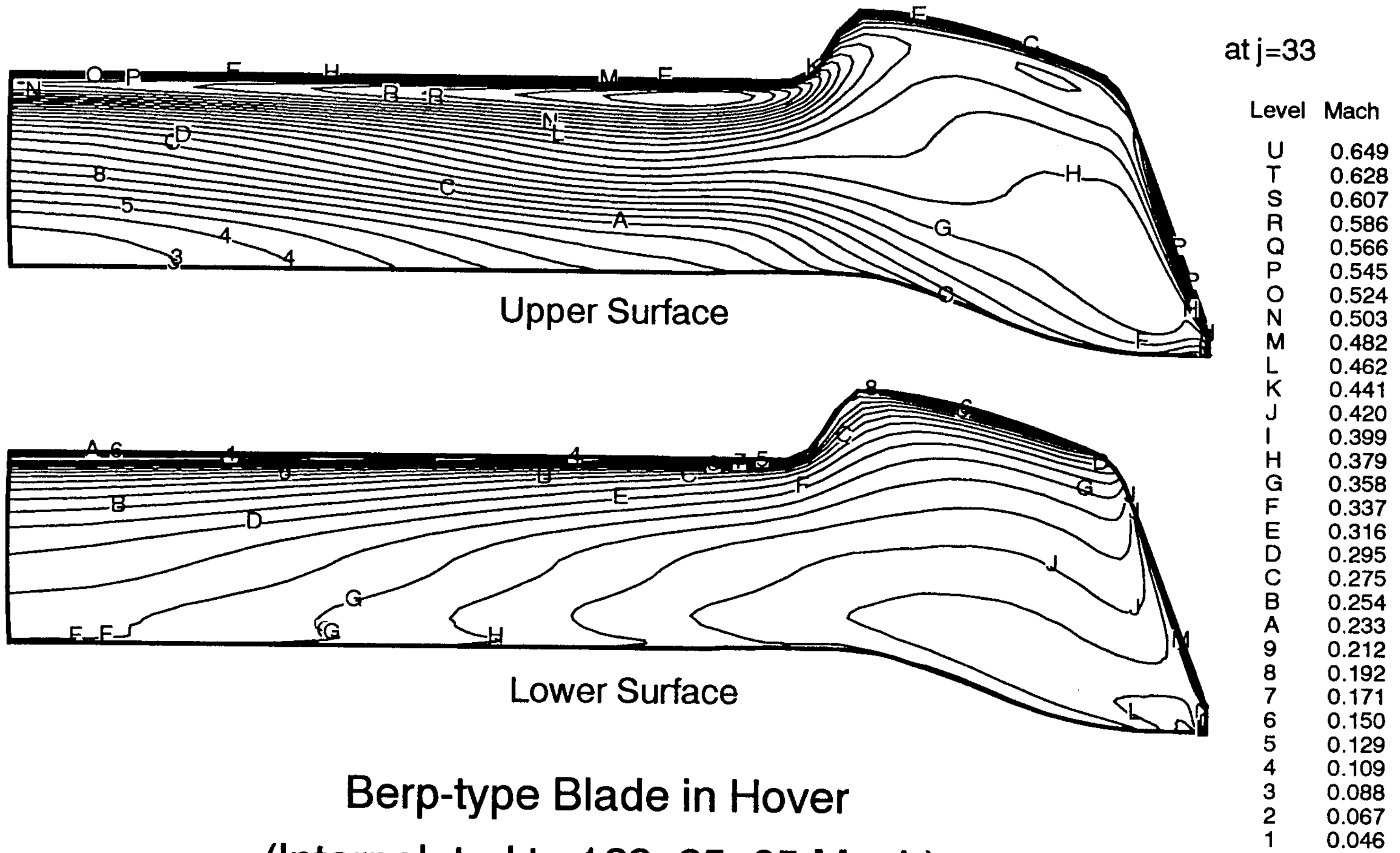

Level	Mach
U	0.649
T	0.628
S	0.607
R	0.586
Q	0.566
P	0.545
O	0.524
N	0.503
M	0.482
L	0.462
K	0.441
J	0.420
I	0.399
H	0.379
G	0.358
F	0.337
E	0.316
D	0.295
C	0.275
B	0.254
A	0.233
9	0.212
8	0.192
7	0.171
6	0.150
5	0.129
4	0.109
3	0.088
2	0.067
1	0.046

Berp-type Blade in Hover

(Interpolated to 129x65x65 Mesh)

$\theta=\alpha=2^{\circ}$, $M_{tip}=.628$, $\Omega=0.0551$, $R_e=3.7\times10^6$, 65x33x33 Mesh

Calculated Local Relative Mach Contours

Figure 86. Calculated local relative Mach contours for Berp-blade in hover.

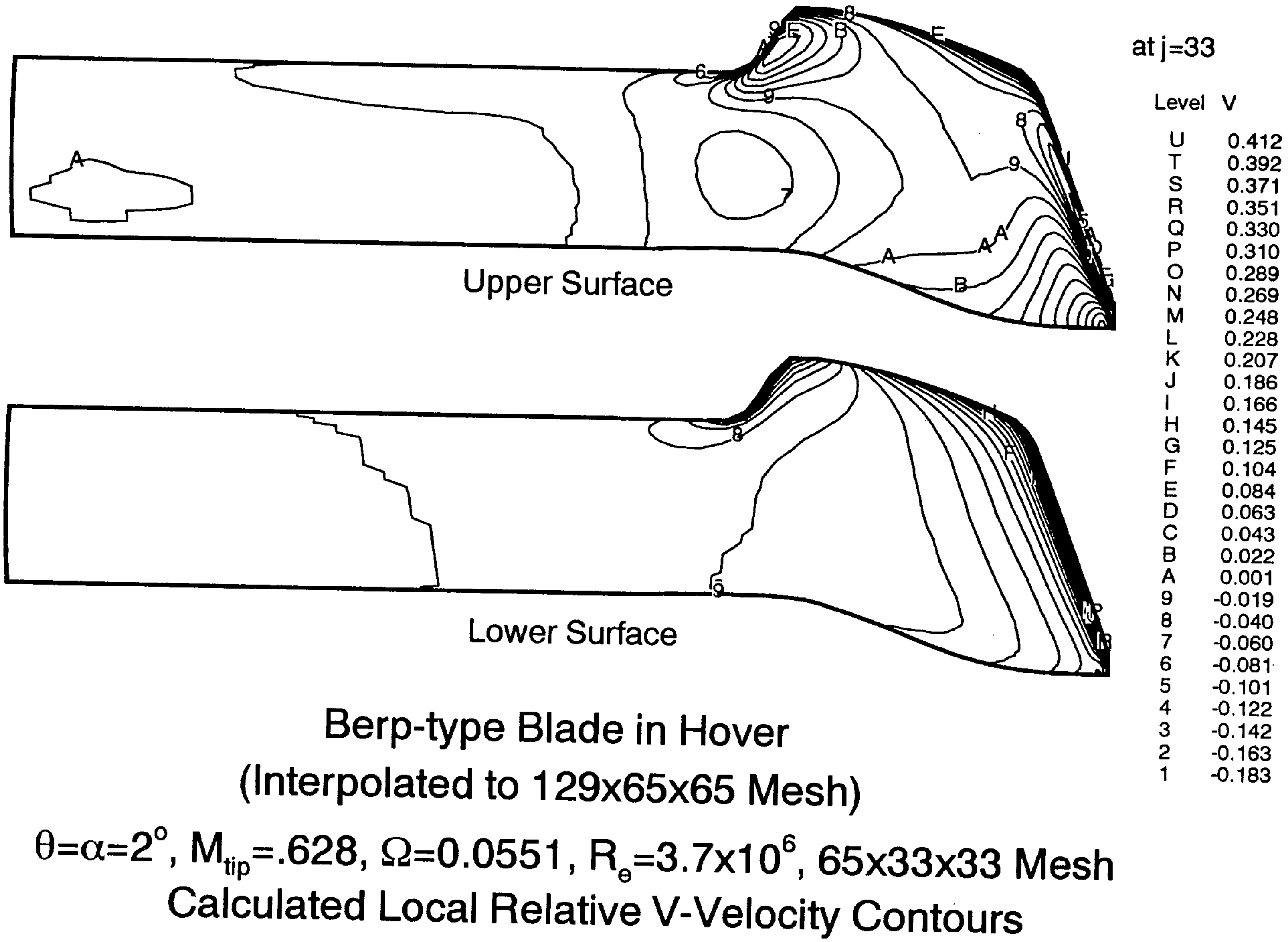

Berp-type Blade in Hover

(Interpolated to 129x65x65 Mesh)

$\theta=\alpha=2^{\circ}$, $M_{tip}=.628$, $\Omega=0.0551$, $R_e=3.7\times10^6$, 65x33x33 Mesh

Calculated Local Relative V-Velocity Contours

Figure 87. Calculated local relative V-velocity contours for Berp-blade in hover.

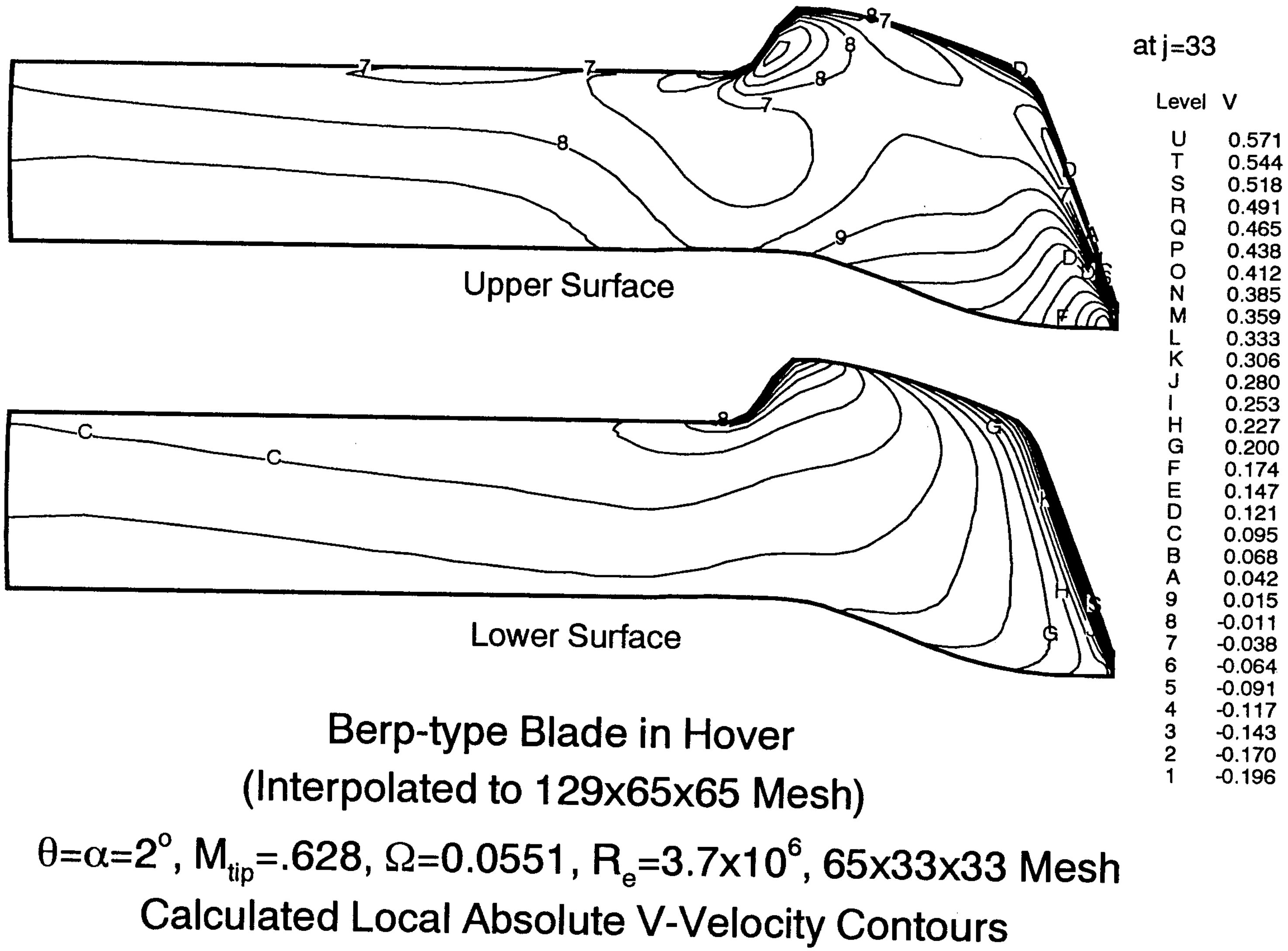

Berp-type Blade in Hover

(Interpolated to 129x65x65 Mesh)

$\theta=\alpha=2^o$, M_{tip}=.628, Ω=0.0551, R_e=3.7x10^6, 65x33x33 Mesh

Calculated Local Absolute V-Velocity Contours

Figure 88. Calculated local absolute V-velocity contours for Berp-blade in hover.

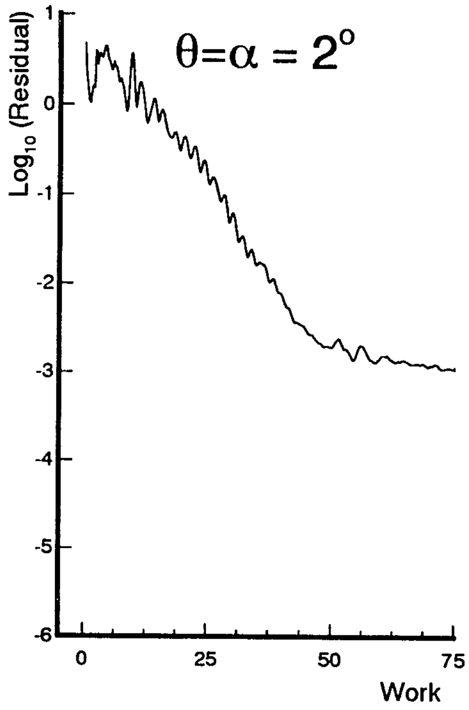

Berp-type Blade in Hover

M_{tip}=.628, Ω=0.0551, R_e=3.7x10^6, 65x33x33 Mesh

Convergence History in terms of Residual

Figure 89. Convergence history in terms of residuals for Berp-blade in hover.

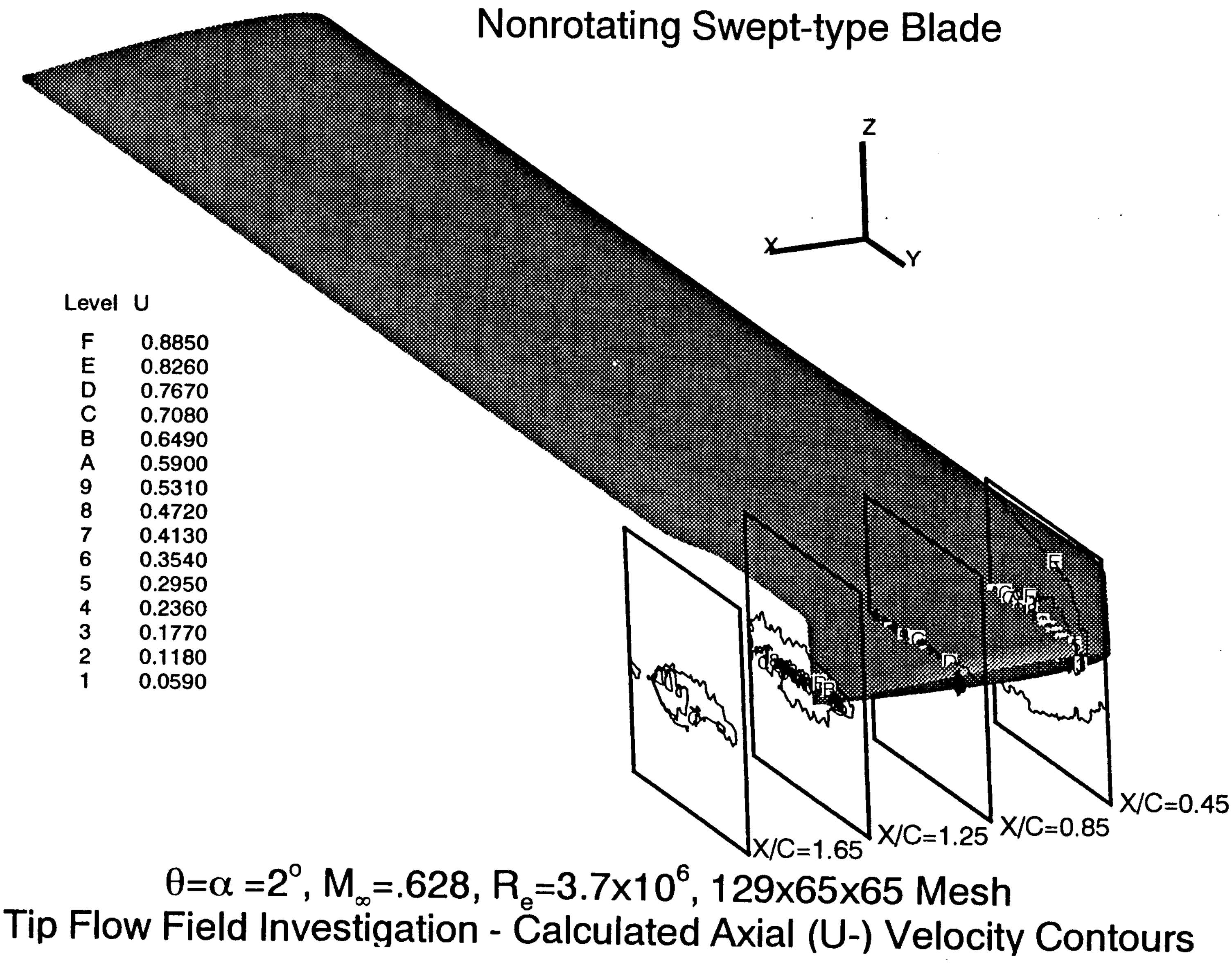

Figure 90. Calculated tip flow field in terms of axial velocity for nonrotating swept-blade.

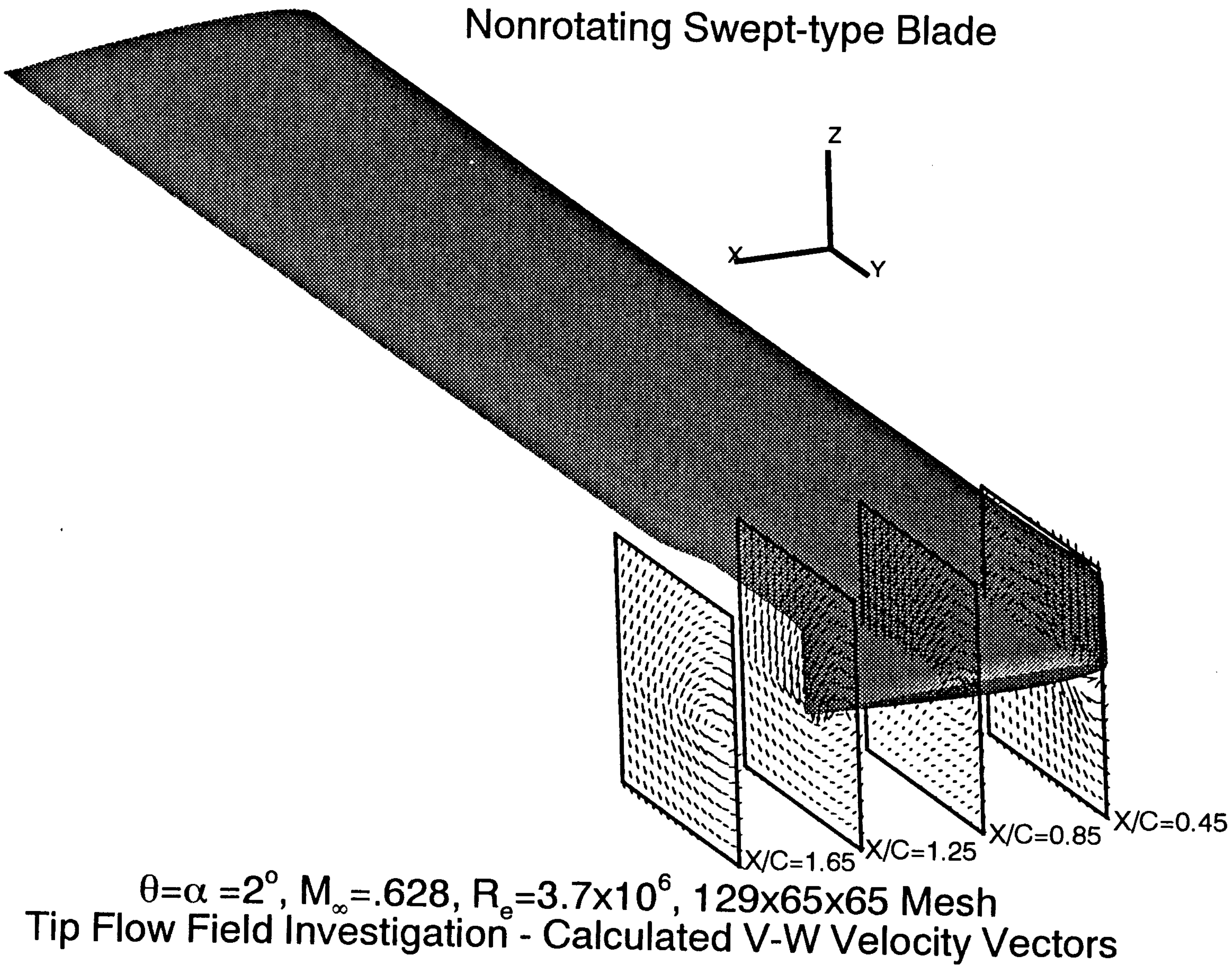

Figure 91. Calculated tip flow field in terms of crossflow velocity vector for nonrotating swept-blade.

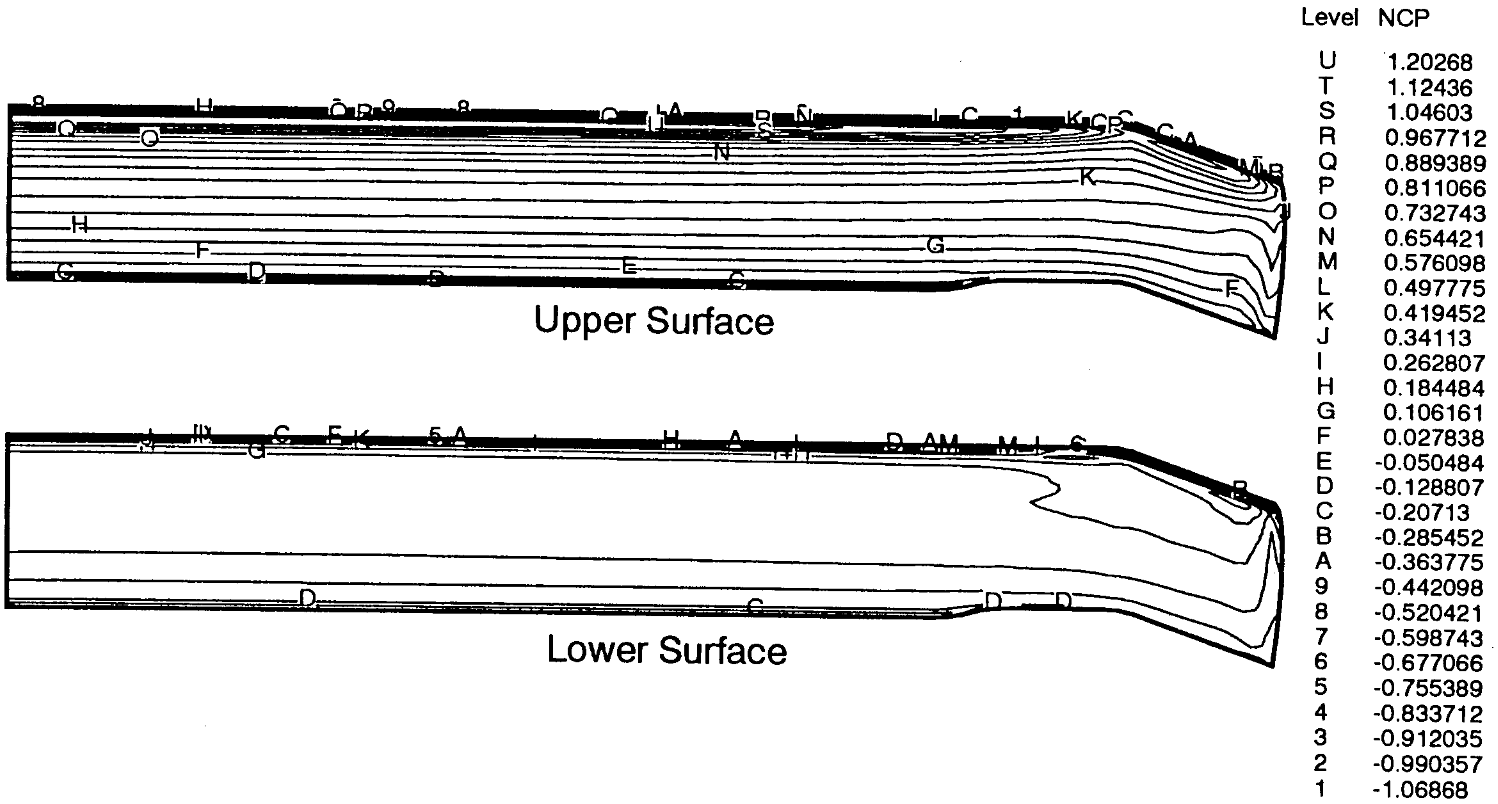

Nonrotating Swept-type Blade

$\theta=\alpha=2^\circ$, $M_\infty=.628$, $R_e=3.7\text{x}10^6$, 129x65x65 Mesh

Calculated Surface Pressure Coefficient Contours

Figure 92. Calculated surface pressure coefficients for nonrotating swept-blade.

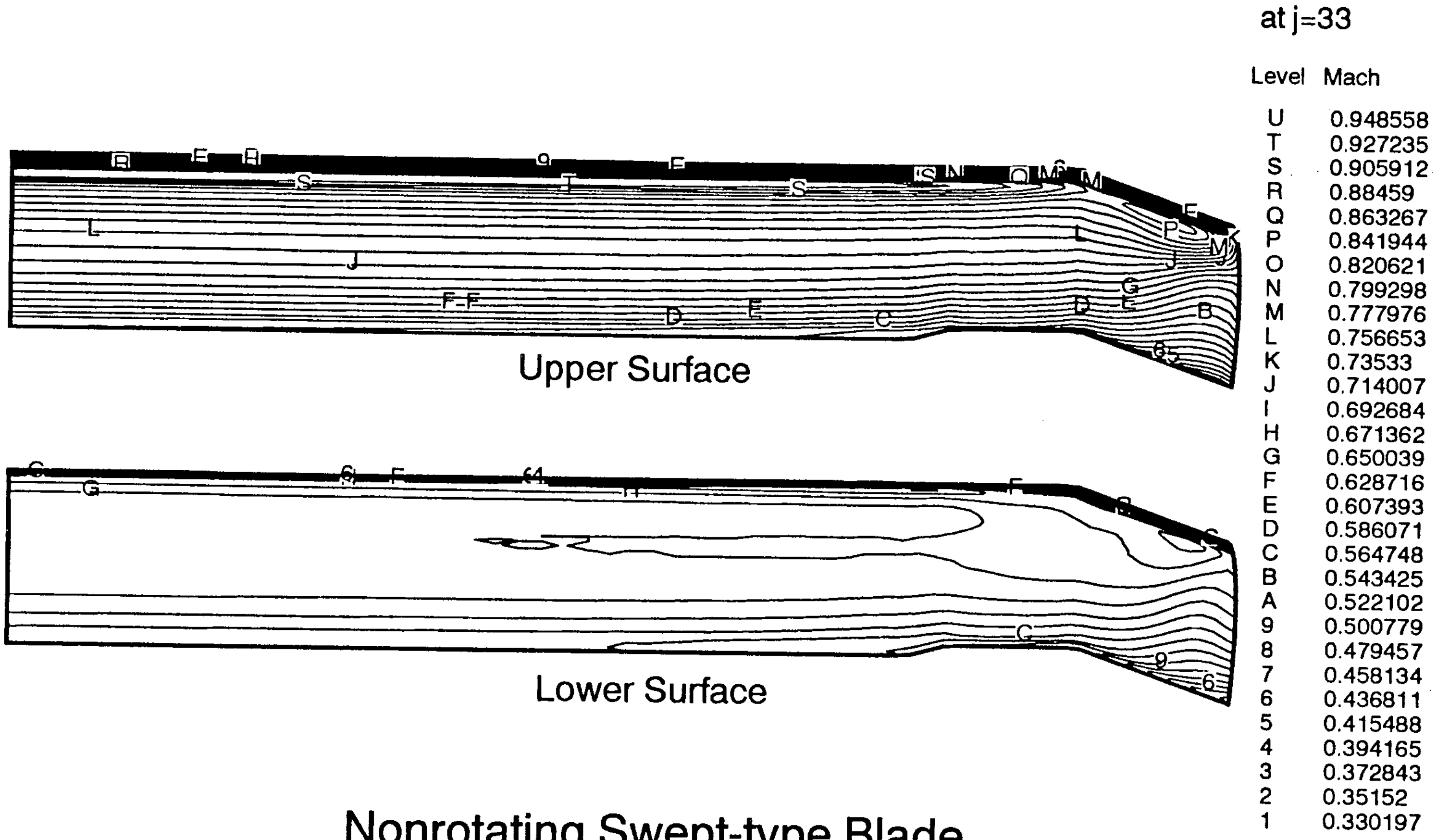

at j=33

Level	Mach
U	0.948558
T	0.927235
S	0.905912
R	0.88459
Q	0.863267
P	0.841944
O	0.820621
N	0.799298
M	0.777976
L	0.756653
K	0.73533
J	0.714007
I	0.692684
H	0.671362
G	0.650039
F	0.628716
E	0.607393
D	0.586071
C	0.564748
B	0.543425
A	0.522102
9	0.500779
8	0.479457
7	0.458134
6	0.436811
5	0.415488
4	0.394165
3	0.372843
2	0.35152
1	0.330197

Nonrotating Swept-type Blade

$\theta=\alpha=2^\circ$, $M_\infty=.628$, $R_e=3.7\times10^6$, 129x65x65 Mesh

Calculated Local Mach Contours

Figure 93. Calculated local Mach contours for nonrotating swept-blade.

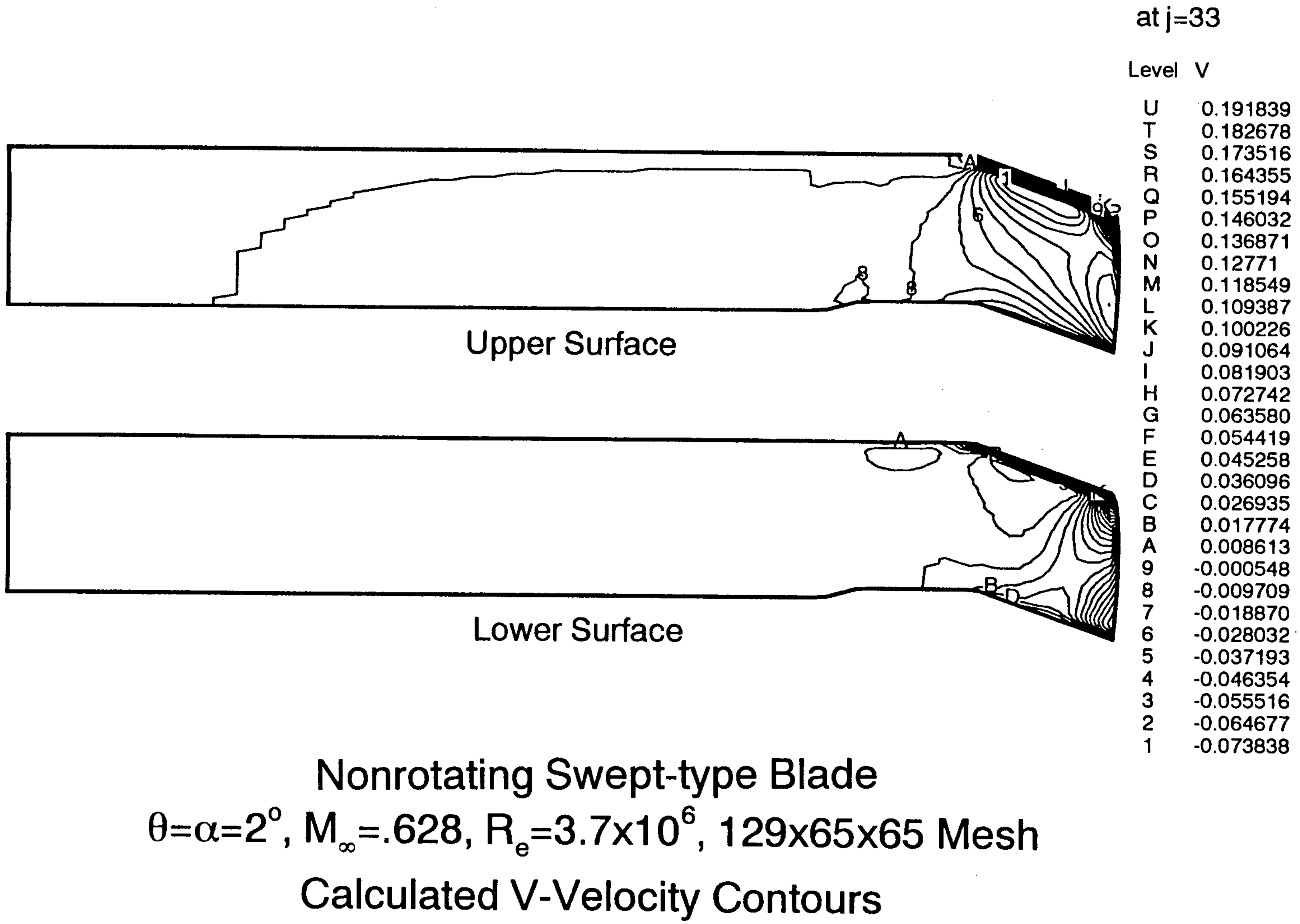

Nonrotating Swept-type Blade

$\theta=\alpha=2^{\circ}$, $M_{\infty}=.628$, $R_e=3.7\times10^{6}$, 129x65x65 Mesh

Calculated V-Velocity Contours

Figure 94. Calculated local V-velocity contours for nonrotating swept-blade.

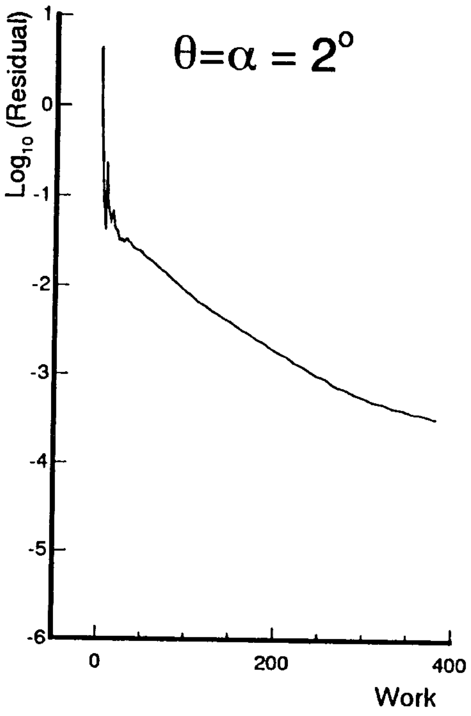

Nonrotating Swept-type Blade

M_∞=.628, R_e=3.7x10^6, 129x65x65 Mesh

Convergence History in terms of Residual

Figure 95. Convergence history in terms of residuals for nonrotating swept-blade.

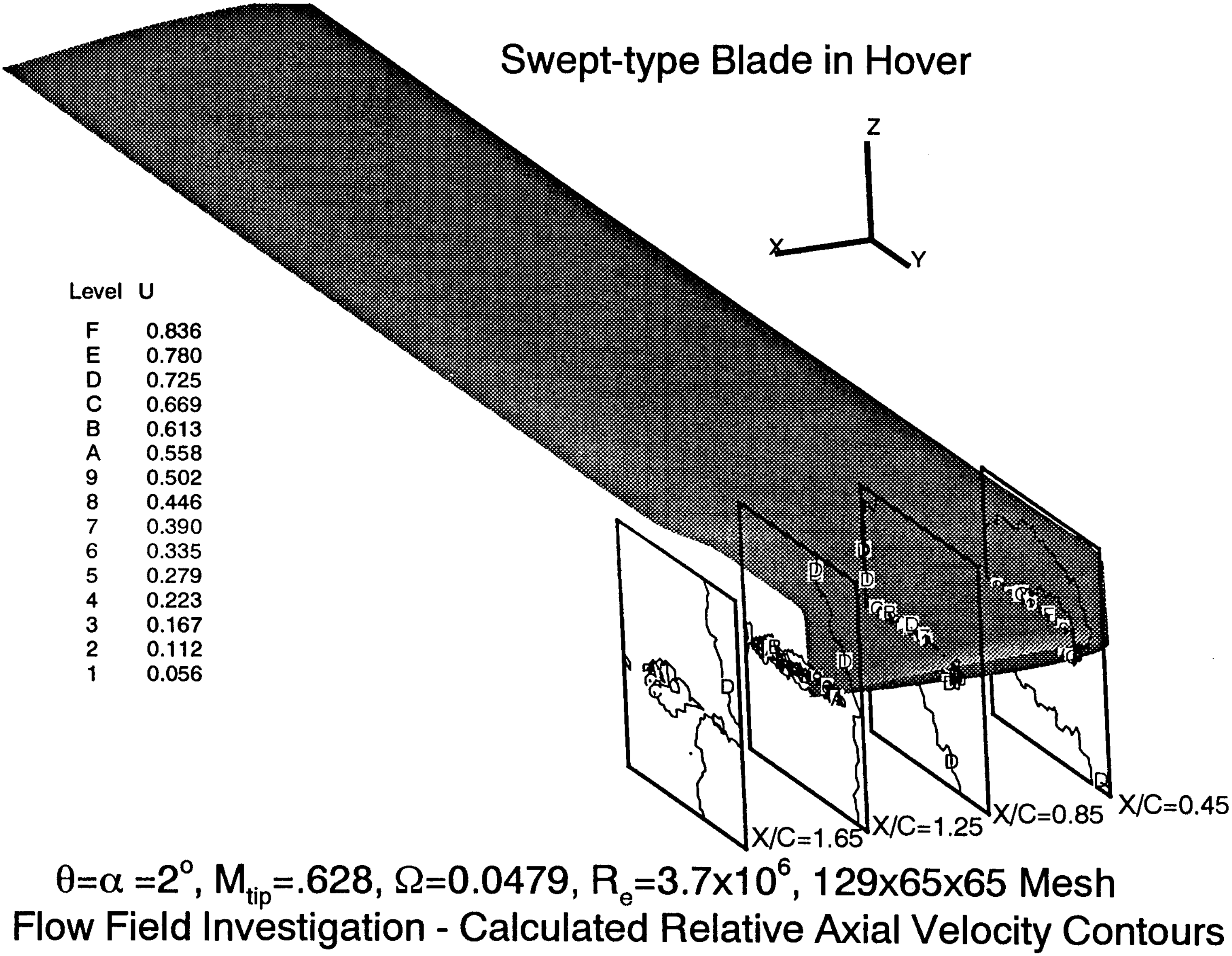

Figure 96. Calculated tip flow field in terms of relative axial velocity for swept-blade in hover.

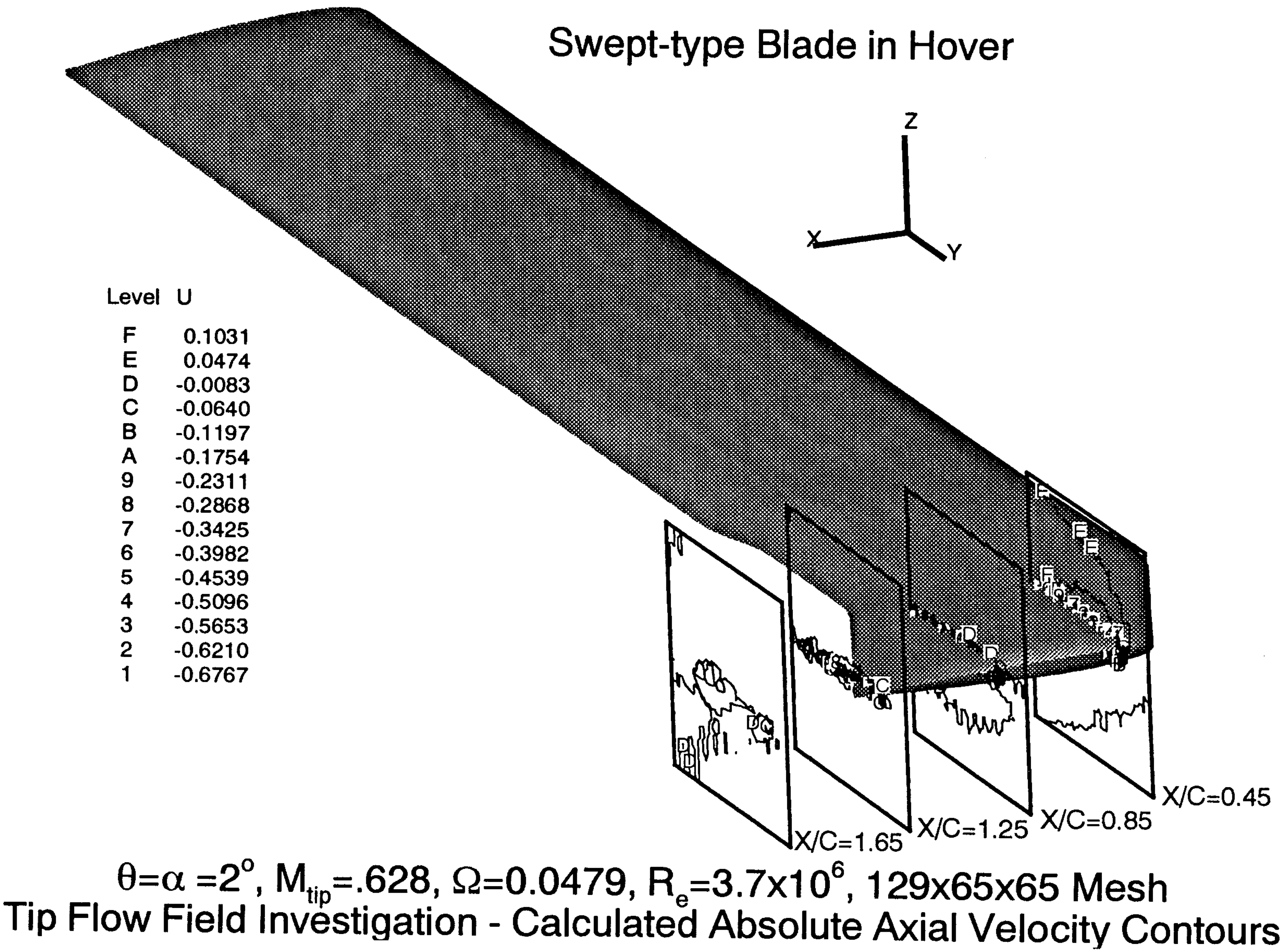

Figure 97. Calculated tip flow field in terms of absolute axial velocity for swept-blade in hover.

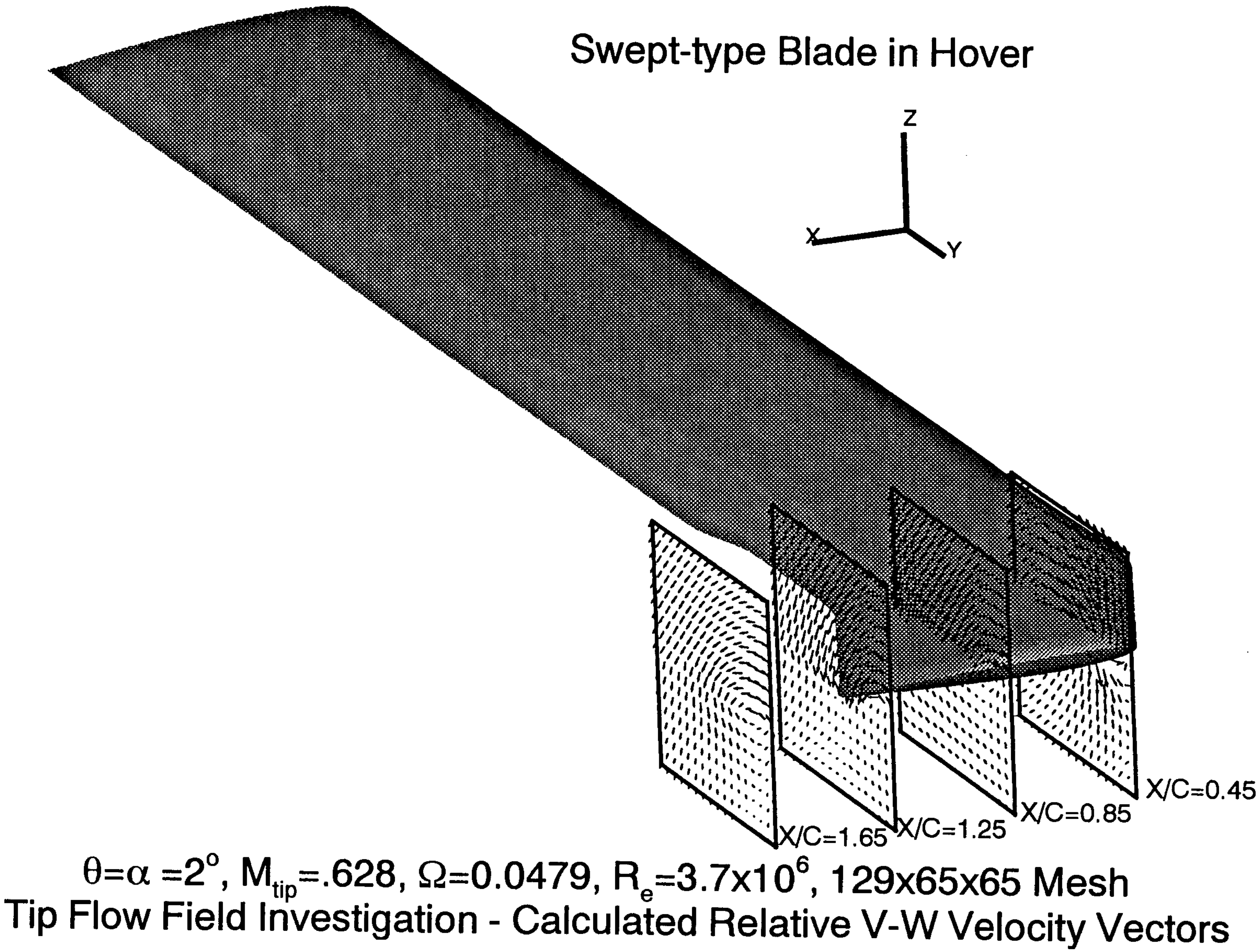

Figure 98. Calculated tip flow field in terms of relative crossflow velocity vector for swept-blade in hover.

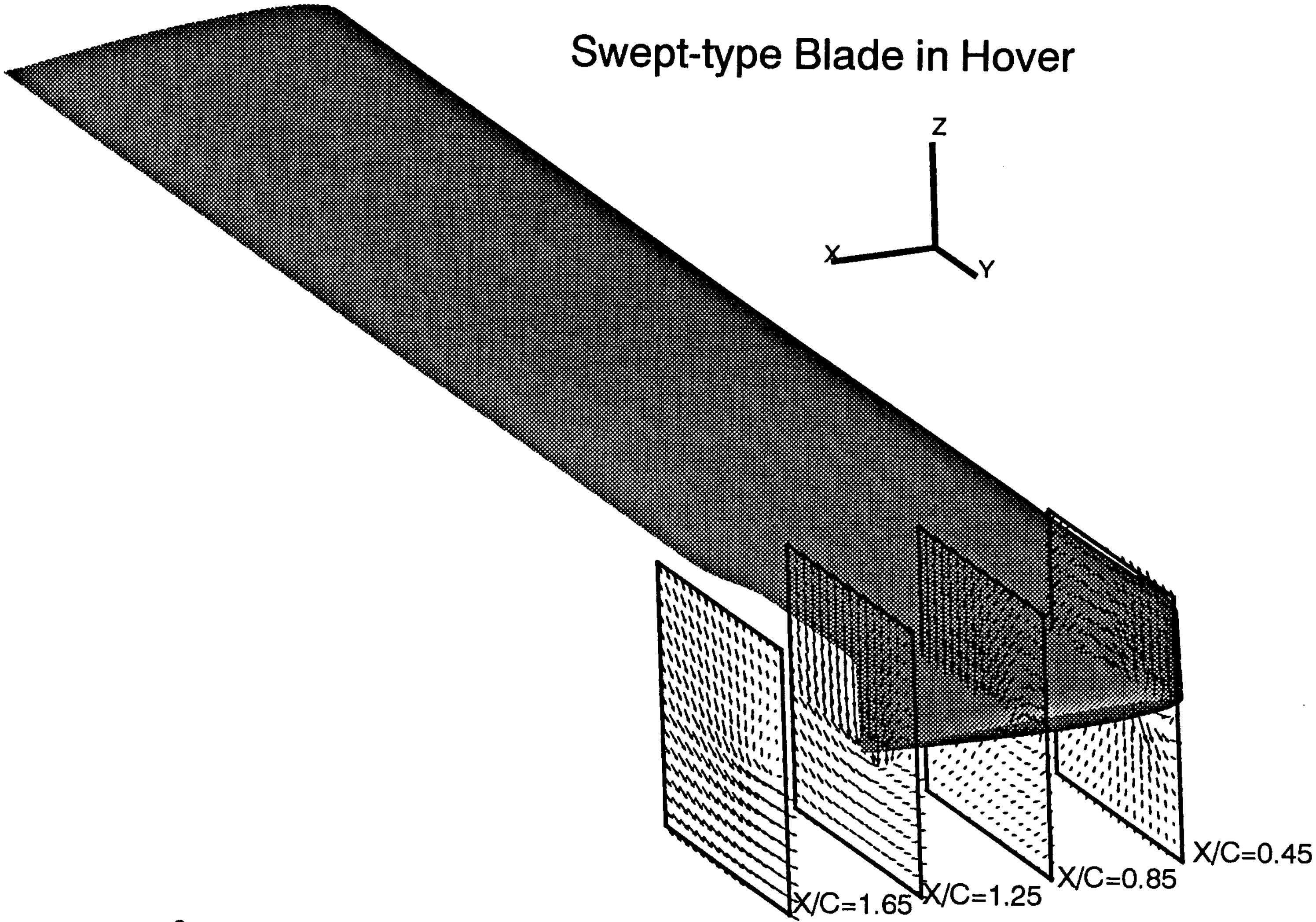

Figure 99. Calculated tip flow field in terms of absolute crossflow velocity vector for swept-blade in hover.

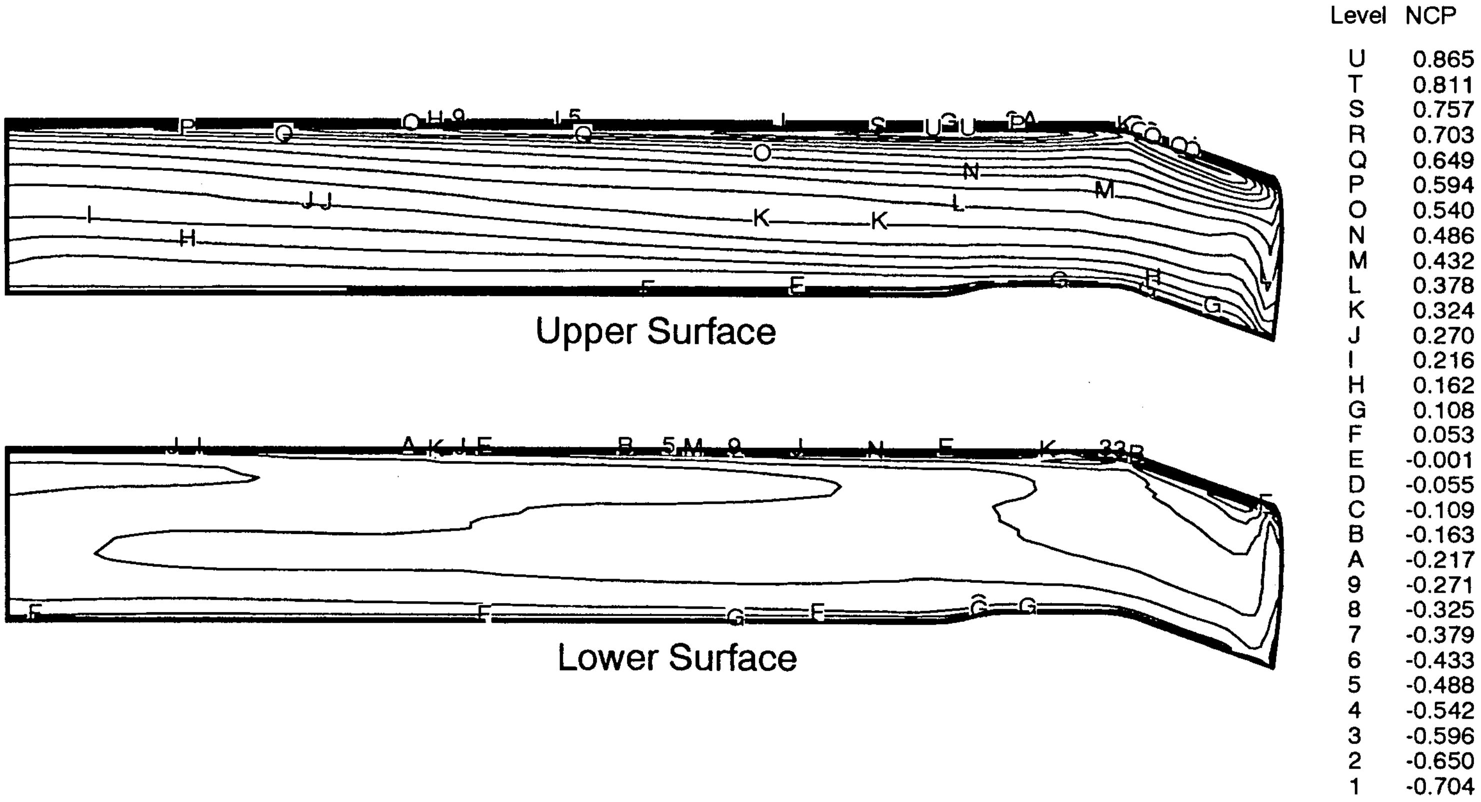

Swept-type Blade in Hover

$\theta=\alpha=2^{o}$, $M_{tip}=.628$, $\Omega=0.0479$, $R_e=3.7\text{x}10^6$, 129x65x65 Mesh

Calculated Surface Pressure Coefficient Contours

Figure 100. Calculated surface pressure coefficients for swept-blade in hover.

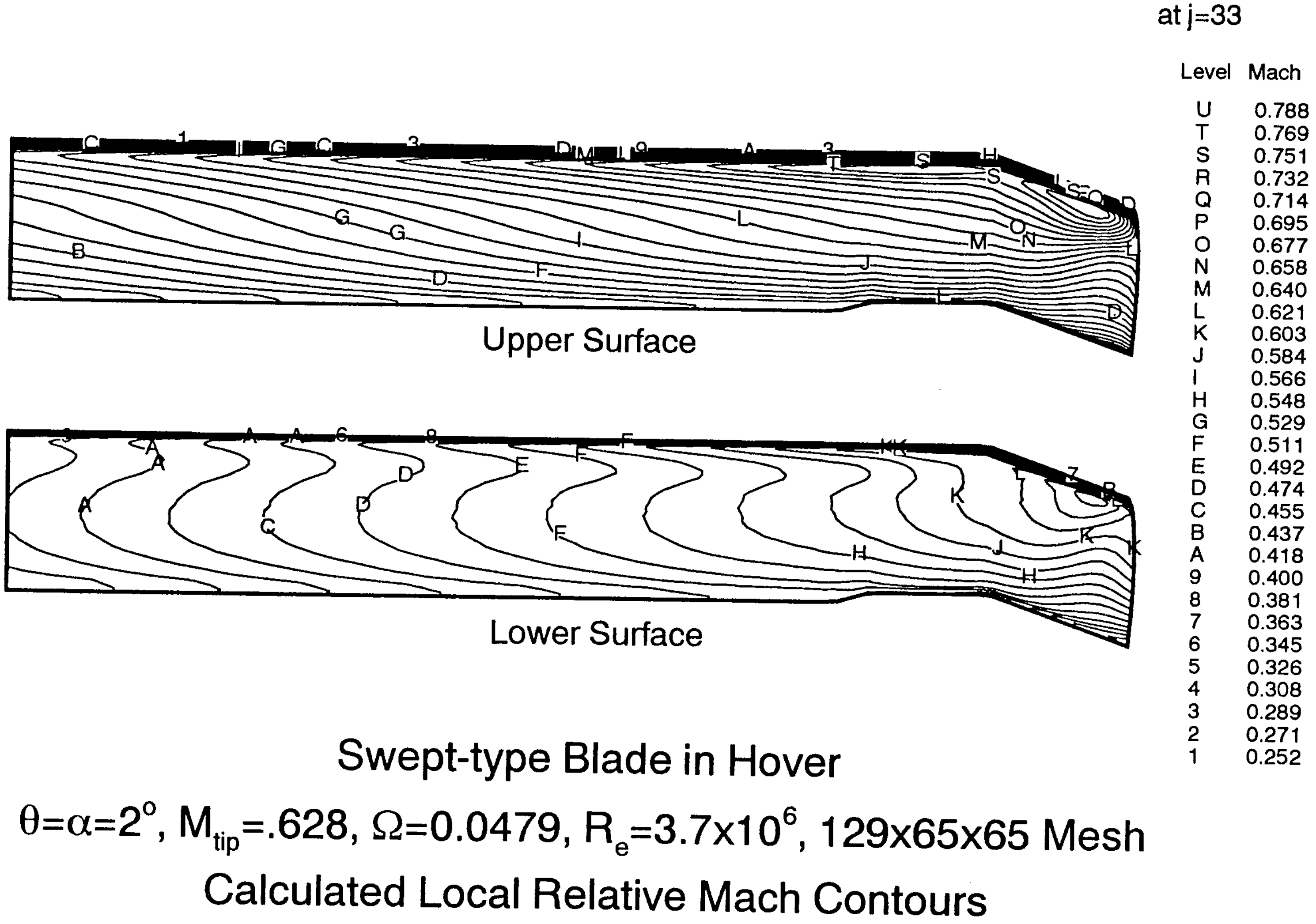

Figure 101. Calculated local relative Mach contours for swept-blade in hover.

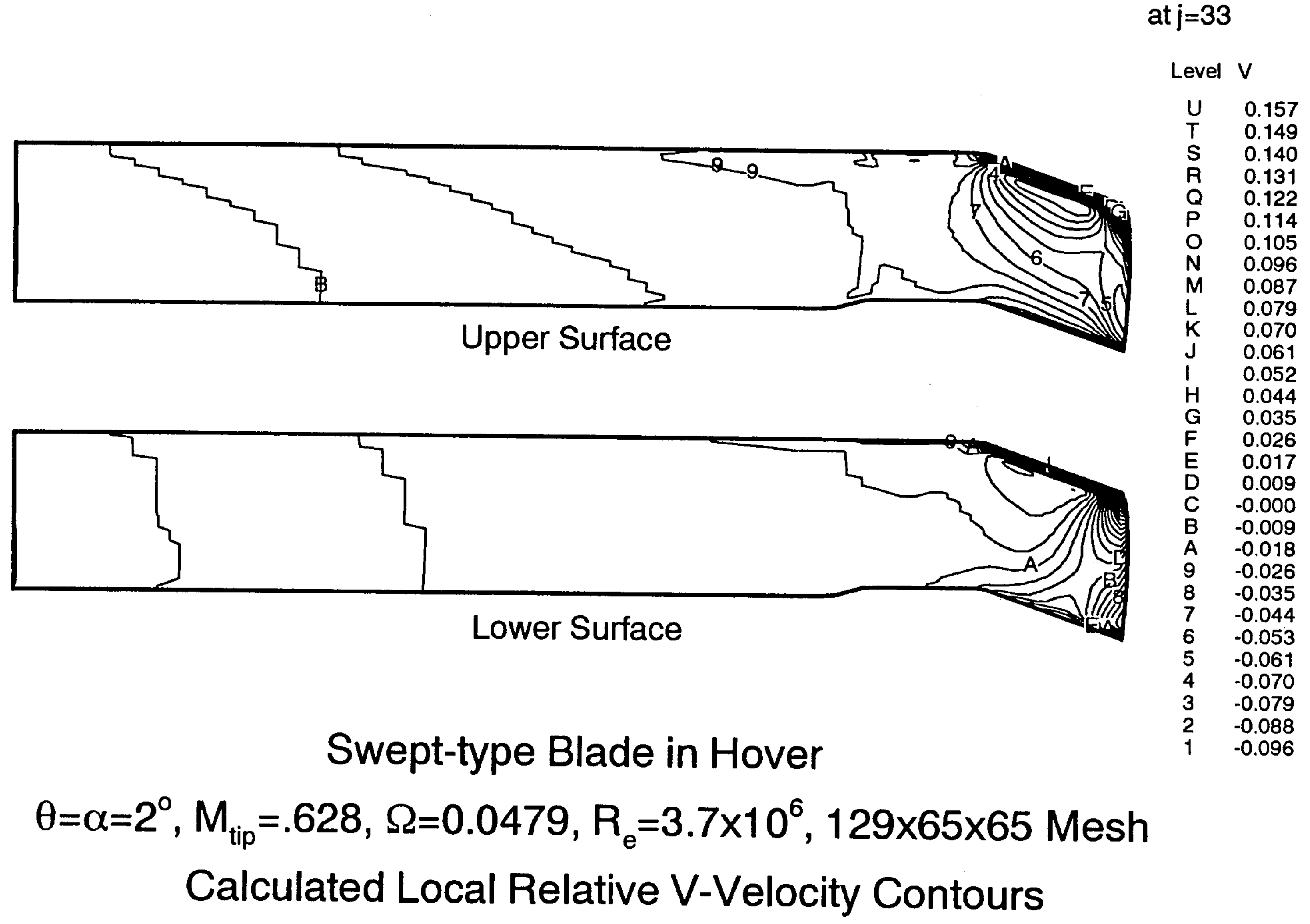

Figure 102. Calculated local relative V-velocity contours for swept-blade in hover.

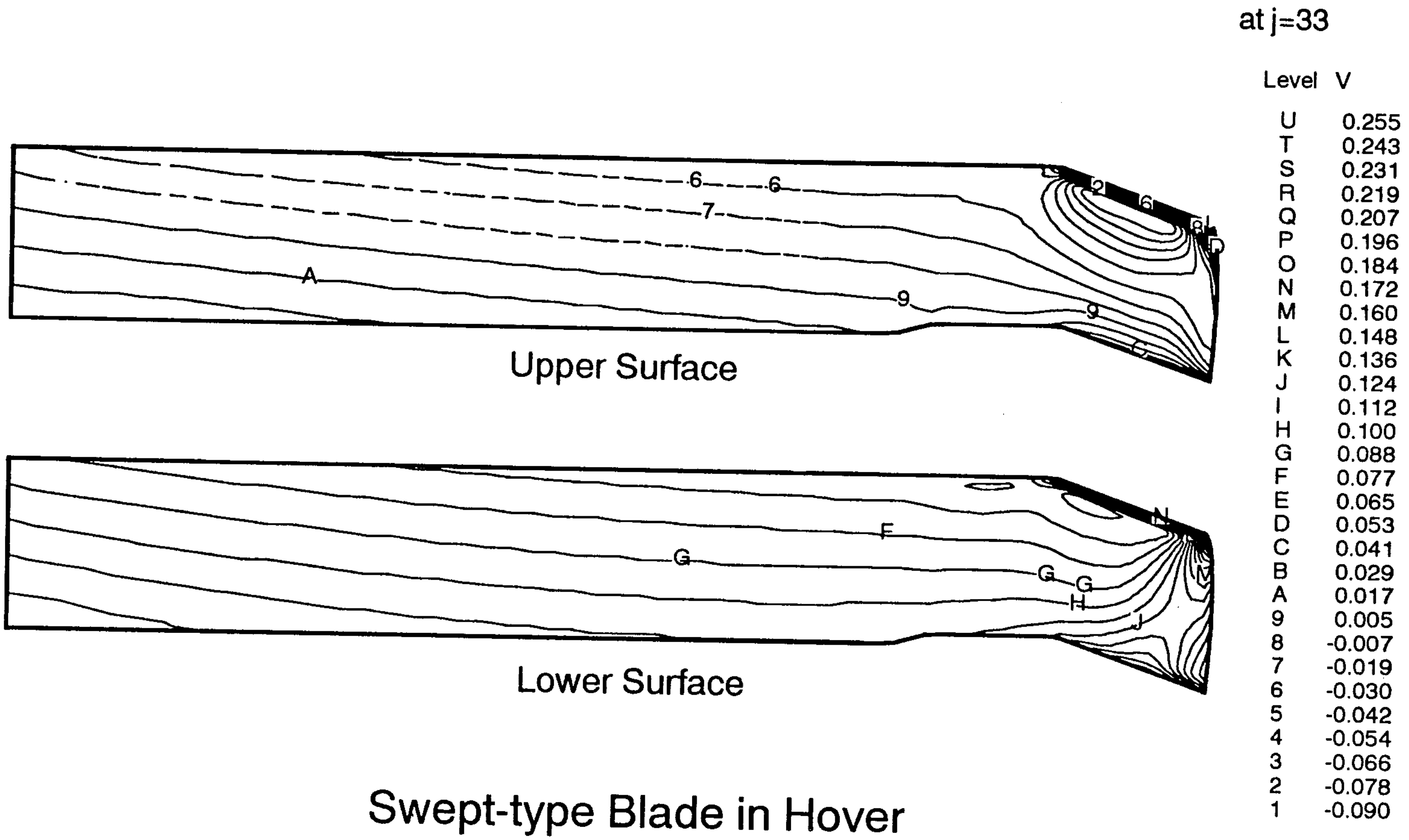

Swept-type Blade in Hover

$\theta=\alpha=2^{\circ}$, $M_{tip}=.628$, $\Omega=0.0479$, $R_e=3.7\times10^6$, 129x65x65 Mesh

Calculated Local Absolute V-Velocity Contours

Figure 103. Calculated local absolute V-velocity contours for swept-blade in hover.

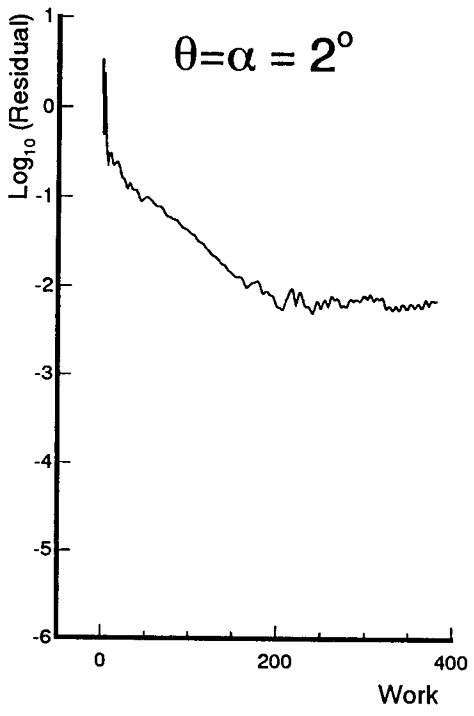

Swept-type Blade in Hover

M_{tip}=.628, Ω=0.0479, R_e=3.7x10^6, 129x65x65 Mesh

Convergence History in terms of Residual

Figure 104. Convergence history in terms of residuals for swept-blade in hover.

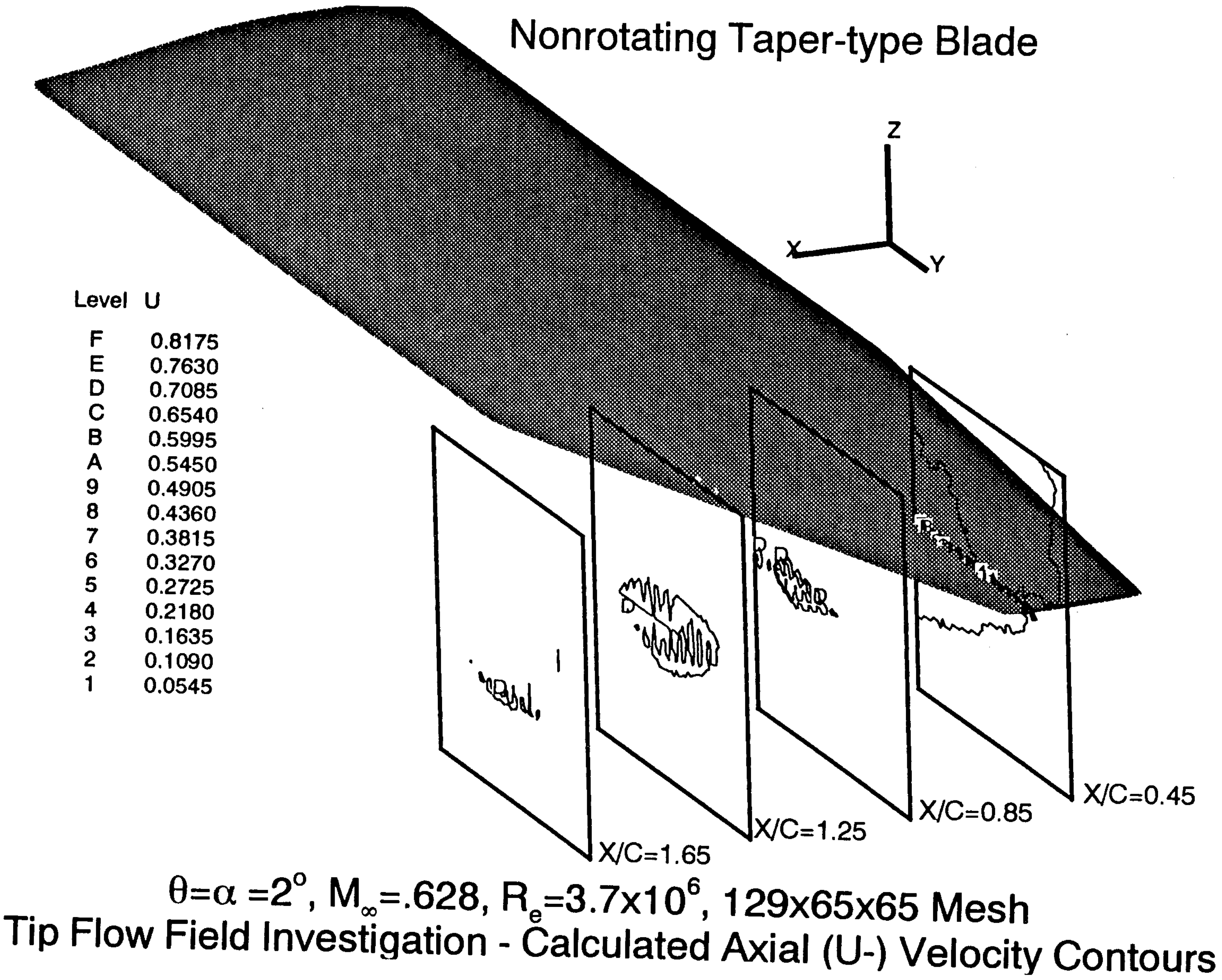

Figure 105. Calculated tip flow field in terms of axial velocity for nonrotating taper-blade.

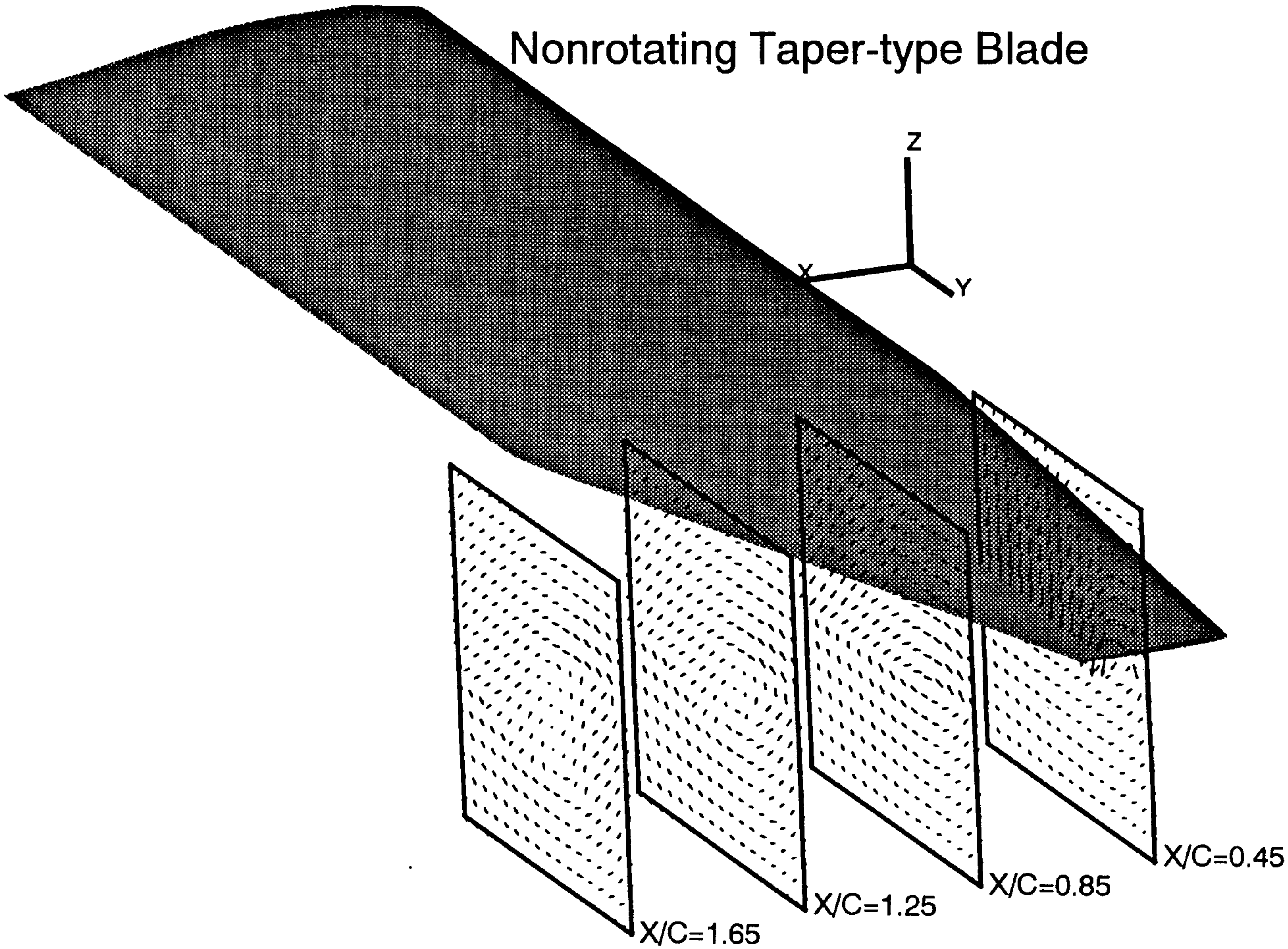

$\theta=\alpha=2^{\circ}$, $M_{\infty}=.628$, $R_e=3.7\times10^{6}$, 129x65x65 Mesh
Tip Flow Field Investigation - Calculated V-W Velocity Vectors

Figure 106. Calculated tip flow field in terms of crossflow velocity vector for nonrotating taper-blade.

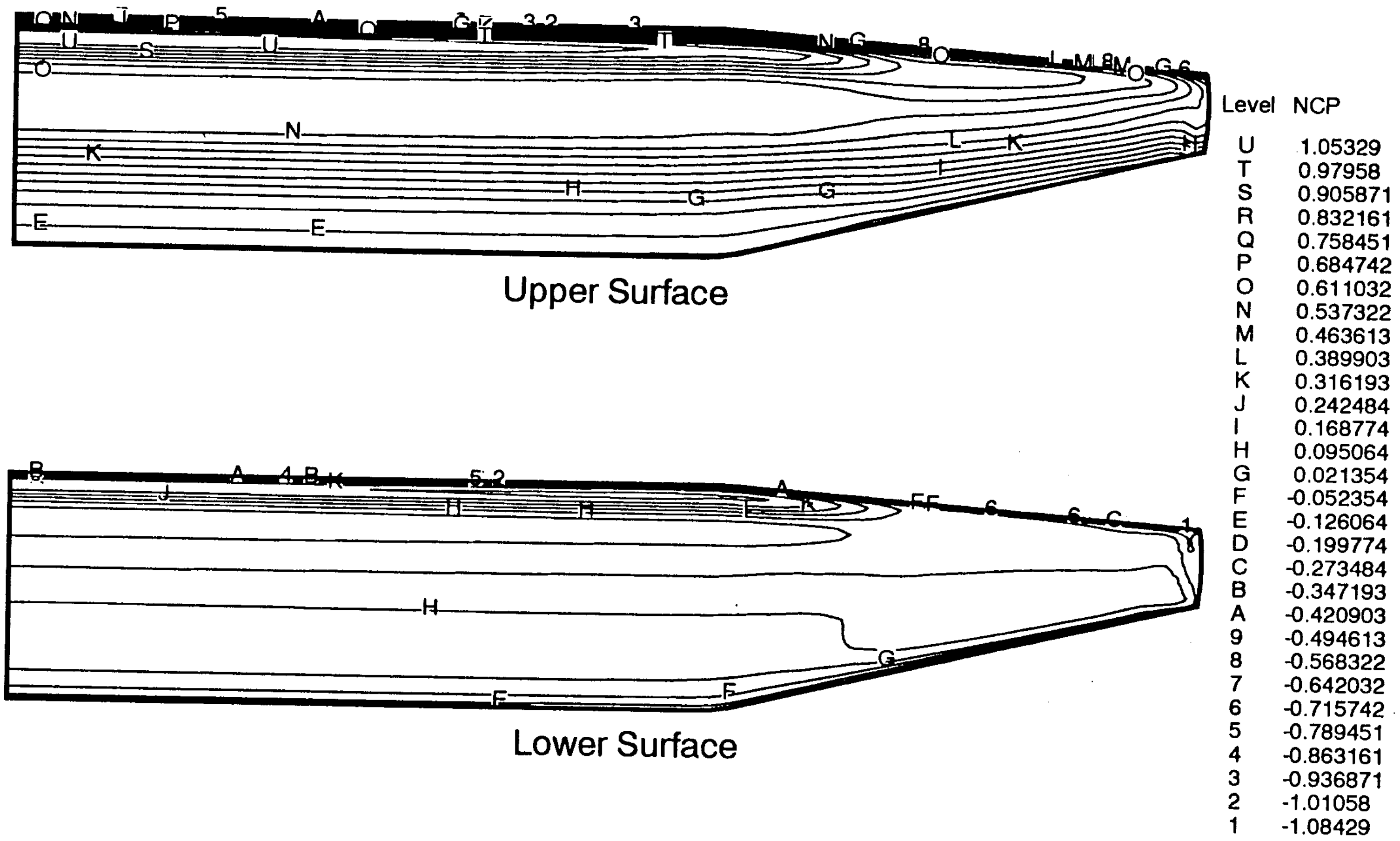

Level	NCP
U	1.05329
T	0.97958
S	0.905871
R	0.832161
Q	0.758451
P	0.684742
O	0.611032
N	0.537322
M	0.463613
L	0.389903
K	0.316193
J	0.242484
I	0.168774
H	0.095064
G	0.021354
F	-0.052354
E	-0.126064
D	-0.199774
C	-0.273484
B	-0.347193
A	-0.420903
9	-0.494613
8	-0.568322
7	-0.642032
6	-0.715742
5	-0.789451
4	-0.863161
3	-0.936871
2	-1.01058
1	-1.08429

Nonrotating Taper-type Blade

$\theta=\alpha=2^{\circ}$, $M_{\infty}=.628$, $R_e=3.7\times10^{6}$, 129x65x65 Mesh

Calculated Surface Pressure Coefficient Contours

Figure 107. Calculated surface pressure coefficients for nonrotating taper-blade.

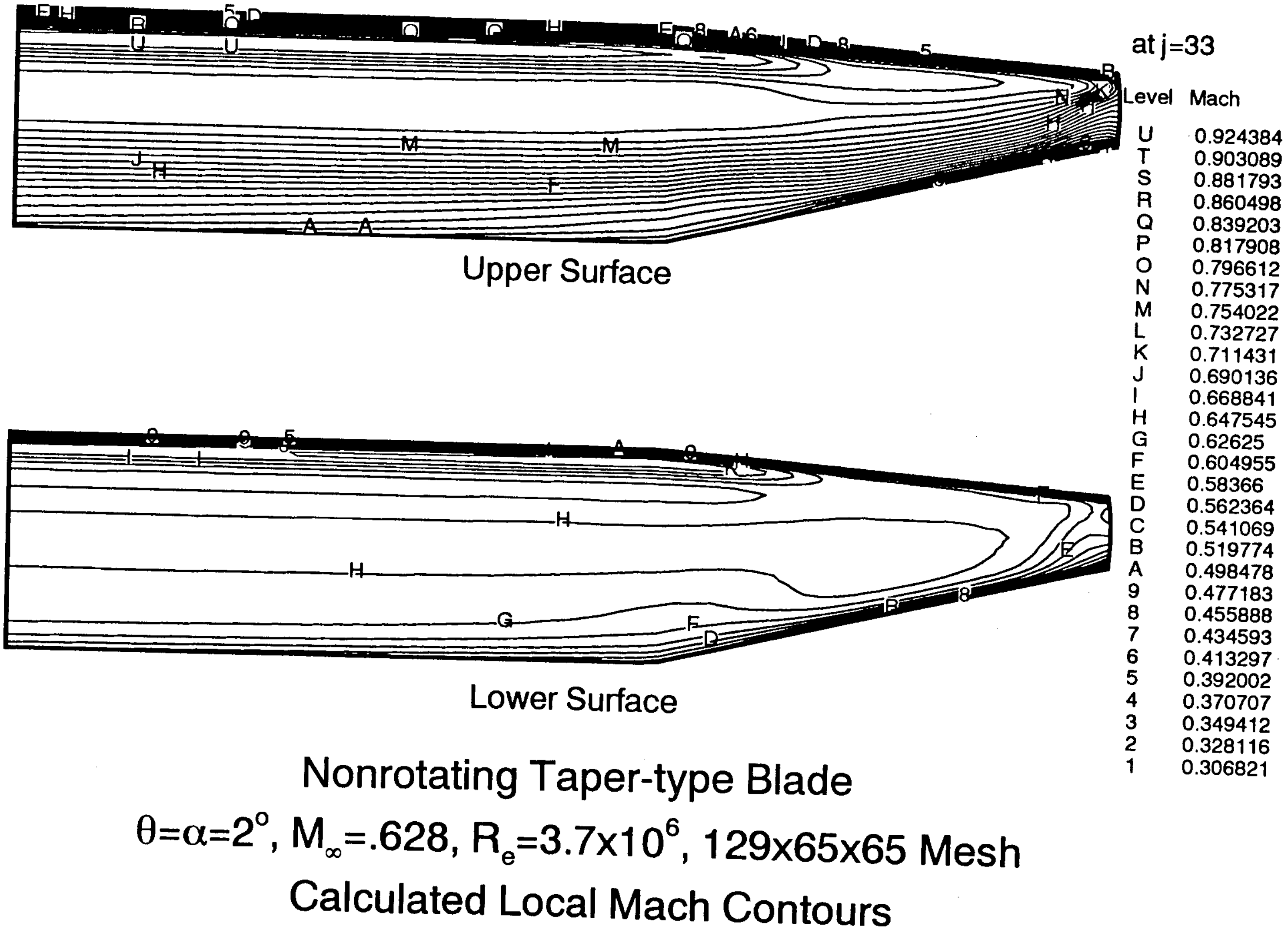

Figure 108. Calculated local Mach contours for nonrotating taper-blade.

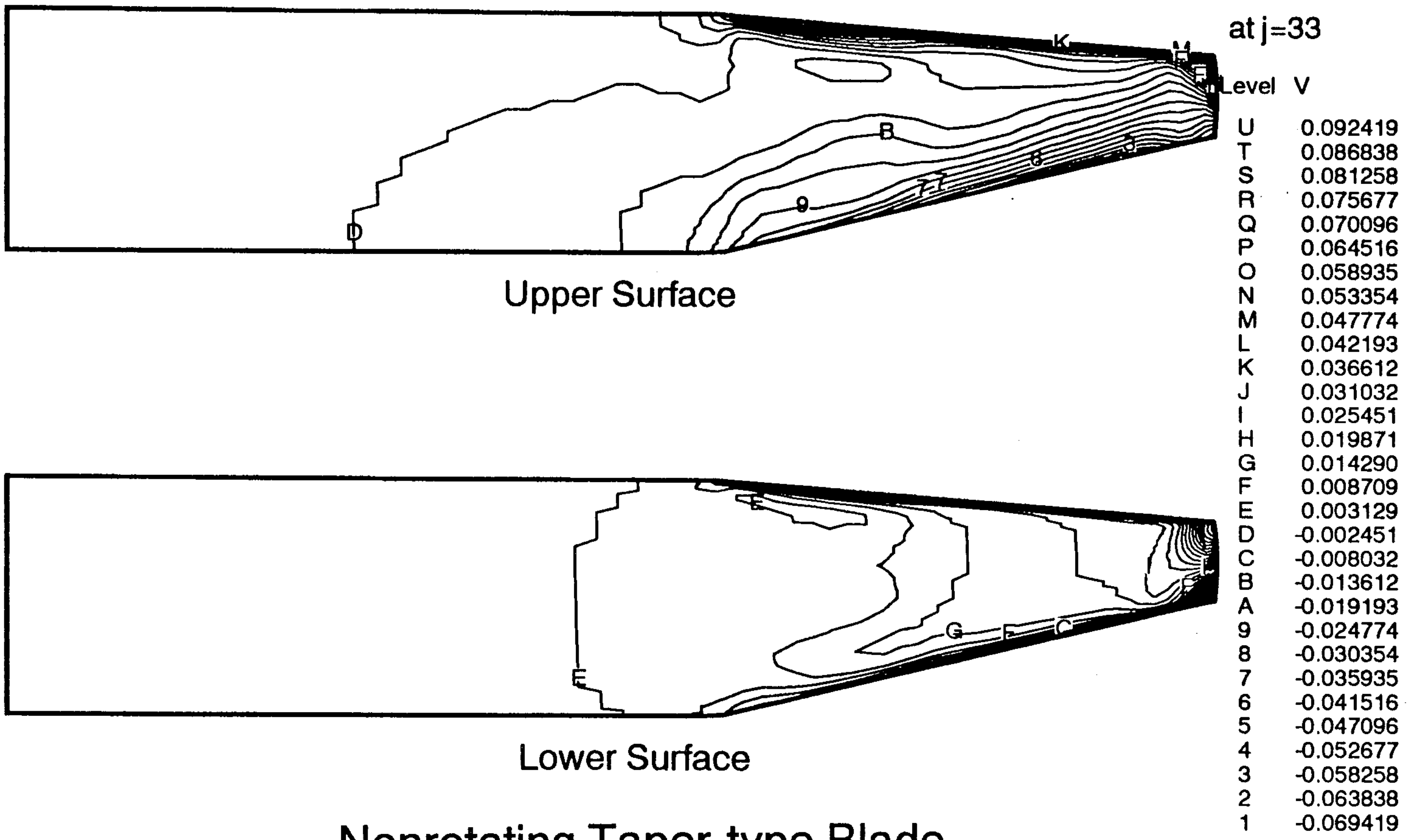

Upper Surface

Lower Surface

Nonrotating Taper-type Blade

$\theta=\alpha=2^{\circ}$, $M_{\infty}=.628$, $R_e=3.7\times10^6$, 129x65x65 Mesh

Calculated V-Velocity Contours

Figure 109. Calculated local V-velocity contours for nonrotating taper-blade.

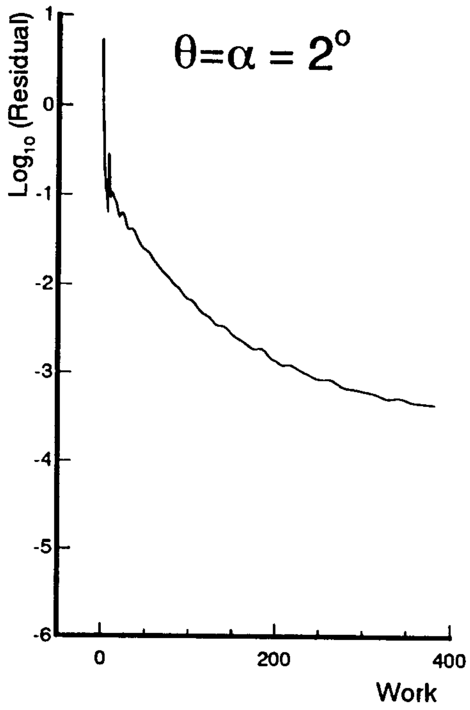

Nonrotating Taper-type Blade

M_∞=.628, R_e=3.7x10^6, 129x65x65 Mesh

Convergence History in terms of Residual

Figure 110. Convergence history in terms of residuals for nonrotating taper-blade.

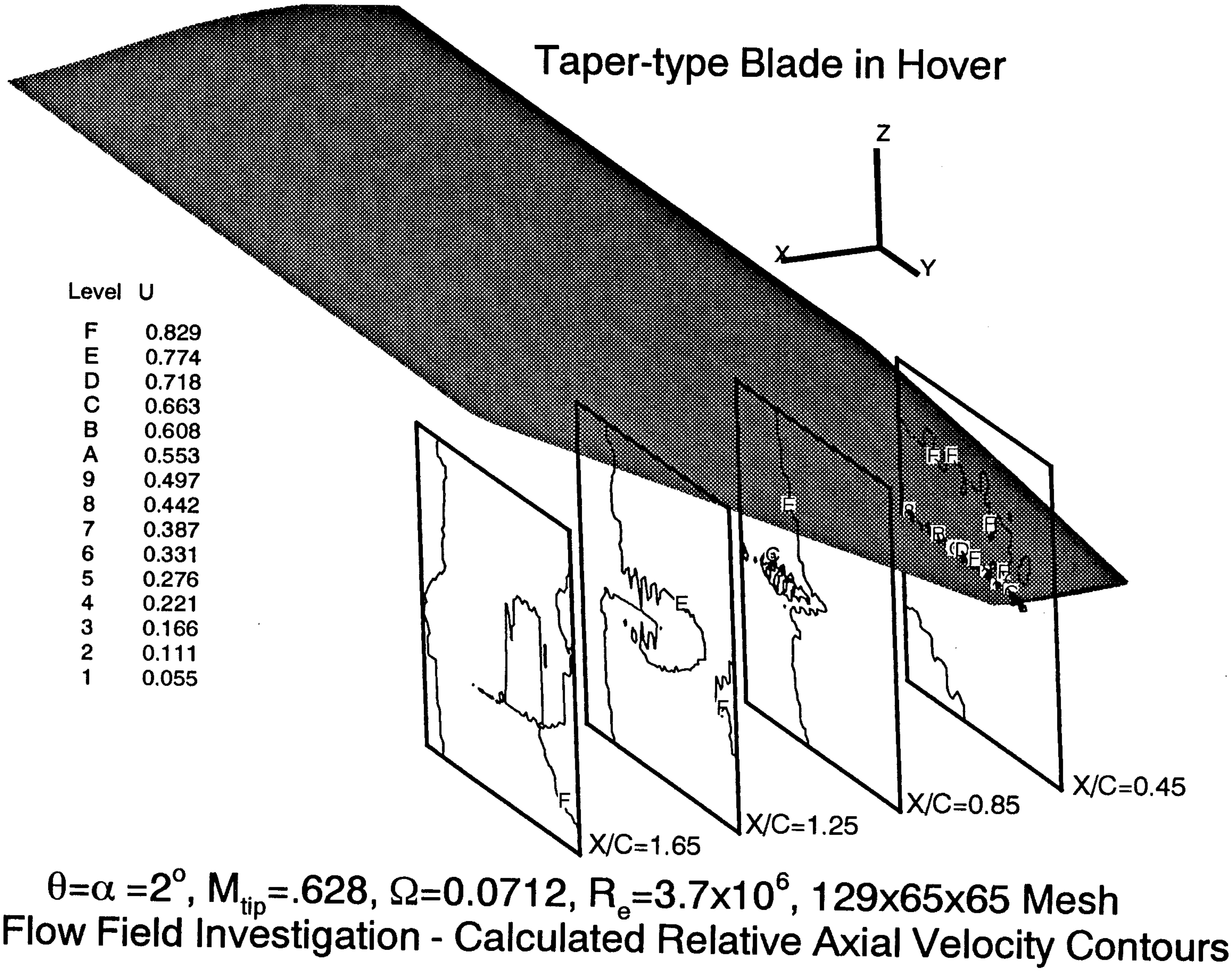

Figure 111. Calculated tip flow field in terms of relative axial velocity for taper-blade in hover.

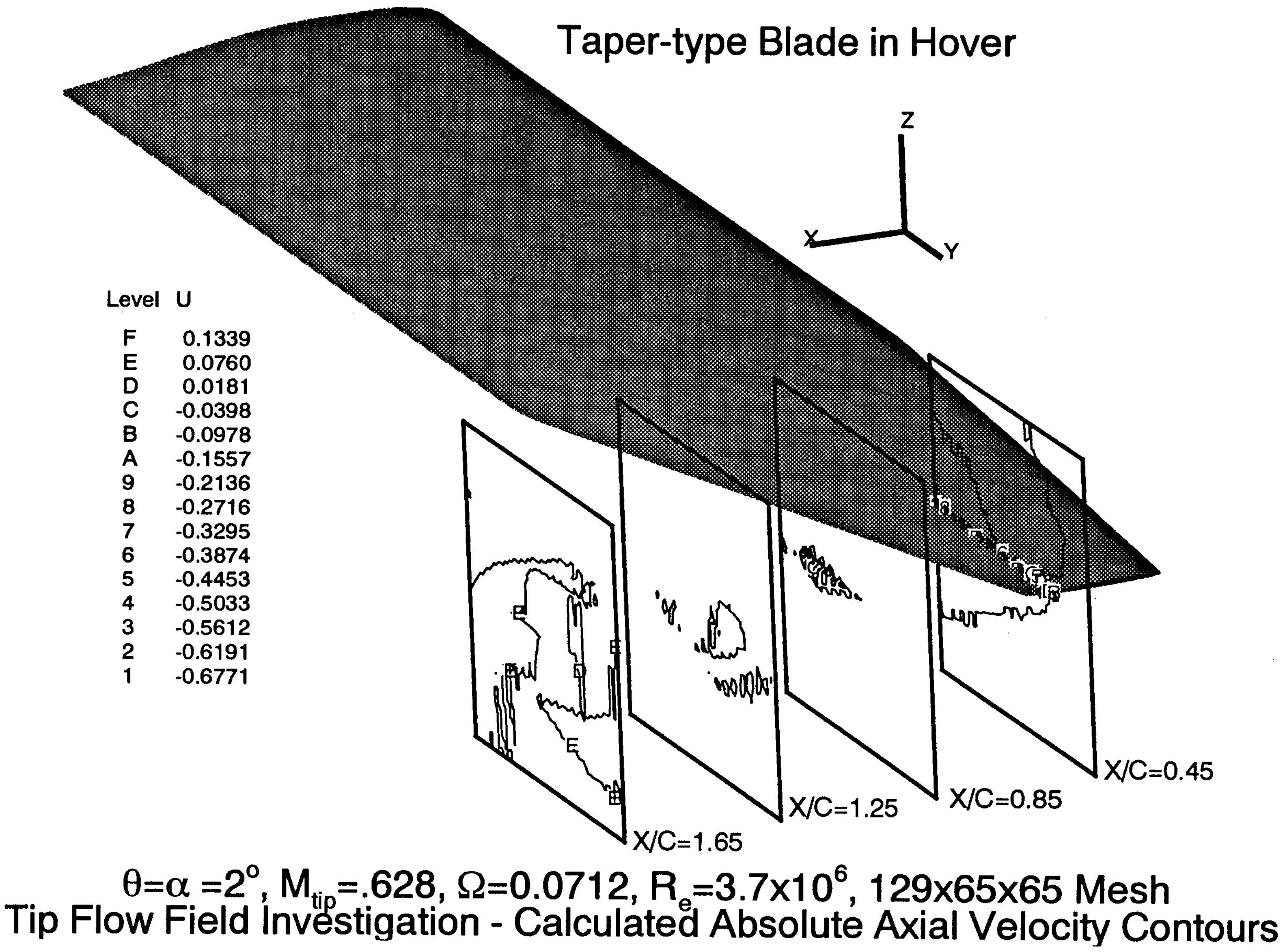

Figure 112. Calculated tip flow field in terms of absolute axial velocity for taper-blade in hover.

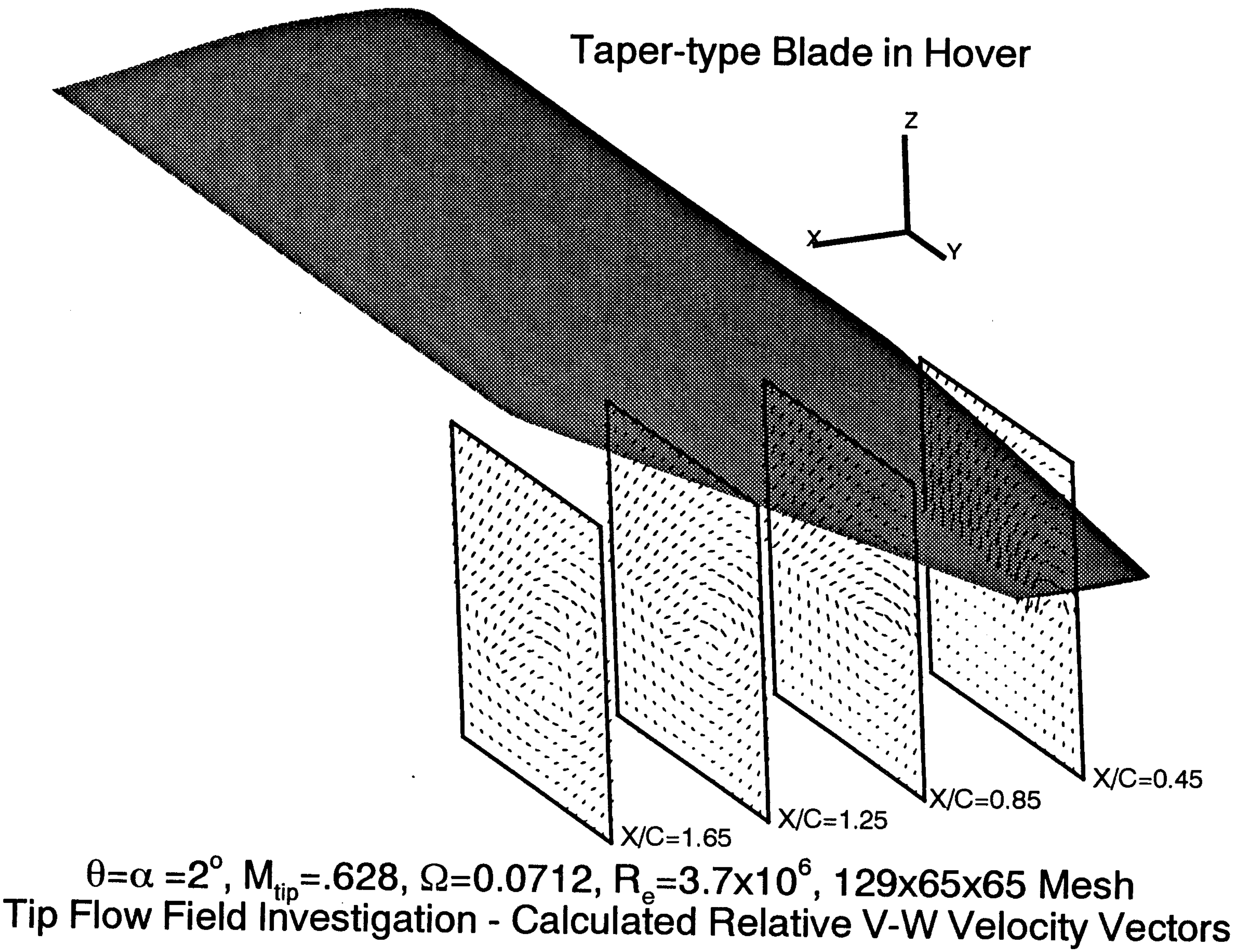

Figure 113. Calculated tip flow field in terms of relative crossflow velocity vector for taper-blade in hover.

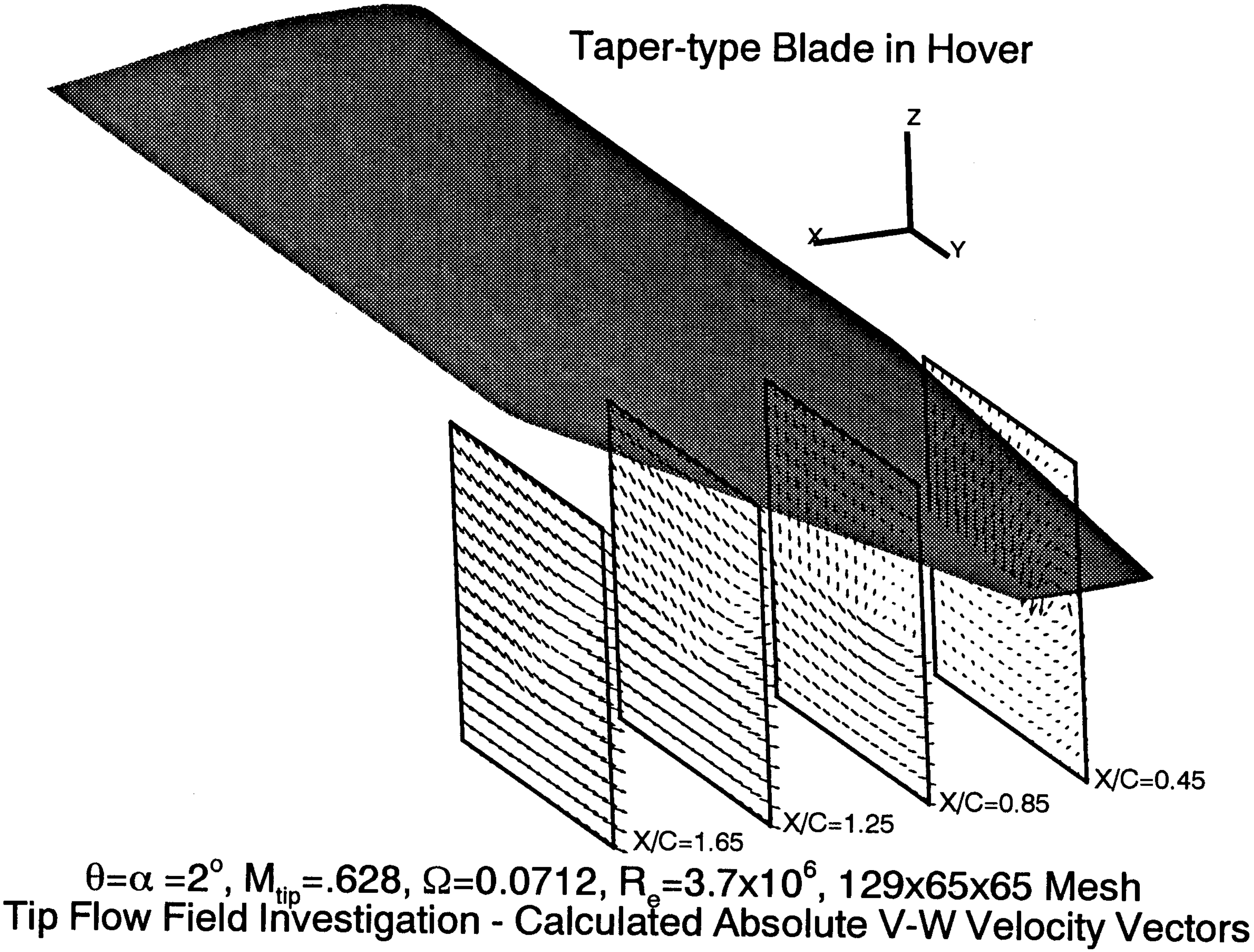

Figure 114. Calculated tip flow field in terms of absolute crossflow velocity vector for taper-blade in hover.

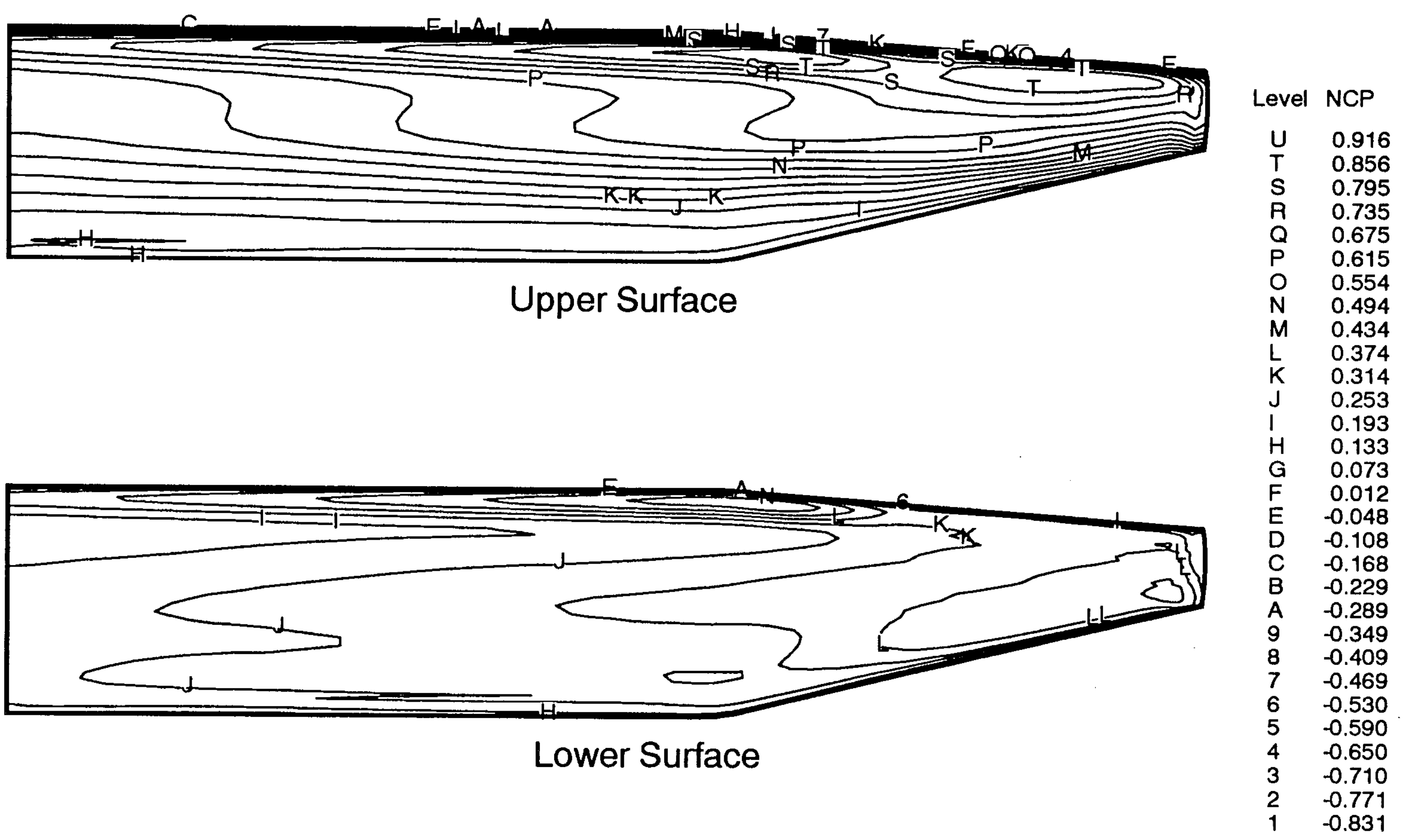

Level	NCP
U	0.916
T	0.856
S	0.795
R	0.735
Q	0.675
P	0.615
O	0.554
N	0.494
M	0.434
L	0.374
K	0.314
J	0.253
I	0.193
H	0.133
G	0.073
F	0.012
E	-0.048
D	-0.108
C	-0.168
B	-0.229
A	-0.289
9	-0.349
8	-0.409
7	-0.469
6	-0.530
5	-0.590
4	-0.650
3	-0.710
2	-0.771
1	-0.831

Taper-type Blade in Hover

$\theta=\alpha=2^{\circ}$, $M_{tip}=.628$, $\Omega=0.0712$, $R_e=3.7\times10^6$, 129x65x65 Mesh

Calculated Surface Pressure Coefficient Contours

Figure 115. Calculated surface pressure coefficients for taper-blade in hover.

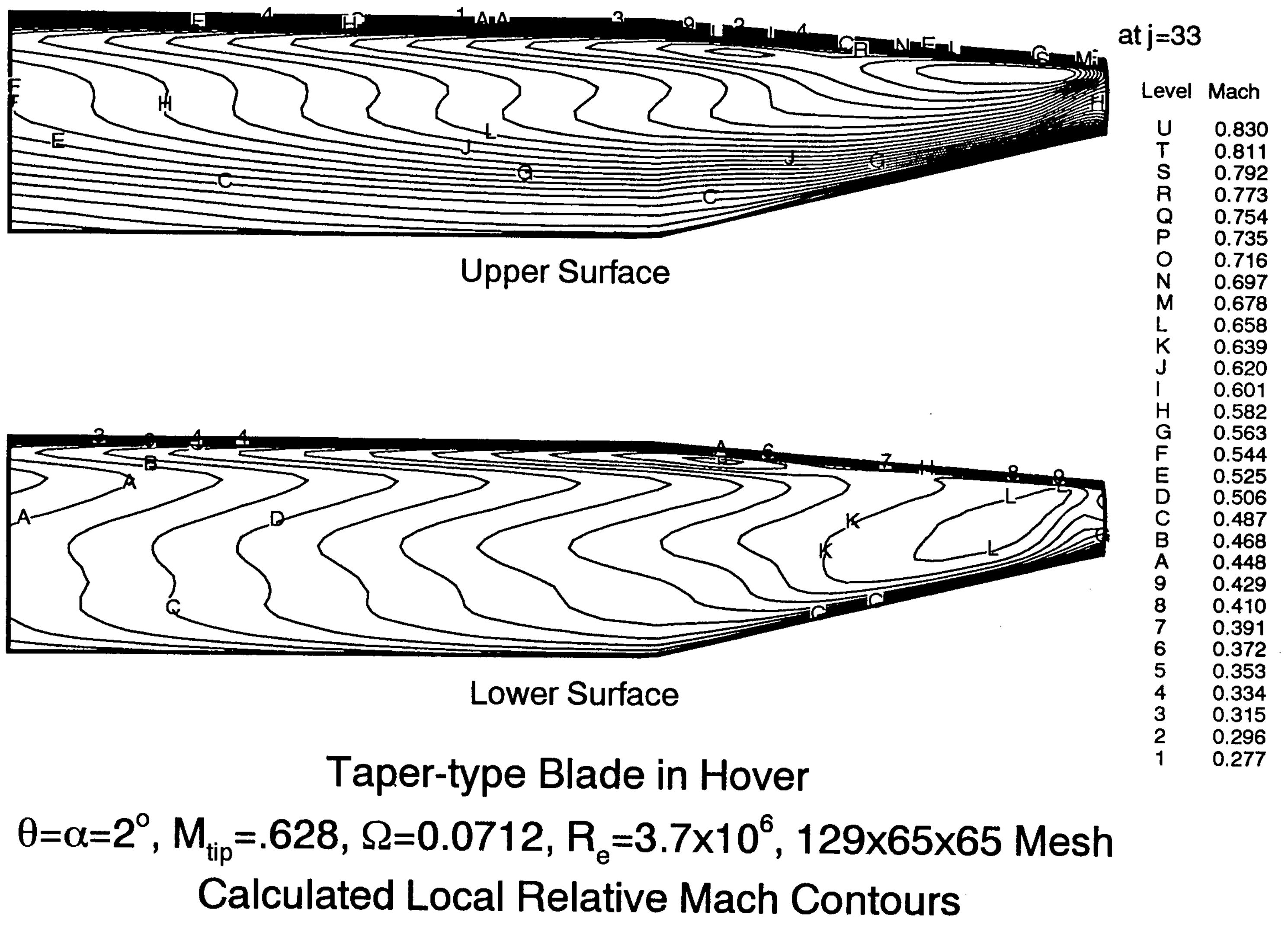

Taper-type Blade in Hover

$\theta=\alpha=2^{\circ}$, $M_{tip}=.628$, $\Omega=0.0712$, $R_e=3.7\times10^6$, 129x65x65 Mesh

Calculated Local Relative Mach Contours

Figure 116. Calculated local relative Mach contours for taper-blade in hover.

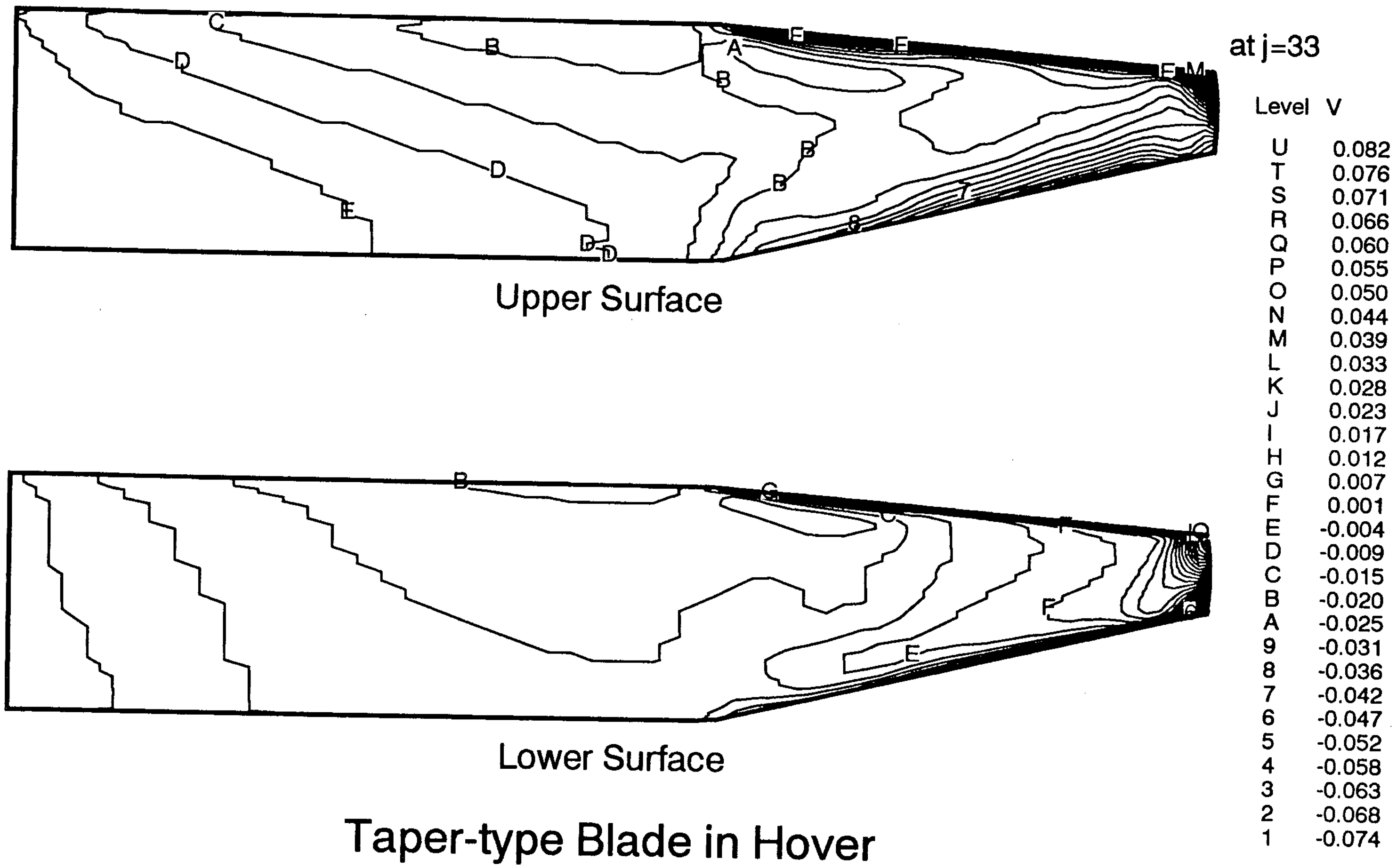

Taper-type Blade in Hover

$\theta=\alpha=2^{\circ}$, $M_{tip}=.628$, $\Omega=0.0712$, $R_e=3.7\times10^6$, 129x65x65 Mesh

Calculated Local Relative V-Velocity Contours

Figure 117. Calculated local relative V-velocity contours for taper-blade in hover.

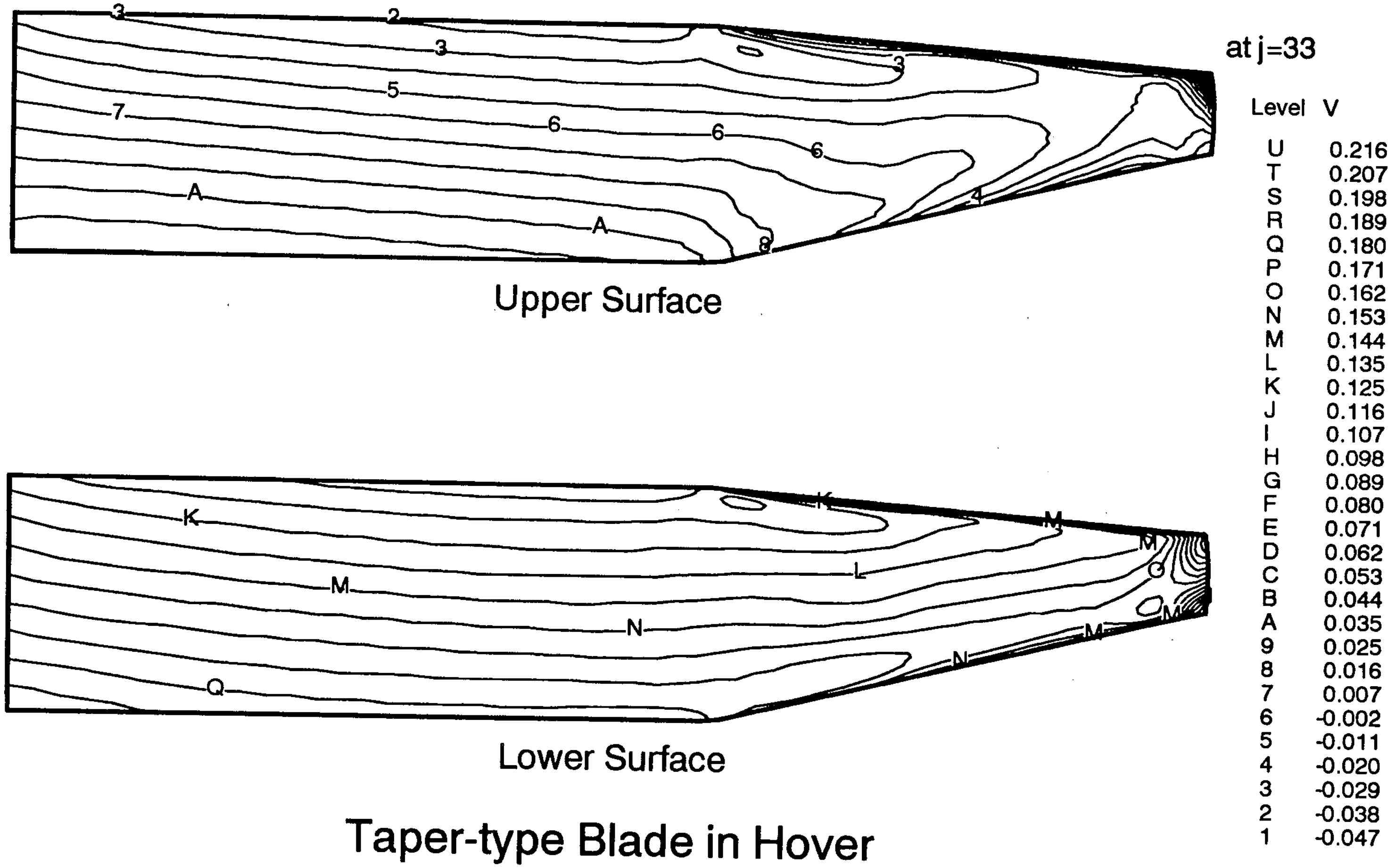

Taper-type Blade in Hover

$\theta=\alpha=2^{\circ}$, $M_{tip}=.628$, $\Omega=0.0712$, $R_e=3.7\times10^6$, 129x65x65 Mesh

Calculated Local Absolute V-Velocity Contours

Figure 118. Calculated local absolute V-velocity contours for taper-blade in hover.

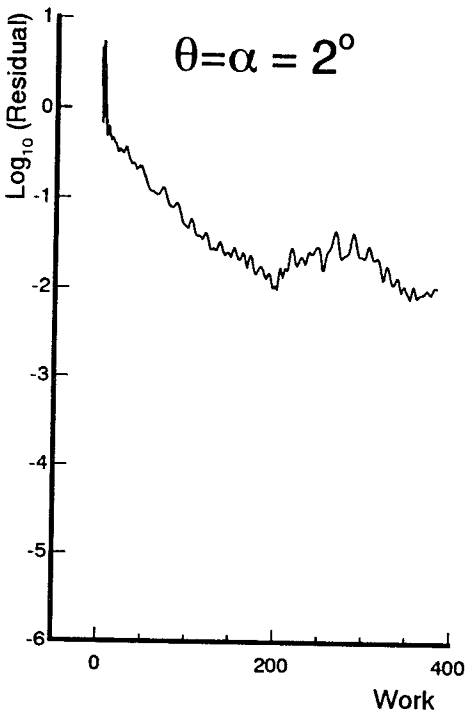

Taper-type Blade in Hover

M_{tip}=.628, Ω=0.0712, R_e=3.7x10^6, 129x65x65 Mesh

Convergence History in terms of Residual

Figure 119. Convergence history in terms of residuals for taper-blade in hover.

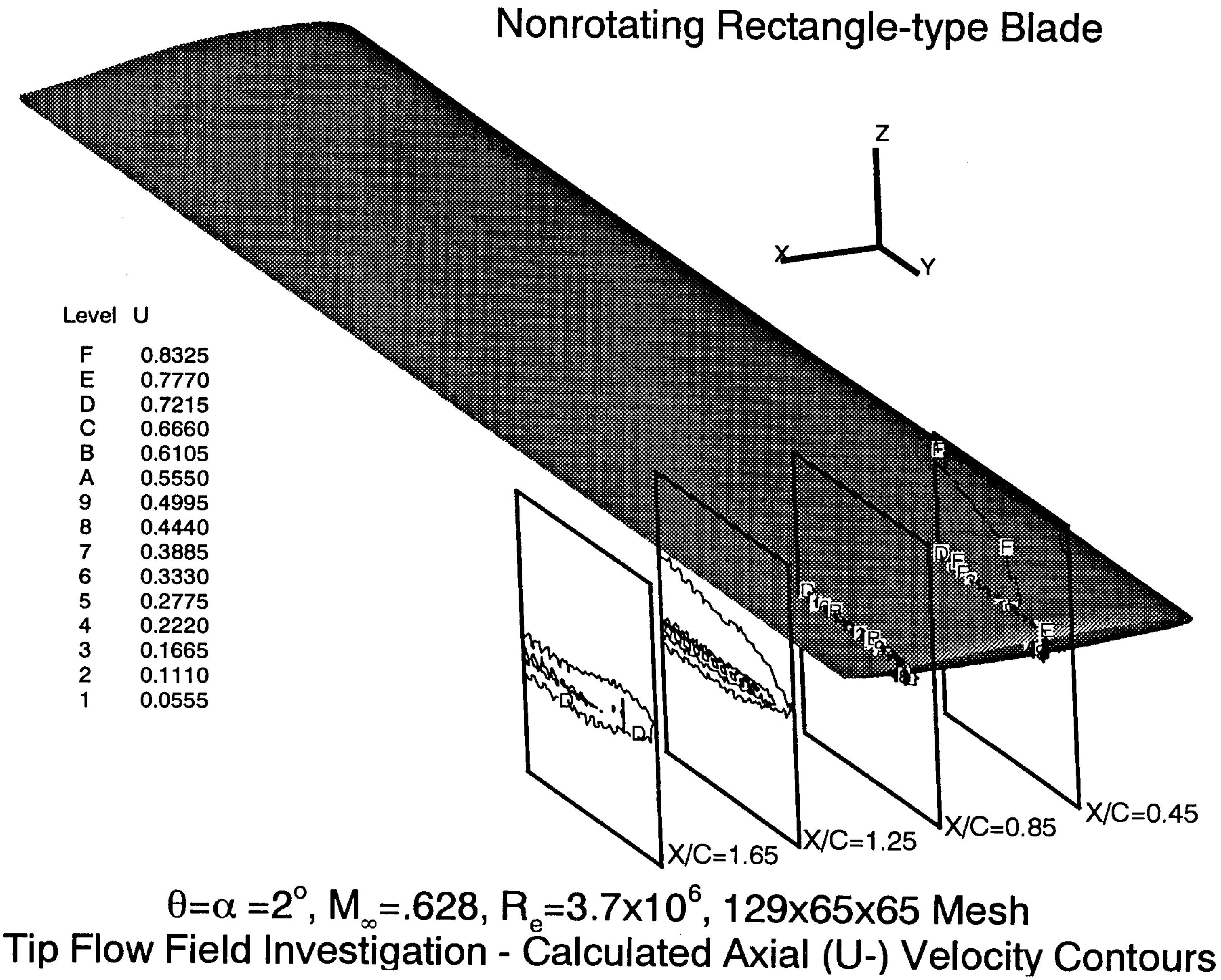

Figure 120. Calculated tip flow field in terms of axial velocity for nonrotating rectangle-blade.

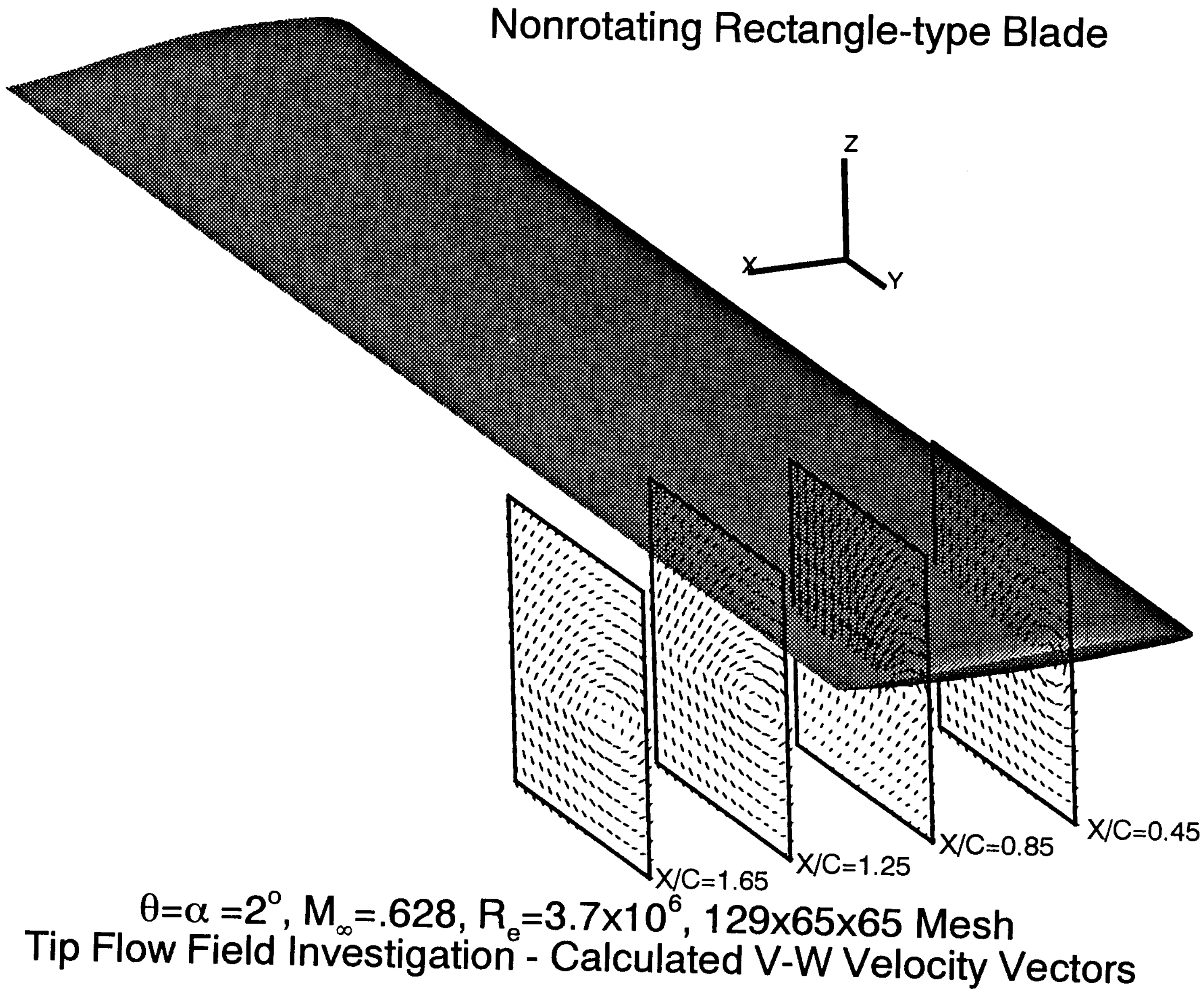

Figure 121. Calculated tip flow field in terms of crossflow velocity vector for nonrotating rectangle-blade.

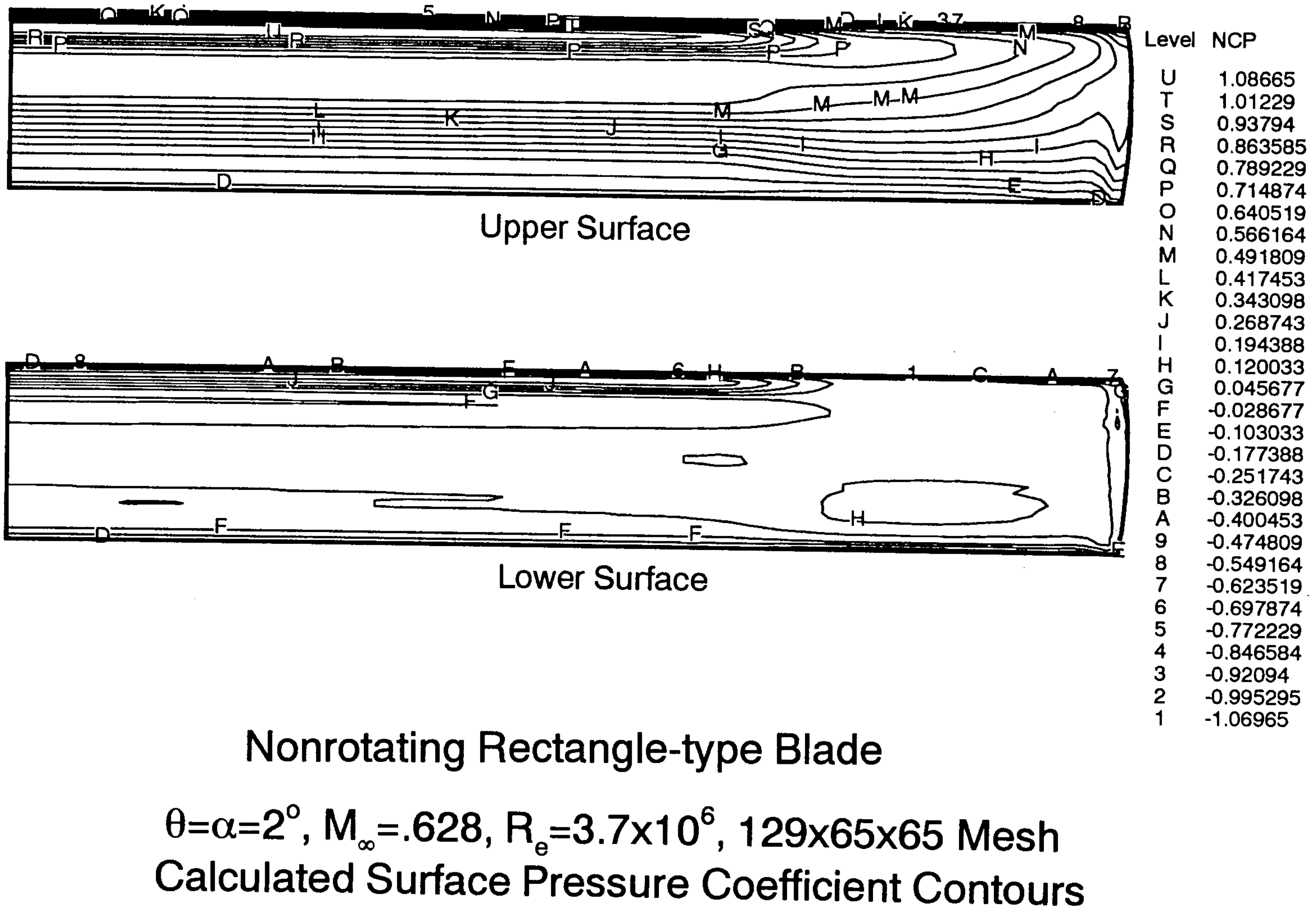

Figure 122. Calculated surface pressure coefficients for nonrotating rectangle-blade.

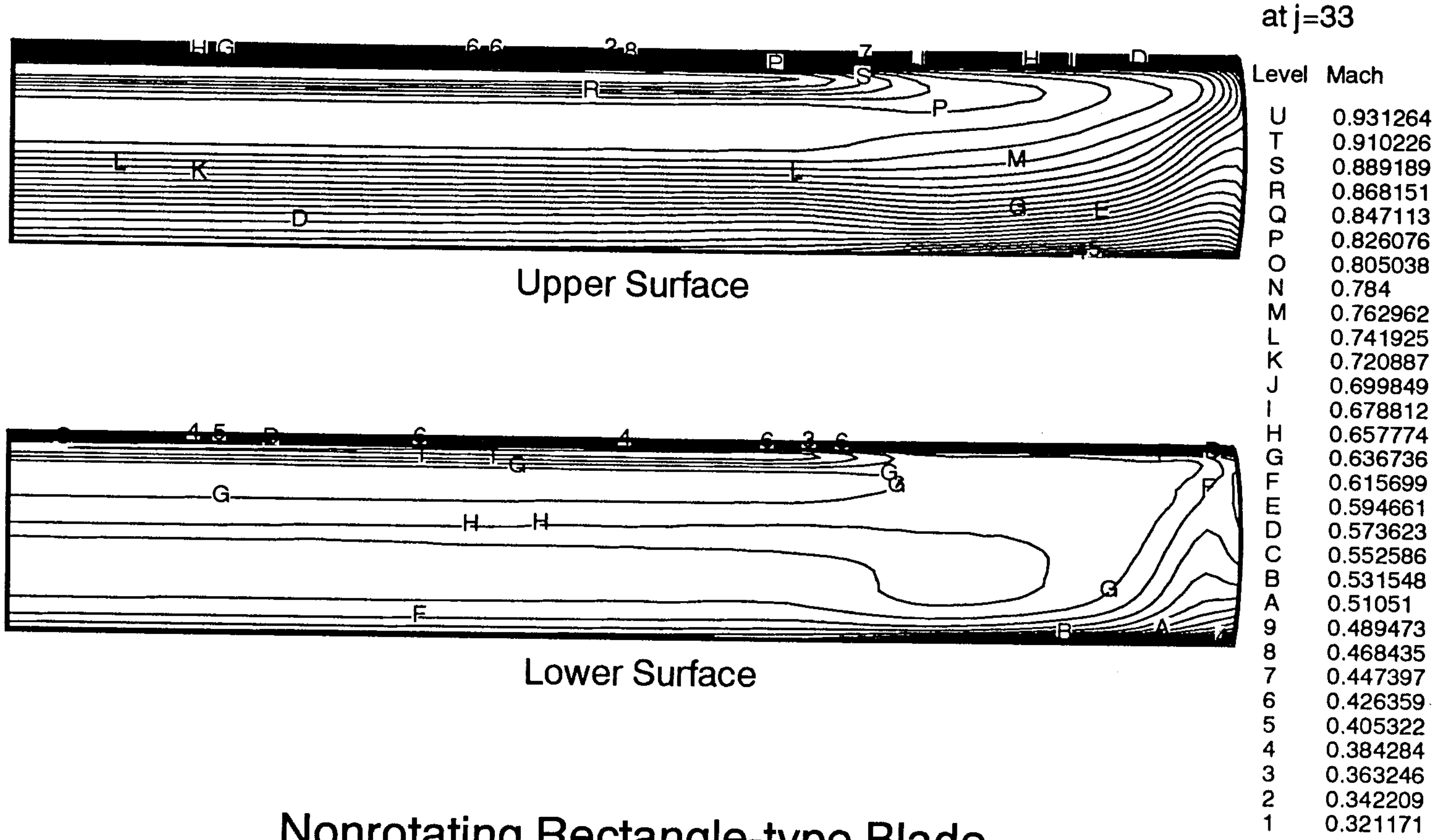

Upper Surface

Lower Surface

Nonrotating Rectangle-type Blade

$\theta=\alpha=2^{\circ}$, $M_{\infty}=.628$, $R_e=3.7\text{x}10^6$, 129x65x65 Mesh

Calculated Local Mach Contours

Figure 123. Calculated local Mach contours for nonrotating rectangle-blade.

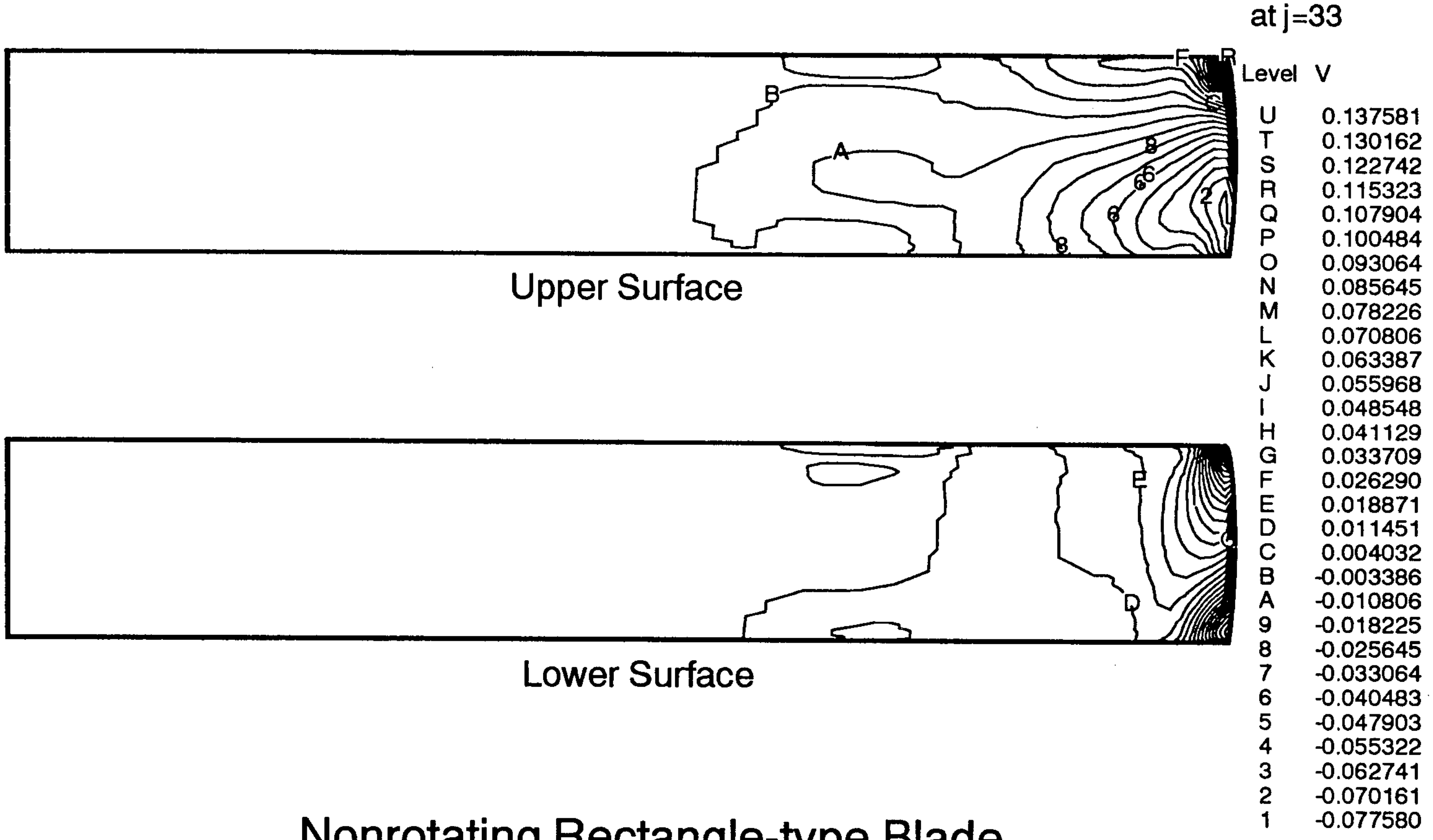

Nonrotating Rectangle-type Blade

$\theta=\alpha=2^{\circ}$, $M_{\infty}=.628$, $R_e=3.7\times10^6$, 129x65x65 Mesh

Calculated V-Velocity Contours

Figure 124. Calculated local V-velocity contours for nonrotating rectangle-blade.

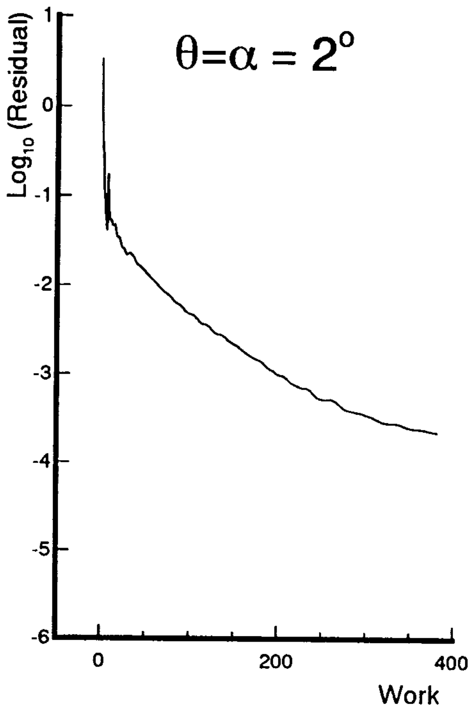

Nonrotating Rectangle-type Blade

M_∞=.628, R_e=3.7x10^6, 129x65x65 Mesh
Convergence History in terms of Residual

Figure 125. Convergence history in terms of residuals for nonrotating rectangle-blade.

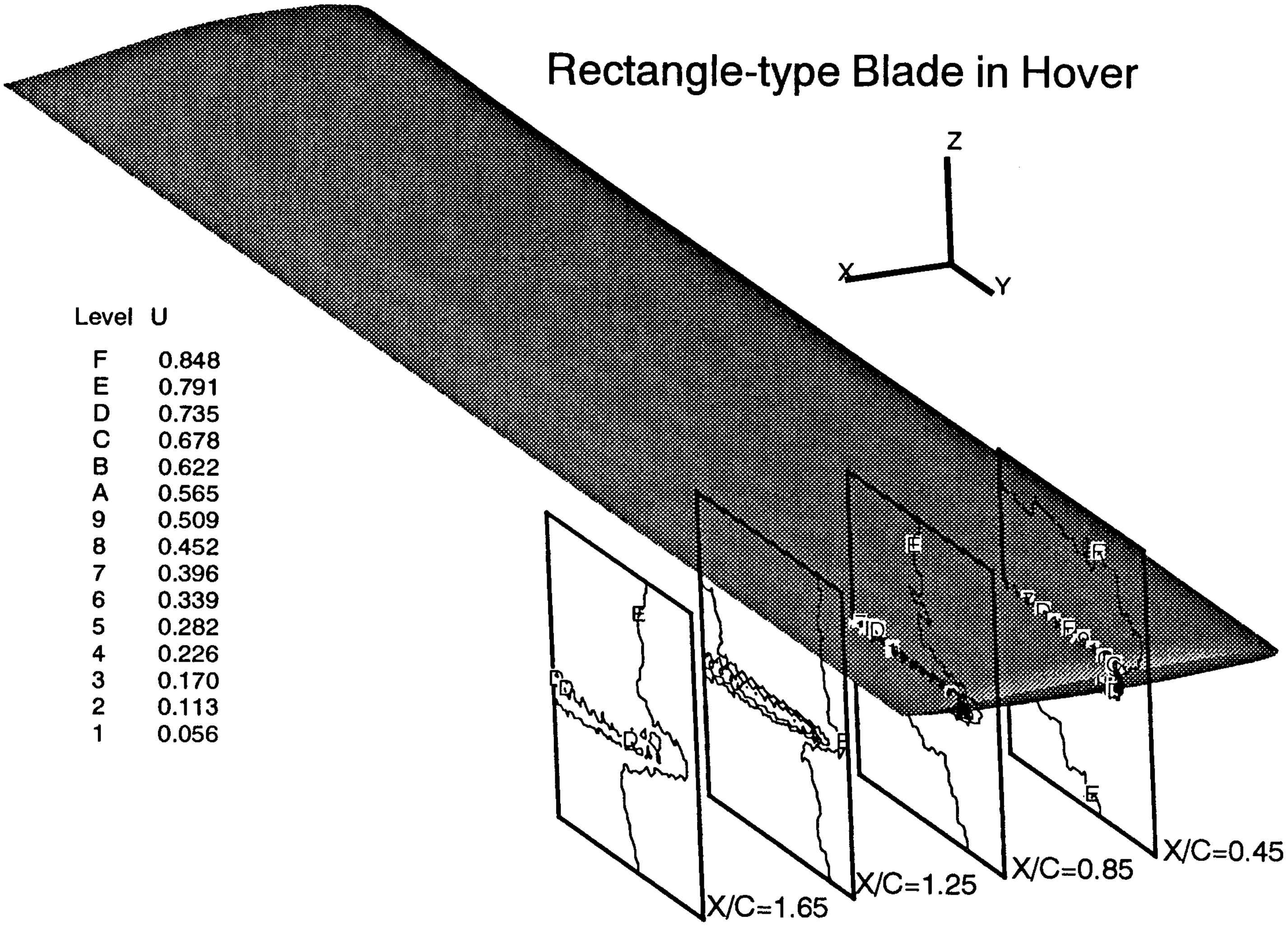

$\theta=\alpha=2^{o}$, $M_{tip}=.628$, $\Omega=0.0589$, $R_e=3.7\text{x}10^6$, 129x65x65 Mesh
Tip Flow Field Investigation - Calculated Relative Axial Velocity Contours

Figure 126. Calculated tip flow field in terms of relative axial velocity for rectangle-blade in hover.

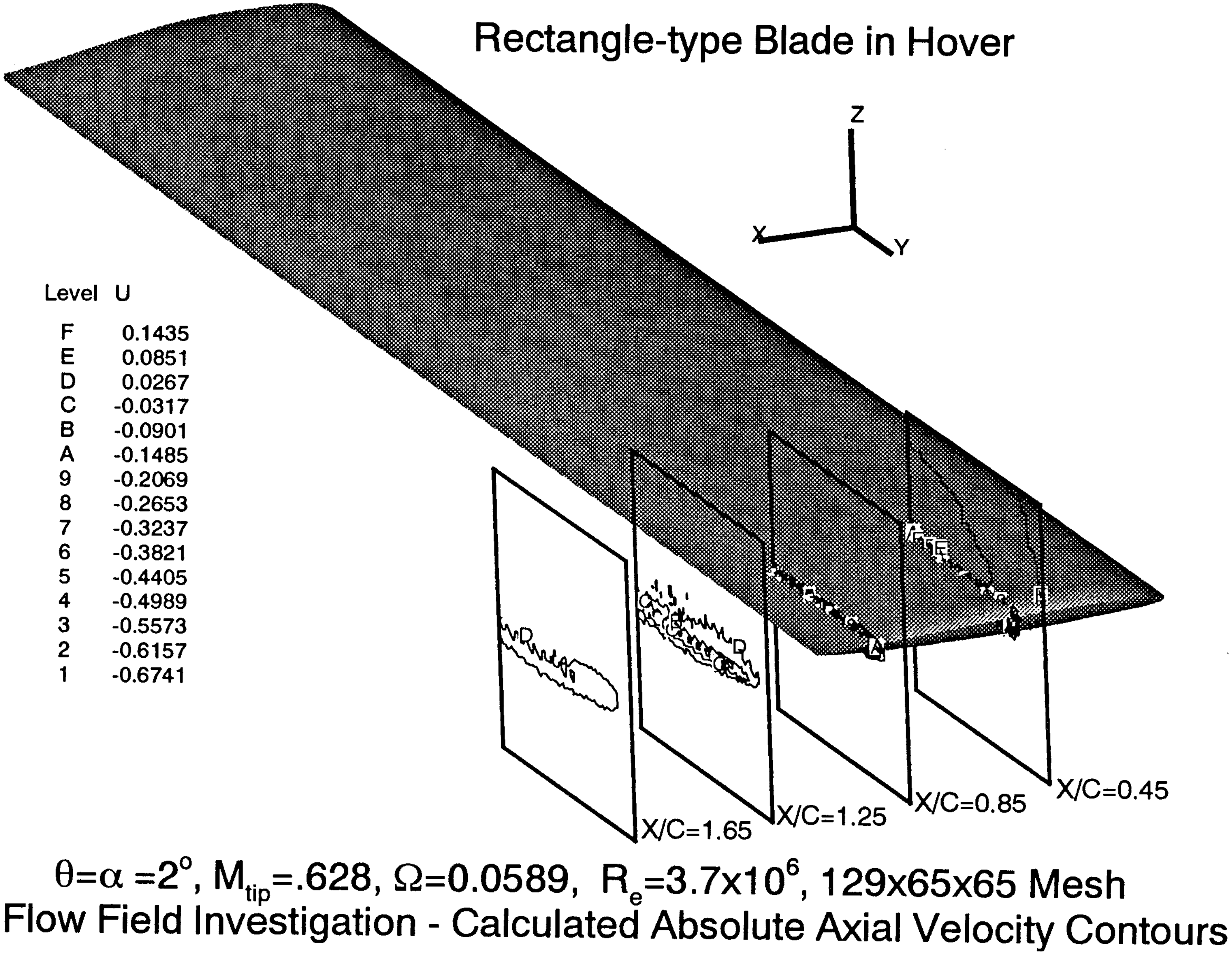

Figure 127. Calculated tip flow field in terms of absolute axial velocity for rectangle-blade in hover.

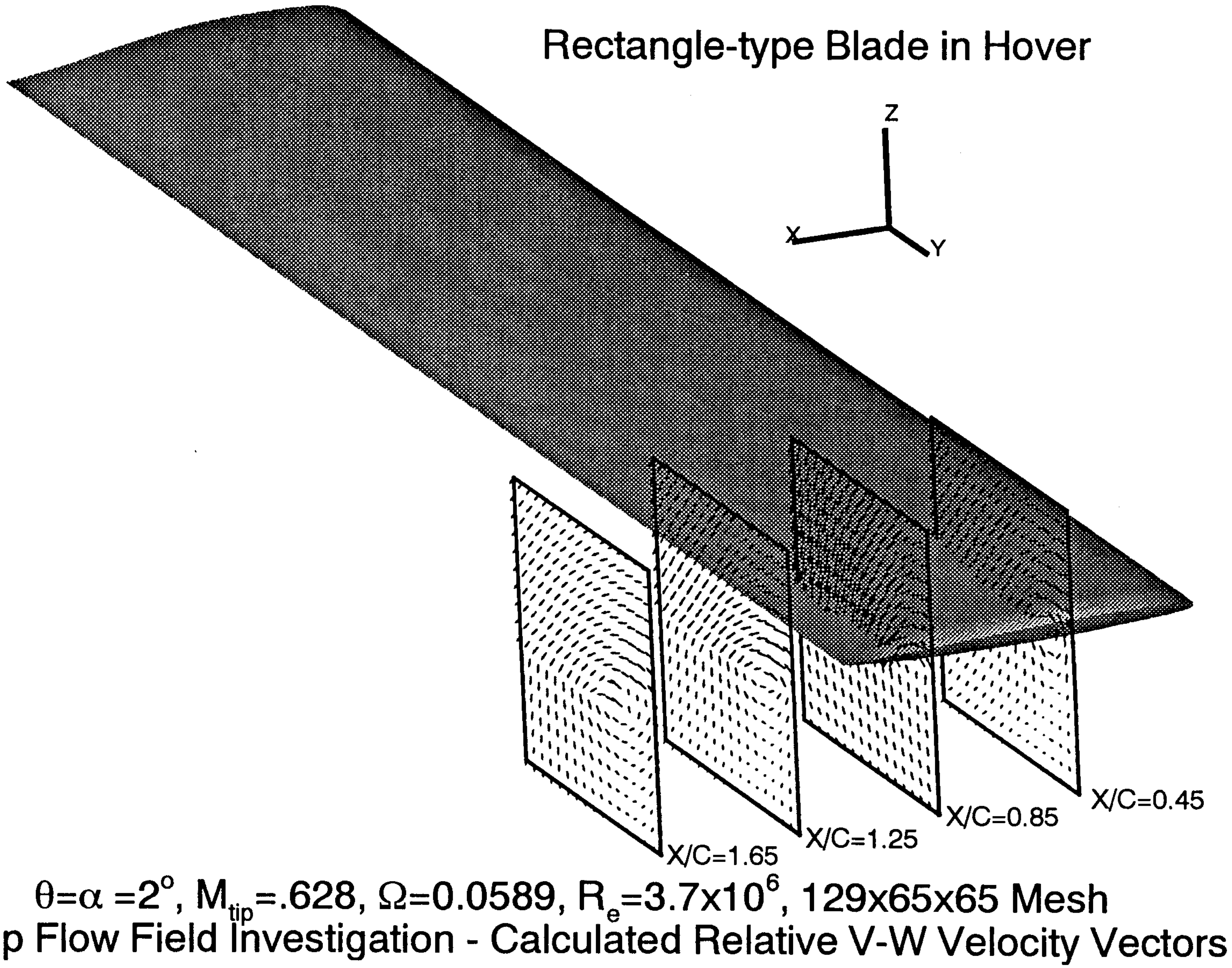

Figure 128. Calculated tip flow field in terms of relative crossflow velocity vector for rectangle-blade in hover.

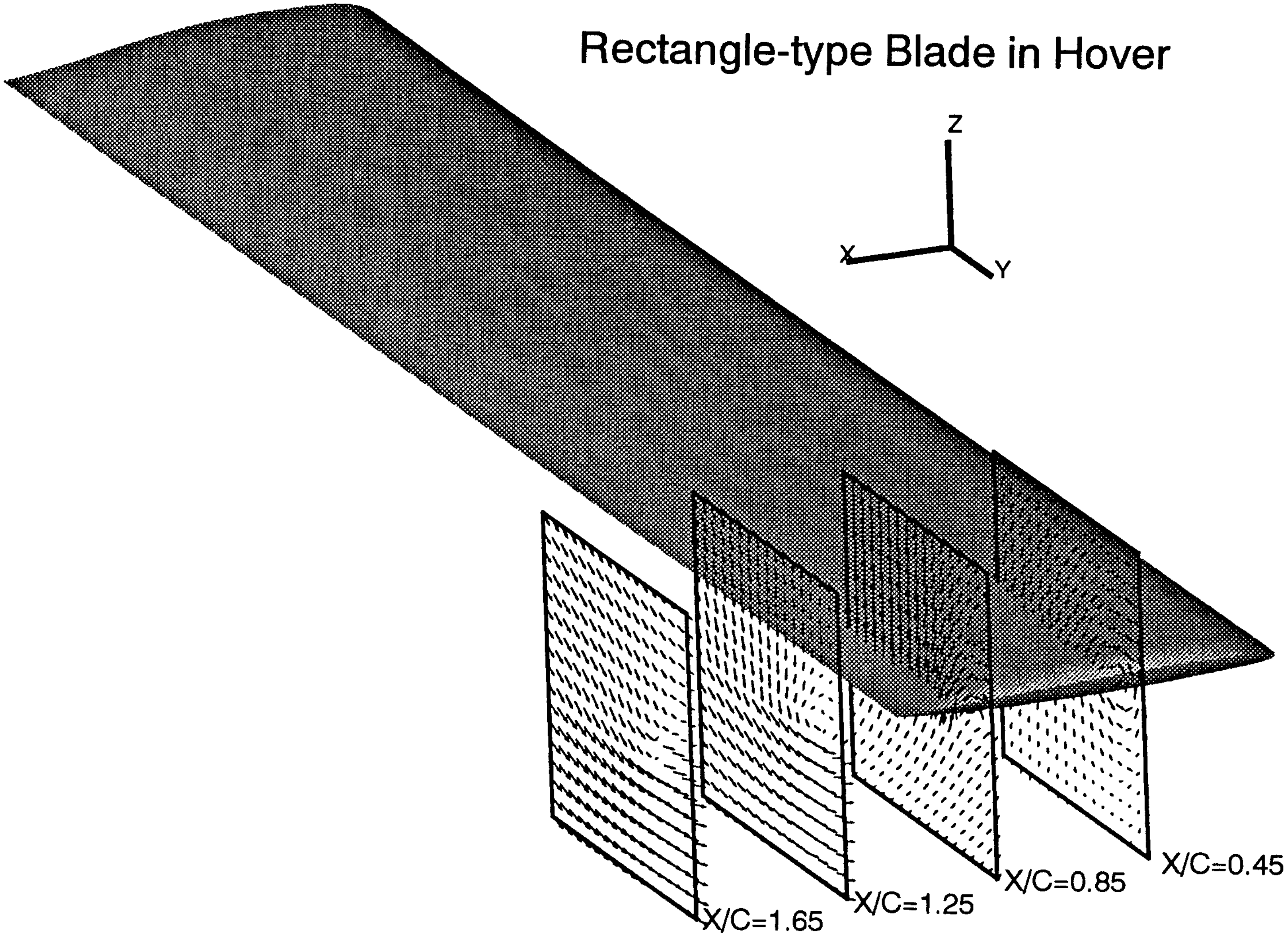

Rectangle-type Blade in Hover

$\theta=\alpha=2^{o}$, $M_{tip}=.628$, $\Omega=0.0589$, $R_e=3.7\text{x}10^6$, 129x65x65 Mesh

Tip Flow Field Investigation - Calculated Absolute V-W Velocity Vectors

Figure 129. Calculated tip flow field in terms of absolute crossflow velocity vector for rectangle-blade in hover.

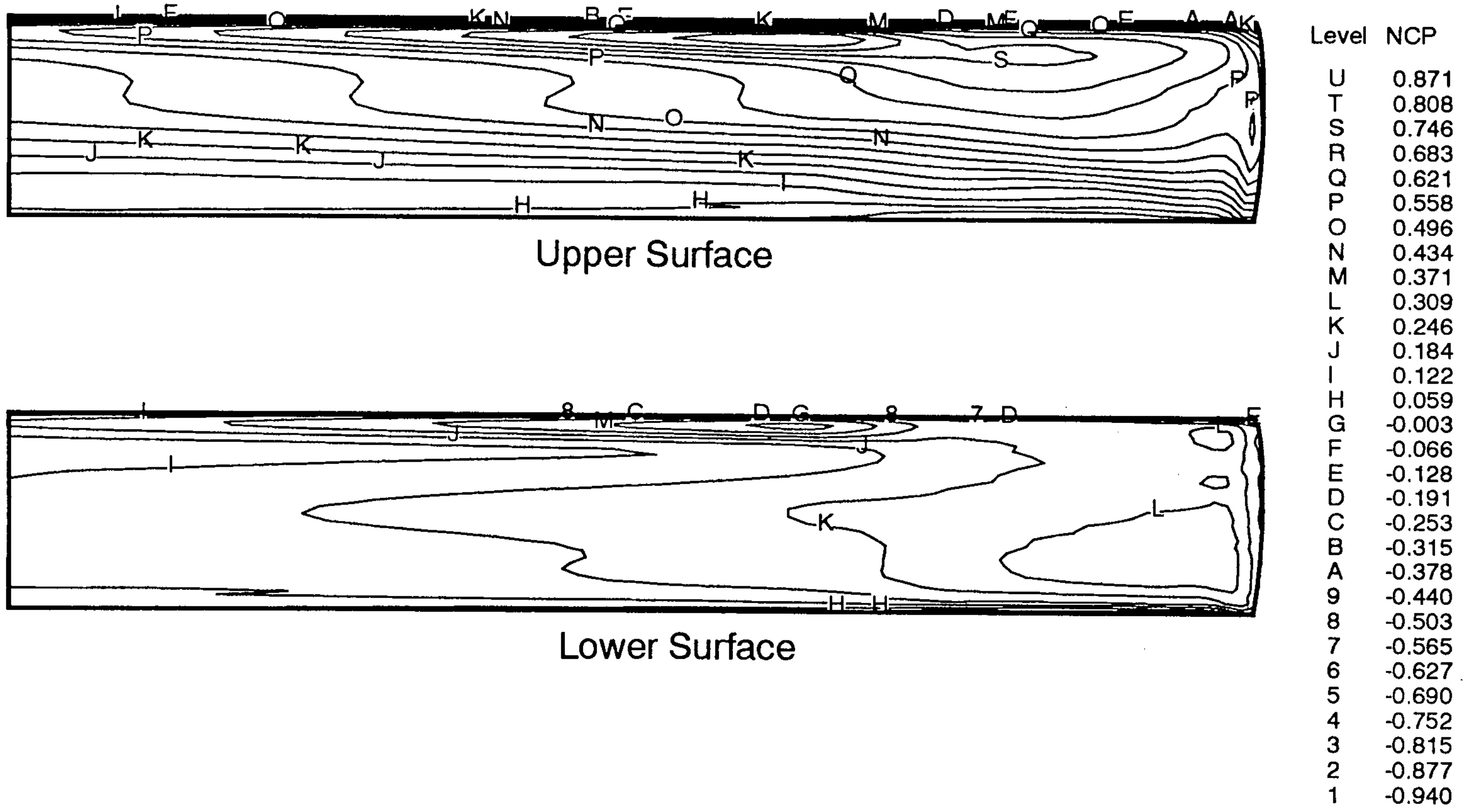

Rectangle-type Blade in Hover

$\theta=\alpha=2^{\circ}$, $M_{tip}=.628$, $\Omega=0.0589$, $R_e=3.7\times10^6$, 129x65x65 Mesh
Calculated Surface Pressure Coefficient Contours

Figure 130. Calculated surface pressure coefficients for rectangle-blade in hover.

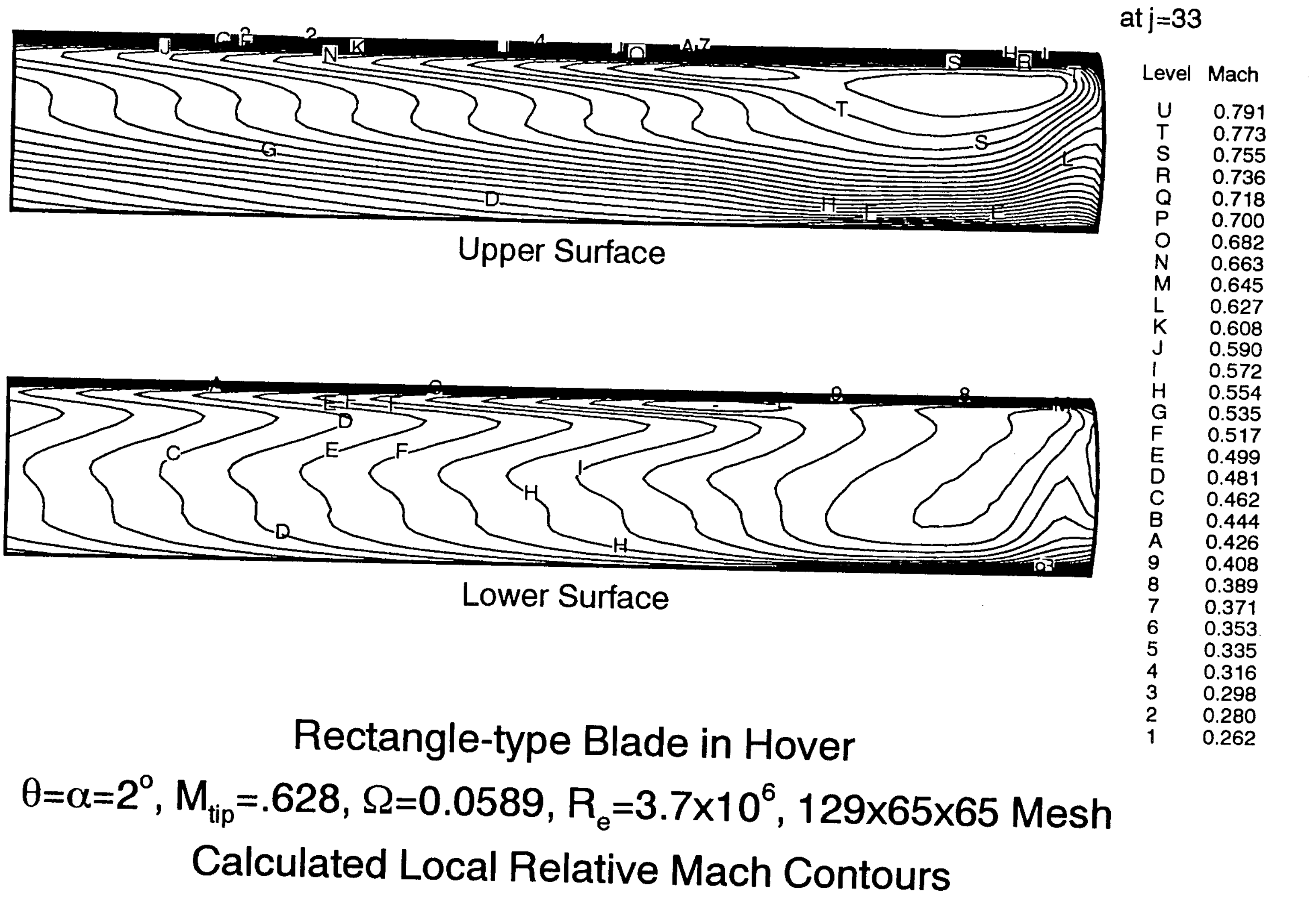

Upper Surface

Lower Surface

Rectangle-type Blade in Hover

$\theta=\alpha=2^{\circ}$, $M_{tip}=.628$, $\Omega=0.0589$, $R_e=3.7\times10^6$, 129x65x65 Mesh

Calculated Local Relative Mach Contours

Figure 131. Calculated local Mach contours for rectangle-blade in hover.

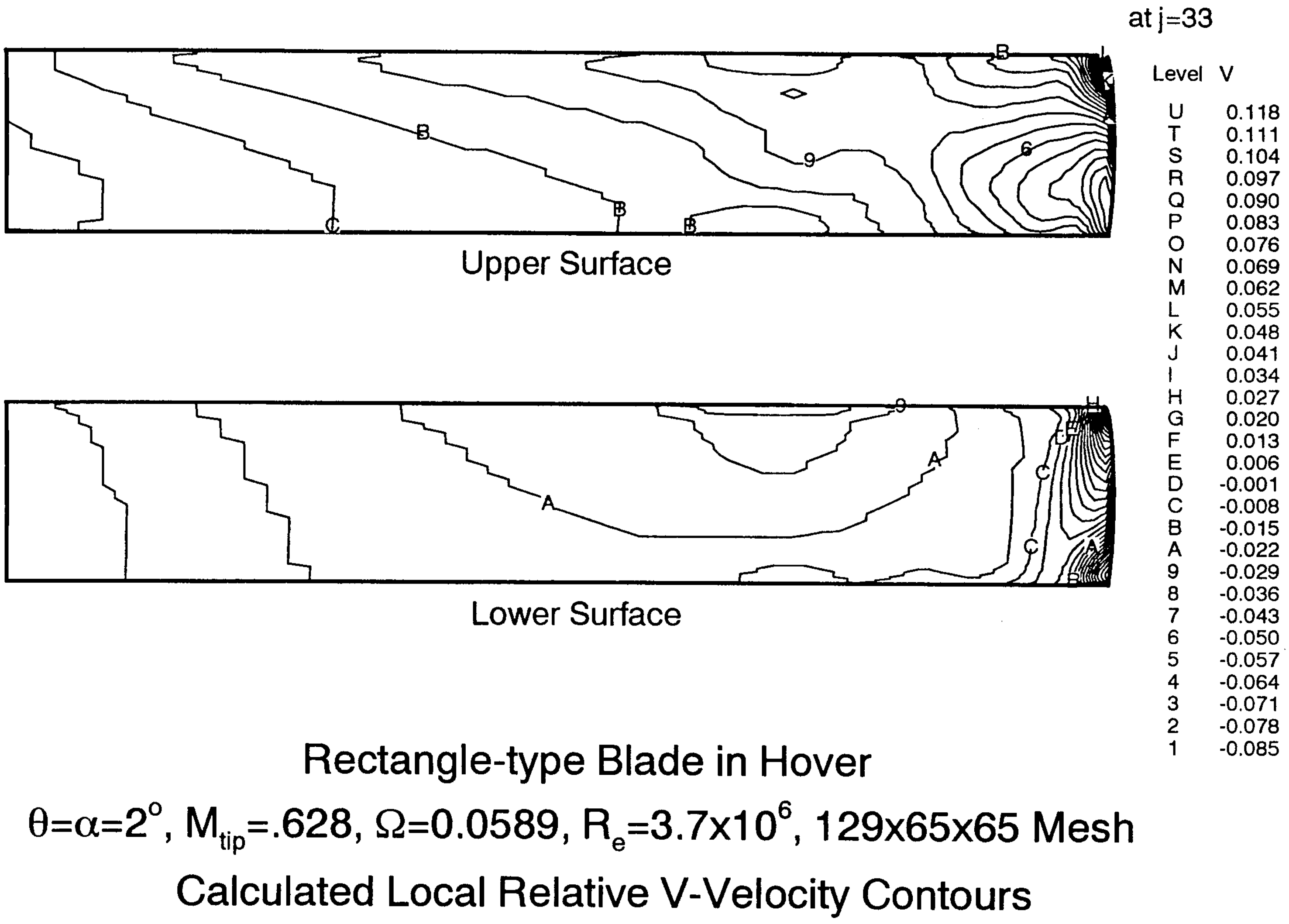

Figure 132. Calculated local relative V-velocity contours for rectangle-blade in hover.

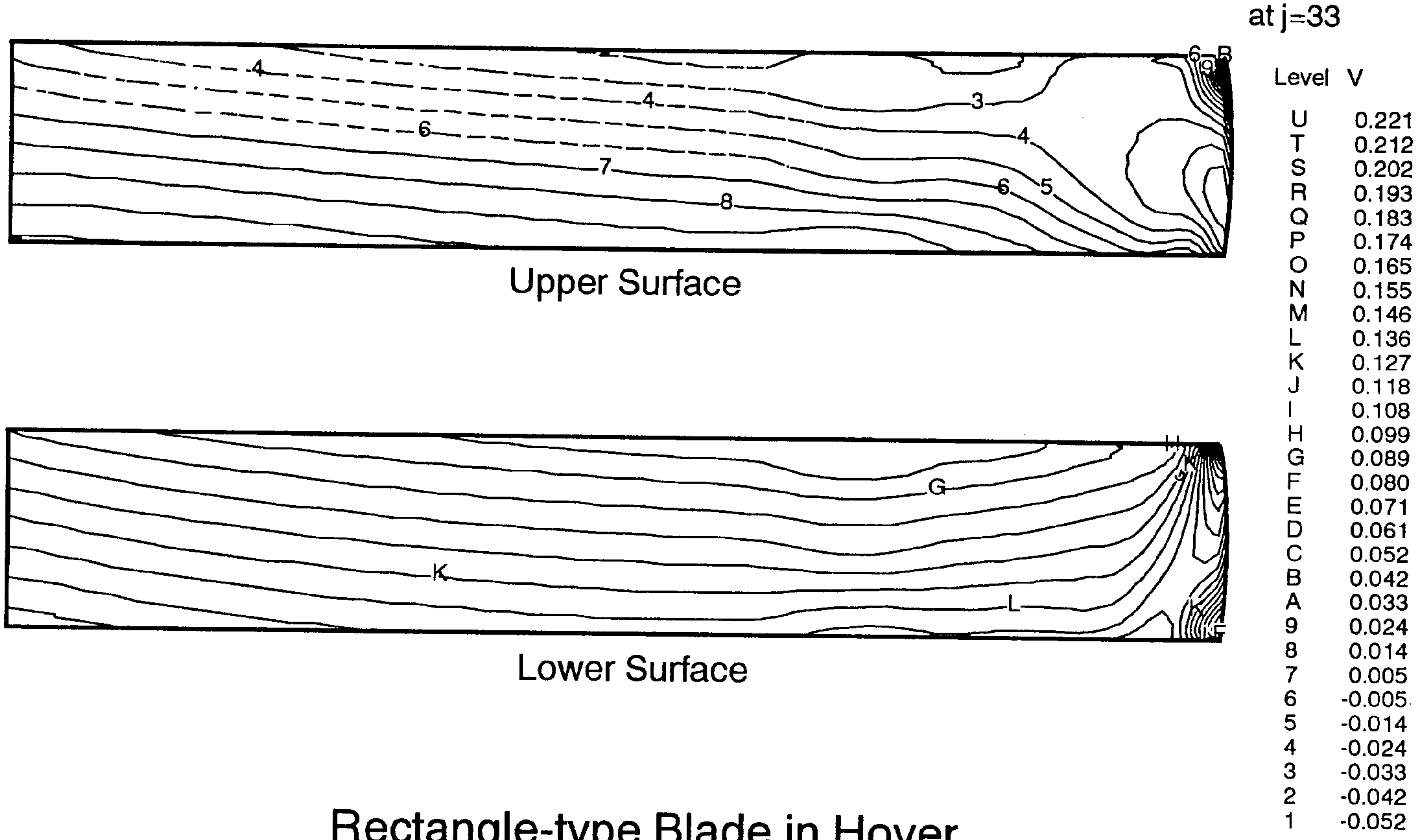

Upper Surface

Lower Surface

Rectangle-type Blade in Hover

$\theta=\alpha=2^{\circ}$, $M_{tip}=.628$, $\Omega=0.0589$, $R_e=3.7\text{x}10^6$, 129x65x65 Mesh

Calculated Local Absolute V-Velocity Contours

Figure 133. Calculated local absolute V-velocity contours for rectangle-blade in hover.

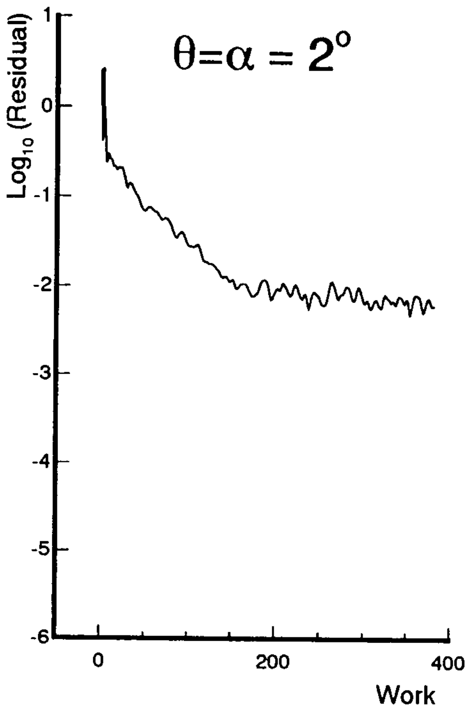

Rectangle-type Blade in Hover

M_{tip}=.628, Ω=0.0589, R_e=3.7x10^6, 129x65x65 Mesh

Convergence History in terms of Residual

Figure 134. Convergence history in terms of residuals for rectangle-blade in hover.

REFERENCES

1. Sankar, N. L., Wake, B. E., Ruo, S. Y., and Malone, J. B., "Numerical Solution of Unsteady Rotational Flow Past Fixed and Rotary Wing Configurations," NASA CP-3022, 1989, pp. 351-374.

2. Srinivasan, G. R., Baeder, J. D., Obayashi, S., and McCRoskey, W. J., "Flowfield of a Lifting Hovering Rotor - A Navier-Stokes Simulation," NASA TM - 102862, 1990.

3. Vatsa, V. N., and Wedan, B. W., "Development of a Multigrid Code for 3D Navier-Stokes Equations and Its Application to a Grid-refinement Study," *Computers & Fluids*, Vol. 18, No. 4, 1990, pp. 391-403.

4. Hu, H., Development of A Rotary Wing Navier-Stokes CFD Code Based on TLNS3D Code, Hampton University, Final Report of DAAL03-92-G-0416, U.S. Army Research Office, P.O.Box 12211, Research Triangle Park, NC 27709, September 1994; also as AIAA Paper 95-1712, 1995.

5. Baldwin, B. S., and Lomax, H., "Thin Layer Approximation and Algebraic Model for Separated Turbulent Flows," AIAA Paper 78-0257, 1978.

SYMBOLS

$\vec{a}_t$	acceleration of transformation velocity
C_p	surface pressure coefficient
c	blade root chord length
D_r	artificial dissipative fluxes
e_r	total energy
F_r	ξ-component inviscid flux
G_r	η-component inviscid flux
G_{vr}	η-component viscous flux
H_r	ζ-component inviscid flux
h_r	total enthalpy
J	transformation Jacobian
M_{tip}	tip Mach number
M_∞	free-stream Mach number
p	pressure
Q_r	all inviscid flux terms
Q_{vr}	all viscous flux terms
R_e	Reynolds number
$\vec{r} = (x, y, z)$	position vector
$\vec{r_p} = (x_p, y_p, z_p)$	pivot point vector or blade axis
S	source term due to moving frame
t	time
U_r	field vector
$\tilde{u}_r, \tilde{v}_r, \tilde{w}_r$	contravariant velocity components
$\vec{V} = (u, v, w)$	absolute velocity
$\vec{V_e} = (u_e, v_e, w_e)$	rotation velocity
$\vec{V_o} = (u_o, v_o, w_o)$	translation velocity

$\vec{V}_r = (u_r, v_r, w_r)$	relative velocity
$\vec{V}_t = (u_t, v_t, w_t)$	transformation velocity
α	angle of attack
γ	gas specific heat ratio
$\bar{\epsilon}$	turbulent eddy-viscosity correction
$\tilde{\epsilon}$	turbulent eddy-conductivity correction
θ	same as α
μ	laminar viscous coefficient
(ξ, η, ζ)	body-fitted coordinates
ρ	density
$\vec{\Omega}$	angular velocity